Universal properties of Self-Organized Localized Structures

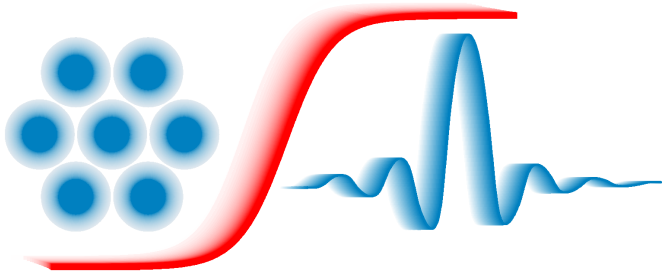

Hendrik Ulrich Bödeker

2007

Experimentelle Physik

Universal properties of Self-Organized Localized Structures

Inaugural-Disseration
zur Erlangung des Doktorgrades
der Naturwissenschaften im Fachbereich Physik
der mathematisch-naturwissenschaftlichen Fakultät
der westfälischen Wilhelms-Universität Münster

vorgelegt von

Hendrik Ulrich Bödeker

aus Bielefeld

-2007-

Dekan:	Prof. Dr. J. P. Wessels
Erster Gutachter:	Prof. Dr. H.-G. Purwins
Zweiter Gutachter:	Prof. Dr. R. Friedrich
Tag der mündlichen Prüfung:	14.05.2007
Tag der Promotion:	13.07.2007

Zusammenfassung

In der Geschichte der Physik hat das Teilchenkonzept bei der Beschreibung von Prozessen auf zahlreichen räumlichen und zeitlichen Skalen eine zentrale Rolle gespielt, angefangen bei der Beschreibung subatomarer Prozessen auf sehr kleinen Skalen bis zu Prozessen wie der Dynamik von Sternen und Planeten auf extrem grossen Skalen. In den letzten Jahren galt ein besonderes wissenschaftliches Interesse selbstorganisierten teilchenartigen Strukturen in selbstorganisierenden Systemen. Solche Strukturen können in einer Vielzahl räumlich ausgedehnter physikalischer Systeme beobachtet werden, so z.B. in nichtlinearen optischen Systemen, Gasentladungen, Halbleitern, granularen Medien und hydrodynamischen Systemen. Trotz großer Unterschiede in den mikroskopischen Eigenschaften der genannten Systeme zeigen die lokalisierten Strukturen eine Vielzahl ähnlicher, scheinbar universeller Eigenschaften auf vergröberten räumlichen und zeitlichen Skalen. Sie können als Ganzes generiert und vernichtet werden, propagieren, in charakteristischer Weise wechselwirken (Beispiele sind Streuung und die Bildung gebundener Zustände) und dynamisch ihre Form verändern.

Ziel dieser Arbeit ist es, einen Beitrag zur Aufklärung der ähnlichen Eigenschaften von selbstorganisierten teilchenartigen lokalisierten Strukturen in den unterschiedlichen Systemen zu leisten. Dissipative Systeme sind dabei von zentralem Interesse. Die Arbeit beginnt mit der theoretischen Betrachtung einiger Prototyp-Modellsysteme wie Reaktions-Diffusions-, Ginzburg-Landau und Swift-Hohenberg-Gleichungen, die jeweils eine größere Klasse verschiedener experimenteller Systeme repräsentieren, in denen lokalisierte Strukturen beobachtet werden können. Da sich die Gleichungen in ihrer Natur stark unterscheiden und alle lokalisierten Strukturen in subkritischen Bifurkationen generiert werden, ist das bisherige Verständnis der qualitativen ähnlichen Phänomene in Bezug auf lokaliserte Strukturen noch sehr beschränkt. Besonderes Interesse gilt daher dem Auffinden von Mechanismen, die das Zusammenwirken verschiedener Komponenten der jeweiligen Gleichungen bei Bildung, Dynamik und Wechselwirkung lokalisierter Strukturen anschaulich machen. Auf diese Art und Weise ergeben sich einige allgemeine Konzepte, die den grundsätzlich verschiedenen Gleichungstypen gemein sind.

Um eine einheitliche Basis für den Vergleich der Dynamik und Wechselwirkung lokalisierter Strukturen in den Feldgleichungen zu schaffen, können letztere mit adiabatischen Eliminationsmethoden auf gewöhnliche Differentialgleichungen reduziert werden. Diese Gleichungen beschreiben die dynamische Entwicklung von langsam veränderlichen Größen der einzelnen lokalisierten Strukturen, typische Beispiele sind Position, Geschwindigkeit und langsame innere Freiheitsgrade. Die reduzierte Beschreibung ist trotz der unterschiedlichen Feldgleichungen von ähnlicher Struktur, die oft maßgeblich von den kontinuierlichen Symmetrien in den Feldgleichungen beeinflußt wird. Unter gewissen Umständen ergeben sich sogar starke formale Ähnlichkeiten zu den Newton-Gleichungen der klassischen Mechanik. Im Detail werden eine Zahl konkreter

Probleme behandelt, darunter Drift von lokalisierten Strukturen in Gradienten, intrinsische Propagation, periodische Formänderungen und verschiedene Arten der Wechselwirkung. Auch der Einfluß von Rauschen in den Feld- und Teilchengleichungen wird diskutiert.

Nach dem gegenwärtigen Stand der Technik sind die Möglichkeiten der numerischen Untersuchung einer größeren Anzahl wechselwirkender lokalisierter Strukturen und ihrer Langzeitdynamik auf der Basis von Feldgleichungen starken Beschränkungen unterworfen. Daher bieten die reduzierten Gleichungen erstmals die Möglichkeit, statistische Eigenschaften großer Teilchenensembles zu untersuchen. Von besonderem Interesse ist dabei ein Vergleich lokalisierter Strukturen und klassischer Newtonscher Masseteilchen. Hierbei stellt sich heraus, daß die Fähigkeit lokalisierter Strukturen, intrinsisch zu propagieren, für eine ganze Reihe neuartiger dynamischer Phänomene verantwortlich ist, die kein klassisches Analogon aufweisen. In diesem Kontext wird zunächst analytisch die Dynamik von zwei lokalisierten Strukturen untersucht, bevor auch größere Ensembles mit Hilfe numerischer Methoden betrachtet werden. Auch Ensembles intrinsisch propagierender Teilchen unter dem Einfluß von Rauschen (aktive Brownsche Teilchen) sind von Interesse.

Strukturen mit teilchenartigen Eigenschaften treten nicht ausschließlich in physikalischen Systemen auf, sondern existieren auch in biologischen Systemen, z.B. in Form von Zellen. In diesem Fall existiert generell keine Feldbeschreibung und es ist daher kaum möglich, eine selbstkonsistente Beschreibung des dynamischen Verhaltens zu finden. Wir betrachten dieses Problem für die eukaryotische Zelle *Dictyostelium discoideum*, die vielen Biologen als Prototyp-System dient. Eine zentrale Grundlage für die Untersuchung der Dynamik einzelner Zellen bilden mikrofluidische Anordnungen. Mit Methoden der stochstischen Datenanalyse gelingt es, aus experimentell gewonnenen Zelltrajektorien Langevin-Gleichungen für die Dynamik isolierter Zellen abzuleiten, die eine Teilchenbeschreibung darstellen und starke Ähnlichkeiten zu den reduzieren Gleichungen für selbstorganisierte Strukturen in physikalischen Systemen aufweisen. Desweiteren kann der Einfluß verschiedener chemischer Stimuli auf deterministische und stochastische Anteile der Dynamik bestimmt werden, was Rückschlüsse auf die zugrunde liegenden Prozesse innerhalb der Zellen ermöglicht.

Abstract

Throughout the history of physics, the concept of particles has always played a central role, going from very small scales as involved in the description of sub-atomic structures up to very large scales as relevant e.g. for the dynamics of stars and planets. In recent times, much scientific interest has been dedicated to localized, particle-like structures in systems capable of showing self-organization. The latter can be observed in various physical spatially extended systems like nonlinear optical systems, gas-discharges, semiconductors, granular media and hydrodynamic systems. Looking at the properties of the localized structures in these systems, it turns out that in spite of strong differences in the underlying physical microscopic processes, many structures have similar, apparently universal characteristics on coarser spatial and temporal scales. They can be generated and annihilated, propagate, interact, show scattering processes as well as the formation of bound states and may perform dynamic deformations of their shape.

This work tries to contribute to explaining the similar behavior of the self-organized particle-like localized structures (LSs) in different systems. The focus of interest lies on systems in which dissipative processes play an essential role. In detail, we first consider several prototype systems like reaction-diffusion, Ginzburg-Landau or Swift-Hohenberg equations which each represent a number of different experimental systems capable of exhibiting LSs. As the equations are structurally rather diverse in nature and all LS are generated in subcritical bifurcations, there is currently a rather limited understanding of the qualitative similarities in the dynamics of the LSs. Consequently, particular emphasis is put on finding illustrative mechanisms which help to understand how the individual constituents of each equation interact in order to allow for the formation, dynamics and interaction of LSs. In this way, a number of basic concepts can be identified that are common in systems of very different nature.

A common basis for comparing the dynamics of single and several weakly interacting LSs in different types of systems can be created reducing the field equations to ordinary differential equations by methods of adiabatic elimination. The reduced equations describe the evolution of quantities like positions, velocities and slowly varying internal degrees of freedom of the LSs. Even for rather different types of field equations the reduced equations are of similar structure, often being essentially influenced by the continuous symmetries present in the field equations. In particular, in some situations there are strong formal similarities to those equations describing the dynamics of classical Newtonian mass particles. Several concrete problems are addressed, including drift of LSs in spatial inhomogeneities, intrinsic propagation, periodic oscillations in shape and different types of interaction behavior. Also, the effect of noise in the field equations and its consequences for the reduced equations are discussed.

As due to current limitations of computational methods the interaction of only small

numbers of LSs can be simulated numerically on the basis of field equations when statistical properties or long-time dynamics are of interest, the derivations of the reduced equations essentially enables the investigation of statistical large particle ensembles. A particularly interesting point is the comparison of LSs to classical Newton particles. It is found that the property of many LSs to propagate intrinsically is responsible for a number of dynamic processes that are very different from their classical counterpart. We first carry out analytic considerations for the dynamics of two localized structures before larger ensembles consisting of many LSs are investigated with the help of numerical simulations. Also, ensembles of actively propagating particles propagating under the influence of noise (active Brownian particles) are analyzed.

Objects with particle-like properties are not found exclusively in the field of physics, but exist also in biological systems, for example in the form of cells. For these structures, there generally exists no description on the level of field equations and consequently is is hardly possible to find a self-consistent description of the dynamical behavior. We address this problem for the eukaryotic cell *Dictyostelium discoideum* which serves as a prototype system for many biologists. A basis for the experimental observation of the dynamics of isolated cells is provided by the use of microfluidic devices. Using methods of stochastic data analysis, Langevin equations for the motion of isolated cells can be extracted from experimentally recorded cell trajectories, representing a description of the cell dynamics on a particle level and showing strong formal similarities to the reduced equations for LSs in physical systems. Furthermore, the dependence of deterministic and stochastic parts of the dynamics on different chemical stimuli can be estimated, giving important implications for the underlying processes inside the cells.

Contents

Chapter 1

Introduction

1.1 Self-organized localized structures and the particle concept

Throughout the history of physics, there are numerous examples for successful theories in which the concept of particles or particle-like structures plays a central role. Already the Greek philosophers believed in the existence of atoms of which all matter is composed. In this way, they notionally divided the objects of natural perception into subunits that may undergo interaction, reducing the understanding of nature to that of understanding the properties of atoms and their interrelations. In order for a concept of subdivision in general and a particle concept in particular to work, the single particles should retain their individuality to a large extent while interacting. As a general rule, particle models are the more convincing as the smaller the number of subunits, the simpler the postulated interaction and the broader the scope of application.

We point out two theories related to the particle image which are of particular relevance due to their extremely wide range of application. On the one hand, there is classical mechanics capable of describing (with appropriate extensions) the dynamics of very small particles like electrons in a plasma to very large objects like stars on the scale of light years. On the other hand, there is the concept of the atom and the periodic table which represents an essential basis for explaining the structure of matter. Furthermore, atoms themselves again consist of subunits like for example electrons, neutrons and protons. To understand processes on larger scales, extended particle concepts play an important role, going from molecules to particles in emulsions and aerosols, grains in granular media and precipitations in alloys. Less evident examples are "quasi-particles" like phonons, magnons and Cooper pairs.

Looking at recent scientific developments, an increased interest has developed in particle-like structures that can be observed on scales above micrometers and -seconds, their existence and dynamics including self-organization as an essential ingredient. Typical examples include living cells, swarms of birds or fish, myosin heads on actin filaments as well as flow of traffic or pedestrians. However, most animate systems are too complex to understand on the basis of quantitative models at the current state of research although there are some examples of particle-like structures like nerve pulses for which a reasonable amount of understanding could already be obtained.

Recent investigations in the field of complex systems have focussed on a number of

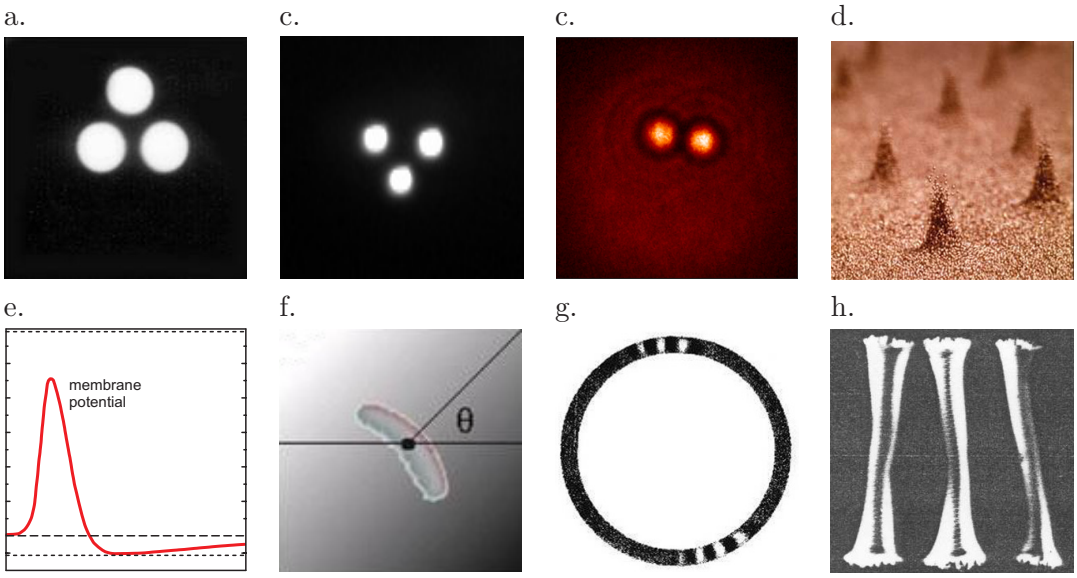

Figure 1.1: Examples for experimentally observed LSs in dissipative systems: a. planar ac gas-discharge system [1], b. planar dc gas-discharge system [2], c. optical single feedback system [3], d. oscillating granular medium [4], e. nerve pulse [5], f. chemical reaction on a catalytic surface [6], g. binary fluid mixture [7], h. semiconductor device [8].

unanimated systems capable of showing the formation of stable localized structures with particle-like properties (LSs) that are particularly suitable to access both experimentally and theoretically. These systems include gas-discharges, semiconductors, optical systems, granular media and hydrodynamical as well as chemical systems (Fig. 1.1). All of the above examples belong to the class of dissipative, nonlinear and spatially extended systems. The mechanisms responsible for the formation of the LSs are far from being well understood in many of the systems up to now. A particularly fascinating aspect is even less clarified: while the systems are very different on a microscopical level, on large scales the dynamics of the LSs shows clear similarities. This idea of "universal" behavior is frequently encountered during research on nonlinear systems. As an example, in very different finite-dimensional dynamical systems, close to special points where the dynamics becomes slow (typically supercritical bifurcation points) the behavior of the system is determined by only a small number of slowly evolving quantities. Using methods of adiabatic elimination like the center manifold theory, it is often possible for such systems to reduce the system to a low-dimensional normal form. The latter are identical for very different systems, allowing for a systematic classification of the possible bifurcations according to criteria like the symmetries of the equations. Normal form theories have also been developed for infinite-dimensional systems, for example for the supercritical transition from a homogeneous to a globally patterned state. Unfortunately, the exploration of the universal properties of LS is far less advanced than it is the case for supercritical bifurcations as the generation of LSs generally occurs in subcritical bifurcations. In this situation, methods like standard perturbation theory can not be applied.

This work tries to contribute to the attempt to overcome the above problems and to

explain the common properties of LSs. The largest part of the investigation focusses on systems in which dissipation plays an essential role. In the remaining introduction, we will look at the history of research on LSs and discuss some key ideas like the role of dissipation, attractors and the definition of LSs. In Chap. 2 we try to explain how LSs are stabilized in different types of field equations and which effects are responsible for dynamic phenomena. Due to the lack of generally applicable mathematical techniques, we put particular emphasis on finding illustrative mechanisms, an aspect that has been neglected in many other theoretical works. In detail, we will have a look at reaction-diffusion, Ginzburg-Landau or Swift-Hohenberg types of equations. While many other equations are known to exhibit the formation of LSs as well, the above equations can be considered prototypical and capable of representing larger classes of experimental systems. Another important aspect is given by the fact that once a stable LS is known to exist, it can undergo changes in its shape during its dynamical evolution. If the deformations are not too strong, it is indeed possible under appropriate circumstances to reduce the field equations to ordinary differential equations using methods of adiabatic elimination. In Chap. 3 we present mathematical methods suitable to accomplish this task and apply them to a number of selected problems involving both isolated and interacting LSs. We will see that on the level of the reduced equations, the dynamics can be described in terms of certain normal forms, there providing a good basis for explaining similarities in the dynamical behavior. Also, we deal with the influence of noise. Apart from reflecting the particle-like behavior of the LSs, the reduced equations also offer a method to treat the dynamics and interaction of large ensembles of LSs, which is usually only possible to a rather limited amount on the basis of field equations due to technical limitations of current computational means. In Chap. 4, investigate the long-time behavior of large ensembles of LSs and compare our finding to classical Newton particles. For actively propagating LSs, a number of new phenomena are found that have no classical counterpart. Again, also the influence of fluctuations on the dynamics is considered as well. Finally, in Chap. 5 we make an excursion to the field of biology where objects with particle-like behavior can be found in the form of living cells. Using methods of stochastic data analysis, we will find a reduced dynamical description that reveals formal similarities with the LSs found in physical systems.

1.2 A historical survey

The fact that structures preserve their shape and properties in the course of time and therefore can be considered as a localized, solitary entity on appropriately chosen scales has been known for a long time. However, the explicit idea that in particular in inanimate systems structures do not simply exist, but can be generated on a homogeneous background state due to mechanisms of self-organization became part of the general perception only in the last decades. In the following, we want to give a rough sketch of some important historic developments in research on LSs.

As early as in 1831 Faraday saw solitary LSs in a vibrating layer of fine powder [9] which today would probably be termed oscillons. Shortly afterwards, Russell observed a solitary water wave on a channel generated by a stopping ship which propagated along the channel without dispersing for several kilometers before decaying [10]. At the time of the above discoveries, the individual observations were considered as curious

phenomena, however they neither triggered an extensive further research nor led to an attempt to compare them. It is known that Russell performed experiments in a large water tank in the following years, finding that two water waves may pass through each other when colliding. Russell's observations were supported by theoretical works performed by Lord Rayleigh [11] and Boussinesq [12] around 1870. These finally led to the derivation of the KdV equation allowing for solitary solutions by Korteweg and de Vries in 1895 [13]. It was realized that the KdV equation is conservative in the sense that one can define an energy which remained conserved during the dynamical evolution. On the experimental side, around 1900 most experimental works on LSs commonly exploited dissipative effects. In 1900 Ostwald conducted experiments on the propagation of chemical pulses on metallic wires [14]. Lehmann found the formation of localized anode spots only two years later [15].

Conservative and dissipative systems received almost equal interest until about 1955, around which a number of highly influential works was published. On the dissipative side, one may mention the discovery of the mechanisms of nerve pulse excitation by Hodgkin and Huxley in 1952 [5] and the simulation of nerve pulse propagation using reaction-diffusion equations and real electrical networks [16]. With an increase of the quality of semiconductor materials from about 1960 onwards the formation of current filaments has been reported for various circumstances. On the conservative side, the special role of the KdV equation was realized by Zabusky and Kruskal in 1965 [17]. They demonstrated that the KdV equation is completely integrable [21] and introduced the inverse scattering technique, which is a way to produce analytical solutions of the nonlinear partial differential equation by transforming the problem to a linear one. Furthermore, they introduced the term "soliton" as a name for the localized solitary solutions of the KdV equation. Although the works on both nerve pulses and the KdV equation can be considered as highly relevant from a modern point of view, they did not trigger similar historical developments. In the wake of Zabusky's and Kruskal's work, a large amount of research was invested in LSs as solution of conservative equations. In particular, one may mention that in 1972 Zakharov and Shabat found another integrable equation and thus demonstrated that the inverse scattering technique is universal and can be applied to a whole class of physically interesting equations [18]. In comparison,

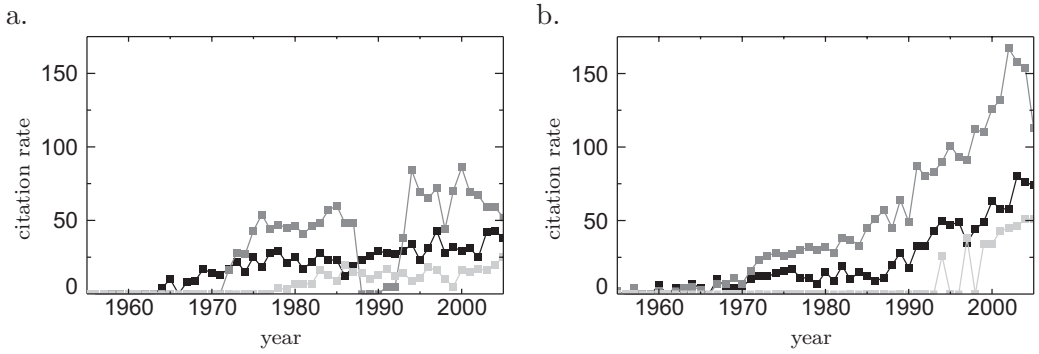

Figure 1.2: Citation rate of a. the three "conservative works" [17] (black), [18] (medium grey) and [19] (light grey) as well as b. the "dissipative works"[5] (black), [20] (medium grey) and [16] (light grey) as a function of the year according to the ISI database (November 2006).

the interest in dissipative structures remained rather low and remained part of the corresponding individual fields of research (for example solid state physics [22–24] etc). We want to quantify this aspect by looking at the yearly citation rates of highly cited articles on conservative and dissipative structures according to the ISI database (Fig. 1.2). For the conservative side, we choose the above mentioned works [17] and [18] as well as an highly cited article by Strauss [19] on solitons in higher dimensions. Dissipative LSs are represented by [5] and [16] as well as the work of Turing on reaction-diffusion equations [20] although the latter is not dealing directly with LSs. Comparing the left graph (conservative case) with the right graph (dissipative case), we indeed see that unlike the dissipative case, the number of conservative citations strongly increases after 1970 with respect to the citation rate in later years.

One may ask for the reason of the explosive increase on works dealing with conservative LSs. A likely explanation is the point that the introduction of the inverse scattering theory did not only allow for finding analytical solutions of nonlinear partial differential equations in a time where numerical techniques were hardly available, but established a connection to various branches of mathematical sciences. Hence, the conservative systems dominated research in the following decade. Up to about 1990 it was common agreement to reserve the term "soliton" for solitary solutions of special nonlinear differential equations like the KdV, the nonlinear Schrödinger (NLS) or the sine-Gordon (SG) equation that were integrable and that could be treated via the inverse scattering technique (see for example [25] for an overview). The equations usually allow for stable solutions only in one spatial dimension. Soon people got interested in stable LSs also in higher-dimensional systems. These can be found by extending the original equations with additional conservative terms (for example higher-order polynomials) which break the integrability of the system. Already here a first conflict arose whether the LSs in the extended systems should be called solitons as well. The term "solitary wave" was introduced for LSs in conservative, yet non-integrable systems. One should again point out that the largest part of works on conservative systems at the time was theoretical.

The overall situation changed after 1980. Fig. 1.2 shows that in this time the works on dissipative LSs experienced a significant increase in their citation rate. Aside from advances in mathematical techniques, an important aspect of this evolution is that computers with a sufficiently large numerical capacities became available for regular research groups so that analytic solutions were no longer a premise for a theoretical treatment. The first systems investigated were reaction-diffusion equations and different forms of the Ginzburg-Landau (GL) equation. On the experimental side, a number of different systems carrying LSs was investigated, many of them involving charge transport [26–29]. As on the conservative side much research had already been carried out, people became interested in weak dissipative perturbations of the original conservative equations. In this case, using perturbative techniques often analytical solutions were possible to obtain (see for example [30] and references therein), showing details of how the solitons decay in the long-time limit. An experimental motivation for the theoretical works was given by the fact that around 1980 the evolution of lasers and materials had advanced far enough to produce the first solitons in glass fibers, which suffered weak losses during propagation and in the stationary case can be described using the weakly perturbed conservative equations. In order to distinguish the solitary LSs in strongly and weakly dissipative systems from those in conservative systems, a number of different terms was introduced, e.g autosoliton (in the Russian literature), spot, pulse and filament. The no-

tion “dissipative soliton” which basically summarizes all important properties appeared in an article title the first time in 1981 [31], but was likely only accepted at that time because the author Petviashvili was already very famous.

After 1990, the interest in LSs in dissipative systems continuously grew (compare Fig. 1.2), accompanied by an increased focussing on self-organization in general. In contrast, the number of works on the classical soliton equations stagnated. Dissipative LSs were found in gas-discharges, semiconductors, optical systems, granular media, hydrodynamics and electrical networks, just to name a few (Fig. 1.1). It became commonly accepted to use the term “dissipative soliton” for LSs in dissipative systems [32–34]. Other more specialized terms were also created, for example oscillon or cavity soliton. More details on these recent developments will be given throughout this work. Although many similarities concerning the phenomenology of the different systems were realized, attempts to compare findings in different classes of systems are just beginning to emerge. One reason for this problem may be the different terminologies and general concepts in the individual fields.

1.3 LSs, dissipation and attractors

Looking at the different terms for LSs introduced in the historical development, one may ask what a good definition for a self-organized, particle-like solitary LS may be. A rather strict definition may state that the LS must be a stable stationary localized state in a system with much larger spatial extension that can coexist with a purely homogeneous stationary state for the same system parameters and that exists independent of the system boundaries. Furthermore, the interaction between several LSs should vanish for a large mutual distance, and on a sufficiently large domain an arbitrary number of LSs should be able to exist.

Many structures in dissipative systems fulfil these claims, and the same holds for conservative systems as well although some care has to be taken concerning the stability definition (see our consideration on attractors below). However, as we will see in the course of this work there are some structures which fulfil most of the claims above and would intuitively be considered to be of solitary nature, but nonetheless violate the strict definition. In certain scenarios, the background state is not stationary and homogeneous, but either patterned with low amplitude or homogeneously oscillating in time. In other cases, the assumption on vanishing interaction for large distances is violated. Here, some type of “integral coupling” occurs that may potentially put the LSs under competition. Nonetheless, it is often reasonable to accept these violations from the strict definition as long as the LSs keep most of their solitary properties.

We want to address the aspect how the above definition of LSs can be applied in a given experimental system. In most cases the latter are typically three-dimensional in space, with one direction being different from the other ones as it marks the main direction in which energy and material is transported. Typical examples are given by gas-discharges with one main direction of the external applied electric field or optical systems with one main propagation direction of the incident light beam. The three-dimensional structures often have a filamentary shape directed along the main direction of transport, so that it is common to identify LSs in a two-dimensional plane perpendicular to the main direction as the structures are clearly localized here (Fig. 1.3). The

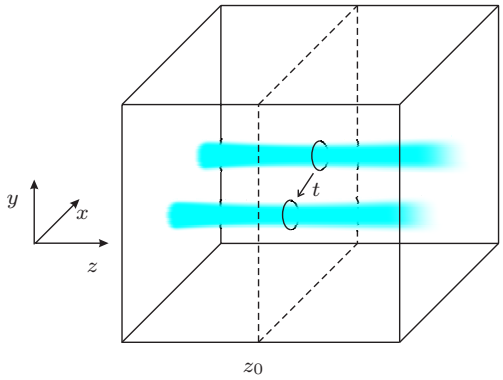

Figure 1.3: Definition of LSs in a three-dimensional system: formation of a filamentary structure in three-dimensional space with the main direction z and homogeneous boundary conditions. In a fixed perpendicular x-y-plane with $z = z_0$ (dashed lines), the structure is localized and undergoes a temporal evolution, thereby defining a LS.

corresponding theoretical models then either describe the full spatial evolution of the system as a function of time or the temporal evolution in the perpendicular plane. The above definition can be applied in both dissipative and conservative systems (examples for LSs in the conservative case are given by water waves or specially designed electrical networks [25]).

A distinction between conservative and dissipative systems seems to be a natural way of classifying pattern-forming systems as from the experience obtained in other field of physics this point makes a central difference in the dynamic behavior of the underlying system. Often, conservative systems even have several conserved quantities, which can be used to implicitly define the dynamics of the system and which restrict the evolution to special manifolds. Solutions from a certain region of the phase space are generally known to be incapable of asymptotically approaching a compact attractor, as it is possible for dissipative systems. Unfortunately, theoretically the aspect of dissipativity is essentially not trivial in the context of LSs because although many systems capable of forming of LSs require an input of energy or material to work, it is unclear in which way a transformation of one form of energy to the other is relevant for the formation of LSs. In some systems like chemical ones, there is not even a clear definition of energy available so that there is currently no unique definition of conservative and dissipative systems in general. In the following, we will briefly discuss a number of concepts, but it will become obvious that all of them have certain drawbacks.

1. In many classical systems, there is often a clear intuition of what energy physically means. Hence, when the system is perturbed, one may check how the energy function or functional evolves under the perturbation. As a simple example, one may consider the damped harmonic oscillator

$$\partial_t^2 x + \epsilon \partial_t x + x = 0 \tag{1.1}$$

where in the conservative case $\epsilon = 0$ the overall energy $E = (\partial_t x)^2/2 + x^2/2$ is constant. It is easy to see that in the general case, $\partial_t E = -\epsilon(\partial_t x)^2$, showing

that energy is dissipated in the non-resting state. The same idea can usually be applied to classical soliton equations like the nonlinear Schrödinger (NLS) equation in which the integral of the energy density is conserved.

2. Gradient systems can be identified by the fact that the evolution of their state vector $\boldsymbol{q}$ can be described by the gradient of a functional, i.e.

$$\partial_t \boldsymbol{q} = -\frac{\partial F(\boldsymbol{q})}{\partial \boldsymbol{q}}. \tag{1.2}$$

Depending on the type of system, F is referred to as free energy, enthalpy, Lyapunov functional etc. Note that Eq. (1.2) has no classical limit. Nevertheless, the system evolves in such a way that $F(\boldsymbol{q})$ is reduced and the minimum of $F(\boldsymbol{q})$ corresponds to the stable final state in agreement with the intuitive idea of dissipation.

3. A rather abstract definition of conservation can be given in finite-dimensional systems by looking at evolution of small volumes in phase space. When an arbitrary volume element stays conserved in measure during the dynamic evolution, the system is called conservative. In systems of the form

$$\partial_t \boldsymbol{q} = \boldsymbol{f}(\boldsymbol{q}) \tag{1.3}$$

with $\boldsymbol{q} \in \mathbb{R}^n$, $\boldsymbol{f} \in \mathbb{R}^n$, there is an easy criterion to check the conservation property as the phase space volume is conserved if and only if

$$\operatorname{div} \boldsymbol{f} = 0. \tag{1.4}$$

Furthermore, in dissipative systems attractors in a certain region are only possible if the phase space is contracted. However, there are two drawbacks concerning this definition. First, for arbitrary types of systems the definition may appear rather abstract and can potentially not be connected to classical energy functionals. Second, there is currently no method of transferring the criterion from system of finite dimensionality to such of infinite one, including in particular partial differential equations.

4. Attractors are generally encountered only for dissipative system (we will discuss this aspect in more detail below). Hence, the observation of an attractor gives a good indication that dissipation plays a role. However, some care has to be taken concerning this point. As an example, a (conservative) system of ideal gas particles in thermodynamical equilibrium always tends to show a Maxwellian distribution, so that care has to be taken about the exact definition of the term attractor.

5. All conservative systems are invariant under the time reversal transformation $t \to -t$. If necessary, the latter is accompanied by the corresponding transformations of some physical quantities, for example, velocities and magnetic fields must change sign as well. Correspondingly one may define a dissipative system as a system

that is not invariant under the time reversal transformation. This is probably the most general definition, evidently implying certain restriction on the dynamics of the system in question. We will therefore generally stick to this definition unless one of the other definitions offers particular advantages.

Commonly it is stated that an exclusive feature of dissipative systems is the existence of attractors. Mathematically, these attractors can be defined in the following way [35, 36]. One defines an evolution operator $\boldsymbol{f}(\cdot, t)$ that maps the initial state of the system $\boldsymbol{q}(t = 0)$ onto the state $\boldsymbol{q}(t = t_0 > 0)$. Then the attractor A is a closed subset of the phase space such that

1. A is invariant under $\boldsymbol{f}$,
2. there is a neighborhood of A called $B(A)$ (the basin of attraction for A) of finite measure with $B(A) = \{s|$ for all neighborhoods N A there is a time T so that for all $t > T$ $f(t, s) \in N\}$. In other words B(A) is the set of points who 'enter A in the limit',
3. there is no subset of A with the above properties.

In the context of LSs, the applicability of the above definition may cause some peculiarities. Let us first consider an infinitely extended system and an initial perturbation of the ground state that should cause a LS to form. In dissipative systems, the perturbation may converge to a LS of fixed shape. If the initial perturbation however is infinitesimally displaced the resulting LS will show the same displacement so that one obtains problems with the closedness of the attractor. The problem can be overcome by defining appropriate equivalence classes via shifts with respect to the continuous symmetries present in the system. In this sense, one now usually observed that slight changes of the shape of the initial perturbation cause the same structure to appear so that the LS is "point-like in phase space" and fulfils the attractor definition above. Considering the same situation for conservative systems, an initial perturbation of the ground state will have a defined overall energy that cannot vanish in the course of time. However, it is commonly found that a LS forms and the excessive energy is radiated away, thereby "vanishing at infinity". Changing the form of the perturbation not only results in a shift with respect to the continuous symmetries of the system, but also in the shape itself. The possible solutions can usually be characterized as a continuous one-parametric family. Here is an important difference to the dissipative systems, the initial conditions are still attracted when appropriate equivalence classes are defined, however intuitively one would not consider the attractor as "point-like". Furthermore, the infinite domain in some sense takes over the role of a dissipative sink.

When going to finite domains, the difference between conservative and dissipative systems becomes more evident. When supplying the conservative systems with "conservative" (for example periodic) boundary conditions the energy cannot leave the domain and commonly no convergence to an asymptotic state is found. In contrast, dissipative systems may converge to a point-like structure even with "conservative boundaries". We see that with sufficient care, we may attribute to dissipative systems the existence of localized attractors, especially when using the definition of broken time-reversal symmetry.

1.4 Particle phenomenology and the role of dissipation

In the above section we have discussed that one of the most significant differences between conservative and dissipative systems is the existence of "point-like" attractors, in particular on finite domains. One may now ask whether there are also essential differences concerning the phenomenology of elementary dynamical processes involving LSs. In this context, elementary dynamical processes shall be defined as generic behavior of the solutions of the underlying field equations reflecting the solitary and particle-like behavior of the LSs. Typical examples are given by single LSs which propagate or change their shape as well as several LSs interacting with different outcomes, preserving their shape or being generated and annihilated. Table 1.1 gives an overview of elementary processes frequently reported in the literature for conservative and dissipative equations. We only consider theoretical systems here to ensure that the nature of the system can be clearly determined according to one of the definitions of dissipativity discussed in the last section. The meaning of most phenomena should be directly clear, however we want to make some remarks. The term "free propagation" refers to the possibility for a solution to propagate with an arbitrary velocity that just depends on the initial conditions. In contrast, the term "intrinsic propagation" refers to the phenomena that there is one special dynamically stabilized propagation velocity to which the solution converges in the long-time limit. The term "breathing" characterized periodic deformations of the shape of the LS. In a merging or fusion event, two LSs collide with one structure remaining, whereas in an annihilation event the structures become totally extinct. More details on the individual phenomena in particular for dissipative systems can be found

	single stationary	many stationary	arbitrary velocity	intrinsic velocity
conservative case	[17, 25]	[25]	[25]	not found
dissipative case	[37]	[34, 38, 39]	[40]	[37, 41, 42]
	breathing	scattering, repulsion	interpenetration	bound states
conservative case	[43, 44]	[45–48]	[49]	[50, 51]
dissipative case	[52, 53]	[54, 55]	[56, 57]	[58, 59]
	rotating clusters	propagating clusters	merging, annihilation	generation
conservative case	[50]	[60]	[45, 47]	[61]
dissipative case	[55, 62, 63]	[55]	[55]	[55]

Table 1.1: Overview on the existence of different "elementary processes" involving LSs in conservative and dissipative systems. A citation indicates that the corresponding process has been documented and gives the source.

in the course of this work.

As the table shows, most phenomena can actually be found in both conservative and dissipative systems. An exception is given by intrinsic propagation which is only found for dissipative systems as it contradicts the Galilean invariance which all classical soliton equations possess. Consequently, the phenomenology of LSs in conservative and dissipative system is not strictly different. On the other hand, looking in more detail on the number of references which report on the individual phenomena it turns out that there are certain phenomena that are characteristic for the individual types of systems and mark exceptions in the opposite type. As an example, the interpenetration of two LSs in a collision event is frequently found in integrable conservative systems and weak dissipative modifications, but seldom observed in strongly dissipative systems. In contrast, intrinsic instabilities like breathing are characteristically found in dissipative systems.

Chapter 2

Models and mechanisms

In the introduction, we have briefly mentioned different classes of experimental systems in which LSs can be found and shown some images of typical findings (Fig. 1.1). In order to describe the individual systems, different types of models have been developed, going from microscopic descriptions on the level of individual particles (based for example on single grains for granular media) over continuum models like reaction-diffusion systems to very universal amplitude-type of equations like Ginzburg-Landau models which can be applied to very different systems. While some of the models are closely connected to first-principle considerations, others have been set up only on a phenomenological basis.

In spite of a large number of theoretical works on the formation of LSs, two important aspects are often attributed only a minor role. On the one hand, a comparison of the model predictions with experimental findings is frequently neglected, in particular on a quantitative level. Second, although many interesting processes are found either in an analytical or numerical way, in many cases no mechanisms are given to obtain an intuitive image of the underlying processes. As the aim of this work lies on finding common properties of LSs in different systems, we will focus in particular on the second aspect. To this end, we have a closer look at three types of equations each of which are known to be capable of describing different classes of experimental systems. These equations are reaction-diffusion, Ginzburg-Landau and Swift-Hohenberg equations. The individual equations can be derived rather rigourously for some experiments and have been phenomenologically motivated to hold for an extended number of systems.

In our investigation, we try to give necessary perquisites for the existence of LSs as well as mechanisms explaining the formation of LSs as interplay of different dynamical effects. Similar considerations are carried out for the dynamic destabilization of LSs in bifurcations (for example to propagating or breathing states) and the interaction of several LSs. At the end of the chapter, we discuss whether there are some general principles that the above equations have in common.

A technical issue that remains to be discussed before starting is that parts of this chapter heavily rely on finding numerical solutions of time-dependent deterministic field equations. Most numerical simulations presented in this and partly in the following chapters have been carried out using the program "COMSOL Multiphysics" which is capable of solving coupled nonlinear partial differential equations using finite element methods. Here, the space of interest is discretized using a fixed grid of triangular elements which in one spatial dimension correspond to equidistant points. The typical number of base points used to produce the results presented below lie around 2000

for a one-dimensional and around 20000 for a squared two-dimensional domain. The time step is performed implicitly and with a variable step width determined by setting critical limits for the error estimates in each time step. As solver algorithm for the linear problems occurring during the solution of the overall nonlinear problem, a direct method using fast algorithms of the BLAS library is used. While the numerical methods do not stand in the center of this work and shall therefore not be treated in too much detail further onwards, it should be pointed out that the validity of the results was assured in different ways. First, the spatial discretization, the setting on the time steps and the solver type was modified to assure that a variation of these quantities does not affect the results. Second, selected problems were implemented into C code with finite difference methods using algorithms according to the numerical recipes book [64] and an explicit time stepping procedure. Third, previously documented results of other authors (both numerical and analytical) were reproduced and compared. In this sense, the used procedures for the numerical simulations can be considered to work correctly.

2.1 Reaction-diffusion systems

In spatially extended chemical systems, locally the presence of one species may influence the concentration of all species in the system by reactions, i.e. generation or depletion of material. Furthermore, material transport can occur. If the dominant mode of transport is diffusion (and other mechanisms of transport are not accounted for), the corresponding system is called *reaction-diffusion system*. In many cases, there is a sufficiently high amount of different reactants present in the reaction volume to describe the dynamics in the continuum limit by using the concentrations of different species. The corresponding models then are locally parabolic differential equations of the form

$$\partial_t \boldsymbol{q}(\boldsymbol{x},t) = \underline{\boldsymbol{D}} \Delta \boldsymbol{q}(\boldsymbol{x},t) + \boldsymbol{R}(\boldsymbol{q}(\boldsymbol{x},t)), \tag{2.1}$$

where $\boldsymbol{q}$ is a vector containing the concentration of the relevant reagents. The first term on the right hand side accounts for diffusion in the system ($\underline{\boldsymbol{D}}$ is a matrix of diffusion coefficients) and we want to make the assumption that the latter is a linear process with $\underline{\boldsymbol{D}}$ being homogeneous and isotropic. The second term models all local reactions.

Chemical reactions may generally involve large and complex cascades of different steps in which a variety of different excited states may play a role. Most reaction-diffusion systems are therefore considered on such time scales where only a small number of slow reaction steps dominate the dynamics, formally corresponding to an adiabatic elimination of the fast scales. The component vector $\boldsymbol{q}$ in the corresponding equations is then rather low-dimensional (compare for example [65–69]). The derivation of the equations itself can be carried out in a variety of different ways, for example by directly setting up rate equations [70], in a semi-phenomenological way via equivalent circuit considerations [55] or other qualitative arguments [71] and finally by simply postulating a certain structure [72, 73]. More detailed overviews are for example given by [74–77].

Chemical reactions in gel reactors and also temperature pulses on surfaces can be described rather directly using reaction-diffusion equations, examples can be found in [67, 69, 78, 79]. However, reaction-diffusion equations can also be set up for systems which one would not directly associate with this type of description of first glance. There

are experiments on discrete electrical networks consisting of up to several thousands of coupled cells with a nonlinear current-voltage characteristic which can be described by discrete reaction-diffusion equations [32, 80–82]. In this context, the components $\boldsymbol{q}$ represent current and voltage for each cell. Using equivalent circuit considerations, it has also been argued that planar gas-discharges with high-ohmic barrier can be considered as reaction-diffusion systems if lateral drift effects can be neglected [55]. Similar arguments have been applied to semiconductor devices [83–85]. Recently, the connection of reaction-diffusion systems to charge-transport systems has been corroborated via a rather rigorous derivation of a reaction-diffusion system from drift-diffusion equations using techniques of adiabatic elimination [86].

Unfortunately, up to date there is no systematic classification of reaction-diffusion system according to possible structures or other relevant features due to the many possibilities for the number of components, the reaction functions etc. Consequently there are many rather independent works in different equations treating similar problems (see Table 2.1 for an overview). We will see that the possibilities to obtain LSs in one-component systems are rather limited. In two-component systems, stationary LSs are possible in any spatial dimension, but propagating structures are only found in the one-dimensional case unless global coupling terms are introduced. Going to three-component systems may overcome the latter restriction. Consequently, based on the possible phenomenology as well as the number of components and spatial dimensions a certain hierarchy can be built up, as we will explain in more detail at the end of this section.

2.1.1 One-component systems

The most simple type of reaction-diffusion systems which were also investigated most early are one-component systems, in particular in one spatial dimension [119, 120], where (2.1) is referred to as KPP (Kolmogorov-Petrovsky-Piscounov) equation. Particularly frequently considered versions are the Fisher equation with $R(q) = q - q^2$ [119] that describes spreading of biological populations, the Newell-Whitehead-Segel equation [121, 122] with $R(q) = q - q^3$ first introduced to describe Rayleigh-Bénard convection, the Zeldovich equation with $R(q) = q(1-q)(q-\alpha)$ and $0 < \alpha < 1$ that arises in combustion theory [123] and its special degenerate realization with $R(q) = q^2 - q^3$ that is sometimes referred to as Zeldovich equation as well [124]. First, we will have a look at stationary solutions either in a fixed or a moving frame. To find the latter, one may introduce a frame moving with arbitrary velocity c via the transformation $t \to t$, $x \to \xi - ct$ in order to find both standing and moving solutions, yielding

$$\partial_t q = D\partial^2_{\xi\xi} q + R(q) + c\partial_\xi q. \tag{2.2}$$

Stationary fronts and localized solutions of (2.2) consequently are heteroclinic and homoclinic orbits of the hyperbolic equation (parameterized by ξ) obtained in the case $\partial_t q = 0$ with the function $q(\xi)$ taking those values for $\xi \to \pm\infty$ which are stable roots of the reaction function. It is clear that a monostable reaction function can not yield a heteroclinic orbit, so that fronts are not possible in this case. But also no localized solutions are possible for the monostable system: generally, the reaction alone will locally

Type of system	sp. dim.	single LSs	interaction	details
Ferrocyanide-iodate-sulfite	1,2	[67, 87]	[87]	bistable media, breathing spots, self replication
Belousov-Zhabotinsky-like	1	[88–90]	[90]	Brusselator, traveling pulses, mesa-type patterns
	1,2		[91, 92]	photosensitive BZ, pulse trains, Oregonator
	2	[69, 93]	[68]	BZ in Aerosol OT Microemulstion, standing and moving waves, stationary and oscillating LSs, oscillatory clusters
Gray-Scott model	2	[70]	[94]	glycolysis, stationary spots, self-replication
	1,2	[54, 95]	[54, 95]	stat. and moving LSs, scattering, annihilation, replication
Bonhoeffer and	1	[16, 37]		FhN: pulse propagation on nerve axons
Fitzhugh-Nagumo	2,3	[41, 55, 96]	[38, 58, 97]	stat. and moving LSs, scattering, molecules,
			[55, 98]	generation and annihilation
	1	[52, 99]		BvP: standing and moving, breathing and wiggling LSs
piecewise linear models	1,2	[72, 100–103]	[72, 102, 103]	moving LSs, collisions, scattering, bound states
semiconductor models	1	[104–108]		diodes, heating, standing and moving filaments
blood clotting	1	[109–111]		running pulses, multihumped LSs
Systems with special properties				
Systems with integral coupling	1,2	[79, 102, 112–114]	[102, 115]	
Systems with cross diffusion	1	[116–118]	[116–118]	running pulses, waves, collisions, splitting, interaction

Table 2.1: Overview over different works in reaction-diffusion systems

return the system to the stable stationary state independent of the local initial condition, and diffusion will support this effect. In a next step, one could therefore consider a multistable system with two stable stationary solutions q_0 and q_2 and one unstable solution q_1 in between, for example by choosing as reaction function a cubic polynomial $R(q) = \lambda q - q^3 + \kappa_1$ with an appropriate choice of λ and κ_1. In the bistable reaction function, basically both homo- and heteroclinic orbits should be possible as the local dynamics is not trivial as in the monostable case. Indeed many one-component systems including the above example allow for both types of solutions, however front solutions are generically stable while localized solutions are unstable.

We will first give a formal mathematical proof for this point before explaining the physical reasons. For non-moving solutions ($c = 0$) with $q_0(\xi)$ being the stationary solution in question and $\tilde{q}(\xi, t)$ being an infinitesimal perturbation such that $q = q_0 + \tilde{q}$, the perturbation is subject to the linear evolution equation

$$\partial_t \tilde{q}(\xi, t) = D\partial^2_{\xi\xi}\tilde{q}(\xi, t) + R'(q_0)\tilde{q}(\xi, t). \tag{2.3}$$

With the ansatz $\tilde{q}(\xi, t) = \sum_n \psi_n(\xi) \exp(-\lambda_n t)$ where the index may represent both a discrete or a continuous spectrum we get the eigenvalue problem

$$\lambda_n \psi_n(\xi) = H(\psi_n(\xi)), \qquad H = -D\partial^2_{\xi\xi} - R'(q_0), \tag{2.4}$$

where negative eigenvalues result in the instability of the solution. The differential operator in (2.3) is of Schrödinger type and for the discrete spectrum one can expect ψ_0 to have no zeros, ψ_1 to have only one zero, ψ_2 only two and so on, i.e. the eigenfunctions can be sorted to an increasing number of knots, and the magnitude of the corresponding real eigenvalue increases monotonically. On the other hand, as the system of interest is translationally invariant, $\partial_\xi q_0(\xi)$ is a neutral eigenfunction with the eigenvalue $\lambda = 0$. One may now see that for a nontrivial solitary solution with $q_0(-\infty) = q_0(\infty)$, the function $q_0(\xi)$ is not monotonic. Therefore the eigenfunction $\psi = q_0'(\xi)$ should have at least one zero, and the corresponding eigenvalue $\lambda = 0$ can not be the lowest one. The latter is therefore negative and the LS is unstable [74]. The same argument shows that a front is stable if it changes monotonically from $q_0(-\infty)$ to $q_0(\infty)$. For moving solutions with $c \neq 0$, the above arguments can not be directly applied, and significantly greater efforts are necessary. More details can be found for example in [125, 126].

Although the above proof is very universal and easy to understand, it gives no information about the physical reasons for the instability of the homoclinic orbits. An illustrative argument can only be given for the rather special case that the LS can be considered as an asymptotic superposition of a front-antifront pair (Fig. 2.1a). We discuss this case in more detail because it is of particular relevance in the context of global coupling effects (see below). For the combined front-antifront solution, Bode chose a representation of a front-antifront pair as

$$q(x, t) = q_f(x - p_1(t)) + q_f(p_2(t) - x) - q_2 + r(x, t) \tag{2.5}$$

with q_f denoting the unperturbed front solution, q_2 the upper stationary homogeneous state and a small r as the deviation from the purely linear superposition [127]. Inserting

this ansatz in the evolution equation and performing a multiscale expansion (compare also the next chapter), he found that for the concrete reaction function $R(q) = \lambda q - q^3 + \kappa_1$, the distance between the fronts evolves according to

$$\partial_t d_{21}(t) = \partial_t[p_2(t) - p_1(t)] = -2c - aD\frac{1 - R'(q_2)}{D} \exp\Big(- [\frac{1 - R'(q_2)}{D}]^{1/2} d_{21}(t)\Big) \quad (2.6)$$

where as above c is the velocity of the unperturbed front q_f and $a > 0$ is a constant factor. Note that $c < 0$ corresponds to an extending upper state q_2 for the isolated front and that $R'(q_2) < 0$ if q_2 is stable.

The relation (2.6) shows that while for $c > 0$ the solution fronts permanently approach, for $c < 0$ a stationary state should be possible (Fig. 2.1a). Let us first look which system properties determine the velocity of the unperturbed front. One may exploit an analogy between a stationary solution of (2.2) and a damped particle moving in a potential $V(q)$ by rewriting (2.2) in the stationary case as

$$0 = D\partial^2_{\xi\xi} q + \frac{\partial V(q)}{\partial q} + c\partial_\xi q, \quad (2.7)$$

where $V(q)$ is an antiderivative of $R(q)$. Looking for stationary heteroclinic solutions of (2.7) depending on c, the mechanical analogy with a classical mass particle in a potential (ξ takes the role of time) tells us that for $\xi \to -\infty$ the particle must start in a stable state corresponding to a local maximum of $V(q)$ and then move through a potential valley with an unstable fixed point as minimum to the other maximum for $\xi \to +\infty$. In this image, c determines a linear damping factor. With $\partial_\xi q = 0$ at $\pm\infty$, during its motion through the potential, the energy difference between the maxima must exactly be balanced by the gain or loss due to the friction term. This balance condition directly produced the relation

$$c = \frac{(V(q_2) - V(q_1)) - (V(q_0) - V(q_1))}{\int\limits_{-\infty}^{\infty} (\partial_\xi q(\xi))^2 \, \mathrm{d}\xi} = \frac{V(q_2) - V(q_0)}{\int\limits_{-\infty}^{\infty} (\partial_\xi q(\xi))^2 \, \mathrm{d}\xi}. \quad (2.8)$$

The relation reflects the so-called Maxwell rule: if there is one dominant stable homogeneous state, a propagating front switches the system from the non-dominant to the dominant state. A measure for this "dominance" is given by the surface under the potential function $V(q)$ (compare Fig. 2.1b). Only if both states are equal (i.e. the areas are the same), the front is at rest.

With this, we can now come back to our front-antifront solution. For $c = 0$, (2.6) tells us that two fronts generally attract although the strength of attraction decays exponentially with distance. The physical reason for this attraction is as follows: when linearly superposing two front solutions, the action of the linear diffusive term is simply the sum of its action on the individual fronts. The reaction function however is nonlinear, and one may find by looking at the slope of $R(q)$ close to the upper fixed point q_2 (dashed line in Fig. 2.1a) that $R(q_f(p_1 + d)) > R(q_f(x + d) + q_f(p_2(t) - d) - q_2)$ for $d \approx d_{21}$,

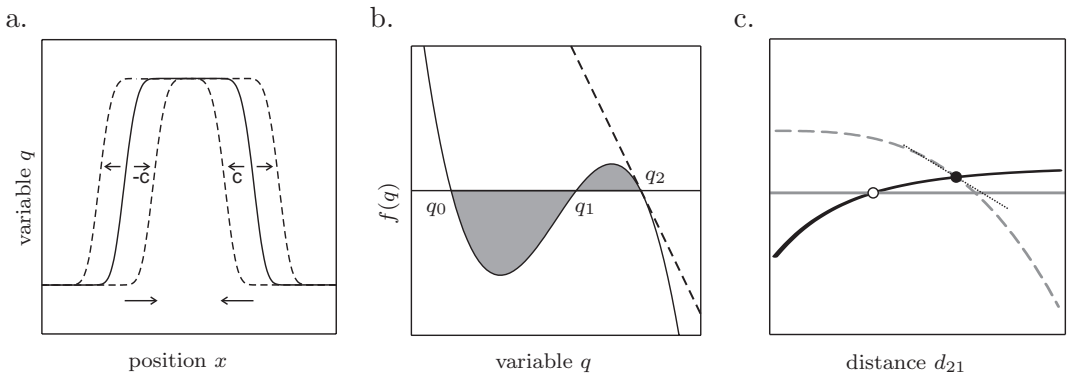

Figure 2.1: Illustrations of the stability of a front-antifront domain in one-component systems: a. expansion and contraction of a front-antifront domain due to a finite front velocity c and mutual front attraction, b. Maxwell rule for the front velocity: the grey shaded areas under the cubic function $R(q)$ (solid line) are a measure for the dominance of the stable homogeneous states (compare Eq. (2.8)). c. Schematic illustration of the two summands in (2.6) (solid grey and black line) forming an unstable fixed point. When the front-velocity becomes distance-dependent for example via an integral term (dashed grey line), the fixed point may become stable if the sum of the slopes in the fixed point becomes negative (dotted line).

meaning that the production of material due to the superposition of two front solution decreases in the connecting region compared to the production caused by the individual front. With diffusion transporting material to the sides, the local concentration of q continues decaying in the course of time, corresponding to an attraction of the fronts. Note that the argument works also for a not purely linear-cubic form of the reaction function as long as the slope of the latter decreases near the upper fixed point q_2.

We see from (2.6) that while for $c < 0$ there indeed may exist a fixed point, it is always unstable as the slope of the second term is positive for all values of d_{21} (Fig. 2.1c). The reason for this that the case $c < 0$ corresponds to fronts moving away from each other, which must be compensated by the attraction of the fronts to produce a stationary state. As the interaction becomes weaker for larger separation, attraction dominates for small and repulsion for large separations which evidently leads to instability. The instable stationary solution forms a "critical germ" or "critical nucleus": initial conditions lying entirely below the nucleus collapse to the ground state q_0, while solutions above switch the system to the upper state q_2.

The arguments for LSs in one dimension may also be applied in a similar way to higher-dimensional systems. While again no localized solutions are possible for the monostable case, in the bistable case we may again try to construct a domain solution from a front solution. In two spatial dimensions, instead of "flipping" a front to obtain a localized state, one now has to revolve the front to obtain a domain state with rotational symmetry. When shifting the center of rotation to the origin, by switching to polar coordinates the starting equation becomes

$$\partial_t q = D\partial_{rr}^2 q + \frac{D}{r}\partial_r q + \frac{D}{r^2}\partial_{\theta\theta}^2 q + R(q). \tag{2.9}$$

The second term on the right-hand side reflects that the area of rings around the origin

increases proportional to their radius. Consequently, if diffusion occurs at the boundary of a circular domain centered around the origin, the material has more space to spread compared to the one-dimensional case which formally causes the additional drift contribution. Neglecting for a moment the third "angular derivative" term and looking at radii large compared to typical diffusion lengths (with $r \approx R$), introducing the new variable $\xi = r - c(R)t$ we may rewrite (2.9) as

$$\partial_t q = D\partial^2_{\xi\xi} q + \Big(\frac{D}{R} + c(R)\Big)\partial_\xi q + R(q). \tag{2.10}$$

which is very similar to our result (2.2) for the one-dimensional case in a moving frame (compare also [75]). For $R \to \infty$ we find $C(R) = c$ with c being the velocity of the one-dimensional front as defined above so that $C(R) = c - D/R$. From this, we directly see even without considering the angular term that domains are again unstable: starting with a domain with radius R_0 and $c(R_0) > 0$, the domain expands to a radius $R_1 > R_0$ and we see that $c(R_1) > C(R_0)$. This means that $c(R_0)$ is a lower bound for the front velocity for all times and the domain expands indefinitely. With an analogous argument, one finds that initially shrinking domains keep shrinking, so that there is again one instable critical nucleus between two global homogeneous states. For three spatial dimensions, the results can directly be applied as well as in the radial part of the Laplacian, only the pre-factor D/r in front of the "drift term" has to be replaced by $2\frac{D}{r}$.

In order to obtain LSs in one-component systems in spite of the above-mentioned problems, one may perform a modification that works in other types of equations as well. When the localized solution collapses or expands, the global amount of "material" is reduced or increased with respect to the previously present amount. Introducing a global coupling term for example by the substitution

$$\kappa_1 \to k_{1,\text{eff}} := \kappa_1 - \kappa_2 \int_\Omega (q - q_0)\,\mathrm{d}x, \tag{2.11}$$

in our concrete example with cubic polynomical, the system tends to dynamically stabilize the integral amount of material in the system. If the overall deviation from q_0 becomes too large, material production is globally reduced or increased, depending on the sign of the deviation.

To obtain an illustration for the action of the integral term in one spatial dimension, one may exemplarily consider a front-antifront structure as shown in Fig. 2.1a, for simplicity on a very large but finite domain. We know from (2.6) that without integral term, the structure is unstable since c is constant. Taking now the integral into account, let us assume that the domain would get infinitesimally larger. In this case, $k_{1,\text{eff}}$ would decrease, thereby making the lower homogeneous state more dominant. As a consequence, the velocity $c(k_{1,\text{eff}})$ of the isolated fronts would decrease as well. For a shrinking domain, the opposite effect is encountered. Practically, this means that c implicitly becomes a function of the front-antifront distance as well. If for given parameters there exists a fixed point of (2.6) with $c = c(d_{21})$ and the stabilizing action of the integral term (its strength characterized by κ_2) can overcompensate the first mutual

front attraction, the front-antifront pair can be stabilized. This is illustrated in Fig. 2.1c showing that how the sum of the slopes in the fixed point becomes negative.

Also for two-dimensional structures an analytic proof of the stabilization of domains by integral terms was given, which however took into account only the radial part of the Laplacian [128]. A remaining question therefore is whether the angular part of the Laplacian is capable of destabilizing the LS or whether the domains are completely stable. For a number of examples, a numerical calculation of the eigenvalues and eigenmodes of the linearization of the reaction-diffusion system around the domain solution with integral term shows that indeed the LSs are completely stable (data not shown). One may also use the above arguments to make this stability plausible. As an example, we take a stable domain structure in two dimensions which we perturb with an shifted Gaussian distribution $G(x, y) = A \exp[-(x^2 + (y - d)^2)/\sigma^2]$. The initial state quickly relaxes to a domain with a bump-like deformation in one side (Fig. 2.2a1). The figure outlines the shape of the domain with a black contour line at $q = 0.8$, and the white circle indicates that the local curvature of the front between the two stable states inside the bump is much larger than in the unperturbed region. This implies that driven by curvature the front locally retracts rather quickly, thereby reducing the deformation. The local curvature then decreases (compare the sequence a1 to a3) and locally causes a re-increase of the front velocity. In the long-time limit, a coaction of integral-

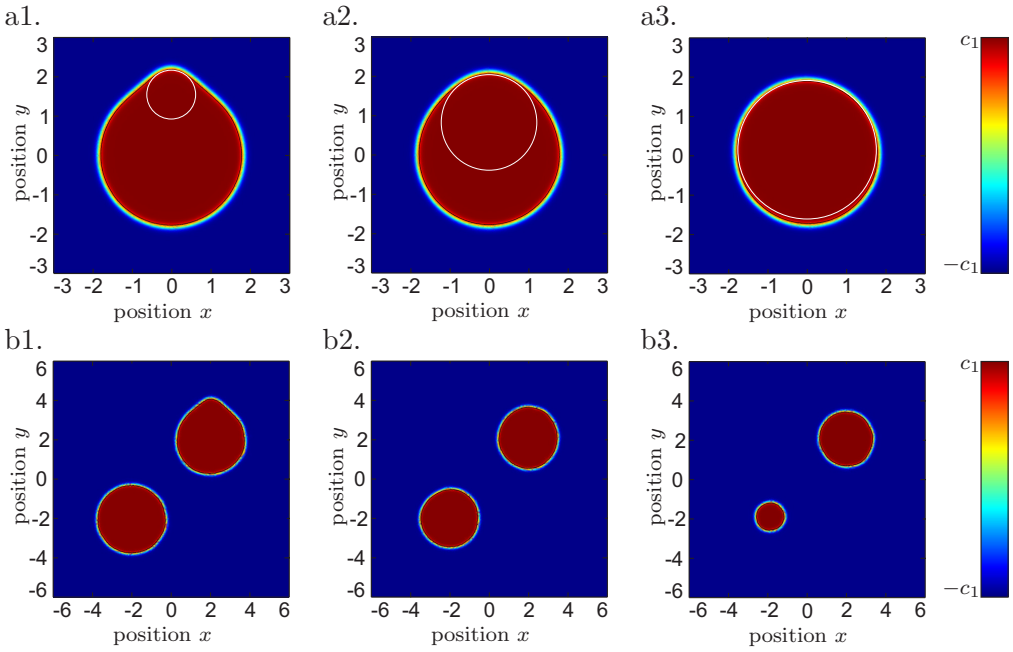

Figure 2.2: Dynamics of domain structures in bistable one-component systems with global coupling. a. Perturbation of a stable domain structure with a Gaussian pulse ($A = 2.2$, $d = 1.1$, $\sigma = 0.4$) and the corresponding distribution of q at $t = 30$ (a1), $t = 80$ (a2) and $t = 800$ (a3). The black line is a contour line at $q = 0.8$ and the white circle indicates the local curvature of the deformation caused by the perturbation. b. Competition of two LSs: a stationary LS and a structure perturbed as in a. are put under competition by integral coupling. Both structures shrink until the perturbed LS "eats up" the unperturbed one, times $t = 30$ (b1), $t = 200$ (b2) and $t = 1000$ (b3). Parameters: $\lambda = 1.2$, $\kappa_1 = 0.05$, $\kappa_2 = -0.0045$, $D = 0.001$, scale $c_1 = 1.2$.

and curvature-dependent contributions to the velocity cause the original rotationally symmetric domain state to be restored.

One large drawback of the integral stabilization is given by the fact that not more that one LS can be stabilized: when two or more not perfectly equal structures are present in the system, they are put in mutual competition by integral coupling terms [112, 128, 129], so that except for a single final structure all solitons are "eaten up" by their competitors. This is illustrated in the sequence in Fig. 2.2b1 - b3 where one stationary and one stationary LS perturbed as above are placed one one domain for the same parameters as in a1 - a3. Because too much material is present in the system, the lower state dominates and both LSs start decreasing in size (b1). During this process, the local curvature of the structures increases which accelerates the shrinking process. Once both LSs have about half their original size (b2), the shrinking process due to the integral coupling comes to a stop, however there is still the curvature-dependent part. Here it is important to recognize that in the considered case, the perturbed LS is slightly larger at this point of time. When both structures continue shrinking, the integral term now opposes this tendency equally for both LSs. However, the curvature-driven shrinking effect is stronger for the smaller structure. In consequence, the larger domain can grow in size and decelerate its shrinking process in favor of the smaller one whose shrinking process accelerates (b3). Eventually, the smaller LS vanishes and the surviving structure converges towards its stationary shape.

Concluding our results on one-component systems, we may state that while the formation of LSs is only possible to a rather limited extent without the use of global coupling, the underlying mechanisms play a central role also in systems with more components. One-component bistable systems with global coupling can be realized experimentally for example on electric networks consisting of many coupled cells with a nonlinear S-shaped

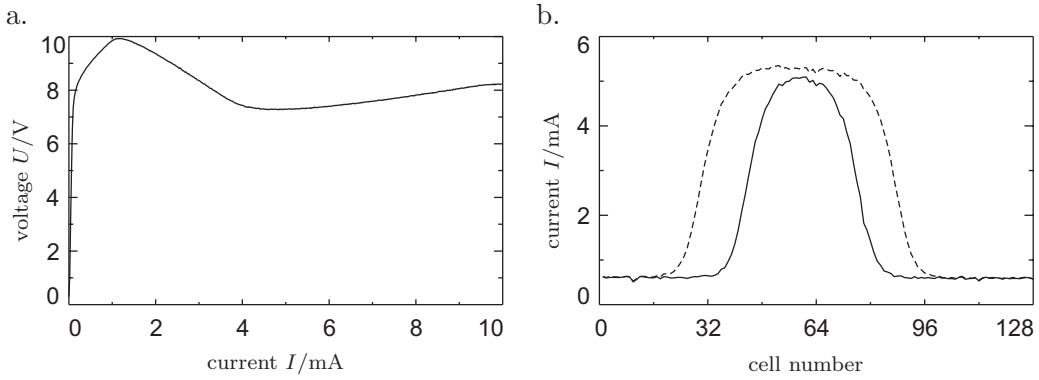

Figure 2.3: Domains in one-dimensional one-component reaction-diffusion systems experimentally realized by coupled cells with nonlinear current-voltage characteristic coupled to a discrete electrical network [32, 80–82]. a. S-shaped current-voltage characteristic of a single network cell corresponding to the nonlinear reaction function $R(q)$. b. Domain structures stabilized by global coupling. The plot shows the current in each cell against the cell number. The domain size can be increased by decreasing the global coupling resistor from $R_0 = 17.3\,\Omega$ (solid line) to $R_0 = 12.6\,\Omega$ (dashed line), which can be interpreted as decreasing κ_2 in (2.11). Other parameters using the notation of the above references: $U_0 = 13.67\,\mathrm{V}$, $R_U = 0$, $R_V = 426\,\Omega$, $L = 33\,\mathrm{mH}$, $C = 0$, $R_I = 1\,\mathrm{k}\Omega$.

current-voltage characteristic (Fig. 2.3a) that can be described by a discrete reaction-diffusion equation [32, 80–82]. As the reacting component can be identified with the current through the cells, a global coupling can be realized in a simple fashion via a global series resistor. Fig. 2.3 shows domain structures in a parameter range where the externally applied voltage U_0 is chosen in such a way that the system is bistable and the low current state is dominant. As the series resistor R_0 can be identified with κ_2 in (2.11), an increase of the latter causes the domain size to shrink as expected from theory.

2.1.2 Two-component systems

From the above consideration, is becomes plausible that in order to generically exhibit the formation of several stable LSs without global coupling, reaction-diffusion equations must at least have two components. It is reasonable to write the general representation of such a system in the form

$$\begin{pmatrix} \tau_u \partial_t u \\ \tau_v \partial_t v \end{pmatrix} = \begin{pmatrix} d_u^2 & 0 \\ 0 & d_v^2 \end{pmatrix} \begin{pmatrix} \Delta u \\ \Delta v \end{pmatrix} + \begin{pmatrix} F(u,v) \\ G(u,v) \end{pmatrix}, \tag{2.12}$$

where compared to the general formulation (2.1) we have split the diffusion constants into typical diffusion times and lengths. In order to keep compatibility with a number of previous works, one may furthermore express time in units of the characteristic activator diffusion time τ_u. With the definition $\tau := \tau_v/\tau_u$, this yields

$$\begin{pmatrix} \partial_t u \\ \tau \partial_t v \end{pmatrix} = \begin{pmatrix} d_u^2 & 0 \\ 0 & d_v^2 \end{pmatrix} \begin{pmatrix} \Delta u \\ \Delta v \end{pmatrix} + \begin{pmatrix} F(u,v) \\ G(u,v) \end{pmatrix}, \tag{2.13}$$

so that time-dependent phenomena can be investigated by varying the ratio τ instead of the individual constants. In order to find LSs in two-component systems, certain premises have to be fulfilled. Following the classical argument of Turing [20], first of all at least one ground state $\boldsymbol{q}_0$ must exist that is linearly stable against perturbations. Checking which types of two-component systems are suitable, one may perturb a potential homogeneous ground state of a given system against the exponential functions $\tilde{\boldsymbol{q}}_k \mathrm{e}^{i\boldsymbol{k}\cdot\boldsymbol{x}}$, $\boldsymbol{k} \in \mathbb{R}^n$ and look at the linear growth rates. The linearization yields

$$\partial_t \tilde{\boldsymbol{q}}_k = \boldsymbol{R}'(\boldsymbol{q}_0)\tilde{\boldsymbol{q}}_k - k^2 \underline{\boldsymbol{d}} \tilde{\boldsymbol{q}}_k, \tag{2.14}$$

where $\boldsymbol{R}'(\boldsymbol{q}_0)$ is the Jacobi matrix of the linearization of $\boldsymbol{R} = (F(u,v), G(u,v)/\tau)$ around $\boldsymbol{q}_0$ and $\underline{\boldsymbol{d}}$ is the matrix with the "new" diffusion constants d_u^2 and d_v^2/τ. Using the well-known trace and determinant criterion for the stability of two-component first order systems, one finds that the homogeneous stationary solution is linearly stable against disturbances if and only if the conditions

$$\mathrm{Tr}(\boldsymbol{R}' - k^2 \underline{\boldsymbol{d}}) = \mathrm{Tr}\boldsymbol{R}' - k^2 \mathrm{Tr}\underline{\boldsymbol{d}} < \mathrm{Tr}\boldsymbol{R}' < 0 \tag{2.15}$$

and

$$\mathrm{Det}(\boldsymbol{R}' - k^2\underline{\boldsymbol{d}}) = \mathrm{Det}\boldsymbol{R}' - (d_u^2 G_v + d_v^2 F_u)\frac{k^2}{\tau} + d_u^2 d_v^2 \frac{k^4}{\tau} > 0 \tag{2.16}$$

are fulfilled for any wave number k, where the coefficients have to be taken at the stationary state. This directly implies that as a necessary condition the Jacobi matrix of the linearization around the ground state must have the following signs (compare for example also [55, 127]):

$$\begin{array}{lllll} I & \begin{pmatrix} + & - \\ + & - \end{pmatrix} & \begin{pmatrix} + & + \\ - & - \end{pmatrix} & \begin{pmatrix} - & + \\ - & + \end{pmatrix} & \begin{pmatrix} - & - \\ + & + \end{pmatrix}, \\ II & \begin{pmatrix} - & + \\ + & - \end{pmatrix} & \begin{pmatrix} - & - \\ - & - \end{pmatrix}, & & \\ III & \begin{pmatrix} - & - \\ + & - \end{pmatrix} & \begin{pmatrix} - & + \\ - & - \end{pmatrix}. & & \end{array} \tag{2.17}$$

Here, we have three equivalence classes of reaction-diffusion systems. The classes are defined by the three transformations exchange of variables as well as reflection of u and v at the ground state in order to preserve the diagonal character of the diffusion matrix. If the trace stability criterion (2.15) is violated for a finite k, it is also violated for $k = 0$ in all three classes. Therefore, the first wave number to become unstable via the trace condition is always $k = 0$, typically resulting in a Hopf bifurcation. LSs are generally created in two-component reaction-diffusion systems closely before a global destabilization sets in. To the best of the authors knowledge, the formation of LSs in reaction-diffusion systems has only been observed up to now in systems in which a finite wave number has the largest growth rate close to the onset of the first global instability, which seems natural as LSs have a dominant finite wavelength themselves that is often found to coincidence with that of the underlying most dominant mode. A finite wave number becoming unstable without $k = 0$ being unstable as well can however be realized via the determinant criterion (2.16) if one additionally claims

$$d_u^2 G_v + d_v^2 F_u > 0. \tag{2.18}$$

Equivalence class I is different from the classes II and III as the former is the only class for which (2.18) can be fulfilled. If the determinant criterion is violated without the trace criterion being violated and (2.18) holds, generically the growth of a stripe or hexagonal pattern is encountered, the corresponding bifurcation is also referred to as Turing bifurcation. As stated above, LSs are usually found below the onset of the Turing instability, but the corresponding wavelength nevertheless plays a strong role for the localized structure. According to its first representative, class I is named the class of *activator-inhibitor systems*: while the activating component (at least close to the ground state) stimulates the production of both species, the inhibitor has an opposite effect.

We will illustrate the mechanisms to generate localized structures via an example, choosing

$$\begin{pmatrix} \partial_t u \\ \tau\partial_t v \end{pmatrix} = \begin{pmatrix} d_u^2 & 0 \\ 0 & d_v^2 \end{pmatrix} \begin{pmatrix} \Delta u \\ \Delta v \end{pmatrix} + \begin{pmatrix} f(u) - \kappa_3 v \\ u - v \end{pmatrix} \tag{2.19}$$

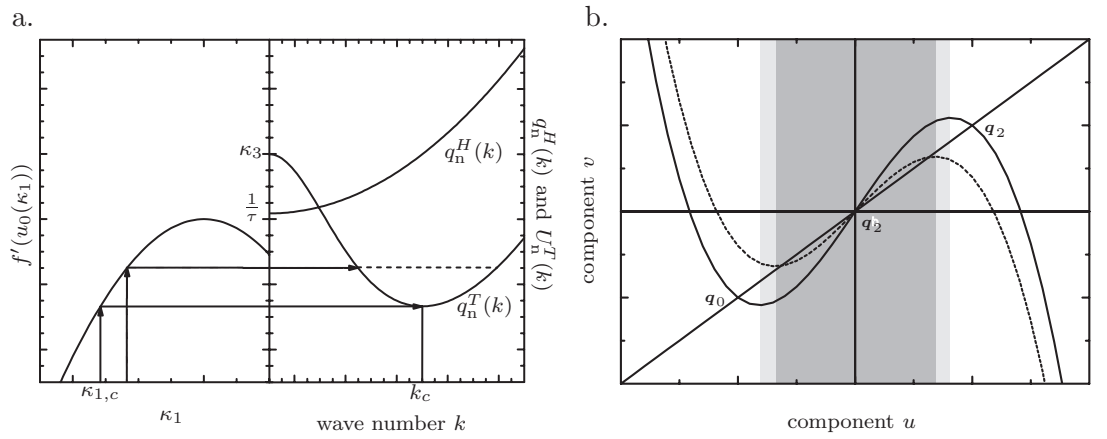

Figure 2.4: Turing and Hopf instabilities illustrated for the special example (2.19). a. Implicit dependence of $f'(u_0)$ on κ_1 (left half) as well as Turing and Hopf stability boundaries (right half) according to (2.20). By increasing κ_1 from small values, at a critical value $\kappa_{1,c}$ a single wave number k_c becomes instable, marking the point of the Turing bifurcation in our example. b. Nullclines of the system for different values of λ and $\kappa_1 = 0$, $\kappa_3 = 1$. Note that the region of self-activation (positive slope of $f(u)$) marked by the grey shadings changes in size when λ is varied.

with $f(u) = \lambda u - u^3 + \kappa_1$ which was used by Fitzhugh and Nagumo to model nerve transmission [16, 37]. Other types of systems generally follow the similar basic principles. We will first carry out the above wave-number considerations for the concrete case. The stability conditions then read

$$\begin{aligned} q_{\rm n}^H(k) &= \frac{1}{\tau} + (d_u^2 + \frac{1}{\tau} d_v^2)k^2 > f'(u_0) = \lambda - 3u_0^2, \\ q_{\rm n}^T(k) &= \frac{\kappa_3}{1 + d_v^2 k^2} + d_u^2 k^2 > f'(u_0) = \lambda - 3u_0^2. \end{aligned} \tag{2.20}$$

In its right half, Fig. 2.4a shows the stability boundary curves for a concrete example. As for our choice of parameters the claim (2.18) is fulfilled, the minimum of the Turing curve lies below the Hopf curve. Furthermore, the parameters were chosen in such a way that there are three stationary homogeneous states of the system, labeled $\boldsymbol{q}_0$ (the ground state of interest), $\boldsymbol{q}_1$ and $\boldsymbol{q}_2$ (Fig. 2.4b). We may now choose for example to vary κ_1, causing the slope of f in the point $\boldsymbol{q}_0$ to change (left side of Fig. 2.4a). At a critical value $\kappa_{1,c}$, the slope $f'(u_0(\kappa_1))$ is such that exactly one wave number k_c violates the stability condition, marking the onset of the Turing instability. If κ_1 is changed further, a whole band of wave vectors becomes potentially unstable (marked by a dashed line in Fig. 2.4a), and one faces a problem of nonlinear wave number selection.

The S-shaped characteristic in the above example marks a prototype nonlinearity for the formation of LSs in reaction-diffusion systems. Generally one distinguishes two cases: the system can either be excitable or bistable. In the first case, one stable fixed point exist, and two stable as well as one instable fixed point otherwise. In both cases, a sufficiently high perturbation of the stationary state can locally activate the system, meaning that the system leaves the fixed point on an orbit that eventually returns to the

fixed point (possible in both cases) or approaches another fixed point (in the bistable case).

2.1.2.1 The excitable case

For the formation of LSs, spatial coupling by diffusion plays an essential role. In the following, we will focus on three possible mechanisms of the formation of LSs which differ in both diffusion and reaction part. Starting with the excitable case, we make a distinction between an excitable medium with fast activator and one with fast inhibitor. The question which case we deal with can be answered by looking at τ in (2.19), if $\tau \gg 1$, we speak of a fast activator, and of a fast inhibitor if $\tau \ll 1$. In order to find the formation of LSs in the fast activator case, one typically has to require $d_u^2 > d_v^2$. The typical formation of LSs then occurs as follows [130]: initially, a small perturbation drives the system out of the ground state. When τ is large, the reaction in the activator component is much faster than the reaction in the inhibitor component if both are approximately equally fast for $\tau \approx 1$. Consequently, the activator grows fast while the inhibitor only grows slowly. In the diagram of the local reaction phase space spanned by u and v, this corresponds to a motion mainly to the right (compare Fig. 2.5a). In parallel, diffusion starts spreading material to the sides, in particular activator material. Finally, the activator nullcline is approached, and the activator reaction gets rather slow. Now, the inhibitor reaction can fully set in, and the dynamics evolves mainly along the activator nullcline until the activator reaction becomes fast again. This part of the dynamics is sometimes also referred to as excitable part (coinciding with the terminology for the whole scenario).

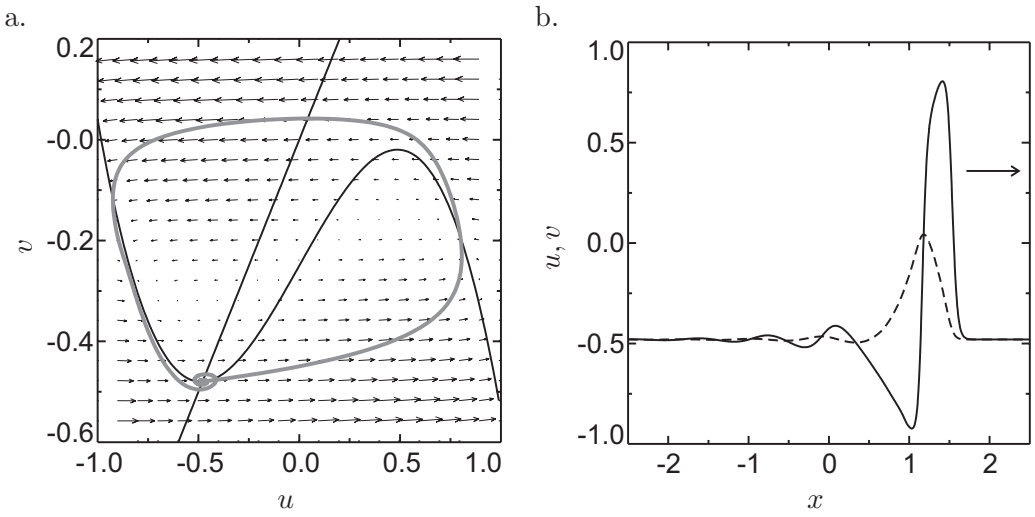

Figure 2.5: Formation of a running pulse in an excitable medium with fast activator: a. nullclines of the "effective" reaction functions $F(u, v)$ and $G(u, v)/\tau$ for the system (2.19). The grey curve corresponds to a traveling pulse solution $(u(x), v(x))$, parameterized by space. b. Activator and inhibitor distributions of the traveling pulse. Parameters: $\lambda = 0.71$, $\kappa_1 = -0.25$, $d_u^2 = 9.64 \cdot 10^{-4}$, $d_v^2 = 1.1 \cdot 10^{-4}$, $\tau = 20$.

Basically, the process now takes place a second time, but in the opposite direction. The activator quickly relaxes to a state close to the ground state, and the inhibitor slowly follows once the dynamics comes close to the activator nullcline. The latter part of the dynamics is also referred to as refractory as in this state, a local perturbation can not excite a new pulse. When the system is close to the ground state, the decay can be monotonous or oscillatory as in our example, depending on the proximity to the Turing bifurcation point. In the excited state activator material is spread to the sides by diffusion, causing the above cycle to occur also in the vicinity of the original excitation. The excitation of neighboring regions however can not reactivate the original excitation site as long as the system at this point is in the refractory period. Consequently, the initial excitation spreads in space and the above mechanism can form localized pulses when the time scales of spreading and de-excitation match appropriately (Fig. 2.5b). Naturally, the pulses are not at rest, but propagate as nothing prevents the excitation from spreading out to the side where no excitation is present, and the pulse velocity is determined both by the time needed to produce a sufficient amount of material for a critical excitation (i.e. the local reaction rate) and the time to spread the excitation in space (i.e. by the diffusion coefficient). When choosing a representation of the pulse as the set of points $\{(u(x), v(x))|x \in \mathbb{R}\}$ (grey line in Fig. 2.5a), due to a constant pulse velocity c we see via the transformation $x \to x_0 - ct$ how each point along which the pulse passes follows closely the path prescribed by the local dynamics in spite of spatial coupling via diffusion. The above described mechanism is extremely suitable to produce propagating LSs, however the pulse only stays localized in one-dimensional systems. In two- or more-dimensional systems, no mechanism is present to confine the activator and the resulting structures are spirals, target patterns or extended fronts [131–133].

LSs in excitable systems with fast activator diffusion are encountered in a variety of real systems, the most prominent probably being nerve pulse transmission [5]. Very early experiments have been carried out on the spreading of reduction pulses on oxidized metal wires [14, 134, 135] which were found to show properties extremely similar to nerve pulse excitation [136]. Experiments using a modified version of the Belousov-Zhabotinsky reaction have been carried out in thin capillaries [137, 138]. Uniformly propagating temperature pulses have been observed on heated catalytic rings [139–141], however the corresponding two-component models include global constraints [142].

In a next step we will discuss the case of an excitable medium with fast inhibitor in which primarily standing LSs can be observed. The central mechanism for the formation of LSs is local activation and lateral inhibition. If a localized pulse is present, a gradient exists that diffusion tries to smooth out. A standing LS can thus only be stabilized if the reaction and diffusion part compensate each other at every position in space. Furthermore, the structure has to stay confined in space (unlike in the propagating pulse case). To this end, the inhibitor has to diffuse stronger than the activator. This fact becomes clearer by numerically simulating the generation of a LS starting from a sufficiently large rectangular perturbation of the activator distribution which we show for a one-dimensional system in Fig. 2.6. With appropriately chosen parameters, in the first moments the local reaction dominates the dynamics, in particular in the fast inhibitor component. Thus, close to the center of the perturbation a strongly increased production in particular of inhibitor material can be found (step b). It is very relevant that this process occurs on a fast scale so that the system does not immediately decay to the ground state as diffusive material transport to the sides sets in (steps b and c). If

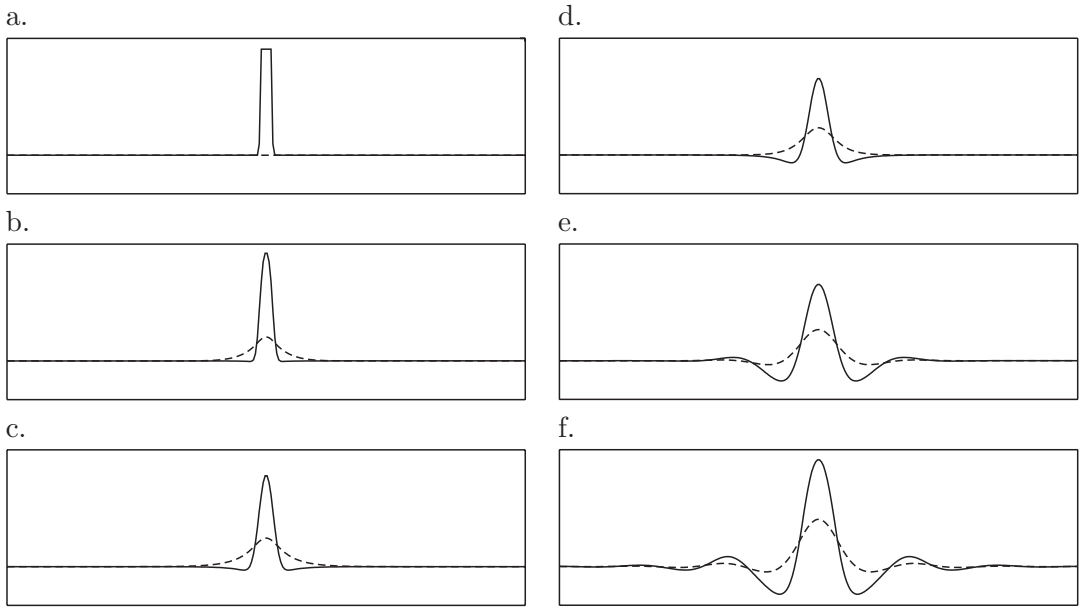

Figure 2.6: LS forming from a rectangular activator perturbation of $[0.02 \times 0.75]$ on the homogeneous ground state in an excitable two-component reaction-diffusion system (2.13) with cubic nonlinearity (compare text) in one spatial dimension. The solid and dashed lines shows u and v as a function of space for different times ($t = 0, 0.1, 0.5, 1, 10$ and 100, in the last image the solution has converged). Parameters: $d_u^2 = 10^{-4}$, $d_v^2 = 9.64 \cdot 10^{-4}$, $\lambda = 0.8$, $\kappa_1 = -0.1$, $\kappa_3 = 1$, $\tau = 0.1$, plot region $[-0.4, 0.4] \times [-0.6, 0.5]$.

the inhibitor diffuses faster than the activator, a surplus of activator producing material is left in the center of the structure to compensate losses by diffusion. This effect also confines the structure: due to diffusive transport inhibitor will dominate at the flanks of the structure, preventing the excited state from spreading to the sides (leading to a typical dip at the side of the structure, steps c-e). As the dip itself produces a small gradient opposed to the gradient generated by the bulk of the LS, the above effect may repeat itself on a smaller scale, leading to oscillatorily decaying tails as visible in the picture (steps e-f). The oscillatory tails are typically observed when the system is close to a Turing destabilization. According to (2.20), the minimum of the Turing nullcline lies at

$$k_c = \left((\frac{\kappa_3}{d_u^2 d_v^2})^{1/2} - \frac{1}{d_v^2} \right)^{1/2} \tag{2.21}$$

leading to a dominant wave length of $\lambda_c = 0.13$ for the parameters used to produce Fig. 2.6 in good agreement with the outcome of the simulation. The simulation in Fig. 2.6 can be repeated on a two-dimensional domain for the same parameters, showing a similar result. However, the width of the initial excitation as to be chosen at least double as large as in Fig. 2.6 due to an enhanced diffusion when going from one- to two-dimensional coordinates.

According to (2.20), one possibility to move further away from the Turing instability boundary is by increasing λ (which also implies approaching the bistable situation we

will discuss below). Figs. 2.7a1 and a2 show again the regular and the phase space representation of the stationary LS in Fig. 2.6 with $\lambda = 0.8$ while Figs. 2.7b1 and b2 show the same data for the LS that is generated when λ is increased to 1.294. While in the first case a characteristic spiralling close to the ground state is found, the latter does not occur for increased values of λ, instead the structure follows closely the activator nullcline close to the ground state. The width of the structure however hardly changes, which one may expect as (2.21) is independent of λ. In the center of the LS, the local dynamics comes very close to the activator nullcline while it keeps its distance to the inhibitor nullcline. An increase of λ corresponds to an increase of the activator production rate for sufficiently high values of u so that unlike in the case shown in Fig. 2.7a there is no dynamic balancing of production and diffusion of activator in the center, but the reaction is self-limiting. In contrast, the inhibitor diffusion is so strong that it can dynamically stabilize the corresponding reaction.

With the presented mechanism, stationary LSs can be stabilized in a large range of parameters. Their formation can occur from a suitably chosen localized activator perturbation, the inhibitor distribution plays no significant role (at least for physically

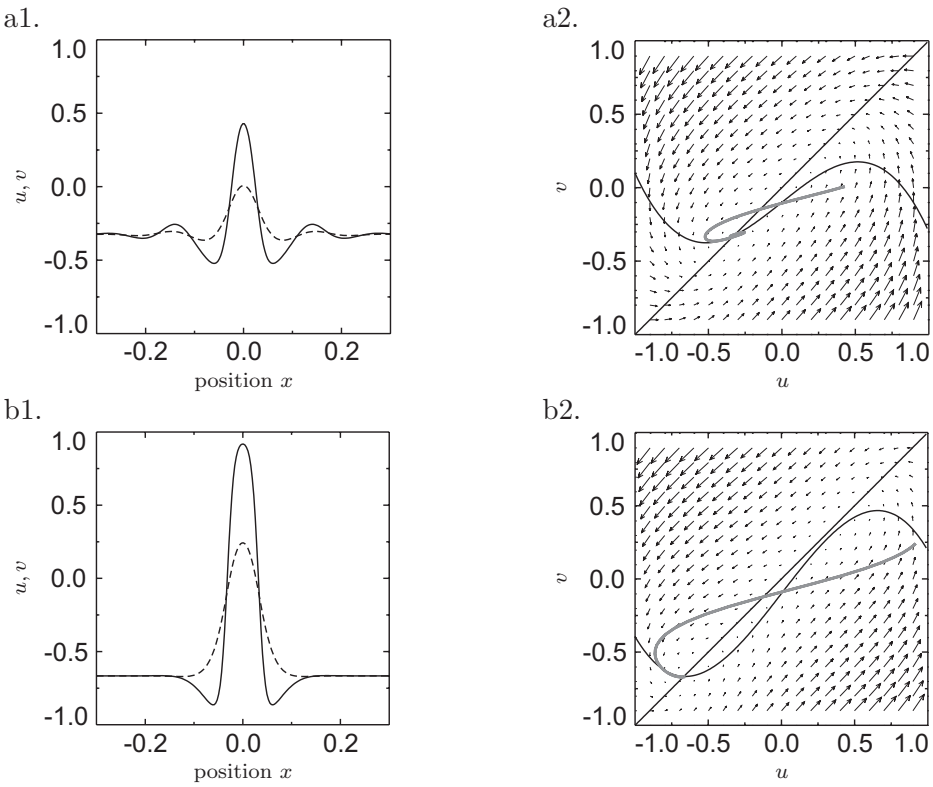

Figure 2.7: Representation of LSs in real space (left images) as well as in a nullcline and phase space plot (right images) for the excitable case with cubic nonlinearity $f(u) = \lambda u - u^3 + \kappa_1$. In the left images, the solid line corresponds to activator, the dashed line to inhibitor. In the phase space plot, the grey curves correspond to the LSs parameterized by their space variable, i.e. they are the sets $\{(u(x), v(x))|x \in \mathbb{R}\}$. a. Oscillatory tails close to the Turing instability (see Fig. 2.6), b. non-oscillatory tails ($\lambda = 1.294$, $\kappa_1 = -0.1$, other parameters as in (a.)).

diffusion lengths	time scale ration τ	reaction to initial condition
$d_u^2 < d_v^2 \approx d^2$	$\tau < 1$	formation of stable LS
$d^2 \gg d_u^2 > d_v^2$	$\tau \ll 1$	decay to ground state
$d^2 \gg d_u^2 > d_v^2$	$\tau > 1$	coexistence of LS and oscillating background (Hopf)
$d^2 \approx d_u^2 > d_v^2$	$\tau < 1$	decay to ground state
$d^2 \approx d_u^2 > d_v^2$	$\tau > 1$	spreading of running pulses
$d_u^2 > d_v^2 \gg d^2$	arbitrary	decay to ground state
$d_u^2, d_v^2 \gg d^2$	$\tau \ll 1$	decay to ground state initial cond. below critical nucleus
$d_u^2 \gg d_v^2$	arbitrary	decay to ground state
$d_u^2 \ll d_v^2$	rather arbitrary	Turing destabilization
$d_u^2 < d_v^2$	$\tau > 1$	Hopf destabilization
$d_u^2, d_v^2 \ll d^2$	$\tau < 1$	decay to ground state, dominance of local reaction

Table 2.2: Evolution of the two-component system (2.13) with $F(u,v) = f(u) - \kappa_3 v + \kappa_1$, $G(u,v) = u - v$, $f(u) = \lambda u - u^3$, $\lambda = 0.8$, $\kappa_1 = -0.1$, $\kappa_3 = 1$ (excitable case) and the initial condition used in Fig. 2.6 for different values of τ and the diffusion coefficients d_u^2 and d_v^2. The first entry corresponds to Fig. 2.6, implying $d^2 = 10^{-3}$.

reasonable choices) as long as the coefficient τ is small enough. However, when the parameter values leave a certain region in parameter space, the LS can lose its stability in several ways. First, we will have a look at the generation scenario presented in Fig. 2.6 and explore how the system reacts if the parameters are changed. To this end, we keep the initial condition fixed (thereby selecting a length scale in the system) and vary d_u^2, d_v^2 and τ. A brief overview of the following system evolution is given in Table 2.2. If the inhibitor reacts too slow (τ becomes large), it can not follow changes of the activator fast enough. In most cases, the initial activator perturbation then simply decays. However, for very large τ a Hopf destabilization may occur, causing the system to oscillate globally. A special case is given by $d_u^2 > d_v^2$, as here one may also arrive at the nerve pulse mechanism discussed above. If $d_u^2 \ll d_v^2$, the inhibitor can diffuse very far and cause gradients far away from the center of the structure. This generally leads to Turing destabilization. If both activator and inhibitor diffusion proportionally become larger and the initial perturbation stays the same, the latter may decay before a structure can form as too much material is transported away because a sufficiently large perturbation (a critical nucleus) must be present in order to allow the reaction to compensate losses by diffusion. If both activator and inhibitor diffusion proportionally become smaller (again with the original initial perturbation), the perturbation also decays as diffusion can not act and the domination of local reaction drives the perturbation to the ground state.

In a second step, let us assume that a stationary stable solution has been generated for a given set of parameters and that starting from this initial condition one or several parameters are varied. Basically, there are different types of possible destabilizations and even for a concrete example a systematic classification may be difficult. We will

nevertheless have a look at some generic results. On the one hand, a parameter change may result in the complete destabilization of a LS and its evolution for example to a homogeneous state or a global destabilization of the system. A schematic example related to a subcritical Turing instability is depicted in Fig. 2.8 showing the amplitude of a stable LS as a function of the parameter κ_1. For intermediate values a LSs can coexist with the homogeneous ground state and the patterned state. For large values of κ_1, the system becomes globally Turing-unstable, while for very small values only the homogeneous ground state can exist. The lower boundary of the stability region is thus marked by equal amplitudes for the stable LS and the critical nucleus (in fact even the coincidence of the entire distribution). Here, one may also illustrate the influence of an integral coupling term on the range of existence. With the substitution (2.11) in the activator component, the effective value κ_{eff} may lie in a region where a LS is stable although the system with κ_1 alone may already be Turing-unstable, so that the integral term enlarges the range of existence. However, again the global coupling causes mutual competition of several LSs.

Many investigations focus on the variation of time parameter τ as the existence and shape of the stationary solution is independent of the latter. Two types of destabilizations of the stable stationary LS are encountered particularly often. The structure is commonly stable if τ is below a critical value τ_c. The reason for this is that a small τ implies that the inhibitor almost instantaneously adapts to the current activator distribution. If the structure is thus stable at $\tau = \tau_c$, it will keep this property for smaller values of τ. Instabilities therefore typically arise when the inhibitor is too slow to adapt to changes in the activator distribution. For the first type of destabilization, let us

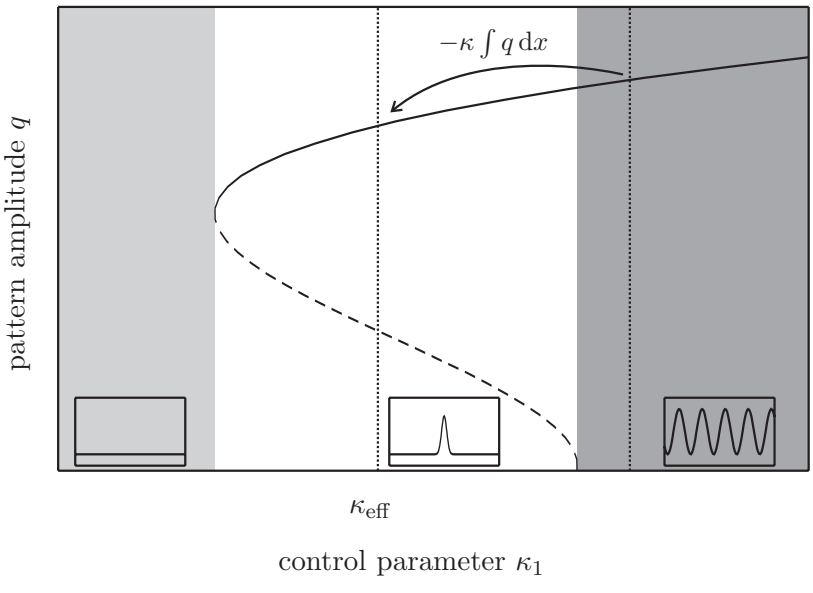

Figure 2.8: Schematic illustration of the change of the amplitude of a LS as function of the parameter κ_1 and possible destabilizations to a homogeneous or globally patterned state. The action of integral coupling may effectively change an additive control parameter κ_1 to κ_{eff} due to the presence of a LS changing the stability region. The grey shaded areas mark monostable homogeneous and patterned regions, whereas the white area marks the bistable state in which also LSs can exist.

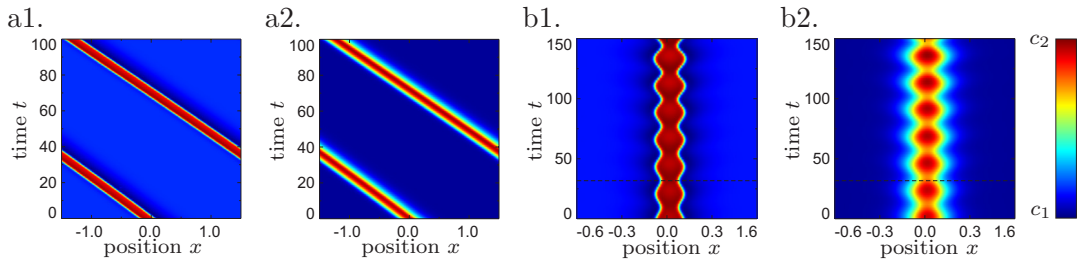

Figure 2.9: Instabilities of single LSs in two-component excitable systems and one spatial dimensions. a. Space-time plots showing the activator and inhibitor distributions of an intrinsically propagating LS as a function of time. Note the strong asymmetry in the structure. Parameters: $\lambda = 4.67$, $d_u^2 = 0.0015$, $d_v^2 = 0.01$, $\kappa_1 = -1.126$, $\kappa_4 = -3.33$, $\tau = 4$, periodic boundary conditions, scaling: $c_1 = -2.2$, $c_2 = 2.2$ (a1), $c_1 = -1.5$, $c_2 = 0.6$ (a2). b. Space-time plots showing the activator and inhibitor distributions of a breathing LS as a function of time. The horizontal line marks a point of time as orientation for the explanations in the text. Parameters as in a. except for $d_u^2 = 4.67 \cdot 10^{-4}$, $\tau = 5$, scaling: $c_1 = -2$, $c_2 = 2$ (b1), $c_1 = -1.5$, $c_2 = 0.5$ (b2).

assume that an asymmetric perturbation is added to the structure, for example in the form of the derivative of the LS itself. A fast inhibitor would quickly follow this deformation and stabilize the structure, resulting in a pure displacement. A slow inhibitor however can not immediately follow, so that the activator has the chance to increase material production at the side where no inhibitor is present. On the opposite side, the inhibitor is dominant and can locally reduce the concentration of both species. This mechanism may produce a dynamically stabilized uniformly propagating state: a small displacement may grow as with larger τ, the activator diffusion time in relation to its inhibitor counterpart becomes smaller so that activator can spread further to the front of the moving pulse. On the other hand, as activator and inhibitor evolution are coupled by local reactions, the displacement of their distributions can not grow arbitrarily large.

Fig. 2.9a shows a numerical example of an intrinsically propagating structure stabilized by the described mechanism. The corresponding bifurcation from a stationary to a moving solution is referred to as drift or traveling bifurcation [41, 113, 143]. In the two-component system, a detailed numerical investigation (data not shown) which is corroborated by different statements in the literature [99, 113, 143] turns out that the drift bifurcation generically occurs subcritically. In particular, there is a region of hysteresis in which both standing and traveling state are stable. Consequently, a perturbation of finite size is required to switch the system from the standing to the traveling state. One may look at the representation of a uniformly traveling pulse (parameterized by the space variable) in the phase space of the local reaction as previously done for stationary solutions (Fig. 2.10a). It turns out that this representation yields a homoclinic loop similar to that encountered for nerve pulse propagation (compare Fig. 2.5), showing that the mechanism causing the propagation is basically the same. For the given example, the decrease of d_u^2 with respect to d_v^2 can be compensated by an increase of τ until the ration of d_u^2 and d_v^2 is approximately in the order of 0.1.

Experimentally, it is often hard to distinguish whether in a two-component system one deals with fast or slow activator diffusion, particularly because the drift bifurcation occurs subcritically. Consequently, our references [5, 14, 134, 135, 137–141] given above

for the "nerve pulse mode" may also belong to the above discussed mechanism. Additional examples arise in planar one-dimensional gas-discharges with high-ohmic barrier [32, 144–146] which have been modeled phenomenologically on the basis of reaction-diffusion systems, and also in p-n-p-n semiconductor devices [104, 106, 147, 148].

A second type of generic destabilization is that to a "breathing" state in which the LS stays at a fixed position in space but performs periodic oscillations of its shape (Fig. 2.9b). It has been shown that for the Fitzhugh-Nagumo type of nonlinearity this type of destabilization is preferred to the traveling destabilization over large ranges of parameters [100, 149, 150]. In the oscillatory instability a complex conjugate pair of eigenvalues of the linearization operator around the stationary solution crosses the imaginary axis while the neutral eigenmode of translation remains non-degenerate. The linearization of the system (2.19) around a state $(\tilde{u}(x), \tilde{v}(x))$ reads

$$\begin{pmatrix} \partial_t u \\ \tau \partial_t v \end{pmatrix} = \begin{pmatrix} d_u^2 u \\ d_v^2 v \end{pmatrix} + \begin{pmatrix} \lambda - 3\tilde{u}^2 & -1 \\ 1 & -1 \end{pmatrix} \begin{pmatrix} u \\ v \end{pmatrix}, \tag{2.22}$$

with u and v denoting the derivation from the state of interest in this special case. Neglecting diffusion for a moment, we see from the linearized reaction function by a comparison with (2.15) in the case $k = 0$ that for τ large enough, the local system is capable of performing self-sustained oscillations around the state $(\tilde{u}, \tilde{v})$.

To understand the breathing dynamics shown exemplarily in Fig. 2.9b, diffusion has to be incorporated into the consideration. Starting with the state marked with a horizontal line, we see both a narrow activator and inhibitor peak. While the activator

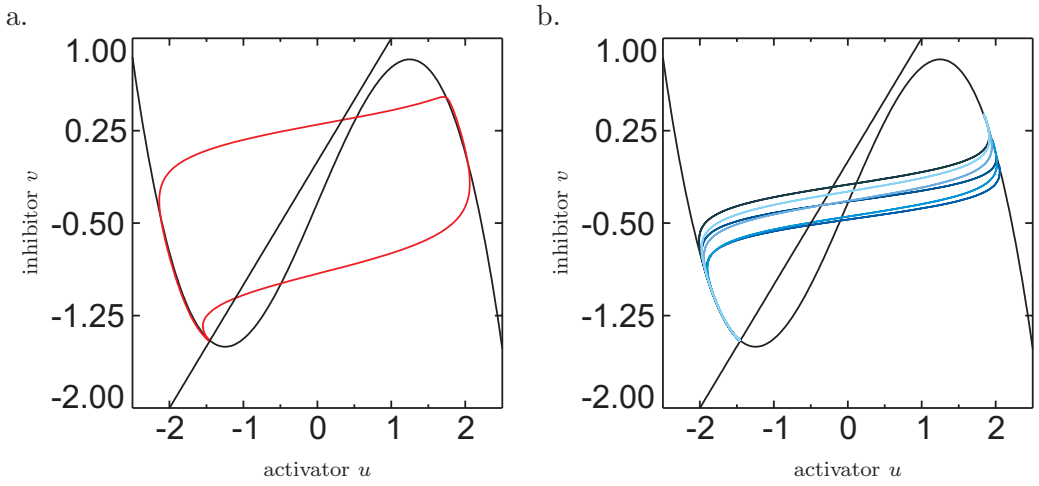

Figure 2.10: Dynamics shown in Fig. 2.9 in the representation of the local reaction space as sets $\{(u(x,t_0), v(x,t_0))|x \in \mathbb{R}\}$, the black lines show the nullclines of the reaction functions. a. The red line is representation of the stationary propagating pulse, compare also the nerve pulse mechanism shown in Fig. 2.5. b. The blue lines (from dark to light blue) illustrate the breathing motion of the LS, starting from the point of time marked by a dashed line in Fig. 2.9b, the time interval between successive lines is $\Delta t = 4$. Note that the period length of the breathing motion is $T \approx 24$.

concentration in the center lies slightly above the equilibrium value relative to the value for the stationary LS, the inhibitor concentration is far below the equilibrium value (again in relation to the stationary LS). Both distributions are narrower than their counterparts in the stationary solution and therefore start spreading to the sides by diffusion, in particular the inhibitor. While the activator decreases only slightly due to this process, the slow inhibitor increases its concentration so strongly due to the local oscillating dynamics of the reaction that this process can overcompensate the losses by diffusion. This can be visualized rather well by choosing a representation in the local phase space (Fig. 2.10b). In the course of time, there is then a surplus of inhibitor distributed over the whole support of the LS. Eventually, the increase of the inhibitor concentration in the center stops, and two effects set in. On the one hand, the global surplus of inhibitor causes a decay of the structure especially at those points where no fast activator is present, i.e. in the tails up to the flanks of the activator distribution. Both activator and inhibitor peaks thus become narrower. Second, the local dynamics and the diffusive losses cause the inhibitor in the center to decay strongly while the activator can thereby slightly rise again, completing the breathing cycle. As a consequence, we have an activator peak which mainly changes its width but not its height and an inhibitor peak alternating strongly in width and height. In the center, activator and inhibitor oscillations are in anti-phase, but the phase difference becomes smaller away from the center due to the effect of diffusion.

Many authors have numerically calculate unstable eigenvalues and the corresponding eigenmodes of the linearization around the stationary LS as function of the varied parameters, thereby showing that if the time constants of the system are varied, the destabilization of the LS commonly occurs either to a traveling or a breathing state [75, 149, 151, 152]. Different excitations are theoretically possible, but the corresponding threshold for the bifurcation parameter usually lies so high that one of the other bifurcations occurs before. Nevertheless, secondary destabilizations are possible. In this case, several instability mechanisms may come into play simultaneously. The outcome may be different: while in some situations one of the mechanisms is so dominant that its corresponding instability determines the system in the long-time limit, in other situations a combined action is possible. In the latter case, the resulting state is a moving and breathing state in which the velocity is coupled to the shape of the LS.

In quasi one-dimensional experiments, contrary to theoretical predictions breathing phenomena have been found only rarely. An observation that may be considered as a manifestation of a modified breathing instability is rocking, i.e. a periodic shift of a LS in position on a very short length scale. This phenomenon has been found in planar dc gas-discharges with high-ohmic barrier [144, 146] as well as in p-n-p-n semiconductor devices [147, 153].

Note that concerning instabilities of LSs in two-component excitable systems, we have considered up to now only one-dimensional examples. Theoretically the above instabilities can also occur in two or more spatial dimensions. A closer look however reveals an important difference between drift and breathing instability. Going from one to two or more dimensions, the stationary LS in the latter case features rotational symmetry. While the breathing instability is compatible with this symmetry in the sense that in the course of the instability the symmetry stays preserved for all times, the drift instability violates this symmetry in one direction while preserving a mirror symmetry in the orthogonal direction. This generically leads to a second instability,

as the following considerations show. In a potential propagating state, activator and inhibitor distribution should be shifted with respect to each other. Due to diffusion, the activator in the front will not only spread in the propagation direction but also laterally. While this process may trigger the production of inhibitor material at the sides, the latter is too slow to effectively confine the structure in the direction orthogonal to the propagation direction. The result is commonly a lateral growth to a "banana-shaped" state which in the long-time limit evolves to a planar excitation front infinitely extended orthogonal to the propagation direction, in particular when the activator diffusion is large. The same problem is encountered when considering the nerve-pulse mode in which the activator diffusion is larger than the inhibitor diffusion, explaining why nerve-pulse-like phenomena in two-component systems are commonly investigated only in one

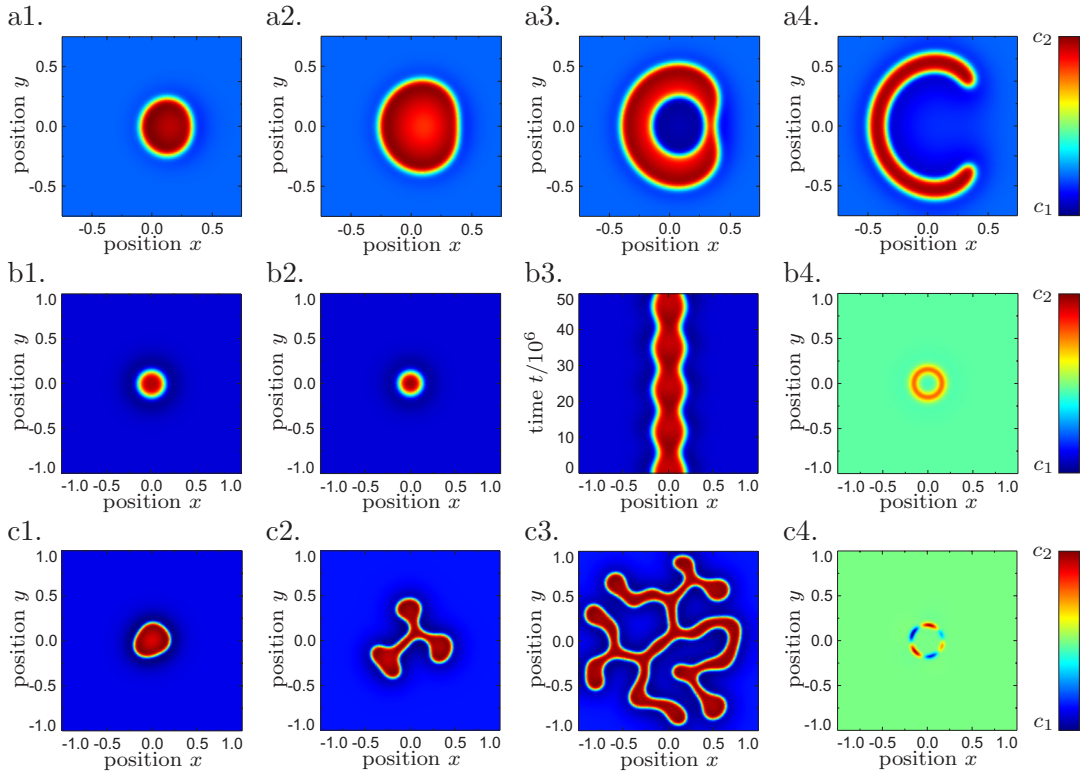

Figure 2.11: Instabilities of single LSs in two-component excitable systems and two spatial dimensions. a. Sequence showing the activator distribution u of the two-dimensional equivalent of a drift instability leading to the formation of a running planar front (times $t = 4$, 8, 12 and 16 from 1 to 4). Parameters: $\lambda = 4.67$, $d_u^2 = 0.002$, $d_v^2 = 0.01$, $\kappa_1 = -1.126$, $\kappa_3 = -3.33$, $\tau = 3$, $c_1 = -1$. $c_2 = 3.5$. As initial conditions, the stationary activator and inhibitor concentrations for lower τ were displaced by $d = 0.05$. b. Breathing instability: activator distribution u at $t = 0$ and $t = 6$ (1 and 2), slice cut through the distribution as a function of time (3) and real part of the critical eigenmode responsible for the bifurcation (4). Parameters as in a. except for $d_u^2 = 0.004$, $\kappa_1 = -1$, $\tau = 1.33$, $c_1 = -1.75$. $c_2 = 2$. c. Time sequence of the activator distribution u showing a destabilization due to a decrease of d_u^2 resulting in the growth of a "dentritic" pattern (1. $t = 50$, 2. $t = 100$, 3. $t = 200$). The last image shows the dominant mode in the destabilization explaining the branching into two new branches. Parameters as in a. except $d_u^2 = 0.001$, $\kappa_1 = -1.14$, $\tau = 0$, $c_1 = -2$. $c_2 = 2$.

spatial dimension. The whole process of the destabilization is visualized in the sequence depicted in Fig. 2.11a. It should be pointed out that some analytical works claim that it is possible to obtain a propagating structure in the two-dimensional case [154], however, no numerical proof was given in this case.

Breathing instabilities are indeed generically found in two-component excitable systems if no asymmetric instability precedes the corresponding destabilization, a numerical example is provided in Fig. 2.11b. For bifurcation parameters other than the time constant τ, modes different from the above mentioned ones may become unstable in the primary bifurcation. A problem for the analytical treatment is given by the fact that the stationary distribution changes its shape before the destabilization point, although some special cases can still be dealt with [96]. In Fig. 2.11c we show an example where a destabilization occurs by decreasing d_u^2. Here, several modes become unstable in the bifurcation which occurs even for $\tau = 0$, and in our numerical example even the discretization of the active area is sufficient to break the radial symmetry of the initial condition. One slightly asymmetric mode dominates the instability in the long-time limit rather independent of the initial conditions (see d4). As this mode has an only weakly broken threefold discrete rotational symmetry, one observes characteristic branching processes in which one existing branch splits into two new ones, thereby inducing the growth of a kind of "dendrite-like" pattern.

One may ask what additional mechanisms can be used to stabilize propagating LSs in the two-component system in two or more spatial dimensions. As during the decay of the running pulse too much material is produced at the sides of the pulse, analogously to the one-component case global coupling (in particular global inhibition) may help to stabilize a single LS as described above also in the propagating case [129, 155, 156]. A frequently problem however is again given by mutual competition of the LSs: non-equally shaped LSs are put into competition by global coupling, and one frequently finds that one LS may grow in favor of the other LSs in the system, so that in the long-time limit only one structure survives [112, 129]. At this point, one has to remark that for symmetric initial conditions, several standing or propagating LSs can exist and interact [102, 113]. The decay due to the integral term in the considered case was found to occur so slow that one may observe interaction of the transient structures on a fast time-scale. Furthermore, there are works on two-component systems in one dimension which indicate the generation of two stable running LSs from an asymmetric initial condition [78, 79].

In the experiment, different types of dynamical destabilizations of LSs in two-dimensional reaction-diffusion type systems have been found. On the one hand, intrinsically traveling isolated LSs have been observed in planar dc gas-discharge systems with high-ohmic barrier and integral series resistor [157, 158]. However, the dynamics is overlaid by fluctuations so that stochastic data analysis methods have to be used to visualize the intrinsic propagation (compare also Sec. 3.2.2.3 below). Breathing has so far only been observed in bistable systems which we will discuss below.

The next point we want to address is the interaction of LSs in excitable media. If no global coupling is present in the system, basically an arbitrary number of remote LSs can coexist independently. When the distance becomes smaller so that the LSs slightly overlap, one observes weak interaction during which the nature of the LSs stays essentially preserved. As we have seen from the previous examples, the decay of the LSs can be oscillatory or non-oscillatory. In the first case, one may generally expect a mixed

attractive-repulsive type of interaction, so that mutual lock-in of the LSs is possible, which is also observed for other types of systems. When the decay is non-oscillatory, both mixed and purely repulsive interaction is possible, see below. An understanding of the mechanisms of interaction is usually possible in terms of local transport and the activation-inhibition-principle, as we will illustrate in the following example in two spatial dimensions.

In our two-component Fitzhugh-Nagumo-type system, we can choose the parameters in such a way that the decay of the LSs is non-oscillatory. Furthermore, choice is such that the individual stationary LSs are stable in both one and two dimensions, making the consideration rather independent of the spatial dimension. We choose a linear superposition of two weakly overlapping LSs in two spatial dimensions as initial condition (a slice cut through the distributions along the connecting line of the LSs is shown in Fig. 2.12a). The numerical simulation shows that in the course of time the LSs separate until they do no longer overlap. In order to understand this observation, we may plot the time derivatives $\partial_t u$ and $\partial_t v$ along the connection line of the LSs as a function of time and space in a filled contour plot (Fig. 2.12b and c). From Fig. 2.12a which shows u, v and in particular $\partial_t u$ in the first instant of the simulation as a thick dotted line, we may see that due to the nonlinear reaction function, close to the center where the overlap of the LSs is strongest the amount of activator material starts to decrease strongly. The reason for this is that while the diffusive fluxes simply add up due to the linear diffusion operator, the production of activator is smaller than twice the value for a single LS due to the nonlinear reaction function. Instantly afterwards, the decrease of activator concentration causes the concentration of the fast inhibitor in the same region to drop as well. This is also illustrated by blue regions in the center of Figs. 2.12b and c for small times, note the nonlinear color scaling. As diffusion sets in, material is transported from the sides to the depletion zone in the center to compensate

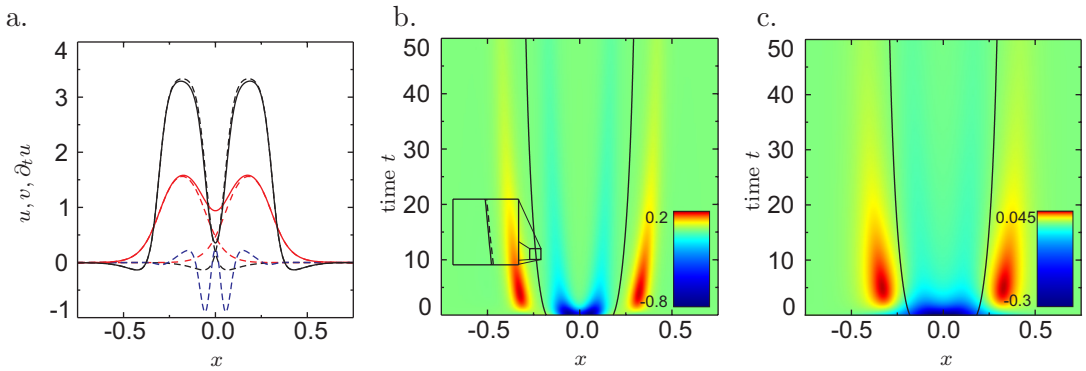

Figure 2.12: a. Activator (black) and inhibitor (red) distributions along the connection line of two stationary two-dimensional distinct LSs with ground state shifted to the origin (dashed lines) and their linear superposition (solid lines) as well as the resulting change $\partial_t u$ of the activator concentration (blue dashed line). b. and c. Resulting change $\partial_t u$ of activator concentration and $\partial_t v$ of inhibitor concentration, resp., as contour plot depending on space and time. The thick lines indicate the positions of the centers of mass of the LSs (in detail, solid lines mark the center of the u and dashed lines the center of the v distribution). Parameters: $\lambda = 4.67$, $d_u^2 = 4.67 \cdot 10^{-3}$, $d_v^2 = 0.01$, $\kappa_1 = -1.126$, $\kappa_3 = -3.33$, $\tau = 0.1$

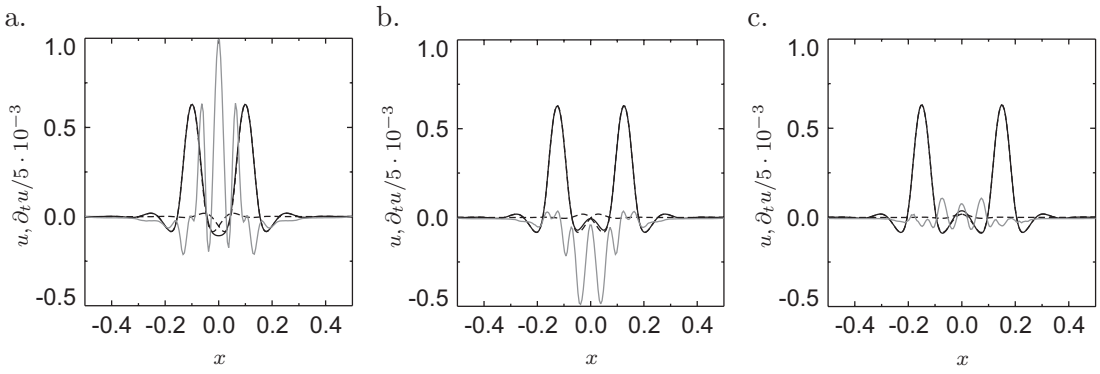

Figure 2.13: Activator distributions u of single and superposed two-dimensional LSs with oscillatory tails (dashed and solid black lines) and resulting instantaneous activator change $\partial_t u$ (grey lines) at different distances of the LSs (a. $d = 0.2$, b. $d = 0.25$, c. $d = 0.3$) corresponding to attraction, repulsion and stable lock-in, resp. Parameters: $\lambda = 0.72$, $d_u^2 = 1.1 \cdot 10^{-4}$, $d_v^2 = 9.64 \cdot 10^{-4}$, $\kappa_1 = -0.1$, $\kappa_3 = 1$.

the steepening of the concentration gradients. As the inhibitor diffusion is much stronger than the activator diffusion, the inhibitor distributions are shifted towards the center to a larger extent than the activator distribution (compare the widths of the blue regions). We have seen above that this asymmetry induces a motion of the LSs to the sides, giving an explanation for the repulsive interaction. The mechanisms works as long as the LSs overlap, however the strength of the effect decreases with distance.

Let us now assume that the LSs have oscillatory tails. Here, aside from the above described repulsion also lock-in behavior, i.e. a mixed attractive-repulsive interaction is possible. With our considerations for non-oscillatory tails above, the explanation of this behavior is rather straight forward. Non-oscillatory tails typically exhibit a monotonous evolution of the tails shape once a certain distance from the center is reached, typically leading to a decrease of the material concentration in the center when the LSs are close to each other. The superposition of oscillatory tails at different distances however allows for a much later range of concentration values to be reached, from "constructive" to "destructive" superposition. The result of the nonlinear superposition depend on the properties of the nonlinearity in the system, however in the first instants one may generally find increased production, decay or the reaction function to be in equilibrium (Fig. 2.13a-c). If the initial concentration in the center decays, one may use the same argumentation as for the non-oscillatory case to see that the LSs increase their distance. On the other hand, if production is increased, material diffuses away from the center to the sides. As the inhibitor diffuses stronger, a surplus of inhibitor builds up in the outer regions of the LS, causing an attractive interaction. To the best of the authors knowledge, in reaction-diffusion systems that were considered up to now a non-oscillatory decay for interacting LSs without intrinsic velocity was always found to lead to repulsion. There are actually some situations in which a number of one-dimensional LSs intrinsically propagating in the same direction may form a bound state or a whole pulse train with a dynamically stabilized distance of the LSs in spite of a non-oscillatory decay [159–161]. However, it seems that the stabilization of the bound state is due to an interplay of intrinsic propagation and repulsion (i.e. a "stacking" similar to a traffic

jam) so that the bound state is not possible without the intrinsic propagation.

Without intrinsic propagation, the number of possible interaction processes is rather limited. Breathing LSs may be positioned at a small mutual distance so that the tails overlap. In this case, numerical simulations carried out by the author for the system (2.19) have shown that unless the initial phase difference of the oscillations of two LSs equals $\Delta\phi = 0$ or π, the displacement of the LSs is accompanied by a synchronization of the phase difference taking place as long as the tails of the structures overlap to a significant amount. If the interaction is purely repulsive, after the separation both LSs oscillate independently with their (equal) intrinsic frequency.

Propagation of the LSs for the two-component system without integral coupling is only possible in one spatial dimension. Let us only consider such interaction processes for which the isolated LSs are initially in a stable state, implying that they propagate with their intrinsic velocity. Fig. 2.9a shows that in this case there is a strong symmetry breaking of the structure just as in the nerve pulse mode depicted in Fig. 2.5 so that when two pulses collide, the leading activator distributions meet without a significant amount of inhibitor being present and directly merge. The resulting state is then surrounded by the trailing large inhibitor concentrations which change only on slow timescales. As a consequence, independent of the exact diffusion constants and time scales the generic outcome of a collision is the annihilation of the involved LSs. A potential alternative is given if the parameters are chosen in such a way that the system is in the narrow bistability regime of standing and moving structures, in this case the merging event may also result in the formation of one standing structure.

We have pointed out above that using global coupling terms may stabilize isolated LSs that are otherwise unstable in more than one spatial dimension. In [113], it was shown that the generically subcritical drift bifurcation could be turned into a supercritical one with the help of integral terms. In this context, collision events were simulated with symmetrical initial conditions, exploiting the fact that initial small asymmetries (for

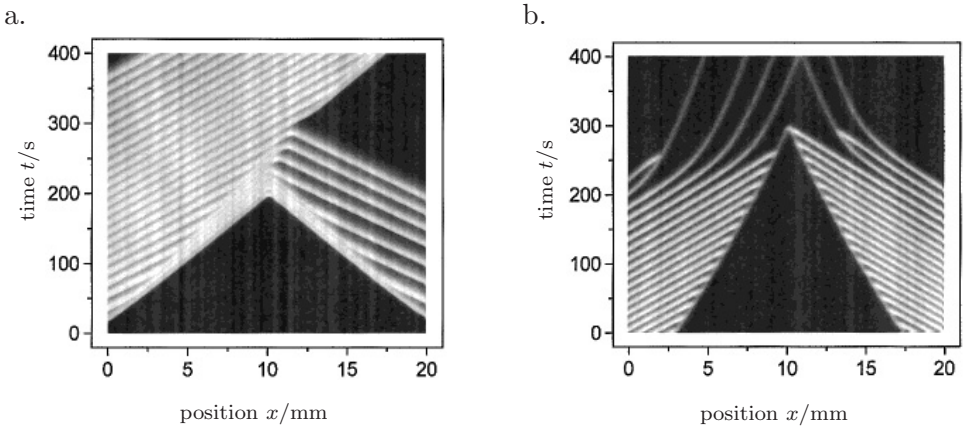

Figure 2.14: Space-time plot of stacking (a.) and merging (b.) of quasi one-dimensional running pulses in capillary tubes observed in a modified version of the Belousov-Zhabotinsky reaction. Bright color indicates the oxidized excited state of the medium whereas dark color represents the rest state. The two depicted scenarios have been found for different concentrations of bromate and cyclohexanedione [137].

example due to numeric discretization) evolved so slow that collisions would take place on a faster timescale. In this context, scattering events, merging processes and generation of new LSs were found. As the situation can be interpreted as a special limiting case of a three-component system, we will discuss further details in the corresponding section.

In the experiment, propagating pulses can be observed for example in thin capillaries. Co-propagating pulses may interact and either show stacking or merging of two successive LSs while counterpropagating pulses generally annihilate in good agreement with our considerations above ([137, 138], see also Fig. 2.14). Mutual annihilation was also observed for propagating pulses on oxidized metal wires [135].

2.1.2.2 The bistable case

Looking at the literature on two-component reaction-diffusion systems, most works focus on the excitable case. Nonetheless, stable LSs can exist in two-component bistable systems without global coupling as well. Two-component bistable systems allow for the generation of two types of LSs, domain solutions as well as structures generated according in the "excitable mode". The existence of the latter type of structure is due to the fact that the excitable and bistable case show strong similarities concerning the phase flow and the topology in those parts of the local phase space which are relevant for the formation of LSs. However, some differences arise as we will explain in the following.

We have seen above that bistable one-component systems may exhibit domain-type solutions which are however generally unstable or marginally stable if no mechanisms like global coupling are present to stabilize the domain size. The latter are potentially undesired to avoid mutual competition of the LSs. Stability considerations for domain solutions in two-component systems can be treated in analogy with the one-component case. To this end, Eq. (2.5) for the two-component case is extended to

$$\boldsymbol{q}(x,t) = \boldsymbol{q}_f(x - p_1(t)) + \boldsymbol{q}_f(p_2(t) - x) - \boldsymbol{q}_2 + \boldsymbol{r}(x,t) \tag{2.23}$$

with $\boldsymbol{q}_f$ denoting the unperturbed front solutions, and evolution equations for the front distance are derived using singular perturbation analysis. The free front velocity c can be determined by transforming the system into a moving frame, directly yielding

$$c = -\frac{H(\boldsymbol{q}_2) - H(\boldsymbol{q}_0)}{\langle u_x | u_x \rangle - \tau \langle v_x | v_x \rangle} \quad \text{with} \quad H(\boldsymbol{q}) = \int_{u_0}^{u} f(s)\,\mathrm{d}s - uv + \frac{1}{2}v^2. \tag{2.24}$$

The distance of the interacting fronts is then a result of the intrinsic front dynamics and the front interaction. For $\tau = 0$, a complete analytical solution was given in [127] which reads

$$\partial_t d_{21}(t) = -2c + F(d_{21}(t)) \quad \text{with} \quad F(d) = a_1 \exp(-b_1 d) + a_2 \exp(-b_2 d(t)). \tag{2.25}$$

The coefficients a_1, a_2, b_1 and b_2 depend on the system parameters and one generally finds $b_1 > b_2 > 0$. While details are given in [127], we just want to state the result

that one may distinguish three cases schematically depicted in Fig. 2.15. First, in the case $f'(u_2) < d_u^2/d_v^2 - 2d_u/d_v$ one has $a_1 < 0 < a_2$ and the front interaction is asymptotically repulsive (note that the first summand in the interaction force dominates for large distances). Even if there is a c leading to a stationary state according to (2.25) (corresponding to an intersection point of the black and the grey line in Fig. 2.15a), the latter is unstable. Second, for $d_u^2/d_v^2 + 2d_u/d_v < f'(u_2) < d_u^2/d_v^2 + 2d_u/d_v$ the coefficients a_1 and a_2 are complex and the interaction varies between repulsion and attraction with the front distance. Here, both stable and instable lock-in points may be possible for either sign of c (Fig. 2.15b). Third, for $d_u^2/d_v^2 + 2d_u/d_v < f'(u_2) < 1$ there is $a_1 > 0 > a_2$ and the fronts are attracting asymptotically. Here, a stable lock-in is possible when the sign of c is positive (Fig. 2.15c). Note that a generalization to the case of finite τ is possible and yields qualitatively similar results as long as $\tau < 1$ (then, the denominator of (2.24) remains positive). In particular, when considering the case of oscillatorily decaying fronts (Fig. 2.15b), the mechanism responsible for the lock-in behavior is the same as for oscillatory tails of LSs in excitable system discussed above. In contrast, when looking back at the one-component case, by linearizing (2.2) around the ground state for $c = 0$ one may directly see that for a positive diffusion coefficient and a stable ground state (meaning a positive prefactor in the linearized reaction function) no oscillations close to this state are possible so that the above lock-in mechanism can not work in one-component systems. Further analytical details on the formation of domains can eg. be found in [127, 162].

While the above considerations show that the extension from one to two components enables the formation of stable domain structures, the latter are found only seldom and even in their range of existence they are very susceptible to perturbations. The reason for this is that in domain structures, a rather weak overlap of two fronts in the central region has to compensate for the intrinsic motion of the individual fronts. The absolute value of the front velocity therefore has to be rather small as well. However, an equality of the upper and the lower state according to the dominance rule (2.24) is not the usual

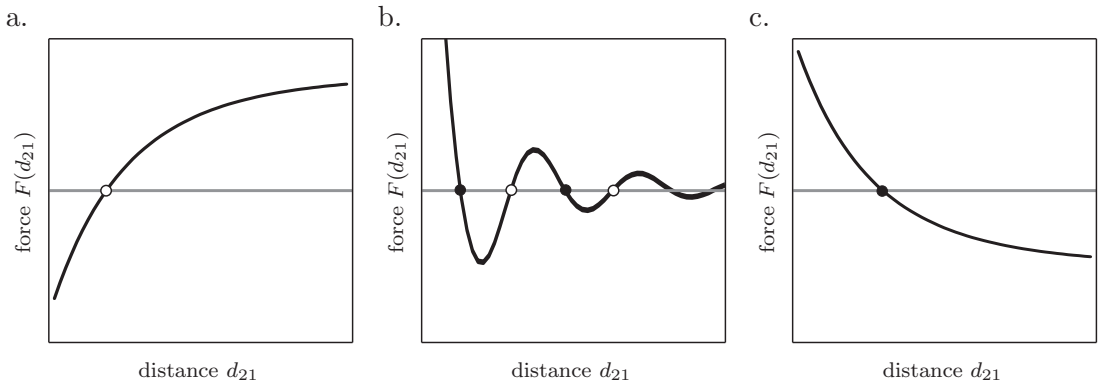

Figure 2.15: Schematic illustration of the possibility of two fronts to form a domain state. The figures show the interaction force $F(d)$ according to (2.25) for large distances a. for repulsion of the fronts, b. for mixed attractive-repulsive behavior, c. for attraction of the fronts. The grey line marks a value of $2c$ for which intersection points with the interaction function are possible, corresponding to stable and instable lock-in distances of the two fronts.

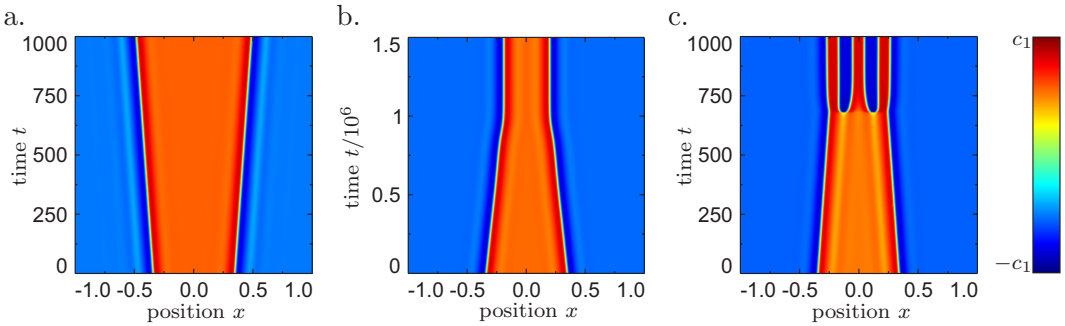

Figure 2.16: Formation of one-dimensional LSs in the form of wide domains by locking of two fronts with oscillatory tails. a. The front velocities are too high ($\kappa_1 = 0.01$), causing the system to switch to the upper state. c. The front velocity is low enough ($\kappa_1 = -10^{-5}$) so that the oscillatory tails can lock in to form a stable domain. c. The negative front velocity is too high ($\kappa_1 = -0.01$) so that the tails can not prevent the front from collapsing. Instead of the system switching to the low state, three stable narrow LSs are created during the process. Other parameters: $\lambda = 1.294$, $d_u^2 = 10^{-4}$, $d_v^2 = 9.64 \cdot 10^{-4}$, $\tau = 0$, $\kappa_3 = 1$, scale $c_1 = 1$, initial condition: superposition of two standing fronts found for $\kappa_1 = 0$ with a distance $d = 0.4$.

case so that the front velocities are often too large to allow for the formation of an equilibrium state according to (2.25). There is however a second possibility to form LSs via the excitable mechanism also in the bistable scenario which is encountered in most cases. We will illustrate the idea using a numerical example. During our study on excitable systems above, in Fig. 2.7 we have chosen $\kappa_1 = -0.1$ and have induced a transition from oscillatory to non-oscillatory tails by going from $\lambda = 0.8$ to 1.294. As $\lambda > 1$ in the latter case, by moving κ_1 to zero and keeping λ fixed we may turn the excitable system into a bistable one. In the bistable case, standing or moving front solutions exist in a large range of parameters and can easily be found numerically by using step functions as initial conditions. For our choice of parameter, these fronts have oscillatory tails and hence should be suitable to produce a front-antifront domain via the above mechanism. The front velocity can be controlled via κ_1, the case $\kappa_1 = 0$ corresponds to stationary fronts as upper and lower state are equal.

In Fig. 2.16a, we choose an initial condition in which the oscillatory tails weakly overlap in the central region by linearly superposing two isolated fronts and choose a positive $\kappa_1 = 0.01$ implying the dominance of the upper state. Although the front velocity is rather low, we find that it is still so high the oscillating tails can not compensate the motion and the system is globally switched to the upper state. In b. we choose $\kappa_1 = -10^{-5}$, implying a very weak dominance of the lower state. In this situation, the interaction can compensate the front motion and a stable domain structure is formed. Moreover, the simulation shows that there is indeed a finite interval of front velocities over which this state can be generated although the region of existence is very small and very small perturbations are sufficient to destroy the integrity of the domain structure. Finally, in c. with $\kappa_1 = -0.01$ the lower state is too dominant for a domain to form, however instead of switching the system to the low state, several narrow LSs are generated which form a stable cluster. In contrast to the wide domain, the narrow LSs can not be considered as weak superposition of two front solutions. For other initial conditions, also other numbers of LSs as well as isolated LSs can be generated. They

are much more robust to perturbations and exist also in the region where the domains are possible.

An explanation for the two types of structures is given by the representation in the reaction phase space (Fig. 2.17). The domain structure shown in Fig. 2.17b corresponds to an heteroclinic orbit connecting the two stable fixed points of the local dynamics. In contrast, by comparing the narrow structure in Fig. 2.17c with the excitable case shown in Fig. 2.7b we find that the narrow LS can be considered to be created via the excitable mechanism in spite of the bistability of the system. In other words, the existence of a second fixed point corresponding to the upper state plays no role as long as the phase space below qualitatively agrees with the excitable case as the inhibitor diffusion prevents the system from locally coming close to this point anyway. We may therefore apply or arguments from the excitable case to the bistable case as well as long as the structures are formed via the excitable mechanism. Indeed, it was possible to reproduce basically all dynamical phenomena from the excitable case in the bistable situation as well (data not shown) whereby in all situations the LS corresponded to the excitable situation. In contrast, it was not possible to produce dynamic destabilizations of the domain structures that did not lead to an immediate decay.

In the experiment, bistable systems have been considered in the form of the ferrocyanide-iodate-sulfate reaction in gel reactors for which both two- [67] and four-component models [87] have been proposed. Observations include domain states which grow in time and eventually perform periodic oscillation which however are related to interactions of the domain state with the system boundaries [67]. Also a self-replication scenario has been found in which domains grow and finally break up into several new domains so that a characteristic average domain size stays preserved in the course of time [163]. It should be pointed out that experimentally no isolated stable stationary domains have been observed, which is in good agreement with our theoretical considerations on the stability of these structures.

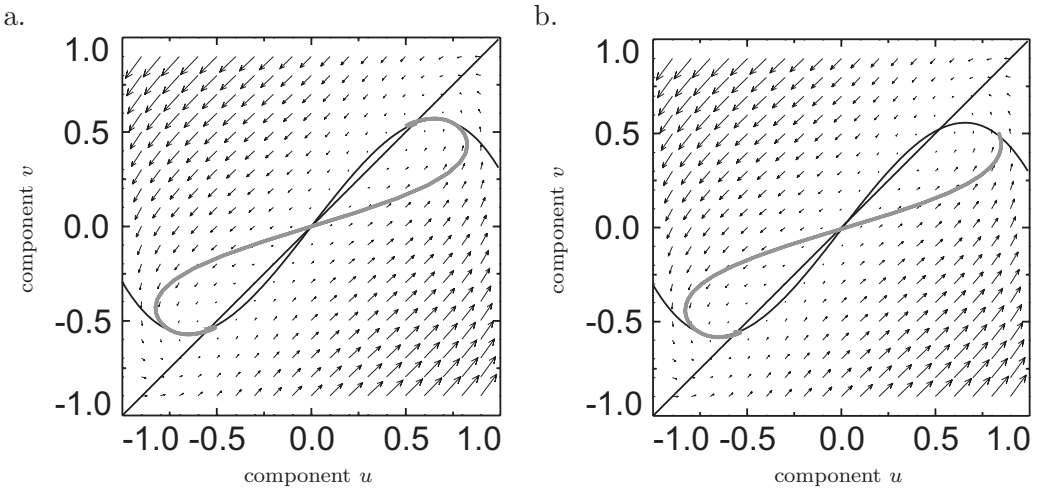

Figure 2.17: Representation of LSs in a nullcline and phase space plot for the bistable case: a. domain structure corresponding to that shown in Fig. 2.16b, b. structure formed via the "excitable mechanism" corresponding to a single structure as formed in Fig. 2.16c.

2.1.3 Three-component systems

Up to now, we have tried to build up a systematic description of reaction-diffusion systems on the number of reacting components and the spatial dimension. In one-component systems a rather complete description is available, and also in two-component systems the classification according to the criterion of excitability and bistability works rather well. Both cases turn out be be rather closely connected as the topology of the phase space is similar in the relevant parts. Going to three- or even more-component systems, up to now no systematic investigations have been carried out and consequently no general statements on the existence of LSs exist. A central problem in this context is that in two-component systems, the mechanism of the formation of LSs is closely connected to the existence of a loop or at least semi-loop in the local phase space so that production could be compensated by diffusion. While one may speculate that this principle will remain of central importance for systems with more components, the complexity of the local phase space alone may increase so vastly for three components that a systematic access appears rather difficult.

Due to these problems, we will not make an attempt towards a possible classification here. Instead, we will look back at the findings in two-component systems and ask what types of dynamics were not possible in these systems. In one dimension, we have found that intrinsic propagation and breathing are possible, thus allowing for a number of interaction phenomena. However, the possible outcomes of interaction processes are rather limited. Furthermore, propagating structures could be generated only in subcritical bifurcations. In two and more dimensions, propagation was not possible unless global coupling was used, thereby greatly reducing the number of possible dynamical processes. A brief overview is on these aspects given in Table 2.3. All observations are related to one essential point. Propagation demands a symmetry breaking that can be realized in reaction-diffusion systems of the discussed type by a delayed reaction of the inhibitor with respect to the activator. Stabilization of a LS on the other hand demands the opposite situation: a fast reaction of the inhibiting component. Both requirements can be

	existence 1 LS	existence n LSs	drift bif. subcritical	drift bif. supercritical	breathing	oscillating tails
1 comp. monost.	n	n	n	n	n	n
1 comp. bistable	n	n	n	n	n	n
1 comp. bist. integral	y	n	n	n	n	n
2 comp. 1D	y	y	y	n	y	y
2 comp. 2D	y	y	?	?	y	y
2 comp. 2D integral	y	n	y	y	y	y
3 comp.	y	y	y	y	y	y

Table 2.3: Summary of the possible existence and observability of different important phenomena in the reaction-diffusion systems investigated in this work.

realized in a non-contradictious way only in one spatial dimension. In three-component systems, the two tasks of the inhibitor can be split up to be taken over by two separate components, a fast and a slow one. The fast component (with a long diffusion range) may confine the structure while the slow one may control potential bifurcations. A straight-forward extension of the two-component extension Fitzhugh-Nagumo type system is given by [38]

$$\begin{pmatrix} \partial_t u \\ \tau \partial_t v \\ \theta \partial_t w \end{pmatrix} = \begin{pmatrix} d_u^2 & 0 & 0 \\ 0 & d_v^2 & 0 \\ 0 & 0 & d_w^2 \end{pmatrix} \begin{pmatrix} \Delta u \\ \Delta v \\ \Delta w \end{pmatrix} + \begin{pmatrix} \lambda u - u^3 - \kappa_3 v - \kappa_4 w + \kappa_1 \\ u - v \\ u - w \end{pmatrix}, \quad (2.26)$$

and the stationary two-component solutions for u and v can be re-obtained by the choice $\lambda \to \lambda + \kappa_4$, $d_w = 0$. For θ sufficiently small and $d_u^2 \ll d_v^2$, inhibitor keeps surrounding the LS, and the previously presented subcritical bifurcations turn into supercritical ones if induced by a change of θ (more analytical details on this point are given in the next chapter). In particular for $\theta = 0$, w adapts instantaneously to u and the solution of $d_w^2 \Delta w - w = -u$ reads

$$w(\boldsymbol{x}, t) = \int G(\boldsymbol{x}, \boldsymbol{y}) u(\boldsymbol{y}, t) \, \mathrm{d}\boldsymbol{y} \quad (2.27)$$

where G is an appropriate Green function being a weak solution for the inhomogeneous linear differential equation $d_w^2 \Delta w - w = -\delta(\boldsymbol{x})$ in the domain of interest. In one dimension on an infinite domain, the Green function for the problem of interest is given by

$$G(x, y) = \frac{1}{2 d_w} \exp\Big(- \frac{|x - y|}{d_w} \Big), \quad (2.28)$$

showing that for $\theta = 0$ the third component acts like an integral coupling with a kernel of limited range. In some sense, the previously discussed global coupling can therefore be considered to correspond to a stabilizing component with infinite diffusion length.

With the three-component extension (2.26), stable propagating LSs are possible in all finite numbers of spatial dimensions and the propagation velocity can take values in a continuous interval from zero to a finite value. For very small velocities of the LSs, only the tails of the LSs overlap when two or more LSs come close to each other. As the coupling structure of the system (2.26) is linear in both inhibitors, the interaction mechanism presented in Figs. 2.12 and (2.13) can be directly generalized, so that one either finds repulsion (i.e. scattering events) or a potentially a lock-in in the case of oscillatory tails if the velocity is high enough to overcome an initial repulsion for large distances. The two cases are depicted in Figs. 2.18 and 2.19, respectively, the central difference in the initial conditions is the time constant τ which is larger in the second case and thus causes a higher intrinsic velocity.

When the interacting LSs however approach each other up to a distance where their cores themselves overlap (which is the case for intrinsic high velocities), one generally observes phenomena where the structure of the individual LS does not stay preserved. Typically, in this case generation and annihilation of LSs occurs. An outcome of such a

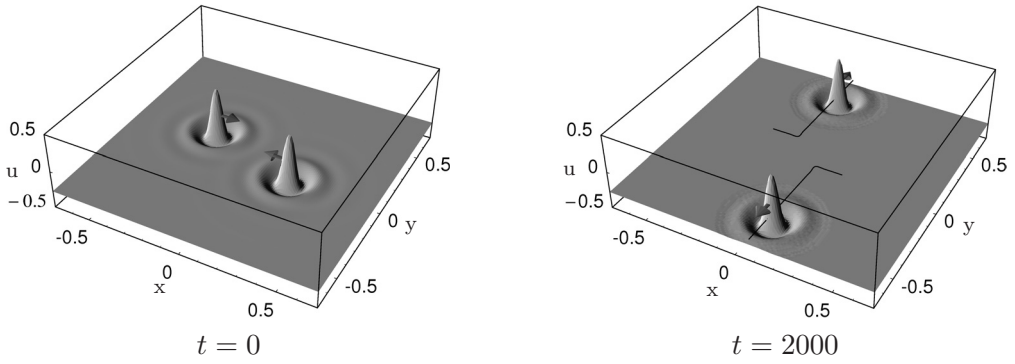

Figure 2.18: Numerical solution for Eq. (2.26) in $\mathbb{R}^2$ showing the activator distribution for a typical scattering process of two LSs and corresponding trajectories of its centers. Parameters: $\tau = 3.345$, $\theta = 0$, $d_u^2 = 1.1 \cdot 10^{-4}$, $d_v^2 = 0$, $d_w = 9.64 \cdot 10^{-4}$, $\lambda = 1.01$, $\kappa_1 = -0.2$, $\kappa_2 = 0$, $\kappa_3 = 0.3$, $\kappa_4 = 1$ and no-flux boundary conditions.

process that is especially frequently observed for LSs with oscillating tails is the generation of a new LS through replication (Fig. 2.20). In the replication scenario, the overlap of several LSs generates a localized excitation that exceeds the critical germ needed to form a new LS. Consequently, LSs are most frequently generated at those distances from the cores where the oscillating tails have local maxima. When there are also stable lock-in distances, replication events are often connected with molecule formation. In some cases, even a whole cascade of generation events may occur, which is termed "self-replication" [164].

A second possibility for the generation of LSs that is generally favored by LSs with purely repulsive interactions is the generation through transient states. Here, the core of an existing LS has a chance to split into two parts, either through a sufficiently large perturbation or through an intrinsic instability. If the two fragments are far enough apart, repulsive interaction sets in, leading to a separation and a relaxation to the stable LS. This scenario is sometimes also termed self-replication in the literature [165, 166].

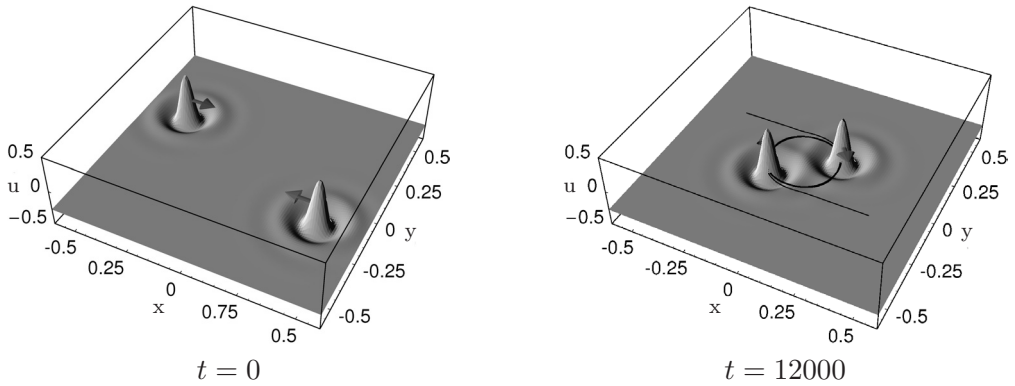

Figure 2.19: Numerical solution for Eq. (2.26) in $\mathbb{R}^2$ showing two LSs which approach and "lock in" on each others tails, resulting in the formation of a stable molecule. Parameters like in Fig. 2.18, except for $\tau = 3.35$.

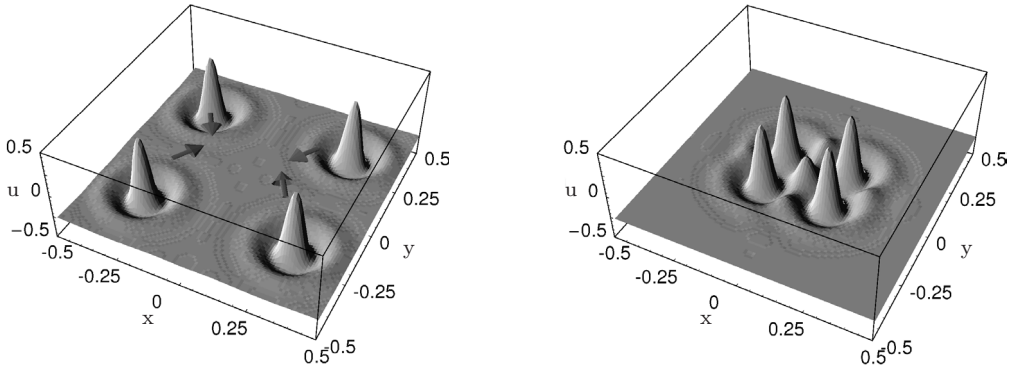

Figure 2.20: Numerical solution for Eq. (2.26) in $\mathbb{R}^2$ demonstrating the generation of a new LS through "replication". Parameters like in Fig. 2.18, except for $\tau = 3.47$.

Similar to generation, there are two scenarios for the annihilation of LSs, one again preferred by LSs with mixed, the other one by such with purely repulsive interaction. The first case is called annihilation by extinction (see Fig. 2.21). The cores of two colliding approach each other until they feel the presence of inhibitor material in the tail around the other core. The fast inhibitor in the tail starts reducing the surplus of activator on its side of the core while the inhibitor pursuing the core reduces the activator on the opposed side. As the activator has no possibility to keep a stable distance from the inhibitor, this mostly leads to a decay of all colliding LSs.

In the repulsive case, annihilation of two LSs usually occurs via merging. As on their leading sides the LSs have no regions of increased inhibitor concentration due to oscillatory tails at high velocities the activator distributions may come close without suffering significant losses. Depending on the relation of local reaction and diffusion, either the merged state decays as a whole (as typical for the nerve pulse case) or relaxes to a stable state with approximately the extension of the merged state, which is a single LS. The reason why the survival of a single LS is more likely than in the nerve pulse

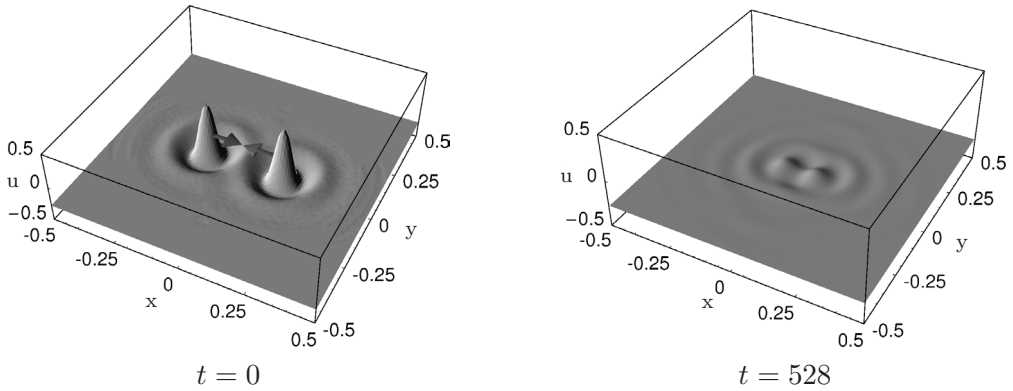

Figure 2.21: Numerical solution for Eq. (2.26) in $\mathbb{R}^2$ demonstrating the annihilation of two fast LSs in a head-on collision. Parameters like in Fig. 2.18, except for $\tau = 3.59$.

case is because the asymmetry of the structure is usually not as large. For reasons of completeness one should mention that merging can also happen for LS with mixed-type interactions, although it is not very likely.

We want to mention that the above explanations on interaction processes partly rely on the fact that the inhibitor components are not coupled in a nonlinear fashion. Such a nonlinear coupling may produce a variety of new effects [54, 167]. Further studies on the dynamics and interaction of LSs in three-component systems can for example be found in [55, 164, 168–170].

There are a number of experimental systems that reproduce the theoretically predicted phenomena for three- and more-component systems. A significant coincidence is found for planar dc gas-discharge systems with high-ohmic barrier. Here, all phenomena depicted in Figs. 2.18-2.21 can be observed [2, 55, 171–173]. Examples for phenomena related to weak interaction during which the nature of the LSs stays preserved (scattering, bound states) are given in the next chapter. The experimental counterpart of a generation event due to the overlap of several LSs as shown in Fig. 2.20 is depicted in Fig. 2.22. A breathing type of dynamics was found for LSs in a Belousov-Zhabotinsky reaction dispersed in a flat layer of Aerosol micro-emulsion [69], in this case the reaction was modeled using both three- and four-component systems. Intrinsically propagating elongated concentration pulses and their interaction (collision, interpenetration and annihilation) were observed for the catalytic oxidation of CO using O_2 on platinum surfaces under low-pressure conditions [6]. A three-component model was found to reproduce these phenomena [174], however calculations were carried out just in one spatial dimension.

At the end of the section on reaction-diffusion systems, we again want to point out that while a large variety of different reaction-diffusion was investigation also with respect to LSs (Table 2.1), most works do not aim at obtaining generally applicable

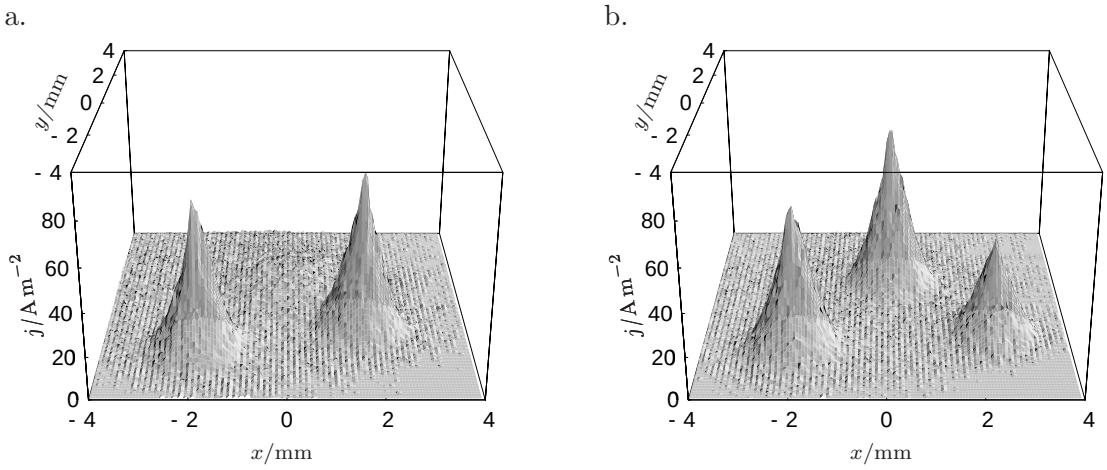

Figure 2.22: Experimentally observed generation of a LS in the form of a current filament found in a two-dimensional planar dc gas-discharge system with high-ohmic barrier. The images show the average current density distribution in the discharge plane recorded with an exposure time $t_{\mathrm{exp}} = 0.2\,\mathrm{ms}$. The time interval between the two images (a.) and (b.) is 104 ms [2, 55]. Note the analogy to the numerically obtained result in Fig. 2.20.

mechanisms. Implicitly or explicitly however, the above presented mechanisms always play an important role. A very interesting aspect that we have not treated here (but concerning which related works are listed in the table) is the influence of cross-diffusion.

2.2 Ginzburg-Landau equations

Ginzburg-Landau (GL) equations are complex field equations without convection terms. The name originates from works by Ginzburg and Landau on superconductivity [175], where the first GL equation appeared. Nowadays, this class of nonlinear wave equations describes a large variety of systems, for example in optics, Bose-Einstein condensation, liquid crystals and even string theory (see [176] and references cited therein).

In most typical applications of the GL equation the underlying system exhibits fast oscillations, for example with a gigahertz frequency in nonlinear optical systems, whereas the observed times scales for patterns are considerably longer. Hence, a natural approach is to consider a slow envelope of the wave and to make the ansatz

$$E(\boldsymbol{x},t) = \hat{E}(\boldsymbol{x},t)\exp\Big(i\omega t + i\varphi(\boldsymbol{x},t)\Big) + \text{c.c.}, \tag{2.29}$$

where for simplicity a scalar electrical field is considered. The enveloping amplitude $\hat{E}$ and the phase φ are considered as slow functions on the time scale $2\pi/\omega$ of the underlying oscillations. The GL equation describes the evolution of the complex scalar $q := \hat{E}\exp(\imath\varphi)$. This also matches the experimental observations, where detectors measure only quantities averaged over the fast timescales.

The most frequently encountered cubic version of the GL equation, first phenomenologically introduced by Newell and Whitehead [177], reads

$$\partial_t q = (d_r + id_i)\Delta q + l_r q + (c_r + ic_i)|q|^2 q. \tag{2.30}$$

Here d_i and c_i describe linear dispersion and nonlinear frequency shifts of the underlying wave, the other coefficients result from dissipative effects. The parameters l_r and c_r account for linear and nonlinear gain at the central frequency, the "diffusion" term $d_r\Delta q$ accounts for spectral filtering [34].

Aside from the usual translational invariance in space, Eq. (2.30) is invariant under phase shifts of $q \to q\exp(i\varphi)$ (gauge symmetry). This simply reflect the fact that the representation (2.29) must be invariant under arbitrary time shifts and therefore any constant phase can be added to $\varphi(\boldsymbol{x},t)$. That is also the reason why Eq. (2.30) contains no second order powers in q and only one of four possible third order products, the other terms do not possess the required symmetry. This aspect can also be understood as follows: when a system oscillates with a frequency ω, nonlinearities will generate higher (multiple) harmonics. If one is interested in the behavior of the original wave amplitude, only such parts of the nonlinearities may be considered which leave the original frequency unaltered.

There are two basic ways how a GL equation can be obtained. In a number of systems a rather straightforward derivation is available, for example by starting from the Maxwell

equations in optic systems. Using the paraxial approximation, these equations can be cast into the so-called paraxial wave equation, which in three spatial dimensions reads

$$\partial_z q(\boldsymbol{x},t) = -\frac{i}{2k}\Big(\Delta_\perp + k^2\chi\Big)q(\boldsymbol{x},t). \tag{2.31}$$

Here, k is the wave vector of the fast-oscillating electromagnetic field and z denotes the main propagation direction. The complex dielectric susceptibility χ depends on the averaged electrical field, therefore one immediately obtains a generalized GL equation when assuming $\chi = \chi(|q|^2)$ and identifying $z = t$. Optical systems with saturable nonlinearities often lead to a GL equation of the form [178, 179]

$$\begin{aligned} \partial_t q &= (d_r + id_i)\Delta q + f(|q|^2)q, \\ f(|q|^2) &= l_r + \frac{s_r + is_i}{1 + c|q|^2}. \end{aligned} \tag{2.32}$$

The above type of nonlinearity can for example be derived by considering the Maxwell-Bloch equations for a laser resonator with a fast medium. After an elimination of the fast atomic variables the corresponding model equations can be cast into the form [180]

$$\begin{aligned} \partial_t q &= (D_r + iD_i)\Delta q + (l_r - \beta)q + \frac{pq}{1 + |q|^2/I_g}, \\ \partial_t \beta &= \gamma\Big(\beta_0 - \beta(1 + \frac{|q|^2}{I_s})\Big), \end{aligned} \tag{2.33}$$

where q represents the envelope of the electric field and β is a measure for the saturation of the absorber with a maximum value β_0. The coefficientγ is the relaxation rate of the absorber and I_g and I_s are gain and absorption saturation intensities (see also [181]). By neglecting the inertia of the absorber ($\gamma \gg 1$), from (2.33) one obtains the Ginzburg-Landau type equation

$$\partial_t q = (D_r + iD_i)\Delta q + l_r q + \frac{pq}{1 + |q|^2/I_g} - \frac{\beta q}{1 + |q|^2/I_s} \tag{2.34}$$

which basically is a special version of (2.32) as all local terms contain only real coefficient, meaning that they are dissipative in nature. While some works directly use saturable functions, others expand the nonlinearity in terms of $|q|$, thereby arriving at a cubic or, more general, quintic GL equation

$$\partial_t q = (d_r + id_i)\Delta q + l_r A + (c_r + ic_i)|q|^2 q + (q_r + iq_i)|q|^4 q, \tag{2.35}$$

which plays a particular role for LSs. Note that while any function $f(|q|^2)$ than can be Taylor-expanded may produce a decomposition as in (2.35) and thus it is sometimes

argued that (2.35) can be considered as a generic nonlinearity, an agreement with a saturable nonlinearity as in (2.32) is only given if $|q|$ does not exceed a certain magnitude.

The second way of obtaining a GL equation is rather indirect and demands a number of transformations and simplifications to bring the dynamic system to its normal form near the instability threshold. In this context, $q(\boldsymbol{x}, t)$ is a slow order parameter, the onset of instability is described by the term $l_r q$ and the nonlinear terms result from an expansion of the nonlinearity around the stationary solution $q = 0$. Usually in these cases at most a qualitative comparison with the experiment is available. Note also that LSs are large-amplitude structures generated in subcritical bifurcations, a separate justification of the amplitude expansion is therefore required. Concrete examples of the derivation of GL equations can for example be found in [182, 183] for Rayleigh-Bénard convection, in [184–187] for optical systems and in [188, 189] for chemical systems. A relation to experiments on binary liquids was pointed out in [7, 190, 191]. GL-type equations in combination with additional equations are the basis for example for models for oscillons [192] in vibrated granular media.

While many different extensions and variations of the cubic GL equation exist, we first restrict ourselves to the above introduced systems with one scalar amplitude. We will also leave behind the connection of the GL equation to a concrete physical system and consider $q(\boldsymbol{x}, t)$ as the only quantity of interest.

2.2.1 The formation of LSs

Formally, Eq. (2.30) can be considered as a hybrid structure of the classical nonlinear Schrödinger (NLS) equation

$$i\partial_t q + d_i \Delta q + c_i |q|^2 q = 0 \tag{2.36}$$

obtained in the limiting case $d_r = l_r = c_r = 0$ and a reaction diffusion equation

$$\partial_t q = d_r \Delta q + l_r q + c_r |q|^2 q \tag{2.37}$$

obtained for $d_i = c_i = 0$. Eq. (2.37) allows real solutions and is sometimes also referred to as a real Ginzburg-Landau equation.

Close to the individual limiting cases, one may try to understand the formation of LSs as a perturbation of the limiting case. The NLS equation is conservative and can be derived from a Hamiltonian function

$$H := \int_\Omega \left(\frac{d_i}{2} |\nabla q|^2 - \frac{c_i}{4} |q|^4 \right) \mathrm{d}^n \boldsymbol{x}, \tag{2.38}$$

so that the energy is only redistributed in space but not produced or dissipated in the system. Localized solutions exist if $d_i c_i > 0$, i.e., when the contributions of the dispersion and nonlinearity are opposed to each other. The central mechanism for the formation of classical solitons in the NLS equation is the balance of dispersion by nonlinear effects. In Fourier space a soliton can be represented as a wave packet that would decay in the

sole presence of dispersion due to the different velocities of the individual frequency components. Due to the nonlinear frequency shift the velocities are matched exactly, so that the packet propagates as a whole.

In one spatial dimension the solitons are stable and the NLS equation possesses a remarkable property: it is completely integrable via the inverse scattering technique [18]. This property is unique, when extending the NLS equation by higher order or saturable nonlinearities, integrability breaks down although soliton solutions are still possible. In particular, for initial conditions close to a stable soliton the extraneous energy is radiated away. In two and three dimensions the solitons of (2.36) are unstable and can collapse (meaning in this special context that they evolve to a singularity in finite time). For instance, in three dimensions the collapsing solution asymptotically obeys the scaling relation

$$|q(\boldsymbol{x},t)| = \frac{1}{\sqrt{t_0-t}} f(\frac{\boldsymbol{x}}{\sqrt{t_0-t}}), \tag{2.39}$$

and blows up to a singularity at $t = t_0$, the latter time being determined by the initial conditions [193]. In a more general quintic Schrödinger equation the collapse can be stopped for large amplitudes where higher nonlinearities become important. In this case stable solitons exist also in several spatial dimensions.

Contrary to the above "wave" explanations, the solution of the dissipative reaction-diffusion Eq.(2.37) can best be understood in terms of local transport of material. For $l_r > 0$ material is produced by the linear term and diffuses away due to the term $d_r\Delta q$. The production usually has a nonlinear cut-off by the term $c_r|q|^2q$ with $c_r < 0$. Therefore the local concentration of matter can not increase indefinitely.

In order to see that the GL equation generically is different from both reaction-diffusion and nonlinear Schrödinger equation, one may rewrite (2.35) in terms of the real and imaginary part, yielding (with $q = a + ib$)

$$\begin{aligned}
\partial_t a &= d_r\Delta a - d_i\Delta b + l_r a + (a^2+b^2)(c_r a - c_i b) + (a^2+b^2)^2(q_r a - q_i b),\\
\partial_t b &= d_i\Delta a + d_r\Delta b + l_r b + (a^2+b^2)(c_i a + c_r b) + (a^2+b^2)^2(q_i a + q_r b).
\end{aligned} \tag{2.40}$$

This system can formally be considered as a reaction-diffusion system with a complicated nonlinearity and a general (non-diagonal) diffusion matrix. One should note however that the "cross-diffusion" terms have conservative nature and do not describe any real time-irreversible diffusion. This fundamentally changes the qualitative properties of the full equation with respect to the two extreme cases. The cross-diffusion term is easily understandable in the frequency image, however the effect of classical diffusion then becomes difficult to understand.

Let us start with some necessary conditions for the existence of LSs. Eq. (2.40) shows that the growth rate of a homogeneous perturbation of the ground state $q = 0$ is directly given by l_r, hence the linear stability of the background $q = 0$ immediately requires $l_r < 0$. In the case $l_r > 0$, the background becomes unstable, but for $c_r < 0$ another homogeneous state can become stable instead. Generally, the latter case may be referred to as supercritical GL equation as a continuous transition from one state to the other can be induced via a change of l_r. There is only one special type of LS possible in this situation, the Nozaki-Bekki shock-hole pair, which we will discuss below.

Another conclusion of the coefficients can immediately be found by considering a small perturbation consisting of an extremely narrow spike. In the region of the spike, the "diffusion" terms will dominate all other terms, and a negative d_r would lead to a further growth of the spike. From this we obtain $d_r > 0$ for the stability of the background. Perturbing the ground state $q = 0$ against plane waves with the wave vector $\boldsymbol{k}$ (a good starting point is provided by (2.40)) yields the trace stability criterion

$$-d_r k^2 + l_r < 0 \tag{2.41}$$

and the determinant criterion

$$(l_r - d_r k^2)^2 + d_i k^4 = (d_r^2 + d_i^2)k^4 - 2l_r d_r k^2 + l_r^2 > 0. \tag{2.42}$$

As a result, we see that for $d_r > 0$, $l_r < 0$ both stability criteria hold and the dominant wave number is always zero. As LSs should exist on an homogeneous background, there must be a "driving" effect opposing the local decay of the solution. For $l_r < 0$ this effect must come from the third-order term, or more exactly from its real part, so we have to require $c_r > 0$. Then, the highest-order terms should cause a saturation, so one may require $c_r > 0$, $q_r < 0$. This situation in which most results on LSs are obtained can be referred to as subcritical GL equation. We can now see that in this situation there is one "driving" effect, associated with the constant c_r, which is opposed by two or three "damping" effects, associated with d_r, l_r and q_r. In order to quantify this aspect in a better way, motivated by the classical NLS equation one may define a local energy density $\rho = |q|^2$ and an impulse density $\boldsymbol{m} = 2d_i \mathrm{Im}(q^* \nabla q)$. The local evolution of ρ in the quintic case is given by

$$\partial_t \rho + \nabla \cdot \boldsymbol{m} = S = d_r(q\Delta q^* + q^* \Delta q) + 2l_r \rho + 2c_r \rho^2 + 2q_r \rho^3. \tag{2.43}$$

This expression has the form of a continuity equation with the flux $\boldsymbol{m}$ and a source term which vanishes in the conservative limit of the GL equation. Note that in this decomposition, diffusive contributions are included in the source term. It is not possible to define a diffusive flux of ρ similar to the conservative flux as ρ is a nonlinear function of the originally diffusing quantities.

We will see that the energy consideration can give a variety of explanations for phenomena related to LSs as it enables a discussion in terms of local transport. An analytical expression for the impulse evolution can be given as well, but is not written out here. Defining an global energy Γ and a global momentum $\boldsymbol{M}$ via

$$\Gamma := \int_\Omega \rho \mathrm{d}x, \tag{2.44}$$

$$\boldsymbol{M} := 2d_i \mathrm{Im}\Big(\int_\Omega q^* \nabla q \, \mathrm{d}x \Big). \tag{2.45}$$

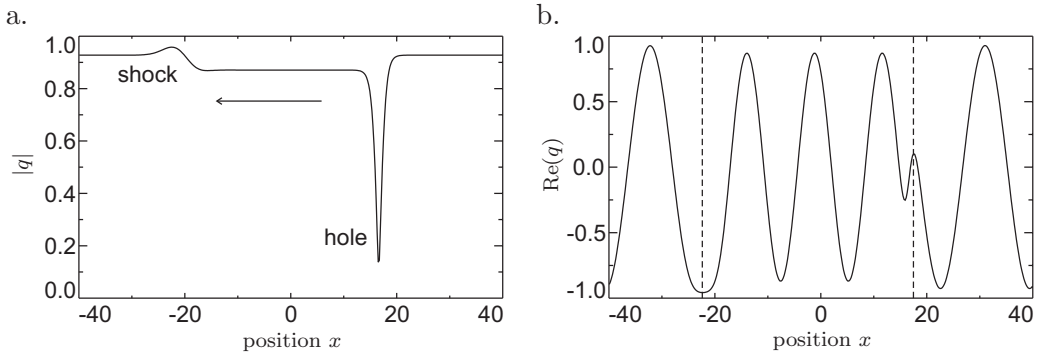

Figure 2.23: Nozaki-Bekki holes. a. Uniformly traveling Nokazi-Bekki hole shock pair in the distribution of $|q|$ as solution of the supercritical GL equation (parameters $d_r = 1$, $d_i = 0.5$, $l_r = 1$, $c_r = -1$, $c_i = -2.3$, periodic boundary conditions). The arrow indicates the direction of propagation. b. The (physically relevant) real part of q for the situation depicted in a., the position of shock and hole are marked by dashed lines. The shock emits waves that are absorbed by the hole.

one can write the corresponding evolution equations as

$$\partial_t \Gamma = 2 \int_\Omega (l_r \rho + c_r \rho^2 + q_r \rho^3 - d_r |\partial_x q|^2) \mathrm{d}x, \tag{2.46}$$

$$\partial_t \boldsymbol{M} = 2\,\mathrm{Im}\Big(\int_\Omega (l_r q + c_r \rho q + q_r \rho^2 q + d_r \Delta q) \nabla q^* \mathrm{d}x \Big). \tag{2.47}$$

Eq. (2.43) now shows that the formation of LSs in the GL equation can be interpreted as the coaction of two mechanisms: on the one hand, there is nonlinearity balancing dispersion like in classical soliton equations. Furthermore, there is a local gain and loss of energy and impulse, and in a stationary state their quantities have to be globally balanced.

As mentioned before, most results on LSs can be obtained in the subcritical GL equation. The only LSs that are known to exist in the supercritical case are found in the cubic one-dimensional version of the GL equation without quintic terms. Here, for $l_r > 0$, $c_r < 0$ there is a single stable ground state of finite amplitude $|q|$. On this ground state, there can exist a bound shock-hole pair also referred to as Nozaki-Bekki pair (Fig. 2.23a) over an extended range of the parameter space. Following our energy considerations (2.43), one finds that the shock acts as energy source while the hole acts as a sink. Looking at the real part of the complex amplitude (Fig. 2.23b), one may furthermore see that the shock emits plane waves which are absorbed when hitting a hole. The dominance of a finite wave number in this case is no contradiction to (2.42) as a positive l_r allows for a finite wave number to be the most unstable one. While the Nozaki-Bekki hole-shock pairs have a number of interesting properties connected with LSs, here we no not want to discuss these in detail and refer to the literature instead [176]. The reason for this is that the Nozali-Bekki pairs are structurally unstable and lose their stability once the cubic coefficients do not vanish any more so that they can be considered as non-generic in some sense.

The regions of existence of stable LSs in the subcritical quintic GL equation have been investigated in different ways. When the GL equation can be considered as a slightly perturbed conservative system close to the nonlinear Schrödinger equation or its generalizations, analytical results can be obtained using perturbation theory [30, 194], otherwise often numerical investigations are necessary. The first investigations carried out were done in one-dimensional systems. Here, a number of analytical solutions are known [195–197], however most of them turn out to be unstable except close to the conservative limit. Two possibilities of determining stability regions are either given by numerical analysis and by the use of trial functions (see Sec. 3.2.1). In one-dimensional systems, there is a rather complete overview on the regions of existence for LSs [198, 199], which we will briefly summarize in the following. One may state that as the cubic gain has to balance all losses in the system, an increase of the losses in the system generally demands the gain to go up in order to keep the LS stable. Concerning the "diffusion coefficient" d_r, all stable localized solutions lie in the region where the cubic GL equation has an unstable background. Furthermore, the solutions lie in bands, i.e. for fixed d_r, there is a lower and an upper limit for c_r where solitons become unstable, marking regions where the LS either decays to the ground state or spreads out in front-like manner, switching the system to the upper stable state. Of course, changing l_r and q_r shifts the bands in the directions one would intuitively expect. Concerning changes of "quintic losses", the region where LSs can exist becomes broader if the absolute value of q_r increases. In this context, the correction q_i of the "nonlinear refractive index" can have either sign, however, the region of existence of LSs is wider for positive q_i. The existence of LSs in the GL equation was also shown for two [40, 59, 62, 200, 201] and even three spatial dimension [202], although the percentage of works on this case is much lower then for example in reaction-diffusion systems. A possible reason for this may be that the number of available analytical methods on one dimension is much greater for the GL equation due to its relation to classical soliton equations.

Let us start by illustrating the mechanisms responsible for the formation of radially symmetric LSs. For this special case, there are no fundamental differences between one- and more-dimensional systems, in contrast to LSs with topological charge which we will consider later on. Let us illustrate the general ideas on two concrete examples in two spatial dimensions: the saturable GL equation with two saturable terms (2.34) resulting from modeling saturable absorbers and the quintic-cubic GL equation (2.35). We choose the parameters in both cases so that stable radially symmetric LSs can form, namely

$$d_r = 0.06, d_i = 1, l_r = -1, a_0 = 2, b = 10, g_0 = 2.11; \tag{2.48}$$

$$d_r = 0.5, d_i = 1, l_r = -0.5, c_r = 2.5, c_i = 1, q_r = -1, q_i = -0.1. \tag{2.49}$$

Looking at these parameters, we see that in the first case (2.48) $d_r \ll d_i$ so that spatial coupling is mainly due to dispersion, hence we can expect the LS to form mainly due to a balance of dissipative local and conservative transport terms. The second case (2.49) is more complex as all coefficients are of the same magnitude. For both cases, we plot three graphs (Fig. 2.24). The first ones (a1 and b1) show the local "reaction function" in the phase space representation previously introduced for reaction-diffusion systems. The phase space itself is spanned by a and b. The LS parameterized by its radial coordinate is also plotted. Note that in both cases the structure oscillates in time,

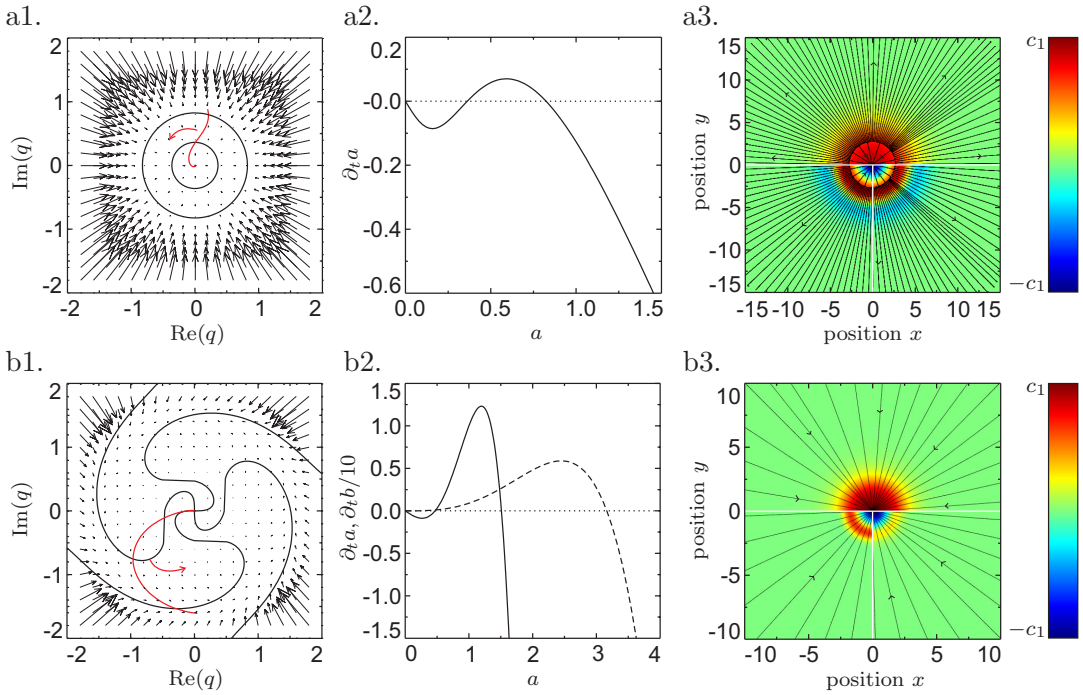

Figure 2.24: Mechanisms of the formation of LSs in the GL equation. a. Stabilization of LSs in the saturable GL equation with parameters according to (2.48). a1. Nullclines of the local "reaction" functions, phase flow and LS parameterized by its radial coordinate in the phase space spanned by $a = \mathrm{Re}(q)$ and $b = \mathrm{Im}(q)$. a2. Derivative $\dot{a}$ as a function of a for $b = 0$. a3. Contour plots of $|q|$ (upper part, $c_1 = 1$), the local source terms (lower left part, $c_1 = 0.1$) and all source terms (lower right part, $c_1 = 0.1$). b. Stabilization of LSs in the cubic-quintic GL equation with parameters according to (2.49). The graphs show the same quantities as in a; in b2, additionally the derivative $\partial_t b$ is plotted. For b3, we used the scales $c_1 = 1.6$ (upper half) and $c_1 = 4.5$ (lower half).

which corresponds to a rotation of the solution around the origin of the phase space with constant velocity. We see that in the saturable case, we have bistability between $|q| = 0$ and a finite value of $|q|$, and in its center the LS takes values of $|q|$ slightly above the finite equilibrium value. The structure has no internal spatial oscillations in its real part as according to the stability criterion (2.42) the dominant wave number is zero. We may look at the changes due to the local dynamics for a fixed value of b depicted in a2 for $b = 0$. Here, we see that above a certain threshold, "material" is produced up to the equilibrium value of $|q|$ and depleted otherwise.

Following (2.43), we may define local dissipative source terms whose position-dependent values with and without diffusive contributions are plotted in the left and right lower half of (a3). As previously predicted, diffusion plays no significant role because of the smallness of d_r. Comparing those regions where energy is produced and depleted with the shape of the LS itself (upper half of a3), we see that energy is produced in a ring-shaped zone corresponding the flanks of the LS. From here, dispersion transports the energy to those regions in the center of the LS and in the tails where energy sinks are located. To visualize this effect, we have plotted stream lines of $\boldsymbol{m}$ over the surface plot in (a3) which point in- and outwards from a critical radius located

inside the energy production zone. We may compare this situation to that in reaction-diffusion systems. In the latter type of system, we also have material production close to the center of the structure and transport (of diffusive type) into the tails where material is depleted. An important difference however is that while diffusive fluxes always correspond to a transport downward a gradient, the dispersive transport can also occur against the gradient of local energy density. One may introduce polar coordinates, $q = |q| \exp(i\phi)$, into the above definition of the flux to see that $\boldsymbol{m} = 2d_i|q|^2\nabla\phi$. From this it follows that the direction of the diffusive flux is determined by the local phase modulation of the solution. As the representation in the *a*-*b*-phase has a characteristic S-shape, we have two signs of the phase gradient in agreement with the two flux directions in (a3). Consequently, in the above case a dissipative sink is possible in the center of the structure, which is commonly not encountered in reaction-diffusion systems.

Let us now consider the second case, which is more complex due to the increased diffusion coefficient and the mixed real-imaginary local terms. In the phase-space representation, there exist again two stable values of $|q|$, however, there is now a stable limit cycle for the finite value, implying that a rotation around the origin is already induced by the local terms. This is in contrast to our previous example, where the rotation resulted from dispersion alone which provided coupling between real and imaginary part. Again, the tip of the LSs lies slightly above the stable value given by the limit cycle. This implies again a decrease of the local variables (b2) and a loss of energy (lower left of b3) due to the local dynamics. A feature that is rather difficult to see in (a3) but which must necessarily exist due to the stability of the ground state is a region of energy loss due to local dissipative terms in the tails of the LS. A closer inspection shows that there is indeed such a region, but the loss rate is very small compared to those rates in the center and on the flanks. When diffusive contributions are also taken into account in the dissipative source terms (right lower half of b3), we see that this implies losses in most parts of the structure, which result in a larger sink in the center and a reduced energy production in the flanks. In the tails however, the situation is special because the diffusive terms transport so much energy into this region that the coaction of local dynamics and diffusion results in energy production everywhere in the tails. By looking at the local phase gradient we see that although the phase modulation is much stronger than in the saturable example due to the dominance of the conservative local terms (compare the dashed line in b2), the phase gradient has one sign independent of the spatial position. This reflects the fact that as diffusion eliminates the energy sink in the tails, the only energy sink left is in the center so that all conservative energy flux is directed from large to small radii (compare the stream lines in b3).

Above we mentioned that for radially symmetric LSs there are no fundamental differences in the stabilizing mechanisms. However, unlike the one-dimensional case, in two or more dimensions there may exist a whole discrete family of stable LSs with different topological charge that can be stable for the same parameters (see for example [63, 201]). For radially symmetric intensity distributions, the members of the family can be represented in two dimensions using polar coordinates as

$$q_m(r,\theta) = A_m(r) \exp\Big(i(\phi_m(r) + m\theta + \omega t)\Big). \tag{2.50}$$

We will have a closer look on LSs with topological charge (sometimes also termed topological or vortex solitons) using the parameters (2.48) and (2.49). Both sets have the

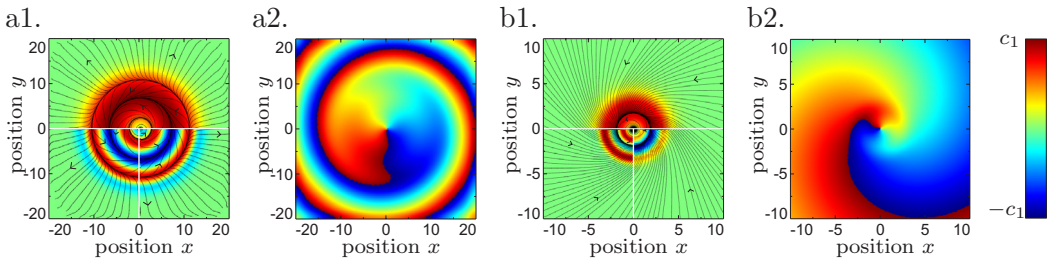

Figure 2.25: LSs with topological charge $m = 1$ for the parameter sets (2.48) (a1 and a2) as well as (2.49) (b1 and b2). The first images show the amplitude $|q|$ (upper half) and the local and total dissipative energy production (lower left and right half) as done in Fig. 2.24a3 and b3 for the case $m = 0$. The second images show the local phase of the field. The scales used are $q_1 = 0.9$ (a1 upper half), $q_1 = 0.2$ (a2 lower half), $q_1 = 1.75$ (b1 upper half), $c_1 = 0.1$ (b2 lower half), $c_1 = \pi$ (a2 and b2).

special property that in two dimension they allow for LSs with $m = 0$ and $m = \pm 1$ to coexist. The "charge" m affects the flow of energy in the structure. To visualize this effect, we consider again the local production and loss of energy plotting the same quantities as in Fig. 2.24a3 and b3. Looking first at the amplitude of the structures in the saturable and cubic-quintic case (Fig. 2.25a1 and b1), we see in both cases a ring-like structure in which the maximal amplitude is taken for a finite distance from the center. In both cases, the maximum again lies slightly above the upper stable stationary state. Turning now first to the saturable case, we see three regions where the local dynamics causes losses (Fig. 2.25a1): close to the center of the LS, close to where the maximal amplitude is taken and in the tails. There are now two gain regions on the inner and outer flanks. Again diffusion plays no significant role, so that conservative energy transport has to compensate the losses. With the given arrangements of zones where loss and gain takes place, for the energy flux there must be one stable fixed point in the center of the LS, surrounded by three limit cycles with alternating stability. As explained above the direction of energy transport is determined by the local gradient of the phase. The latter is plotted as a function of space in Fig. 2.25a2. We see that the vorticity of the field gradient has the same sign everywhere, reflecting the dominance of the term $m\theta$ in the polar representation of the solution.

Turning to the cubic-quintic case, the shape of the amplitude distribution is similar to the first example. Looking at the local source terms (Fig. 2.25b1), we again see three zones of energy loss and two zones of energy gain as above. However, there is a significant change of energy transport due to diffusion. Transport via the latter occurs in radial direction from the radius where the amplitude is maximal both to the center and to the tails. This effect increases energy losses close to the maximal amplitude, but acts as a source in the center and in the tails which can even overcompensate losses due to the local dynamics. Conservative energy transport now does not have to compensate losses in three zones, but only close to the maximal amplitude. Consequently, the topology of the conservative energy flow is much more simple consisting only of one unstable fixed point in the middle and a stable limit cycle. We will see below that this may affect the interaction behavior of the LSs in a significant way.

It is interesting to note that non-bell-shaped LSs can also be formed without vorticity.

In one-dimensional systems where no vorticity is possible for topological reasons it is possible to obtain multi-humped solutions which were termed composite solitons [203]. The latter types can be obtained from the usual bell-shaped LSs by increasing the gain in the system, and a comparison of the global energy with other possible patterns reveals that composite solitons are actually a tight compound state composed of a normal LS and one or two front structures. A composite soliton can not exist in two or more dimensions as fronts are not localized in more than one dimension. Increasing the energy gain above a critical threshold therefore typically results in a transition wave globally switching the system to a high-energy state [201].

In spite of many theoretical works on the GL equation, a direct comparison with experimental works has been carried out only rarely in the literature. As mentioned in the beginning of this section, optical resonators partly filled with saturable absorbers can directly be described using a GL equation with saturable nonlinearity. Fig. 2.26 shows different clusters of basically rotationally symmetric bell-shaped LSs found in such a set-up. Unfortunately, to the authors knowledge this system is the only one in which a direct comparison of experiment and theory on the basis of a rigorous derivation was performed. For some other experimental systems, it was possible to derive equations that are structurally rather similar to the types of GL equations discussed above, but nonetheless show some differences. An example for such a system are single mirror feedback systems in which LSs with oscillatory tails [3, 205] as well as whole families of LSs can be found [206]. In [207] a model of the form

$$\partial_t q = id_i \Delta q + l_r q + b_r(|q|^2 + |u|^2)u \tag{2.51}$$

was proposed, where u represents the incoming light field. Eq. (2.51) has the same symmetries as the regular GL equation but a different local nonlinearity. Last but not least there are experimental systems in which LSs have been found and for which a connection to the GL equation has been established only on a loose phenomenological basis. Such systems include oscillons in granular media ([4], see [192, 208] for theory) and binary liquid convection ([209–211], see [7, 191] for theory).

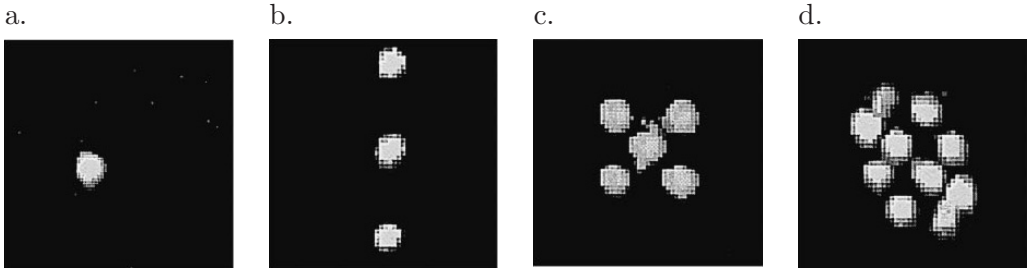

Figure 2.26: a-d: Clusters consisting of different numbers of LSs observed in a resonator set-up with a nearly confocal resonator geometry and partly filled with a saturable absorbing medium. The structures are obtained starting from a patterned state found for high input power by lowering and re-increasing the input rate of the pumping laser. From a. to d. the time after which to pump rate is re-increased becomes smaller [204].

2.2.2 Dynamics of LSs

Let us now come to dynamical processes, starting with one LS in one spatial dimension. One may first ask whether there exist propagating LSs like for example in reaction-diffusion systems. There are basically two possibilities of obtaining a LS with the required properties. A rather simple possibility is to choose the parameters is such a way that the system is Galilean invariant, which is for example the case for $d_r = 0$ [40, 195]. This of course allows for LSs with arbitrary velocity, but the latter is determined by the initial conditions and is not dynamically stabilized. Furthermore, the choice of parameters is rather non-generic. A second type of LS that can indeed propagate intrinsically with a dynamically stabilized velocity in one spatial dimension is given by a compound state of a stationary LS and a propagating front [203]. The velocity of the compound state is always lower than for the single front. One may note that the transition from a standing to a moving state is accompanied by a strong deformation (Fig. 2.27a) and thus the transition is subcritical, so consequently standing and the moving states can coexist in a range of parameters. A symmetric and thus non-propagating composite structure is obtained in a subcritical bifurcation from the moving LS by again increasing the gain in the system (for example by increasing c_r in the cubic-quintic case). One also finds other types of destabilizations for single LSs in one dimension. Among these are periodically

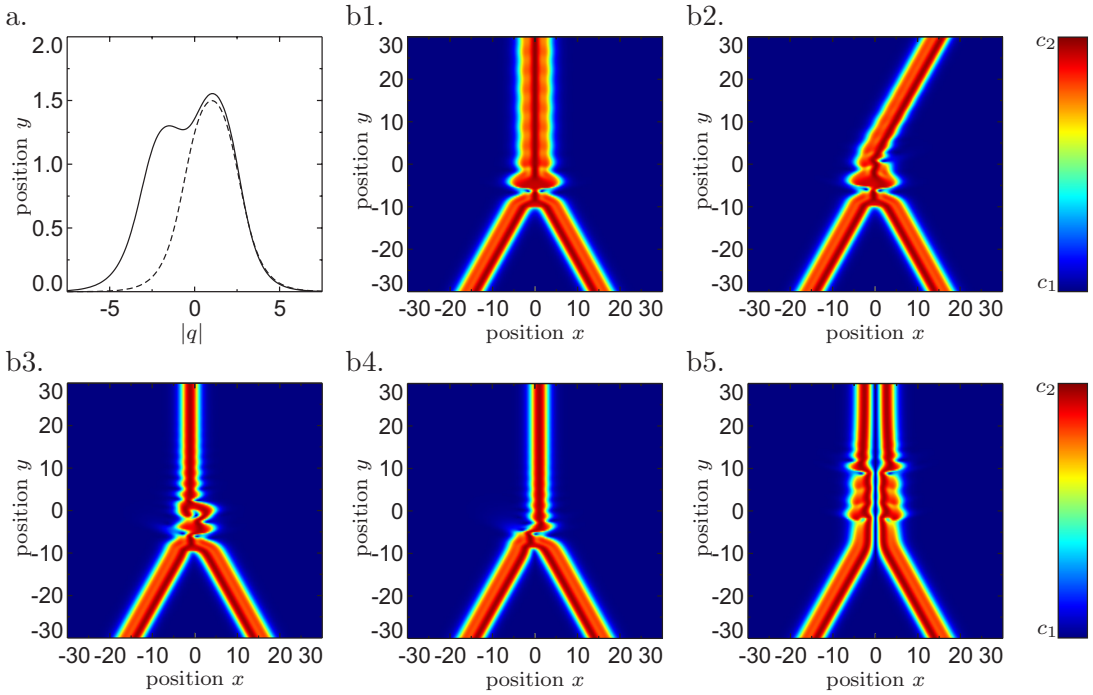

Figure 2.27: Propagating LSs and their interaction in the GL equation. a. Amplitude $|q|$ of a stable symmetrical LS (solid line) and a propagating compound state composed of a LS and a moving front (dashed line) coexisting for the same parameters in one spatial dimension. b. Space-time plots of two colliding compound structures for various initial mutual phase differences $\Delta\phi$: (b1) $\Delta\phi = 0$, (b2) $\Delta\phi = \pi/4$, (b3) $\Delta\phi = \pi/3$, (b4) $\Delta\phi = 3\pi/4$, (b5) $\Delta\phi = \pi$. Other parameters: $d_r = 0.5$, $d_i = 1$, $l_r = -0.1$, $c_r = 1.8$, $c_i = 1$, $q_r = -0.8$, $q_i = -0.1$, scale $c_1 = 0$, $c_2 = 1.6$.

pulsating or breathing [212, 213] as well as "exploding" LSs [214], i.e. LSs which retain their shape for some time before performing chaotic oscillations in their size and shape before returning to the original state.

In two or more spatial dimensions, the situation is different from that in one dimension. While in systems with Galilean invariance propagation is still possible, the moving compound state of front and LS can not exist. Although there is currently no rigorous proof, it seems likely that similar to the findings in reaction-diffusion systems the introduction of another component or field with a second time-scale is necessary to observe intrinsic propagation (compare for example [42]). However, other types of destabilizations like stable periodic oscillations are possible in the GL equation without modifications [202]. A possibility to obtain a propagating state is to break the restriction that only one single LS is involved, we will discuss more details in the following.

LSs in the GL equation are capable of forming bound states and well of performing different interaction processes. We have seen that in reaction-diffusion systems, concerning the weak interaction of stationary LSs the distance between the structures plays an essential role. This holds for LSs in the GL equation as well, however another important quantity is the phase difference between the LSs involved in the interaction process. Again, the mechanism responsible for the interaction processes are due to a coaction of local dynamics and transport as we will illustrate in some examples. To this end, we will take the stationary LSs obtained for the parameter sets (2.48) and (2.49) and place two LSs at such a distance that the overlap is only weak. In more detail, we first look at structure without topological charge and consider the three phase differences $\Delta\phi = 0$, $\frac{pi}{2}$ and π.

For the saturable case (Fig. 2.28a) we choose the initial distance $d = 12$ and look at amplitudes, dissipative production as well as conservative energy flux as a function of space at times $t_1 = 1$ and $t_2 = 20$. It is worth noting that the complete evolution of the interaction process takes place on a time interval of $\Delta t \approx 30$. For a phase difference $\Delta\phi = 0$ (Fig. 2.28a1), we see that although for isolated LSs energy losses occur in the tails, in the initial stage at time t_1 there is a "constructive" overlap of the structures along their connecting line in the sense that the amplitude become so large that gain takes place. Furthermore, conservative energy flux takes place into the central region. Close to the center the flow lines bend sharply up- and downwards. In the course of time, the amplitude increases in the center which further enhances the energy-producing mechanisms. The center finally reaches the upper stable state, however the resulting structure is too broad to exist. The structure now contracts, first along the original connection line (compare the state at t_2) and then in the orthogonal direction along which energy has been transported by conservative flux. As a final state, only one LS in the center remains. Looking now at $\Delta\phi = \pi/2$ (Fig. 2.28a2), we see that there is an asymmetry both in the initial amplitudes as well as in the conservative energy flux. Due to the nonlinear superposition, the LS on the left is smaller compared to its equilibrium state and surrounded by a wide loss zone, in particular close to the center of the initial distribution. In contrast, the LS on the right is wider than usual and has an extended zone of gain close to the center of the initial distribution. The dynamics is evidently a result of this initial setting: the structure on the right hand side initially grows in size, but due to the lossy region close to the second LS the LSs can not merge. Instead, the right LS after some time relaxes to its initial size performing a slight motion to the left. In contrast, the left LS starts shrinking at first, encountering losses primarily

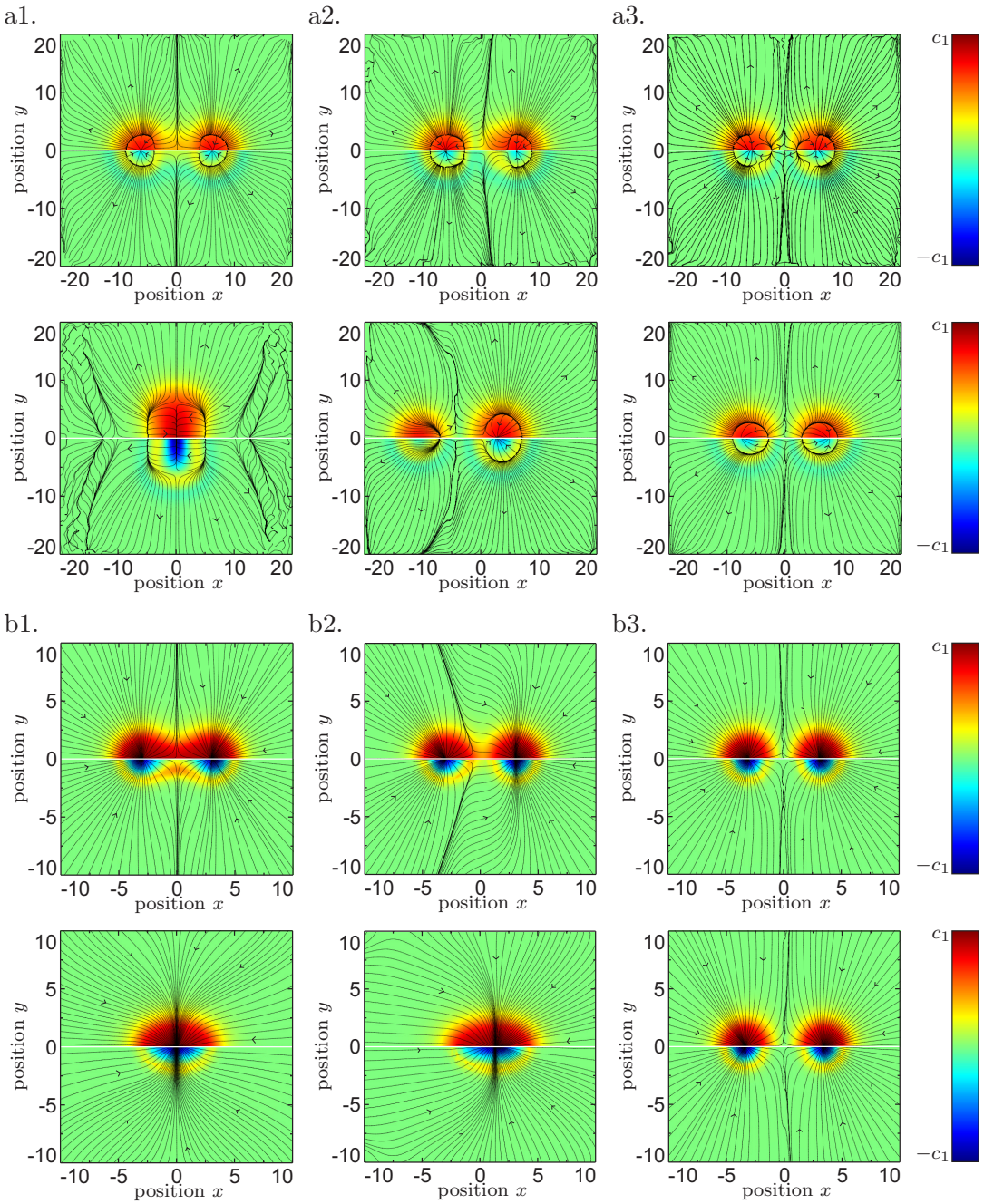

Figure 2.28: Interaction of two stationary LSs with no topological charge in the two-dimensional GL equation and different initial phase differences of the LSs. The upper half of each image shows $|q|$ as a function of space, while the lower half shows the overall dissipative energy production. Conservative energy stream lines are added. a. Saturable case for the parameters (2.48) and an initial separation $d = 12$. From the initial conditions, each upper image was taken at $t_1 = 1$ and each lower image was taken at $t_2 = 20$. The scale for $|q|$ is $c_1 = 1.2$ and $c_1 = 0.4$ for the dissipative energy production. The initial phase differences are (a1) $\Delta\phi = 0$, (a2) $\Delta\phi = \pi/2$ and (a3) $\Delta\phi = \pi$. b. Cubic-quintic case for the parameters (2.49) and an initial separation $d = 6$. Each upper image was taken at $t_1 = 1$ and each lower image was taken at $t_2 = 12$. The scale for $|q|$ are $c_1 = 1.65$ and $c_1 = 5$, respectively, the initial phase differences are as in a.

at its right-hand side. This also reduces the losses in its center, so that the resulting conservative energy transports causes a shift of the LS to the left. If we now finally look at the situation $\Delta\phi = \pi$ (Fig. 2.28a3), we see that initially each LS is surrounded by a lossy region similar to that found for the isolated states. In the center, losses and gain are almost in balance. In this situation, there is only a very weak repulsion of the LSs.

We may compare our findings in the saturable case with the cubic-quintic case (Fig. 2.28b). As the LSs have a smaller extension, we choose the initial separation as $d = 6$, furthermore we look at times $t_1 = 1$ and $t_2 = 12$ (the whole interaction process takes on an interval of about $\Delta t = 16$). For the phase difference $\Delta\phi = 0$ (Fig. 2.28b1), we again have dissipative energy production in the center. Although unlike the saturable case due to the influence of diffusion conservative energy transport takes place away from the center of the "molecule" to the center of the individual structures, dissipative gain in the center is so strong that the upper stationary state can be reached. Then, the dynamics is basically similar to the saturable case, the structure contracts until a single LS in the center remains. For $\Delta\phi = \pi/2$ (Fig. 2.28b2), there is an essential difference to the saturable case. For the chosen initial separation, diffusive energy transport from the centers of the individual LSs is efficient enough to overcompensate the losses in the center of the overall initial distribution (exactly this effect was not present in the saturable case). We know already that when the distribution in between the LSs experiences overall gain, usually the LSs merge, which exactly is observed here as well. Finally, the case $\Delta\phi = \pi$ (Fig. 2.28b3) is strongly similar to the saturable case: the overlap results in an almost vanishing energy production in the center causing a weak repulsion.

With the above behavior, we have found interaction processes typical for a number of optical systems: attraction and merging for constructive overlap, repulsion for destructive overlap. Note however that this is not a general rule. When considering for example an overlap of LSs with $\Delta\phi = 0$ and a large initial separation, it is potentially possible to enhance losses in the tails due to the nonlinear superposition which commonly results in repulsion. A combination of repulsion and attraction may result in stable lock-in distances of the LSs which are present without the LSs showing oscillatory tails. As an example, in the classical cubic-quintic GL equation it was found that two LSs with a phase difference $\Delta\phi = 0$ or $\Delta\phi = \pi$ may not form bound states, while states with $\Delta\phi = \pi/2$ may be either weakly stable or unstable, but always restless [39, 62, 215, 216]. In contrast to this, in the GL equation with saturation one may find the opposite situation with stable lock-in distances for $\Delta\phi = 0, \pi$ [63, 217].

In reaction-diffusion systems, we have seen that a number of new dynamical phenomena may arise when the LSs propagate with an intrinsic velocity. As mentioned above, in the one-dimensional GL equation such structures can be generated systems via a subcritical bifurcation for a sufficiently high dissipative gain in the system. In Fig. 2.27b, we have a look at the central collisions of two of the structures shown in Fig. 2.27a for a number of initial phase differences between the colliding structures. Independent of the phase difference, the interaction is strong in the sense that the shape of the individual LSs is not preserved, making it difficult to explain the outcome of the interaction process. For the symmetric situation $\Delta\phi = 0$ (b1), we may expect a constructive superposition of the LSs before the actual collision which results in energy production. The outcome of the collision process is a symmetrical oscillating compound state. Its overall energy is close to the above-mentioned composite soliton state consisting of two

fronts and a LS, but the coefficient d_r is to small to stabilize the latter. Increasing the phase difference to $\Delta\phi = \pi/4$ (b2), we face an asymmetric situation in which the overall amount of energy in the system is reduced during the collision. As a consequence, the outcome is the survival of only one propagating LS. The losses in the collision can be increased when choosing $\Delta\phi = \pi/2$ (b3). The collision now results in the generation of a standing LS whose integral energy lies below the propagating state, but which coexists with the latter for the chosen set of parameters. The situation is similar for $\Delta\phi = 3\pi/4$ (b4). Finally, for $\Delta\phi = \pi$ (b5) the losses are reduced so that an instable bound state of two standing LSs forms up. However, perturbing this state (not shown in the figure) results in the generation of a running LS.

In two- and more-dimensional systems the generation of intrinsically propagating LSs due to an increase of the gain coefficients does not work, commonly the system in this case globally switches to the upper state. One possibility to overcome this problem is to make the system Galilean-invariant by choosing $d_r = 0$ which basically works in any spatial dimension. Interaction events in this case have been investigated in [40]. We therefore do not want to go into too much detail here, in summary, both weak and strong interaction are possible, and scattering, merging and annihilation have been observed. Alternatively, one may arrange a number of stationary LSs to form a rigid cluster [218]. To this end, neighboring LSs must have a suitable phase difference $\Delta\phi_n$ which is π in the saturable case. In Fig. 2.29a, we have composed a triangular cluster of three LSs. With respect to the leading LS, the trailing LSs both have a phase difference of $\Delta\phi_n = \pi$ (compare Fig. 2.29b). The fact that the trailing LSs have a mutual phase difference of $\Delta\phi_n = 0$ does influence the stability of the arrangement as these LSs are too far apart from each other to interact significantly. We seen from the local energy production that in between the LSs the production and dissipation of energy is almost in balance. In spite of the stationarity of its constituents, the cluster propagates with a dynamically stabilized finite velocity, the only symmetry axis marks the direction of propagation. Note however that no bifurcation between standing and moving state can take place. Using our knowledge about the interaction between single stationary LSs, we may explain the outcome of a central collision of two counter-propagating clusters for varying initial phase differences $\Delta\phi_c$ between the individual clusters. Starting with $\Delta\phi_c = 0$ (Fig. 2.29a), the leading LSs of the clusters collide with equal phase, resulting in a merging process as already seen in Fig. 2.28a1. During the transient phase, the central compound experiences a strong decay, and the trailing LSs are repulsed from the center. The comparison with Fig. 2.28 also helps to understand the case $\Delta\phi_c = \pi/2$. We have seen that the two stationary LSs are not equal and one structure may push the other away. This is also of central importance for the cluster collision: while the "pushing part" of the cluster (which is delayed by a quarter of an oscillation period, right side of the figure) keeps its shape during the collision, the leading LS of the pushed part (on the left side) quickly changes its direction of propagation, thereby inducing a flip of the whole cluster along an axis perpendicular to its symmetry axis (this is indicated by two white arrows in the figure). The final state is a large compound of two stacked clusters with the same orientation which conducts oscillations while propagating to the left. Finally, we have learned that for $\Delta\phi_c = \pi$ two isolated LSs can form a bound state. This occurs also in the cluster collision during which a stable stationary compound of six LSs is formed, all neighboring LSs have a phase difference of π. Due to the symmetry of the resulting state, the cluster remains at rest.

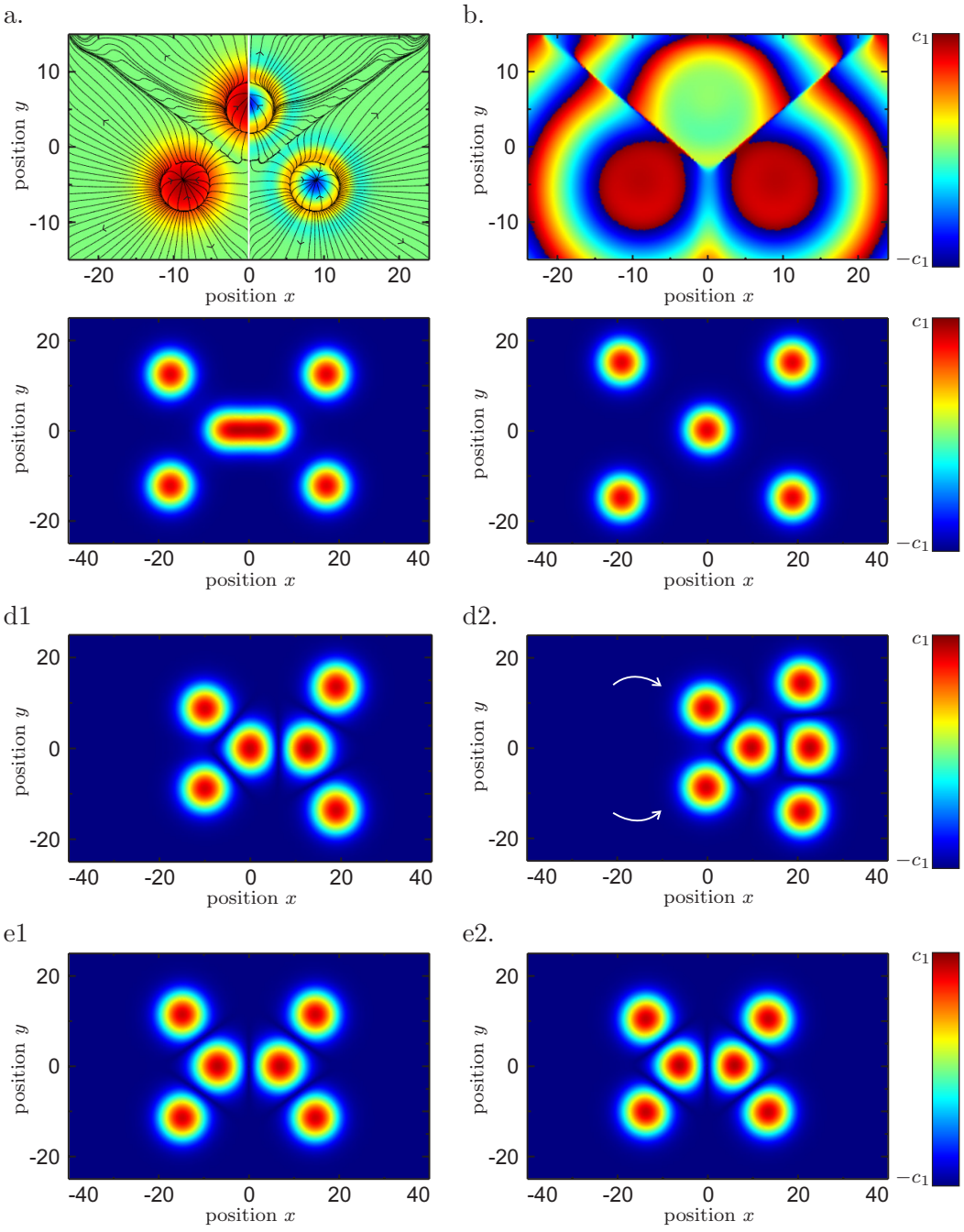

Figure 2.29: Collision of two propagating compounds of three LSs shown for three initial phase differences of the individual clusters. a. Amplitude (left half), overall energy dissipation (right half) and energy stream lines as a function of space for a single compound. Propagation takes place along the white line in the middle. b. Local phase distribution for the compound shown in a. c. Snapshots of the local amplitude showing the collision of two clusters as depicted in a. for $\Delta\phi_c = 0$ at times $t_1 = 120$ (c1) and $t_2 = 240$ (c2) with $c_1 = 1$. The initial separation of the clusters at $t = 0$ is $d = 40$. d. The same sequence as in c. for $\Delta\phi_c = \pi/2$. e. The same sequence as in c. for $\Delta\phi_c = \pi$. Parameters are chosen according to (2.48).

A last point that we want to address in the context of interacting LSs is the influence of topological charge in the interaction processes. Here, rotational and curvilinear motion of whole clusters as well as of parts of clusters can be found [63]. The effects can be understood in a similar way as the linear propagation of clusters without topological charge. The arrangement of several LSs with topological charge in a cluster may break the rotational symmetry of a system but preserve a degree of symmetry high enough to prevent propagation of the center. The outcome is then typically a purely rotational motion. When the degree of symmetry becomes low enough, curvilinear motion may set in. One may again distinguish between weak and strong interaction. In the latter case, closely connected compound of several LSs may form that may rotate in the course of time.

One may ask which dynamical phenomena discussed above have up to now been observed in the experiment. In [204], as depicted in Figs. 2.26c and d clusters of stationary LSs have been found. There seems to be a well-defined lock-in distance when the LSs are close although the LSs show no oscillatory tails, which agrees with the theoretical predictions. Oscillons in granular media show similar properties. In addition, one may state that generally no intrinsic propagation of single LSs has been reported for two-dimensional systems which are related to the GL equation. Unfortunately, experimentally observed dynamical interaction processes of several LSs have up to now hardly been reported for systems directly related to the GL equation. Nonetheless, in particular the mechanisms shown for interaction processes (attraction of LSs with equal phase, repulsion for opposite phase) are found in a number of other experimental systems with self-focussing media such as photorefractive media [219]

2.2.3 Variations of the GL equation

Up to now, we have discussed the dynamics of LSs in the classic cubic-quintic GL equation and some closely related other versions. Different extensions and modifications to these equations have been made in the course of research, either physically motivated or artificially. The connection between the different versions is much clearer than for example in reaction-diffusion systems. In the following, we will give a brief overview and present consequences for the observed phenomena.

- *Anisotropy, external pumping etc.*

  The "standard" cubic-quintic or saturable GL equation itself allows for a number of extensions to account for special properties of the underlying system. It was found that systems with anisotropically distributed coefficients allow for anisotropically shaped stable LSs [220]. When the system under consideration is parametrically excited (for example pumped by an external beam), the simplest way to account for this effect is to add additional terms $p_l q^* + i p_c |q|^2 q^*$ to the GL equation (see for example [221]). These additional terms break the gauge symmetry of the original equations, but nevertheless LSs can exist. Another possibility to break the isotropy of the original equations is to consider nonlinear gradient terms [212]. In this case, single propagating LSs are possible.

- *Coupled systems of GL equations*

  As explained in the beginning, a single GL equation may describe the amplitude of a fast-oscillating field with frequency ω. In order to model several frequencies

(for example higher harmonics of ω), one may thus consider a set of coupled GL equations, in which the mixed nonlinearities reflect the nonlinear frequency mixing (see for example [222]). A similar situation is given for the case of a cascaded set of quadratic nonlinearities, which may show properties similar to those expected for cubic and higher nonlinearities [222–224]. Coupled GL equations were also derived for binary mixture convention where the amplitude dynamics couples to other slow modes in the system [225, 226]. An important point is that coupled GL equations have stable localized solutions even if the individual equations have no quintic or saturable terms. As the coupled systems can be considered to consist of multiple components, the LSs are in this case also termed vector solitons in the literature. Generically, the coupled equations show a larger variety of possible phenomena due to an increased number of degrees of freedom, for example the coexistence of differently sized pulses [226]. When considering coupled equations for counterpropagating beams, one generally obtains "convective" terms of the form $\pm \boldsymbol{v} \cdot \nabla q$, which can not be transformed away as for a single equation. In these equations, LSs may be convected in opposite directions and thus collide, opening up the possibility of a variety of interaction phenomena [227, 228].

Apart from the coupling of several GL equations, one may also look at a GL equation coupled to other types of equations. As an example, one may couple a GL equation to a simple linear dissipative equation in order to stabilize an otherwise globally unstable background, so that LSs can exist in an otherwise unstable regime [53]. The combination of GL equations with equations for charge transport(for example drift-diffusion) or temperature may describe LSs in active cavities, photorefractive systems etc. [229]. We already mentioned that the introduction of a slowly varying temperature field may lead to intrinsic propagation [42, 230].

- *Discrete GL equations*

  There is a number of systems described by GL equations that are discrete and lattice-like in nature. Examples are given by photonic crystals, semiconductor laser arrays and nonlinear oscillators. While some investigations consider the direct discrete analogue of the GL equation where terms involving no spatial coupling stay local [231], others make generalizations where cubic or quintic terms are nonlocal in space [232, 233]. Basically, the discretized GL equation retains some properties of its continuous counterpart, for example the fact that to find stable LSs, nonlinearities higher than cubic ones have to be considered [234].

  Some findings however have no continuous counterpart. One finds both single point (on site) LSs, two point (intrasite) LSs [231], LSs distributed over many sites [233] and even coexistence of different types. Furthermore, the dispersion properties and the sequences of bifurcations are different from both conservative discrete and continuous dissipative systems.

We end our section on Ginzburg-Landau equations with an overview table on published works on the GL equation (Table 2.4). Further overviews and reviews are for example given in [30, 34, 187, 248, 249].

system	phenomenon	literature	details
cubic GL equation	Nozaki-Bekki holes	[176]	structurally unstable
cubic-quintic GL equation	existence of LSs	[30, 62, 194, 198, 199, 201, 235]	perturbation theory / numerics
	propagation of single LSs	[40, 195, 203, 212]	intrinsic or Galilean invariance
	other types of destabilizations	[212–214]	breathing, explosions
	weak interaction	[39, 62, 215, 216]	compare Sec. 3.3
	strong interaction	[40, 203]	merging / annihilation
saturable GL equation	existence of LSs	[200, 236]	perturbation theory / numerics
	dynamics of single LSs	[202]	breathing
	weak interaction	[59, 63, 217]	compare Sec. 3.3
	strong interaction	[63]	compound states
extensions/modifications	anisotropy, driving	[220, 221]	changed symmetry properties
of the GL equation	discrete GL	[231–234]	new types of LSs
	coupled equations	[222–228]	extended dynamics
real SH equation	localized Turing patterns	[237–243]	Liapunov functional
	nonlinear spatial coupling	[244]	preference of squares
complex SH equation	existence of LSs	[57]	numerics 1D/2D
	interaction	[57]	collisions, interpenetration
	anisotropy	[245]	“worms”
	nonlinear spatial coupling	[246, 247]	square patterns, oscillons

Table 2.4: Overview over different works on the GL equation and the SH equation.

2.3 Swift-Hohenberg equations

2.3.1 General properties

In the preceding section, we have seen that the GL equation can be considered as a prototype equation for a large number of different systems. It can be derived either in a direct fashion (typically for optical systems with fast nonlinear medium) or indirectly (in a variety of other systems). In this section, we will consider the Swift-Hohenberg (SH) equation, which can in some sense be considered as a generalization of the GL equation. It can be written as

$$\partial_t q = (s_r + is_i)\Delta^2 q + (d_r + id_i)\Delta q + l_r q + (c_r + ic_i)|q|^2 q + (q_r + iq_i)|q|^4 q, \qquad (2.52)$$

so that the essential difference to the quintic complex GL equation (2.35) are the fourth order derivative terms on the right-hand side. Before turning to the discussion how the additional terms influence the solutions compared for example to the GL equation, we will briefly have a look at the origin of the equation. For many optical systems, the reaction of the nonlinear medium to the exposure of an incident light beam is rather slow. A typical example is given by a photorefractive crystal which can be described by the set of equations [250]

$$\partial_t q = \kappa[-1(1+i\beta)q + in^* + ia\Delta q], \qquad (2.53)$$

$$\partial_t n = -\gamma[n - in - n_s \frac{q^*}{1+|q|^2}] \qquad (2.54)$$

with q representing the normalized electric field of the incident light wave and n being the photorefractive index, all other parameters are constants. While in the saturable absorber example (2.33) in the GL section we have adiabatically eliminated the medium, here usually $\gamma \ll \kappa$ so that one may adiabatically eliminate the field, i.e. setting $\partial_t q = 0$. On a new time scale $\tau = \gamma t$ this yield the relation

$$\partial_\tau q = -(1-i)q + \frac{in_s}{1+i\beta-ia\Delta}\frac{q^*}{1+|q|^2}. \qquad (2.55)$$

By tailor-expanding both differential the operator and the "saturable" term on which it acts, one finally obtains

$$\partial_\tau q = (\frac{n_s}{2} - 1)(1-i)q - (1+i)|q|^2 q - i\frac{n_s}{2}(\beta - 1 - a\Delta)q - \frac{n_s}{8}(\beta - 1 - a\Delta)^2 q. \qquad (2.56)$$

We now have obtained a cubic version of (2.53), one may still recognize how the fourth order derivative results from the Taylor expansion of the differential operator. A number of other examples from the optical field can be found for example in [181, 251, 252]. SH equations have also been proposed to describe oscillons in vibrated granular media [244], the dynamics of flames [253] or electroconvection [245]. As in the GL equation, in some

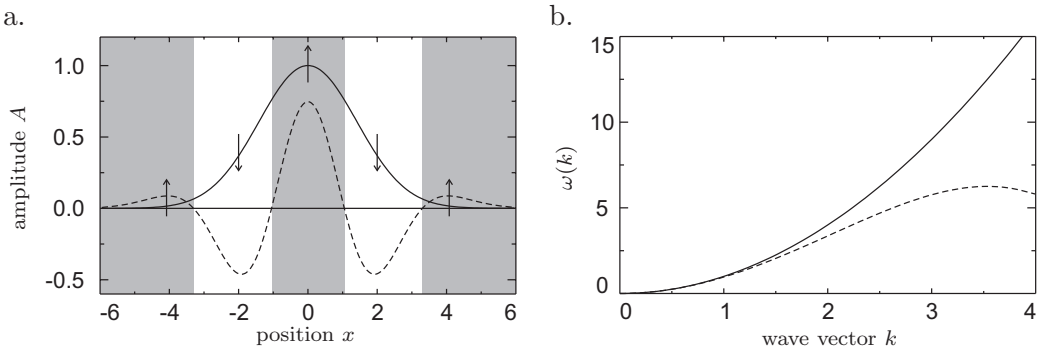

Figure 2.30: Effect of the fourth-order derivative terms in the SH equation. a. Real second order derivative (dashed line) acting on a Gaussian distribution in one spatial dimension (solid line), thereby increasing the local curvature in regions where it is already positive (marked in grey) and decreasing it in regions of negative curvature. The consequence is a steepening of the structure typically leading to instability. b. A typical dispersion relation $\omega = k^2$ (solid line) with a globally positive group velocity space as encountered for example in the GL equation is modified by the additional imaginary fourth order derivative so that the group velocity may locally become negative (dashed line, $\omega = k^2 - 0.04k^4$).

cases one finds real versions of the SH equation [240] which can be obtained by setting all "imaginary coefficients" to zero.

We now want to shed some light on the meaning of the new terms related to fourth-order derivatives. Turning to the real part s_r, the corresponding term in the SH equations can be considered as "superdiffusion". In Fig. 2.30a, we show the action of superdiffusion on a Gaussian pulse. While normal diffusion has the effect of smoothing out gradients in the course of time, superdiffusion tries to smooth out the second order spatial derivative. For a curve $q(x)$, the local curvature κ is given by relation

$$\kappa(x) = \frac{\partial_x^2 q}{\sqrt{1 + (\partial_x q)^2}^{3/2}} \approx \partial_x^2 q \quad \text{for} \quad (\partial_x q)^2 \ll 1 \tag{2.57}$$

so that for not too steep curves superdiffusion can be interpreted to increase the curvature of a given distribution. As the effect is the stronger the larger the curvature, the Gaussian in Fig. 2.30a typically steepens at the positions marked by the arrows, thereby leading to instability. As the fourth order term dominates all other terms on small spatial scales, we have to claim $s_r < 0$ to avoid a global instability. Looking at the fourth order derivative with imaginary coefficient, we may recall for a plane waves, a general dispersion relation in one spatial dimension can be written in the form

$$\begin{aligned}\omega(k) = \omega_0 + \partial_k\omega(k_0)(k-k_0) + \frac{1}{2}\partial_k^2\omega(k_0)(k-k_0)^2 + \frac{1}{6}\partial_k^3\omega(k_0)(k-k_0)^3 \\ + \frac{1}{24}\partial_k^4\omega(k_0)(k-k_0)^4 + \ldots\end{aligned} \tag{2.58}$$

While the phase velocity $\partial_k\omega(k_0)$ can always be eliminated by a transformation to a moving frame, generally $\partial_k^2\omega(k_0)$ (corresponding to the group velocity) does not vanish.

Fourier-transforming the SH equation (2.52) shows that the latter coefficient is directly related to d_i. While higher order terms are thus not accounted for in the GL equation, the SH equation contains the coefficient s_i which is related to the fourth-order coefficient of the Taylor expansion (2.58). The third-order Taylor coefficient would result from third-order derivatives in the underlying field equation which are not present in the SH equation. From this we may conclude that the SH equation may only account for situations in which the general dispersion relation (2.58) has no third-order contributions.

Before coming to LSs, let us now compare plane-wave stability in the GL and the SH equation. The analogues of the stability criteria (2.41) and (2.42) of the GL equation for the SH equation take the form

$$s_r k^4 - d_r k^2 + l_r < 0 \tag{2.59}$$

according to the trace criterion and

$$(s_r^2 + s_i^2)k^8 - 2(d_r s_r + d_i s_i)k^6 + (d_r^2 + d_i^2 + l_r s_r)k^4 - 2l_r d_r k^2 + l_r^2 > 0. \tag{2.60}$$

according to the determinant criterion. From (2.59) and the claim $l_r < 0$ to stabilize the homogeneous ground state $q = 0$ we directly see that we have to require $s_r < 0$, meaning that the superdiffusion has a stabilizing effect. We may now distinguish two cases. In the GL equation we had to require $d_r > 0$ which leads to an enhancement of stability in (2.59) and (2.60). In such a situation and with $d_i s_i$ being sufficiently small, $k = 0$ remains the wave number most close to instability for the SH equation as well. Usually, the fourth order derivatives are then only small corrections to their second order counterparts, and no fundamental differences to the GL equation can be expected so that for the formation and dynamics of LSs the arguments from Sec. 2.2 can be applied. A comparison of the GL and the SH equation in this case can be found in [254].

The situation becomes fundamentally different however if $d_r < 0$. The process of "anti-diffusion" seems rather unintuitive when the actual transport of matter is involved (although such processes indeed exist [244, 245]), but occurs rather naturally in optical systems for example when considering resonators or cavities with a detuning from the resonance frequency [237, 247]. We will hence focus on this case in the following.

2.3.2 LSs in the real SH equation

We will first consider the real SH equation for a real amplitude q. An inspection of (2.59) and (2.60) shows that for $d_r < 0$ small enough a whole band of finite k-value may become unstable while $k = 0$ remains stable. A generic observation in this case is the formation of stripes and sometimes also hexagons in a Turing instability depending on the properties of the higher order local terms. LSs in this type of equation were investigated for example in [239] and are generated due to an elementary mechanism that leads to localization also in more complex versions of the SH equation. We first consider a case in which the parameters are chosen such that although $c_r > 0$ and $q_r < 0$, the only stable stationary state is $q = 0$. In addition, the system can be brought close enough to a subcritical Turing instability such that the ground state $q = 0$ and

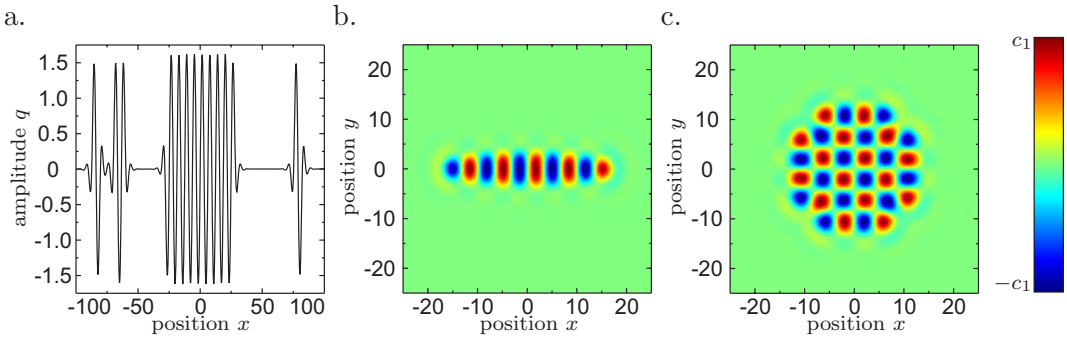

Figure 2.31: LSs in the real SH equation. a. One-dimensional stable localized patterned domains (Turing structures) of different width on a homogeneous background state. Note the weakly bound state of two domains on the left side. Parameters: $l_r = -2.6$, $c_r = 3$, $q_r = -1$, $d_r = -2$, $s_r = -1$. b-c. Localized stable stripe and square patterns in two spatial dimensions coexisting for the same parameters as in a. except for $l_r = -2.505$, scale $c_1 = 1.7$. Compare also [239].

a spatially modulated state can coexist. Similar to one-component bistable reaction-diffusion systems for which we considered domains of one homogeneous state on the background of the other state, following an idea by Pomeau [255] one may consider localized domains of the modulated state on a homogeneous background state. It turns out that contrary to the reaction-diffusion case, the modulated state can indeed exist and form stable domains of various widths on the background state (Fig. 2.31a). The structures exist over extended ranges of the system parameters. However, it is found by associating with the SH equation the Liapunov functional

$$L = -\int \Big(\frac{l_r - \frac{d_r^2}{4s_r}}{2} q^2 + \frac{c_r}{4} q^4 + \frac{q_r}{6} q^6 + \frac{s_r}{2} ([\frac{d_r}{2s_r} + \partial_{xx}]q)^2 \Big) \, \mathrm{d}x \tag{2.61}$$

via the relation $\partial_t q = -\delta L / \delta q$ that stable LSs can only exist if the "energy" of the homogeneous ground state lies below that of the patterned state [239]. In other words, the homogeneous state must be the dominant one. At this point, we should recall that in the reaction-diffusion case a domain structure can be considered as the result of a weak two-front interaction compensating the motion of the isolated fronts. In the SH case however, one state is strongly modulated such that in order to change the extension of the latter, one stable structure of large amplitude has to be replaced by another state. Consequently, it is evident that when considering the structure in the SH case as composed of two front as well, the front interaction is much stronger so that the structure stays stable in a large parameter range.

Stable localized domains can also exist in more than one spatial dimension. Here, two possible generalizations of the one-dimensional structure exist. On the one hand, as reported in [239] the domain may keep its characteristic modulation length in only one direction (Fig. 2.31b). In the orthogonal direction the curvature of the structure is rather small, which is favorable compared to a state with higher curvature due to a lower energy according to the generalization of the Liapunov functional (2.61). The

number of oscillations of the stable structure is again dependent on the initial conditions. However, there is also a second type of stale LS which in contradiction to [239] can exist for the same parameters as the state depicted in Fig. 2.31b and in particular without the introduction of local symmetry breaking terms. This state is shown in Fig. 2.31c: we see that here the characteristic length of the one-dimensional system is preserved in both directions and we thus obtain a stable localized square pattern which can be regarded as generic extension of the one-dimensional structure. Note that the square structure may be generated from unsymmetrical initial conditions (to produce Fig. 2.31c, we used the initial condition $q(x, y, 0) = 2.5 \exp(-(x^2 + y^2)/15^2) \sin(x/1.2) \sin(x/1.5)$).

LSs in the real SH equation can also be found in the case $l_r > 0$, $c_r < 0$ and $q_r = 0$. The difference to the above considered case is that the system has two equally dominant stable homogeneous states $q_h = \pm\sqrt{-l_r/c_r}$ while the state $q = 0$ becomes unstable. Note that for the same choice of the parameters in the case of the GL equation, the only LSs are the structurally unstable Nozaki-Bekki holes. In one spatial dimension, one again encounters localized Turing structures on a homogeneous background which seem to be stabilized analogously to their counterparts in the case $l_r < 0$. It is interesting to note that similar results can also be found when one generalizes the local terms according to

$$f(q) = m_r + l_r q + n_r q^2 + c_r q^3 + \dots \tag{2.62}$$

(see for example [237, 242]), showing that the structures in the SH equation are indeed structurally stable. LSs in this case may exist also in more than one dimension and were first observed in connection with domain patterns [240]. Looking at the stability regimes of different stationary states (patterns and LSs) by varying the individual parameters in (2.62) [237], one finds strong indications for the statement that the existence range of localized patterned domains coincidences with the intersection of the regions where at least one stable homogeneous state and globally extended Turing states exist. In particular, if the nonlinear function (2.62) allows for bistability of two homogeneous states

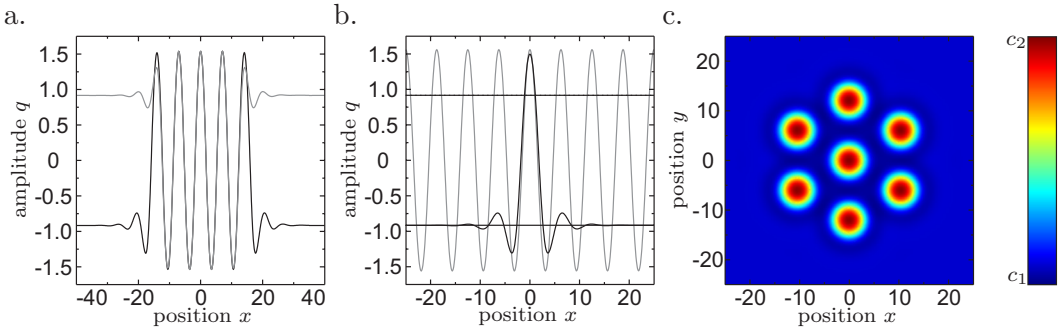

Figure 2.32: Coexistence of homogeneous, patterned and localized states. a. For bistability of two homogeneous states, LSs with equal amplitude can exist on both backgrounds (black and grey lines). b. Multistability of two homogeneous states, the Turing pattern (grey line) and a LSs in one spatial dimension, note that the amplitude of the LS matches that of the Turing pattern. c. Hexagonal arrangement of LSs in two spatial dimensions due to mixed attractive-repulsive interaction caused by oscillatory tails of the LSs, scale $c_1 = -1.1$, $c_2 = 1.3$. Parameters: $l_r = 0.84$, $c_r = -1$, $q_r = 0$, $d_r = -2$, $s_r = -0.4$.

with the patterned state, a localized patterned domain can exist on either background (Fig. 2.32a).

An interesting aspect is given by the comparison of the localized patterned domains with the domain structures encountered for example in bistable reaction-diffusion systems (compare Fig. 2.16). To clarify this aspect, we may exemplarily consider a LS with only one central peak existing on one of two possible ground states (Fig. 2.32b). With the LS existing on the lower state as background state, one finds that the amplitude of the LS corresponds to the underlying Turing pattern and thus lies significantly above the upper homogeneous state. This is in contrast to Fig. 2.16 where only small oscillations around the upper homogeneous state are encountered. Consequently, one may consider the structure to be dynamically stabilized as observed for example for excitable reaction-diffusion systems or the subcritical GL equation (Fig. 2.24).

As the Turing wavelength is always dominant when LSs exist for the real SH equation, it was also argued that oscillatory tails may help in stabilizing the individual structures [241]. In any case, the tails may cause a stable lock-in of two LSs which may also lead to the formation of larger clusters, typically with hexagonal arrangement (Fig. 2.32c, compare also Fig. 2.31a). In this sense, larger domains with several peaks can also be interpreted as an arrangement of several individual structures with very small lock-in distances. Note that by comparing the situation to one-component reaction-diffusion systems in which the decay of a structure to the ground state is always monotonic and requires a second component to become oscillatory it becomes clear from (2.59) and (2.60) that the oscillatory tails in the SH case are the result of an interplay of second and fourth-order spatial derivatives.

Aside from interacting stationary LSs and transients during the generation of LSs, the possible dynamics in the real SH equation appears to be rather limited. This aspect is connected to the existence of the Liapunov functional (2.61) which imposes strong restrictions to the possible dynamics. Note also that a variety of effects could be induced in two-component reaction-diffusion systems by a slow response of one component, which is not possible for the real SH equation either. Before turning to the complex version of the SH equation, we want to mention a number of analytical works treating the localized domains in terms of amplitude equations [242]. In particular, a relation to the concept of homoclinic snaking was considered [243]. Furthermore, the role of the Liapunov functional (2.61) and appropriate generalizations was discussed in more detail [238]. Extensions of the real SH equation by nonlinear gradient terms have been proposed, which are for example of the form [244]

$$e(q) = f_1 \nabla \cdot [(\nabla q)^3] - f_2 q (\nabla q)^2 - f_3 q^2 \Delta q. \tag{2.63}$$

The additional terms may cause the system to favor a special type of pattern (for example squares) which may phenomenologically account for corresponding experimental observations.

An experimental example for which a real supercritical SH equation could be derived in a rather rigorous way [258] are systems involving degenerate wave mixing. The experimental set-up is basically a resonator partly filled with a saturable medium, but the pumping is done with several beams via an active medium like $BaTiO_3$ [259]. Consequently, the phase of the optical field can not take arbitrary values but is coupled to

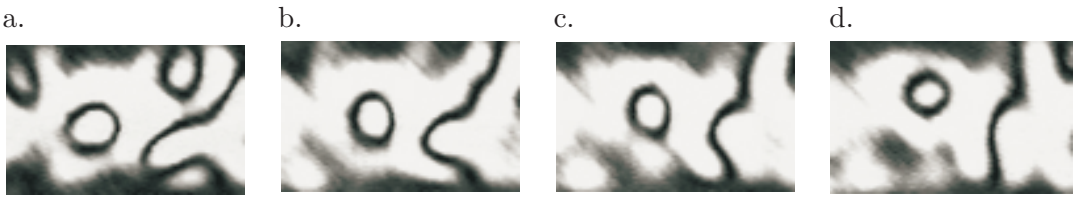

Figure 2.33: Experimentally recorded sequence showing the coexistence of a LS and a front connecting two domains in degenerate four-wave wave mixing in $BaTiO_3$. The figures show the intensity distribution in the set-up as a function of time, the LS retains it shape while the domain boundary contracts. The time interval between successive images was not given in the original reference [256], however can be assumed to lie in the order of a few seconds by comparison with other works [257].

the phase of the pumping fields. A good agreement between the predictions of the SH equation and the experimental observations was found. In particular, it was observed that domain-type solutions separated by steep fronts and LSs as shown in Fig. 2.32 can coexist [256, 257]. Fig. 2.33 shows an experimentally recorded sequence depicting a contracting domain and a stable LS that keeps its shape in the course of time. A loose connection was also argued to exist between the real SH equation and forces chemical reactions like the Belousov-Zhabotinsky reaction in which also domain boundaries and LSs have been found [260].

2.3.3 LSs in the complex SH equation

While we have shown the existence of a variety of different LSs in the real SH equation, generally no dynamical phenomena are observed due to the existence of a Liapunov functional. This situation changes when turning to the complex SH equation. Just as the complex GL equation shows hybrid properties of the NLS equation and reaction-diffusion systems, the complex SH equation takes a similar role with respect to the real SH equation and the complex GL equation.

An essential feature of the LSs in the real SH equation with $d_r < 0$ is the coexistence of a short and a longer spatial wavelength so that the LSs could be considered as localized Turing domains. The LSs in the complex SH equation preserve this property even when the "imaginary" coefficients become large [57]. We start by again first considering one-dimensional systems. Fig. 2.34a shows for a one-dimensional domain structure. The distribution of $|q|$ (left half of the image) is stationary and consists of several peaks with very steep valleys in between. A look at the real part of q (right half of the image) shows that similar to the complex GL equation, the structure oscillates periodically in its phase so that both real and imaginary parts of the q-distribution correspond to standing waves. Similar to the real SH equation, using different initial conditions various domain structures of different width can be created whose internal structure is always dominated by the same wavelength.

Considering the domains structures as stationary LSs, it is interesting to note that also traveling LSs are possible for the same system parameters. Fig. 2.34b shows a typical solution obtained for the parameters of Fig. 2.34a. Contrary to the domain structures, the running LS has a fixed extension. A look at the amplitude $|q|$ reveals

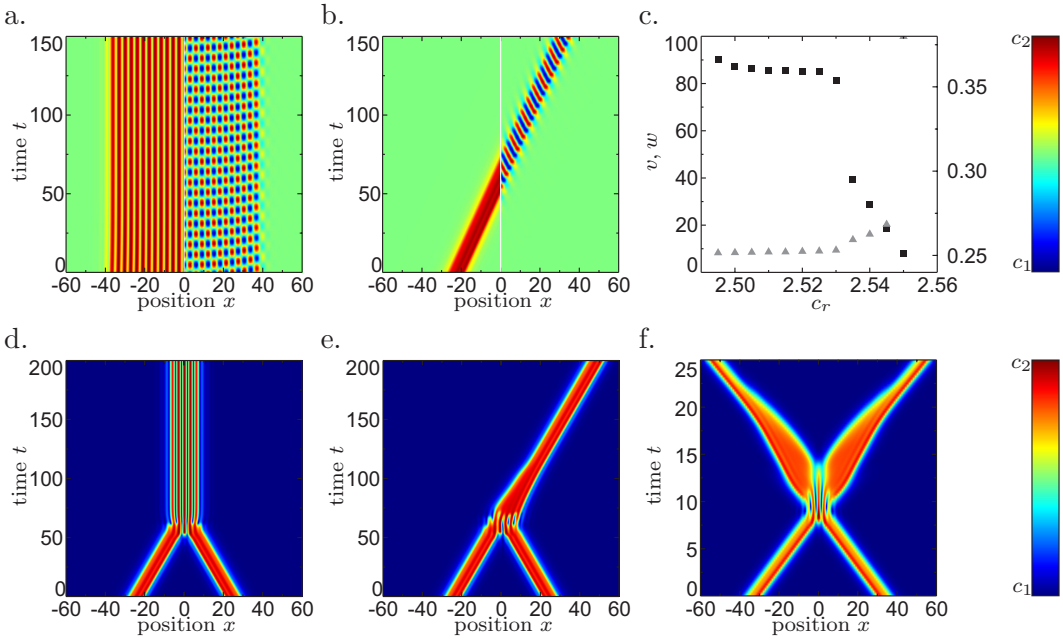

Figure 2.34: Structures in the one-dimensional complex SH equation. a. Space-time plot showing $|q|$ (left half) and Re(q) (right half) for a domain structure internally consisting of a standing wave pattern. Parameters: $l_r = -2.1$, $c_r = 2.5$, $c_i = 0.5$, $q_r = -1$, $q_i = 0$, $d_r = -2$, $d_i = 0.3$, $s_r = -1$, $s_i = 0$, scale $c_1 = -1.5$, $c_2 = 1.5$, b. Space-time plot showing $|q|$ (left half) and Re(q) (right half) for a traveling LS coexisting with the domain structure in a., c. dependence on the width w (grey triangles, left scale) and the velocity v (black squares, right scale) of the traveling structure shown in b. as a function of c_r, d. and e. space-time plot of $|q|$ for collisions of two traveling LSs as shown in b. for $\Delta\phi = 0$ and $\Delta\phi = \pi/2$, scale $c_1 = 0$, $c_2 = 1.5$, f. space-time plot of $|q|$ showing a collision with $\Delta\phi = 0$ resulting in interpenetration, note the changed parameters $l_r = -1.7$, $c_i = 1$, $d_i = 2$.

a strongly asymmetric shape of the envelope, however the distribution of Re(q) shows that in a co-moving frame the structure has again the form of a standing wave pattern with the same dominant short scale as the standing domains. After a relaxation of initial transients the propagation velocity is constant in time. As the coexistence of standing and propagating structures already indicates, the latter are generated in a subcritical bifurcation. This is confirmed by starting with an existing structure and varying the corresponding system parameters in small steps. We illustrate the results of the procedure by varying c_r, the real coefficient in front of the cubic term which we identified as being responsible for local energy gain in the complex cubic GL equation. In Fig. 2.34c we plot the propagation velocity (black squares) and the width of the propagating pulse (defined via the distribution above the critical amplitude $|q_b| = 0.8$) under a variation of c_r while keeping the other parameters constant. Below $c_r = 2.495$ the traveling LS can not exist. Above the critical value there is a region in which the pulse exhibits an almost constant width and velocity. At $c_r = 2.535$, this behavior changes in a drastic way. The initial pulse widens as the leading edge of the pulse propagates with a higher velocity than the trailing one. After some time, the trailing edge adapts its velocity and a pulse of constant width stabilized which is larger than

that obtained for smaller values of c_r. In addition, the velocity decreases significantly. The large jump in the velocity curve of Fig. 2.34c indicates that a subcritical bifurcation may have taken place. Above the bifurcation point, the width of the stationary pulse increases extremely strongly with the parameter. It remains to be clarified whether the running pulses may become arbitrary wide when further increasing c_r.

The running LSs in the complex SH equation show a certain similarity with those in the complex GL equation (compare Fig. 2.27). However, an important difference arises when going from one to two spatial dimensions. Up to now, no isolated running LSs have been observed in the two-dimensional GL equation although asymmetric compound states were found to move intrinsically. In contrast, the complex SH equation allows for isolated propagating LSs [57]. Such a structure is depicted in Fig. 2.35a. While the envelope $|q|$ of the structure shows only a weak derivation from radial symmetry, a look at $\mathrm{Re}(q)$ reveals that internally the LS consists of a single period of the standing wave pattern also found in the one dimensional case (compare Fig. 2.34b).

With the existence of intrinsically propagating LSs in one and two dimensions, various interaction processes become possible. As in the complex GL equation, the mutual phase difference of the interacting LSs has a significant relevance for the outcome of the interaction process. In the one-dimensional case, we may repeat the simulations on collision processes shown in Fig. 2.27. Figs. 2.34d and e show space-time plots of two colliding counter-propagating structures for $\Delta\phi = 0$ and $\Delta\phi = \pi/2$, respectively. Considering the first case, the result of the collision is the formation of a stable symmetric domain structure. One may recall that we found a similar result in the GL equation, here the outcome in the corresponding collision is a symmetric composite soliton if the initial energy in the system is high enough. For $\Delta\phi = \pi/2$, the LSs merge and form a single traveling LS. This scenario in direct analogy to the GL case. Varying the system parameters in such a way that the "conservative" coefficients become more dominant (but dissipative terms are still significant), one may also observe a phenomenon that is typically associated with classical soliton equations: Fig. 2.34f shows an interpenetration event with two LSs merging into a compound state which again re-emits two pulses of the original shape. The outcome of the event thereby is independent of $\Delta\phi$. In spite of a apparent similarity to classical soliton behavior, one should keep in mind that while in classical soliton equations the energy stays globally conserved, in the collision event shown in Fig. 2.34e the same quantity increases by a factor 2 before relaxing to its initial value in the long-time limit.

In two dimensions, aside from interpenetration processes as reported in [57] similar to the one-dimensional case a number of different interaction processes can be found. We exemplarily depict two of them in Figs 2.35b and c. Here we have simulated the central collision of two structures as shown in Figs 2.35a for $\Delta\phi = 0$ and $\Delta\phi = \pi/2$, the dynamics of the process is visualized via a space-time plot of the $|q|$-distribution along the connecting line of the LSs. In the first case, the LSs approach until they feel a repulsive interaction and then change their direction of motion. During the collision, a third LS is formed in the center (note the similarity to the reaction-diffusion example in Fig. 2.20), however it decays again in the course of time. In the second case, one again has repulsive interaction, however one LS decays after the collision. For $\Delta\phi = \pi$ (not shown here), both LSs are annihilated in the collision. Additional simulations can be carried out for non-central collisions. Here, one either observes weak interaction leading to scattering or one of the processes described above.

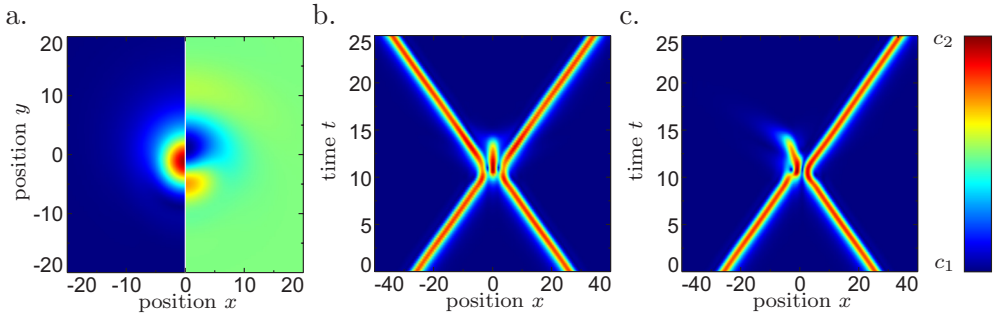

Figure 2.35: Traveling LSs in the two-dimensional complex SH equation. a. Distributions of $|q|$ (left half) and $\mathrm{Re}(q)$ (right half) for a LS traveling upwards. Parameters: $l_r = -1.5$, $c_r = 2.35$, $c_i = 2$, $q_r = -1$, $q_i = 0$, $d_r = -2$, $d_i = 2.5$, $s_r = -1$, $s_i = 0$, scale $c_1 = 0$, $c_2 = 1.5$ (left half), $c_1 = -0.75$, $c_2 = 0.75$ (right half), b and c. space-time plots showing the central collisions of two LSs as depicted in a. via the distribution of $|q|$ along the connecting line of the LSs for a phase difference $\Delta\phi = 0$ and $\Delta\phi = \pi/2$, scale $c_1 = 0$, $c_2 = 1.7$.

As a last point, one should mention that like for the complex GL equation and the real SH equation different extensions have been proposed for the complex SH equation. In order to model pattern formation in electroconvection, an anisotropic two-dimensional SH equation has been proposed [245]. Here, worm-like structures with particle-like properties have been found. Other works deal with terms similar those to in (2.63). These terms either arise for example from an approximation of underlying first-principle equations [247] or phenomenologically like in our example for the real SH equation [246].

Note that a tabular summary on the literature dealing with LSs in the SH equation is contained in Table 2.4.

2.4 Summary on mechanisms

In this chapter, we have discussed how LSs are generated in three different classes of model systems, what conditions are necessary for their stability and how dynamical destabilizations can occur. Concerning our goal to investigate the universal properties of LSs, the generation of LSs poses the largest problems as on a first glance the discussed systems show large discrepancies. As an example, while reaction-diffusion systems are naturally discussed in terms of local transport, the complex GL equation does not instantaneously offer the same intuition. However, we have seen that by looking at local energy and impulse functionals a certain analogy can be established as in this way the concept of transport can be introduced into the GL equation as well. In this sense, the SH equation can be considered as a hybrid structure involving mechanisms from both reaction-diffusion and GL equations.

In the following, we want to try to summarize our findings on a more detached level. Rather independent of the exact type of system under consideration the most elementary type of solution in the presence of bistability between two homogeneous states is a front solution. An asymptotic superposition of a front-antifront pair to a domain solution thus appears to be the most simple way to construct a localized solution. The stability of such a structure can then be interpreted to be the consequence of a balance between

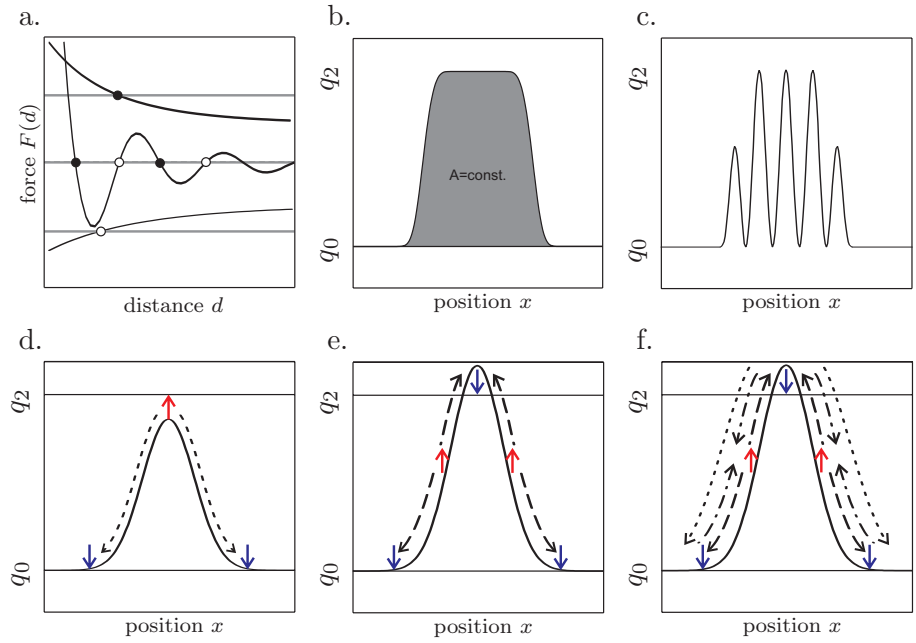

Figure 2.36: Schematic illustration of mechanisms capable of stabilizing LSs. a. In an asymptotic front-antifront superposition the front dynamics (grey lines) must be balanced by interaction forces (black lines), b. global constraints regulate the deviation from the ground state (grey area), c. domains of patterned states on a homogeneous background, d-f. balance of local gain (red arrows) and loss (blue arrows) by diffusion, dispersion and other transport mechanisms (dashed and dotted arrows).

the dynamics of the isolated fronts and the interaction caused by the nonlinearities in the system (Fig. 2.36a, compare also Fig. 2.15). If there exists a separation at which the effects compensate each other, the corresponding state os stable only if the overall attraction of the pair get stronger when the distance gets larger and vice versa. This is for example possible when the mutual interaction is repulsive and the individual fronts without interaction approach each other or when the interaction strength oscillates with distance. The latter phenomenon is typically observed when the system is close to a global instability with a dominant finite wave number (for example a Turing or modulational instability).

While the front-antifront structure seems conceptually rather simple to realize, it is observed only seldom in many systems, which is due to two primary reasons. On the one hand, an asymptotic superpositions of two fronts yields an interaction force that is rather weak in strength. Consequently, the front velocities must be small as well to balance this effect. While in some systems the bistable states are totally equal due to symmetry reasons, in most known examples one of the states dominates so strongly that the velocities of the transition front are too high to allow for a domain structure to form. The second problem concerning domains arises in two or more spatial dimensions. Here, domains arise as revolved one-dimensional front structures. In this way, the action of spatial coupling terms at the transition boundary depends on its local curvature which in turn affects the front velocity as well. This may lead to curvature-driven instabilities

in which deformations of the rotationally symmetric structure are enhanced, thereby leading to a decay of the structure.

Due to the above arguments, in many systems there are additional mechanisms leading to stabilization or the LSs exist to to a dynamical balance as we will explain below. A method of stabilization that works in almost all types of systems is the introduction of global coupling terms or constraints that limit the overall deviation of the system from a ground state (marked in grey in Fig. 2.36b). A single LS is generally very stable under these conditions, however the coupling implies long-ranged interactions and several LSs are mutually put into competition, often leading to then survival of only one structure. A possibility to avoid this problem is by introducing integral coupling terms with kernels living on a bound support [261] so that the interaction range of a given LS becomes finite. In our section on the SH equation, we have also seen one may consider localize domains of a patterned state on a homogeneous background (Fig. 2.36c). The mechanisms stabilizing the pattern are generally rather strong in nature and may thus be used to avoid the problems for two homogeneous states [255].

Many LSs can not be considered as domain states (i.e. as a combination of individually stable structures), but as the result of a strongly dynamic interplay of local terms and transport mechanisms. A typical situation is depicted in Fig. 2.36d, illustrating a LS on a lower homogeneous state with its peak lying significantly "below" a second upper homogeneous state. Close to the individual homogeneous states, the local dynamics will evolve towards the respecting equilibria (compare the colored arrows in the figure) so that the effect of diffusion (dotted line) is a natural mechanism to compensate for the local dynamics. When the tip of the LS lies above the upper homogeneous state, transport must be directed from the flanks of the structure both to the tails and to the center (Fig. 2.36e) which can typically be realized by dispersion as in the GL equation. Generally, one observed an interplay of different types of spatial transport (Fig. 2.36f) whose net effect must be balanced by local terms. An example is given by the complex SH equation. A parameter-dependent stability analysis of LSs in a given system can generally be connected rather well with opposing mechanisms of transport and production.

The balance of production and transport becomes particularly relevant when investigating interaction of LSs. In the discussed examples, satisfying explanations for interaction processes could be found by first considering the nonlinearity on the system locally acting on the superposed solution of two LSs and comparing this result with the individual local dynamics. In a second step, the reaction of the transport mechanisms to the resulting perturbations was used to explain the dynamic evolution.

The mechanisms for dynamic destabilizations of LSs turn out to be manifold, however again some common aspects can be found. A particularly relevant process is the propagation of LSs. One finds that the latter is occurs in two ways. Either the system of interest in Galilean invariant or the structure has dynamically induced broken symmetry at least with respect to one axis. This may either be the case for a single structure or an asymmetric compound composed of several structures. The prior case is often connected to symmetry-breaking bifurcations of an originally symmetric state.

Looking at the model equations we have considered so far, an essential difference is that the spatial coupling terms appear in a linear fashion. A generic example for nonlinear spatial coupling is found for hydrodynamic systems in which the normal time

derivative is replaced by the substantial derivative

$$\frac{d}{dt} = \frac{\partial}{\partial t} + (\boldsymbol{v}\nabla) \tag{2.64}$$

with $\boldsymbol{v}$ representing a macroscopic flow. Another example arises in drift-diffusion equations which can be used to model LSs in systems with charge transport [262]. Nonlinear transport terms may cause an essential change in the mechanisms responsible for the formation of LSs, possible consequences may range from simple advection of LSs [263] up to developed turbulence. It will remain a task for future works to investigate mechanisms and universal properties in these kinds of systems.

Chapter 3

Particle description of LSs

3.1 The concept of order parameters

In the previous section, we have considered different types of models which find application in a larger class of experimental systems and which exhibit the formation of LSs. In particular, several basic mechanisms leading to the formation and dynamics of LSs could be identified. Nonetheless, many aspects remain connected to special properties of the underlying field equations. To explore the universal aspects of the particle-like behavior of LSs in different systems, it would be good to have a description of the particle phenomenology on a level which is structurally more uniform than the field equations.

While setting up such a "normal form description" for the generation of LSs poses severe problems due to the subcritical nature of the generation process, we have seen that once stable LSs are known to exist for a given system, possible destabilizations of the stationary state often occur supercritically, implying that there are only small changes in the shape of the structure. The same holds for the case of weak interaction, meaning that during the interaction process under consideration the tails of the LSs overlap only weakly so that the shape again stays essentially preserved. Consequently, as long as only weak deformations of a fixed number of LSs are encountered during the dynamic evolution (which excludes for example generation and annihilation processes), many systems indeed offer the possibility to reduce the dynamic description to a low-dimensional system of ordinary differential equations with structure similar to those equations encountered either in the normal form theory for supercritical bifurcations or in classical Newton particle.

The basis for the derivation is provided by adiabatically eliminating most degrees of freedom of the field equations and considering just the slowest timescales. As it has been proposed by Haken [264, 265], the variables corresponding to these slow degrees of freedom are also termed order parameters (the term was adapted from the theory of phase transitions). In Hakens original interpretation, the order parameters were usually direct physical quantities like positions, amplitudes, velocities of the LSs. A closely related idea is given by the concept of the center manifold to which the dynamics should quickly converge [266]. While being rather rigorous concerning the underlying mathematical theory, the application of the center manifold theory has the consequence that the resulting equations in some cases do not only describe the evolution of direct physical quantities, but also of rather unphysical "mixed quantities" (for example products of

direct quantities), making an intuitive understanding more difficult. In the following, we will use the term order parameter as a general expression for a slowly evolving quantity independent of the method of derivation.

In the context of LSs, the idea of order parameters in many situations provides a possibility to compare and classify the possible dynamical evolution of different systems in a much more simple fashion that on the level of the underlying field equations. Also, the comparison for example with the dynamics in classical Newton equations becomes much easier. As we will see in the course of this chapter, the general structure of the order parameter equations is often essentially influenced by the continuous symmetries of the system so that a knowledge of the latter already allows for a basic prediction of the possible dynamical phenomena.

3.2 Dynamics of single structures

After the observation of LSs in a given system, a frequently asked question is how important quantities like position, velocity or amplitude evolve either as a function of time or of the system parameters. For LSs in the classical NLS, KdV and SG equations, the above questions can be generally be answered in a direct way as complete analytic solutions are available via the inverse scattering theory. However, already when considering perturbed versions of the classical equations, significant problems arise. In some cases, inverse scattering techniques can still be applied to obtain analytical solutions [267, 268]. However, there are strong restrictions for the use of this method, in particular when the equation of interest can not be considered as perturbed version of a classical equation.

In current research, to the authors knowledge there are two main methods to overcome the above problems by reducing the complexity of the system. The first one which we will refer to as "trial-function based method" relies on the existence of an approximate analytical solution whose time-dependent parameters serve as order parameters. While we will briefly review some more details below, one may stress that the necessity of an analytical form usually demands a close relation of the field equation of interest to a classical field equation like the NLS or the KdV equation for which exact solutions are known. The second technique relies on a weakly nonlinear analysis of deviations from the stationary state which are expressed in terms of eigenmodes of the corresponding linearization operator. The amplitudes of the eigenmodes become time-dependent, and fast modes are adiabatically eliminated to extract the slow dynamics. As this technique has a wider range of applicability we will put the main focus on this point in the following. An overview on the current literature focussing on the topic of order parameter equations is given in Table 3.1, including also interaction phenomena which we will treat further below.

3.2.1 Trial function methods

Trial function based methods can be applied when an approximate analytical solution for a LS in a given system is known, which is usually the case either when the field equation under consideration is a modification of a classical soliton equation or when one has been able to find a numerical solution which can be fitted with an analytical expression. As a precondition for the method to work, one has to require that in the parameter range of interest, the shape of the solution varies only slightly. The central ideal is to capture

technique	type of system	citation	details
single LSs			
trial functions			
momentum and trial function	GL	[199, 213, 269]	fronts, pulse stability, pulsating LSs
	double well ϕ^4	[270]	Langevin equation
Hamiltonian/Lagrangian	Landau-Lifschitz, Heisenberg chain	[271, 272]	perturbed conservative systems
minimization of residual energy	perturbed NLS, GL	[273–275]	dispersion-managed fibers
projection-based			
	perturbed NLS, forced GL	[276, 277]	traveling pulses
	Fitzhugh-Nagumo type	[41, 96, 98, 278]	drift bifurcation
	semiconductor model	[42]	prop. by temperature field
interaction of LSs			
mode expansion	KS equation	[279]	Fourier
trial function			
inverse scattering based	perturbed NLS/GL	[215, 280, 281]	"Karpman-Solov'ev" approach
Lagrangian	perturbed/coupled NLS	[282–285]	various forms of perturbations
effective Hamiltonian	pert. NLS/GL equation	[216, 286, 287]	interaction potentials
momentum eqns.	NLS/GL/KdV equation	[39, 288]	
projection-based			
	GL-based eqns.	[59, 62, 217]	asymptotic expressions
	reaction-diffusion	[289, 290]	pulse trains
	reaction-diffusion	[58, 169]	inner degrees of freedom
	Benney equation	[291, 292]	pulse trains
	others	[293, 294]	neural and active-dispersive media

Table 3.1: Overview on current literature dealing with order parameter equations for single and interacting LSs divided according to the methods used and whether single or interacting LSs are treated.

temporal changes in the shape of the LS by making the parameters characterizing the solution (for example position, width, amplitude, velocity) explicitly time-dependent, thereby artificially choosing the analytic parameters as order parameters of the problem. Obviously, the choice of this trial solution confines the dynamics of the solution to a part of the parameter space without a rigorous justification by center-manifold theory etc, but it is found that nevertheless the idea works in a number of cases.

A central problem is that when inserting a trial ansatz with time-dependent parameters into the field equation, it will generally not be an exact solution of the system. Consequently, if order parameter equations are obtained by direct insertion, they can generally not be fulfilled and produce a contradiction. A solution to this problem that originates from mechanics is to find a "weaker" evolution equation that still reflects the important parts of the dynamics while at the same time being compatible with the trial solution. Depending on the individual problem, there are different possibilities to obtain the new evolution equation, but the overall strategy is similar in all cases: the local equation is replaced by an integral one. One possible approach is that of moments [295], which is also widely used in many mathematical and physical disciplines, for example in statistics. In the context of nonlinear field equations and LSs, moment integrals of the local fields as well as more complicated integral relations play an important role because in several systems the position of the LSs as well as general conservation laws can be expressed via such integrals. A typical example is given by the NLS equation (2.36) where the conservation of the particle number is expressed by the integral relation

$$\int |q|^2 \,\mathrm{d}V + i \int (q\nabla q^* - q^*\nabla q)\mathrm{d}\mathbf{S} = 0 \tag{3.1}$$

between volume and surface integrals. In some cases such expressions lead to important further conclusions. As an example, for the NLS equation one may consider the evolution of the "virial" moment integral [296]

$$I(t) = \int r^2 |q|^2 \,\mathrm{d}V \tag{3.2}$$

that is calculated using the "probability" function $|q(\boldsymbol{x}, t)|^2$. A direct calculation shows that

$$\frac{\mathrm{d}^2 I}{\mathrm{d}t^2} = \left(\frac{2}{n} + 1\right) H - (n-2) \int |\nabla q|^2 \,\mathrm{d}V \tag{3.3}$$

where H is the conserving Hamiltonian function and n is the spatial dimension of the system. The connection to trial function methods is made by using the integral relations as weakened evolution equation for the parameterized solution. A good application of this approach is given by the complex GL equation that can be rewritten in the form

$$i\partial_t q + d_i \partial_x^2 q + c_i |q|^2 q = i(l_r q + d_r \partial_x^2 q + c_r |q|^2 q + q_r |q|^4 q). \tag{3.4}$$

The integral relations are obtained similarly to (3.1) but contain more complicated terms on the right-hand side with integrals proportional to the dissipative coefficients d_r, l_r,

c_r and q_r. The vital choice of the trial function is motivated by the one-dimensional localized solution of the NLS equation, but again contains time dependent parameters. According to [199, 213, 269] such an approach provides a very good correspondence between the full solution and the reduced dynamics.

Other authors suggested to obtain new evolution equations by minimizing the residual energy, i.e. the functional

$$E = \int |q(\boldsymbol{x}, t) - q_{\mathrm{tr}}(\boldsymbol{p}, t)|^2 \, \mathrm{d}\boldsymbol{x}, \tag{3.5}$$

where q and q_{tr} represent real and trial solution and $\boldsymbol{p}$ the order parameters. In this way, the solution is supposed to remain close to the phase space of the original solution, however, there is usually no rigorous justification for this claim.

A third possibility is to set up a Hamiltonian or Lagrangian formulation. This was for example done for the complex GL equation in [297], where for the radially symmetric case the equation was expressed via two Lagrangians as

$$\frac{\delta}{\delta q^*} \int \left(L_c + iL_q\right) r^{D-1} \, dr = 0, \tag{3.6}$$

where the conservative (real) part has the standard form

$$L_c = \frac{i}{2}\left(q\partial_t q^* - q^*\partial_t q\right) + |\nabla q|^2 - \frac{1}{2}|\nabla q|^2 - \frac{q_i}{3}|\nabla q|^6 \tag{3.7}$$

whereas the dissipative (imaginary) part is

$$L_q = l_r|q|^2 - d_r|\nabla q|^2 + \frac{c_r}{2}|\nabla q|^2 + \frac{q_r}{3}|\nabla q|^6. \tag{3.8}$$

As trial function, a reasonable choice that was originally introduced for the optical fibers [298] is

$$q = A(t) \exp\left[-\frac{r^2}{2R(t)^2} + iC(t)r^2 + i\Phi(t)\right]. \tag{3.9}$$

Inserting (3.9) into the evolution equation, one gets a system of four coupled first order ordinary differential equations for the unknown parameters.

As our examples indicate, trial function based methods are frequently applied in optical problems, but for example not in reaction diffusion equations where no integral conservation equations exist.

3.2.2 Projection based methods

An alternative and more universally applicable approach to trial function methods is given by "projection based methods". Here, order parameters are determined in a rigorous way using the linearization problem around a stationary solution, and evolution

equations for the relevant modes are obtained by projections or solvability conditions. In a general framework, one may choose a fixed set of parameters and formally eliminate all fast modes adiabatically [299]. We will first consider this method which shows the origin of different terms in the order parameter equations and carry out a generalization to include degenerated eigenmodes. A problem in this case is given by the fact that one may not directly say how the order parameter equations change under a variation of the system parameters. Concerning this point we will show how normal forms can be estimated using the symmetries of the system under consideration close to bifurcation points. Another problem is that the derived expressions contain infinite sums. To overcome the above problems, an alternative option is to conduct a perturbative treatment on the level of the original field equations.

3.2.2.1 Formal derivation

To illustrate the procedure of formally obtaining order parameter equations, we will start with a general field equation

$$\partial_t \boldsymbol{q} = \boldsymbol{F}(\boldsymbol{q}, \boldsymbol{\sigma}), \tag{3.10}$$

which represents most of the model systems introduced in Chap. 2. Here, $\boldsymbol{q}(\boldsymbol{x}, t)$ is the vector describing the state of system at a given time and point in space, $\boldsymbol{\sigma}$ represents the parameters and $\boldsymbol{F}$ is a functional which may contain derivatives and integrals alike. As LSs generally exist on a stable homogeneous background, we will shift this state into the origin, so that $\boldsymbol{F}(\boldsymbol{0}) = \boldsymbol{0}$. Furthermore, for some parameters there should exist a stationary localized solution, which we will denote by $\boldsymbol{q}_0(\boldsymbol{x})$. For an arbitrary, but small perturbation of the stationary state, it is reasonable to decompose the general solution as the sum of the stationary state and a derivation, i.e.

$$\boldsymbol{q}(\boldsymbol{x}, t) = \boldsymbol{q}_0(\boldsymbol{x}) + \tilde{\boldsymbol{q}}(\boldsymbol{x}, t). \tag{3.11}$$

As the stationarity of $\boldsymbol{q}_0$ corresponds to $\boldsymbol{F}(\boldsymbol{q}_0, \boldsymbol{\sigma}) = \boldsymbol{0}$, the function $\boldsymbol{F}$ may be expanded around this solution using Fréchet derivatives if both the functional $\boldsymbol{F}$ and the function $\boldsymbol{q}$ fulfill certain regularity issues. The result is then

$$\partial_t \tilde{\boldsymbol{q}} = \boldsymbol{F}'(\boldsymbol{q}_0, \boldsymbol{\sigma})\tilde{\boldsymbol{q}} + \boldsymbol{F}''(\boldsymbol{q}_0, \boldsymbol{\sigma}) : \tilde{\boldsymbol{q}} : \tilde{\boldsymbol{q}} + \ldots \tag{3.12}$$

Here, $\boldsymbol{F}'$ is a linear operator, and $\boldsymbol{F}''$ denotes a functional quadratic in $\tilde{\boldsymbol{q}}$ etc.

The linear stability analysis starts by only taking the linear equation into account, i.e.

$$\partial_t \tilde{\boldsymbol{q}} = \boldsymbol{F}'(\boldsymbol{q}_0, \boldsymbol{\sigma})\tilde{\boldsymbol{q}}. \tag{3.13}$$

It is reasonable to express $\boldsymbol{q}$ and $\tilde{\boldsymbol{q}}$ in terms of eigenmodes of $\boldsymbol{F}'$ in order to decouple the problem. They are defined by

$$\boldsymbol{F}'(\boldsymbol{q}_0, \boldsymbol{\sigma})\boldsymbol{\phi}_i(\boldsymbol{x}) = \lambda_i \boldsymbol{\phi}_i(\boldsymbol{x}) \tag{3.14}$$

with the index denoting both discrete, continuous or mixed sets. For the eigenvalue decomposition of $\boldsymbol{F}'$, there are two basic possibilities: the operator can either have a (generalized) complete spectrum, in which case the operator is a member of the class of *spectral operators*, or the spectrum is incomplete or overcomplete. Here, we will focus on the first case which is generally assumed to hold for most practical problems. If $\boldsymbol{F}'$ is self-adjoint, the eigenvalues are real and there exists a corresponding basis of orthogonal eigenmodes which may form a discrete, continuous or mixed set. The evolution equation (3.13) for $\tilde{\boldsymbol{q}}$ then has an explicit solution, namely

$$\tilde{\boldsymbol{q}} = \sum_i d_i \boldsymbol{\phi}_i(\boldsymbol{x}) \exp(\lambda_i t), \tag{3.15}$$

with coefficients d_i depending on the initial conditions. We have used the (discrete) sum sign here for simplicity, however generally summation may comprise integration as well. The reason for this choice is that in contrast to many works dealing with spatially extended patterns, in the fairly largest part of works connected with LSs the "relevant modes" are part of the discrete spectrum.

In many physically relevant cases the linear operator $\boldsymbol{F}'$ is not self-adjoint, and the corresponding theory is more complex. This situation is of particular relevance for supercritical bifurcations of LSs in which an operator with an otherwise complete spectrum may lose this property when a real eigenvalue passes the imaginary axis due to a change of the system parameters. Furthermore, there are systems with a natural degeneracy of eigenmodes for example due to Galilean invariance. If the simple eigenvalues form no complete set, one may try to construct a generalized complete basis by considering Jordan chains for the degenerated eigenvalues (see for example [300] for more details on spectral operators). The Jordan chains are defined via the generalized eigenmodes $\boldsymbol{\phi}_i^j$, given by

$$(\boldsymbol{F}' - \lambda_i)^j \boldsymbol{\phi}_i^j = 0, \quad (\boldsymbol{F}' - \lambda_i)^{j-1} \boldsymbol{\phi}_i^j \neq 0. \tag{3.16}$$

In a matrix representation of $\boldsymbol{F}'$, the occurrence of generalized eigenmodes corresponds to the fact that the matrix can not be fully diagonalized and instead, Jordan blocks appear. Instead of considering fixed amplitudes d_i for an eigenmode $\boldsymbol{\phi}_i$ as in (3.15), one may instead look at the generalization

$$\tilde{\boldsymbol{q}} = \sum_i J_i(\boldsymbol{x}, t) \exp(\lambda_i t). \tag{3.17}$$

where

$$J_i := \sum_{j=0}^{n(i)} d_{i,j} \sum_{k=0}^{j} \boldsymbol{\phi}_i^k t^{j-k} \tag{3.18}$$

with $n(i)$ denoting the dimension of the subspace spanned by the generalized eigenmodes of the eigenvalue λ_i.

Treating now such cases where at least a generalized complete spectrum is available, (3.17) may give us information about the stability of the LSs: as all summands in (3.18)

are algebraic in time, from (3.17) it is obvious that an infinitesimal perturbation decays if the real part of all eigenvalues involved in the decomposition is negative (meaning that the solution is linearly stable). If there are modes with $\mathrm{Re}(\lambda_i) > 0$, these modes will grow exponentially in the linear system, although in the full system the growth will be affected by nonlinear effects. The real parts of the λ_i can be considered as the inverse of a characteristic time of growth or decay, and the imaginary part of the eigenvalues determines whether the growth or decay is monotonous or oscillatory. Obviously, the modes with $\mathrm{Re}(\lambda_i) \approx 0$ are of particular relevance even if their real part is not strictly positive. A central idea of the projection-based methods is that one makes a transition from constant to time-dependent amplitudes of the eigenmodes so that the amplitudes of the critical modes become the order parameters. While generally the critical modes can also be part of the continuous spectrum, this case is hardly discussed in the current literature, so we will focus on the discrete case.

Basically, critical modes can arise in two ways. First, they are generated by all continuous symmetries of a system. Each symmetry-related variable c_i can be associated with a whole continuous family of stationary solutions $\boldsymbol{q}(\boldsymbol{x}, c_i)$ which be generated from an initial solution $\boldsymbol{q}(\boldsymbol{x}, 0)$. Examples are given by

$$\boldsymbol{q}_0(\boldsymbol{x}, c_i) = \boldsymbol{q}_0(\boldsymbol{x} - c_i \boldsymbol{e}_i) \qquad \text{translational invariance,} \tag{3.19}$$

$$\boldsymbol{q}_0(\boldsymbol{x}, c_j) = \boldsymbol{q}_0(\underline{\boldsymbol{R}}(c_j)\boldsymbol{x}) \qquad \text{rotational invariance,} \tag{3.20}$$

where $\underline{\boldsymbol{R}}$ represents an orthogonal matrix. The list may also contain Galilean invariance, however, in many systems the shape of the LS changes with the velocity in a nontrivial way, so that it is difficult to give a general form in this case. Also, hidden symmetries like scaling transformations may arise. From the stationarity of the transformed solution one immediately sees that

$$\frac{\partial}{\partial c_i}\boldsymbol{F}(\boldsymbol{q}(\boldsymbol{x}, c_i)) = \boldsymbol{F}'(\boldsymbol{q}(\boldsymbol{x}, c_i))\frac{\partial}{\partial c_i}\boldsymbol{q}(\boldsymbol{x}, c_i) = \boldsymbol{0}, \tag{3.21}$$

i.e. the derivative of the solution with respect to c_i is a critical mode being the generator of the corresponding symmetry group. Second, aside from these modes which are always critical, a change of the system parameters can cause previously uncritical modes to become critical as well. When decomposing a general solution as $\boldsymbol{q} = \boldsymbol{q}_0 + \tilde{\boldsymbol{q}}$, in order to ensure $|\tilde{\boldsymbol{q}}| \ll |\boldsymbol{q}_0|$ in the course of time when a continuous symmetry is present in the system one may define the symmetry group operator $D(\boldsymbol{c})$ to act as $D(\boldsymbol{c})\boldsymbol{q}_0(\boldsymbol{x}, \boldsymbol{0}) = \boldsymbol{q}_0(\boldsymbol{x}, \boldsymbol{c})$. Then one may write the general solution as

$$\boldsymbol{q}(\boldsymbol{x}, t) = D(\boldsymbol{c}(t))\Big(\boldsymbol{q}_0(\boldsymbol{x}, \boldsymbol{0}) + \sum_i \sum_{j=0}^{n(i)} \gamma_{ij}(t)\boldsymbol{\phi}_i^j(\boldsymbol{x}, \boldsymbol{0})\Big). \tag{3.22}$$

Comparing the representation (3.22) to (3.17) which was used in the linear case, one may now see that the simple time dependence $d_i \exp(-\lambda_i t)$ from the linear case has been replaced by general time-dependent amplitudes $\gamma_i(t)$ in order to account for nonlinearities and non-decaying perturbations. Second, in (3.17) the individual terms were

sorted to eigenvalues end elements of the Jordan chains. In order to simplify notation, we will split up the Jordan chains and instead sort the sum according to eigenmodes and (generalized) eigenvalues.

While the critical modes due to symmetries have been taken care of introducing the parameters $\boldsymbol{c}$, other critical modes resulting from bifurcations are accounted for by $\tilde{\boldsymbol{q}}$. Inserting (3.22) into the evolution equation yields (compare also Eq. (3.12))

$$\begin{aligned}&\partial_t \boldsymbol{c} \cdot \nabla_{\boldsymbol{c}}[\boldsymbol{q}_0(\boldsymbol{x},\boldsymbol{c}) + \sum_i \sum_{j=0}^{n(i)} \gamma_{ij} \boldsymbol{\phi}_i^j(\boldsymbol{x},\boldsymbol{c})] \\ &+ \sum_i \sum_{j=0}^{n(i)} \partial_t \gamma_i \boldsymbol{\phi}_i^j(\boldsymbol{x},\boldsymbol{c}) = \boldsymbol{F}'_{\boldsymbol{q}_0} \tilde{\boldsymbol{q}}(\boldsymbol{x},\boldsymbol{c},t) + \boldsymbol{F}''_{\boldsymbol{q}_0}(\boldsymbol{q}(\boldsymbol{x},\boldsymbol{c},t)) : \tilde{\boldsymbol{q}}(\boldsymbol{x},\boldsymbol{c},t) : \tilde{\boldsymbol{q}}(\boldsymbol{x},\boldsymbol{c},t) + \ldots,\end{aligned} \tag{3.23}$$

A central problem is now to extract appropriate equations for the time-dependent amplitudes. To this end, the corresponding modes have to be "projected out" of Eq. (3.23). This technique is frequently applied in linear systems, for example in quantum mechanics. Suitable projectors can be found by considering by the adjoint operator of $\boldsymbol{F}'$ (with respect to the canonical scalar product in $L^2(\mathbb{R}^n)$ or another suitably chosen space), denoted by $\boldsymbol{F}'^{\dagger}$. It has the same symmetries and eigenvalues as $\boldsymbol{F}'$ except for complex conjugation, however the eigenmodes are generally different as the operators under consideration are usually not self-adjoint . We will use the notation

$$\left(\boldsymbol{F}'^{\dagger}(\boldsymbol{q}_0, \nabla, \boldsymbol{\sigma}) - \lambda_i^*\right)^j \boldsymbol{\phi}_i^{\boldsymbol{F}'^{\dagger},j}(\boldsymbol{x}) = \boldsymbol{0}. \tag{3.24}$$

The product for two (generalized) eigenvectors of $\boldsymbol{F}'^{\dagger}$ and $\boldsymbol{F}'$ is always zero when they belong to different eigenvalues, which is a very useful property for the projection. For the same eigenvalue, there is no similarly clear statement, at least when the eigenvalue is degenerated. The problem is that an eigenvalue $\boldsymbol{\phi}_i^{\boldsymbol{F}'^{\dagger},j}$ is not automatically a suitable projector for $\boldsymbol{\phi}_i^j$. However, using an appropriate orthogonality decomposition method one may always linearly combine the (generalized) eigenmodes $\boldsymbol{\phi}_i^{\boldsymbol{F}'^{\dagger},j}$ of $\boldsymbol{F}'^{\dagger}$ for a given eigenvalue (i.e. for fixed i and $j = 0, \ldots, n(i)$) to construct projectors $\boldsymbol{\Phi}_i^j(\boldsymbol{x},\boldsymbol{c})$ which fulfill the orthogonality relation

$$\langle \boldsymbol{\Phi}_k^m | \boldsymbol{\phi}_l^n \rangle = \delta_{k,l} \delta_{m,n} \tag{3.25}$$

and can be normalized so that they fulfill also the completeness relation

$$\sum_{l,n(l)} |\boldsymbol{\phi}_l^n(\boldsymbol{x},\boldsymbol{c})\rangle \langle \boldsymbol{\Phi}_l^n(\boldsymbol{x},\boldsymbol{c})| = \mathrm{id}, \tag{3.26}$$

which explains their suitability for the projection. In other works, the use of projections is sometimes introduced with a different argumentation, for example to obtain a solvability condition according to the Fredholm alternative or in order to rule out resonant terms.

Let us first assume that no generalized eigenmodes appear. This situation generically occurs when the system is either sufficiently far below a bifurcation point or when the system is close to a bifurcation point which is marked by a pair of complex conjugate eigenvalues crossing the imaginary axis. In order to assure the uniqueness of the decomposition (3.22), we claim

$$\langle \mathbf{\Phi}_i^j(\boldsymbol{x}, \boldsymbol{c}) | \boldsymbol{\phi}_{0,c_i}^1(\boldsymbol{x}, \boldsymbol{c}) \rangle = 0. \tag{3.27}$$

where $\boldsymbol{\phi}_{0,c_i}^1 = \partial_{c_i} \boldsymbol{q}_0$. When carrying out the projection for an arbitrary mode (critical or non-critical) one finds

$$\partial_t \gamma_i + \sum_k \partial_t c_k \gamma_k \langle \mathbf{\Phi}_i^1 | \boldsymbol{\phi}_k^1 \rangle = \lambda_i \gamma_i + \sum_{k,l} P_{ikl} \gamma_k \gamma_l + \dots, \tag{3.28}$$

where P_{ikl} is defined by

$$P_{ikl} = \langle \mathbf{\Phi}_i^1 | \boldsymbol{F}''(\boldsymbol{q}_0, \boldsymbol{\sigma}) : \boldsymbol{\phi}_k^1 : \boldsymbol{\phi}_l^1 \rangle. \tag{3.29}$$

An analogous statements holds for the c_i as well, namely

$$\partial_t c_i + \sum_k \partial_t c_k \langle \mathbf{\Phi}_{0,c_i}^1 | \boldsymbol{\phi}_k^1 \rangle = \sum_{k,l} P_{ikl} \gamma_k \gamma_l + \dots, \tag{3.30}$$

note that in this particular case $\lambda_i = 0$. The fact that the left hand side expressions in (3.28) and (3.30) potentially contain more than one spatial derivative term is a consequence of considering the problem in a moving reference frame (see (3.23)).

A further general treatment of the equations (3.28) and (3.30) is difficult due to the second term on the left hand side. Friedrich proposed a complete explicit formal solution for the case of constant $\boldsymbol{c}$ [299]. In this case, the problematic terms vanish. Then, distinguishing between critical and noncritical mode we rename the γ_i by α_i and β_j, where the α_i denote slow, critical modes (index c) and the β_j denote fast, non-critical modes (index nc). The slaving principle implies that there are functional relations $\beta_j(t) = \beta_j(\alpha_i(t))$ so that the entire dynamics is reflected by the $\alpha_i(t)$.

We know that on a long-time scale, the amplitude of non-critical modes decay, so that the critical modes contribute the main part to the sum in (3.28). Neglecting the small contributions of the non-critical modes, the linear inhomogeneous equation is explicitly solvable [299], yielding

$$\beta_j = \int_{-\infty}^{t} \exp(\lambda_j (t - t')) \Big[\sum_{k,l}^{c} P_{jkl} \alpha_k(t') \alpha_l(t') + \dots \Big] \mathrm{d}t'. \tag{3.31}$$

Here, the c over the sum sign shall indicate that a summation should take place just over the critical modes. The dots indicate that in general, higher order terms can be

taken into account, which necessary if the second order terms vanish for some reason or resonance effects occur (see below), the index c over the sum sign reflects that the summation has to be done for critical modes only (this notation will also be used in the following equations). The fast decay of the non-critical modes can be used for a further simplification of (3.31): on the (fast) time scale for which the exponential in (3.31) yields a significant contribution to the integral, the possible significant change in $\alpha_k(t')$ and $\alpha_l(t')$ may only be due to a fast phase shift (as no restrictions on the imaginary parts of the corresponding λ_k and λ_l were made). Hence we assume

$$\alpha_k(t') \approx \exp\Big(i\mathrm{Im}(\lambda_k)(t'-t)\Big)\alpha_k(t), \tag{3.32}$$

yielding an explicit solution of Eq. (3.31):

$$\beta_j(t) = \sum_{k,l}^{c} \frac{P_{jkl}}{i\,\mathrm{Im}(\lambda_k+\lambda_l)-\lambda_j}\alpha_k(t)\alpha_l(t). \tag{3.33}$$

With this expression, we have formally found a system of order parameter equations for the critical modes. Note that resonances can not appear in the summands of (3.33) as the real part of the λ_j is always different from zero. Inserting the above result into (3.28) one finds that when only nonlinearities up to cubic order are considered, relevant contributions to the sum are only given if at least one of the modes in the product is critical, yielding the important result

$$\partial_t\alpha_i = \lambda_i\alpha_i + \sum_{k,l}^{c} P_{ikl}\alpha_k\alpha_l + \sum_{k,l,m}^{c}\Big(\sum_{j}^{nc}\frac{(P_{ijk}+P_{ikj})P_{jlm}}{i\,\mathrm{Im}(\lambda_l+\lambda_m)-\lambda_j}\Big)\alpha_k(t)\alpha_l(t)\alpha_m(t). \tag{3.34}$$

where c and nc marks summation over critical and noncritical modes. When generalized eigenmodes have to be taken into account in the above derivation, the result is basically similar to (3.34), however some changes arise in the linear part. For those eigenvalues whose eigenspace is non-degenerate we obtain the same result as in (3.34) except for the fact that the generalized eigenmodes have to be included in the summation over the critical modes. In contrast, for those modes whose eigenvalues are degenerate, the equivalent to (3.34) reads

$$\partial_t\alpha_i^j = \lambda_i\alpha_i^j + (1-\delta_{n(i),j})\alpha_i^{j+1} + \sum_{k,l}^{c} P_{j(i),kl}\alpha_k\alpha_l + \dots. \tag{3.35}$$

We recall that i denotes the eigenvalue, j the order of the eigenmode and $n(i)$ the degree of degeneracy of the eigenvalue. The coefficient $P_{j(i),kl}$ implies to use the projector mode $\boldsymbol{\phi}_{p,i}^{j}$ in (3.29). Although (3.34) illustrates in a rather clear fashion where the individual contributions to the nonlinear terms of the order parameter equations result from, a slight disadvantage is given by the fact that the coefficients in the equation require a calculation of an infinite sum.

3.2.2.2 Perturbative techniques and normal forms

We see that with the above method, a complete analytical solution is possible for fixed parameters when continuous symmetries do not have to be considered. A question that generally can not be answered directly is how the coefficients of a given equation behave under a change of the system parameters. This problem arises for example when asking for normal forms of supercritical bifurcations. Furthermore, continuous symmetries are relevant in a number of cases as well, for example in the context of drift bifurcations.

A perturbative approach may be helpful to overcome the above problems. Looking first at the formal derivation sketched above, one may try to perturb the order parameter equation obtained for given fixed parameters. This method allows for the derivation of some normal forms in an easy way, so that we briefly look at this point. We will start by assuming that a pair of complex conjugate eigenvalues crosses the imaginary axis away from the origin in a supercritical bifurcation of a stationary LS. This scenario is typical for example when the a rotationally symmetric LSs undergoes a bifurcation to a breathing state. We denote the amplitudes of these modes by α_1 and α_1^*, the corresponding eigenmodes are complex conjugate. Generic order parameter induced by the symmetries of the system are the position $\boldsymbol{p}$ of the LS as well as one or several angles θ characterizing the angular orientation of the LS. In order to make a connection to (3.34), we have to assume that these order parameters are not affected in the bifurcation, which is typical for a breathing destabilization. In the bifurcation point, according to (3.34) we then have

$$\partial_t \alpha_1 = i\omega\alpha_0 + \sum_{k,l}^{c} P_{ikl}\alpha_k\alpha_l + \sum_{k,l,m}^{c} \Big(\sum_{j}^{nc} \frac{(P_{ijk}+P_{ikj})P_{jlm}}{i\,\mathrm{Im}(\lambda_l+\lambda_m)-\lambda_j} \Big) \alpha_k(t)\alpha_l(t)\alpha_m(t) + \dots \quad (3.36)$$

We may ask which terms must vanish if the resonance condition between different harmonics are not fulfilled. Due to the dominance of the linear term one may choose a representation $\alpha_1(t) = A(t)\exp(i\omega t)$ where the time-dependence of $A(t)$ is slow. Then, we may only look at those terms which oscillate with the frequency ω. No expressions quadratic in the critical modes may yield such terms (compare also our consideration for example on the GL equation in the previous chapter) so that (3.36) simplifies to

$$\partial_t \alpha_1 = i\omega\alpha_1 + P|\alpha_1|^2\alpha_1 + \dots \quad (3.37)$$

where P abbreviates the infinite sum leading to the cubic expression (its sign should be negative for a supercritical bifurcation). The complex conjugate value must fulfill an analogous equation, namely the complex conjugate version of (3.37). When we slightly move away from the bifurcation point, the critical modes remain critical, and (3.37) turns into

$$\partial_t \alpha_1 = \Big(\epsilon + i(\omega + f_1(\epsilon))\Big)\alpha_1 + \Big(P + f_2(\epsilon)\Big)|\alpha_1|^2\alpha_1 + \dots, \quad (3.38)$$

where $\epsilon \ll 1$ and $f_1(\epsilon)$ is an unknown function of $O(\epsilon)$. In order for the derivation to be correct, α must be small enough, more precisely we have to require $P|\alpha|^2 \sim O(\epsilon)$. Therefore, we may neglect $f_2(\epsilon)$ with respect to the other terms. Rewriting (3.38) in

terms of the above introduced polar coordinates and combining with the equation for the complex conjugate eigenvalue yields

$$\partial_t A = \epsilon A + P|A|^2 A + \ldots, \tag{3.39}$$

i.e. the normal form of a Hopf bifurcation as one would expect for well-known considerations in low-dimensional systems, when a discrete pair of eigenvalue becomes unstable. Note that the frequency change of the underlying oscillation is determined by f_1. Typical examples have been presented in the last chapter, for example in form of the breathing destabilization in Sec. 2.1.2.1.

In the experiment, breathing LSs are for example found in reaction-diffusion systems like the ferrocyanide-iodate-sulphite or Belousov-Zhabotinsky reaction in a two-dimensional gel reactor [67, 69], as rocking current filaments in p-n-p-n devices [147, 153], as cavity solitons in semiconductor microresonators [301, 302] or in the form of soliton pulsation in fiber lasers [213]. Unfortunately, to the authors knowledge up to now no characteristic scaling relation according to (3.39) was measured.

3.2.2.3 Perturbative approach on the level of the field equations

When one is interested in the evolution of order parameters related to continuous symmetries or in finding concrete values for the coefficients in the order parameter equations, it is often reasonable to start the perturbative analysis on the level of the field equations and the mode decomposition itself. We begin our treatment of this aspect using (3.23) as a starting point. The latter equation was split into fast and slow modes with large and small amplitudes, however the approach contained no quantitative statements on this issue. The key approach to this problem is usually to consider the system either below or only closely above a supercritical bifurcation point. For simplicity, we will assume that the bifurcation can be expressed through the change of one parameter σ (i.e. it is of codimension 1, which is the generic case), the reference solution is then given by $(\boldsymbol{q}_0, \sigma_0)$, where σ_0 marks the bifurcation point. We introduce a smallness parameter $\epsilon \ll 1$ that quantifies the deviation from the state of interest from this stationary state via the definition $\sigma = \sigma_0 + \epsilon\sigma_1 + \epsilon^2\sigma_2 + \ldots$. All quantities depending on $\boldsymbol{q}$ and σ will generally experience small deviations from the stationary values depending on $(\boldsymbol{q}_0, \sigma_0)$ and can hence be expanded in powers of ϵ. In particular we have

$$\boldsymbol{F}'_{\boldsymbol{q}_0}(\sigma) = \boldsymbol{F}'^{0}_{\boldsymbol{q}_0}(\sigma_0) + \epsilon \boldsymbol{F}'^{1}_{\boldsymbol{q}_0}(\sigma_0) + \ldots, \tag{3.40}$$

$$\boldsymbol{F}''_{\boldsymbol{q}_0}(\sigma) = \boldsymbol{F}''^{0}_{\boldsymbol{q}_0}(\sigma_0) + \epsilon \boldsymbol{F}''^{1}_{\boldsymbol{q}_0}(\sigma_0) + \ldots \tag{3.41}$$

The deformation of the LS from the stationary state can also be decomposed in ϵ, and we rewrite the solution of the system as

$$\boldsymbol{q}(\boldsymbol{x}, t) = \boldsymbol{q}_0(\boldsymbol{x}, \boldsymbol{c}) + \epsilon \boldsymbol{\alpha} \cdot \boldsymbol{\phi}(\boldsymbol{x}, \boldsymbol{c}) + \epsilon^2 \boldsymbol{r}(\boldsymbol{x}, t). \tag{3.42}$$

In this abbreviating notation, we have written the sum over the critical modes as a scalar product, and the non-critical modes have been lumped up into the summand $\boldsymbol{r}$

as their significance in the solution is low. As a last aspect, one may use the parameter ϵ to introduce different time scales by defining $T_i := \epsilon^i t$, $i \in \mathbb{N}_0$. Considering these time scales as independent, one generally has to assume that non-critical modes live on all time scales (i.e. $\boldsymbol{r} = \boldsymbol{r}(T_0, T_1, T_2, T_3)$) while depending on the problem under consideration, often special assumptions for the slow critical modes critical modes can be made (for example by taking $\boldsymbol{c}(t) = \boldsymbol{c}(T_1, T_2, T_3)$). The big advantage of the perturbative approach is that while from the general consideration (3.12) it is not directly clear up to which order nonlinear terms have to be considered, the precision of the multiscale expansion is determined by the orders of ϵ taken into account. Inserting all terms into the evolution equation (3.12), one obtains

$$\begin{aligned}\sum_{l=0}^{\infty} \epsilon^l \partial_{T_l}[\boldsymbol{q}_0 + \epsilon\boldsymbol{\alpha}\cdot\boldsymbol{\phi} + \epsilon^2\boldsymbol{r}] = \boldsymbol{F}(\boldsymbol{q}_0) + \boldsymbol{F}'^0_{\boldsymbol{q}_0}[\epsilon\boldsymbol{\alpha}\cdot\boldsymbol{\phi} + \epsilon^2\boldsymbol{r}] + \boldsymbol{F}''^0_{\boldsymbol{q}_0}[\epsilon\boldsymbol{\alpha}\cdot\boldsymbol{\phi} + \epsilon^2\boldsymbol{r}]^2 \\ + \epsilon\boldsymbol{F}'^1_{\boldsymbol{q}_0}(\sigma_0)[\epsilon\boldsymbol{\alpha}\cdot\boldsymbol{\phi} + \epsilon^2\boldsymbol{r}] + \epsilon\boldsymbol{F}''^1_{\boldsymbol{q}_0}(\sigma_0)[\epsilon\boldsymbol{\alpha}\cdot\boldsymbol{\phi} + \epsilon^2\boldsymbol{r}]^2 + \dots,\end{aligned} \tag{3.43}$$

where the dependencies on different time scales were not explicitly written out to preserve a certain overview. Eq. (3.43) is then sorted according to orders of ϵ and the resulting hierarchy is evaluated. Note that aiming to obtain a certain normal form, most works do not take the full expansion (3.43) into account, but already assume certain terms to vanish, to be irrelevant or scale just to appear in certain orders of ϵ. In particular, many summands in the second term of the formal calculation (3.28) appear in a higher order of ϵ and can thus potentially be eliminated in the calculation. The problem of the expansion is that the outcome of the calculation is sometimes rather hard to estimate a priori. We will consider two examples below, one of low and one of higher complexity.

Example 1: Spatial inhomogeneities

Many experimental systems face the problem of showing slight spatially inhomogeneously distributed parameters, for example due to material preparation, non-planar beam profiles etc. The system under consideration is thus almost translationally invariant with a slight perturbation depending on the spatial coordinates. Examples for concrete situations can be found for example in [303, 304] for a Fitzhugh-Nagumo type reaction diffusion systems with a special parameter choice (vanishing inhibitor diffusion constant). Examples from optics are dealt with in [305, 306], however it should be noted that in these works the phase invariance of the system is broken so that only one critical modes has to be considered (see below).

The problem of small additive inhomogeneities can be modeled by introducing a small perturbation in the general field equation:

$$\partial_t \boldsymbol{q} - \boldsymbol{F}(\boldsymbol{q}, \nabla, \int, \boldsymbol{\sigma}) = \epsilon \boldsymbol{I}(\boldsymbol{x}). \tag{3.44}$$

For $\epsilon = 0$, we assume the existence of a stable solution $\boldsymbol{q}_0$, in any case with translational invariance. In a first step, the LS is furthermore considered to exhibit rotational

symmetry, and ho hidden invariances (for example with respect to phase shifts etc) are supposed to be present. Then, $\boldsymbol{c} = \boldsymbol{p}$, i.e. the only slowly varying parameter is the position of the LS. The equation has to be projected onto the neutral modes of translation, and the only contribution to (3.43) on the right-hand side arises from $\boldsymbol{I}(\boldsymbol{x})$. As furthermore the coupling to other non-critical modes is of order $O(\epsilon^2)$ or higher, defining $\boldsymbol{\phi}^1_{0,\xi} = \partial_\xi \boldsymbol{q}_0$ we find

$$\partial_t p_\xi = \epsilon \langle \boldsymbol{\Phi}^1_{0,\xi}(\boldsymbol{p}) | \boldsymbol{I}(\boldsymbol{x}) \rangle, \quad \xi = x, y, \ldots, \tag{3.45}$$

meaning that generally, the LS will drift due to the inhomogeneity.

Considering as an illustration the reaction-diffusion system (2.19), for each spatial direction ξ the neutral modes at the position $\boldsymbol{p}$ are given by the derivative of the stationary solution in this direction, i.e. $\boldsymbol{\phi}^1_{0,\xi}(\boldsymbol{x}, \boldsymbol{p}) = \partial_\xi \boldsymbol{q}_0(\boldsymbol{x} - \boldsymbol{p}) = (\partial_\xi u_0, \partial_\xi v_0)(\boldsymbol{x} - \boldsymbol{p})$. From this also generally valid statement, one may find for the special system that the corresponding projector modes are (except for normalization) given by $\boldsymbol{\Phi}^1_{0,\xi}(\boldsymbol{x} - \boldsymbol{p}) = (\partial_\xi u_0, -\kappa_3 \tau \partial_\xi v_0)(\boldsymbol{x} - \boldsymbol{p})$ (see for example [96]). Eq. (3.45) thus tells us that when a gradient is applied in the ξ-direction to the u-component on a scale long compared to the width of the LS, the latter will start to drift up the gradient. In contrast, if a gradient is applied to an inhibitor component, the LS will drift downward the gradient. In particular, for a linear approximation in the form $\boldsymbol{I}(\boldsymbol{x}) = (a_u(\xi - p_0), a_v(\xi - p_0))$, the drift velocity is constant and can be determined analytically, yielding

$$c = \epsilon \frac{\int (a_u \xi \partial_\xi u_0 - a_v \xi \partial_\xi v_0) \mathrm{d}\boldsymbol{x}}{\int ((\partial_\xi u_0)^2 - \kappa_3 \tau (\partial_\xi v_0)^2) \mathrm{d}\boldsymbol{x}} = -\epsilon \frac{\int (a_u (u_0 - u_h) - a_v (v_0 - v_h)) \mathrm{d}\boldsymbol{x}}{\int ((\partial_\xi u_0)^2 - \kappa_3 \tau (\partial_\xi v_0)^2) \mathrm{d}\boldsymbol{x}}. \tag{3.46}$$

Here, u_h and v_h denote the homogeneous ground state. Note that this statement holds for $\tau\kappa_3 < 1$ and it was made use of the fact that the decay of the LS to the ground state is stronger than linear. The above relation shows that a simultaneous application of an appropriately chosen gradient in several components may even result in a standing trapped LS.

In the reaction-diffusion system under consideration the above results can be understood as follows. Let us assume that an increasing gradient is applied only to the activator component (Fig. 3.1a). Then, activator production is enhanced on the right hand side of the LS and reduced on the left hand side. As the inhibitor reacts quickly for stationary structures away from any bifurcation points, the overall amount of material on the left side is reduced, while on the right side material can spread further to the sides, which in combination results in an effective shift of the LS to the right. In contrast, the same gradient applied to the inhibitor (Fig. 3.1b) has the opposite effect. Inhibitor concentration is increased on the right and reduced on the left. Consequently, material concentration in generally diminished on the right, which on the left activator has the chance to increase, efficiently corresponding to a shift of the LS to the left.

In Fig. 3.1c, we compare our analytical predictions with solutions of the full field equation. To this end, we choose two cases with a LS starting in the origin (meaning $p_\xi(t = 0) = 0$). The first one corresponds to a linear gradient in the activator component with $\epsilon = 0.03$, $a_u = 1$, $a_v = 0$ (the parameters imply a gradient weakly varying in space with respect to the size of the LS). The second case shows a trapping event by an inhomogeneity and is given by $\epsilon = 0.01$ and $\boldsymbol{I}(\boldsymbol{x}) = (\sin(\xi/a_u), 0)$, $a_u = 0.015$. Note

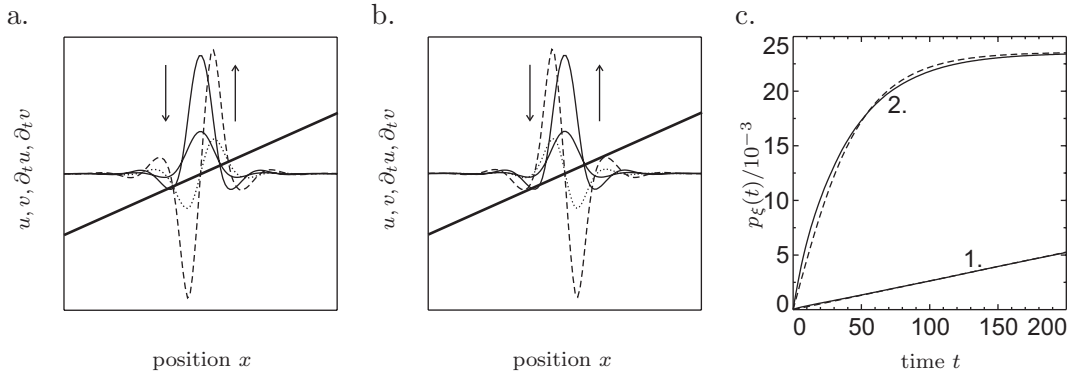

Figure 3.1: Drift of a LS as solution of the reaction-diffusion system (2.19) in parameter gradients: a. application of a linear gradient (thick solid line) to the LS (activator u and inhibitor v as thin solid lines). The arrows indicate the local change in the activator growth, while the dashed and dotted line shows the resulting overall change of activator and inhibitor, respectively. b. The same scenario with the inhomogeneity applied to the inhibitor component, the arrows indicate the change of inhibitor production, everything else as in (a.). c. Change of the position of the LS as a function of time according to the full field equations (solid line) and to the reduced equations (dashed lines) for the two spatial inhomogeneities (1. linear perturbation and 2. sinusoidal perturbation) as given in the text. Parameters: $\lambda = 0.71$, $d_u^2 = 1.1 \cdot 10^{-4}$, $d_v^2 = 9.64 \cdot 10^{-4}$, $\kappa_1 = -0.1$, $\kappa_3 = 1$, $\tau = 0.3$.

that in this case the gradient varies strongly on the typical length scale of a LS which lies in the range $l \approx 0.1$. In the second case no complete analytical solution is possible, but one may at least find the simplification

$$\partial_t p_\xi = \epsilon \frac{\int \sin(\xi/a_u)\partial_\xi u_0(\xi - p_\xi)\mathrm{d}\boldsymbol{x}}{\int((\partial_\xi u_0)^2 - \kappa_3\tau(\partial_\xi v_0)^2)\mathrm{d}\boldsymbol{x}} = -\frac{\epsilon}{a_u}\frac{\int(u_0 - u_h)\cos((\xi + p_\xi)/a_u)\mathrm{d}\boldsymbol{x}}{\int((\partial_\xi u_0)^2 - \kappa_3\tau(\partial_\xi v_0)^2)\mathrm{d}\boldsymbol{x}}. \tag{3.47}$$

In both cases there is an extremely good agreement between full and order parameter equations. The trapping site in the considered case is a consequence of the asymmetric critical eigenmode and the symmetry with respect to the trapping point. Also, from the figure one may see the overdamped character of the dynamics when the LS gets trapped by the oscillatory inhomogeneity.

When the structure under consideration contrary to our examples has no rotational symmetry although the system itself shows this symmetry, a rotational mode may also come into play. This is for example the case for deformed LSs or rigid molecules. In two spatial dimensions, the structure can then be additionally characterized by an angle θ (i.e. $\boldsymbol{q}_0 = \boldsymbol{q}_0(\boldsymbol{x}, \boldsymbol{p}, \theta)$) for which we have an additional equation analogous to (3.45). Consequently, the structure may propagate and rotate at the same time.

Finally, a generalization of the above considerations to other "non-additive" inhomogeneities is rather straightforward. One may for example consider a stationary LS in the inhomogeneous reaction-diffusion system

$$\partial_t \boldsymbol{q} = \nabla \cdot (\underline{\boldsymbol{D}}_0 + \epsilon \underline{\boldsymbol{D}}_1(\boldsymbol{x}))\nabla \boldsymbol{q} + \boldsymbol{R}_0(\boldsymbol{q}) + \epsilon \boldsymbol{R}_1 \boldsymbol{q} \tag{3.48}$$

where $\boldsymbol{R}_1$ is assumed to be a linear operator resulting as lowest order term from a perturbative expansion as given by (3.42). Then, the lowest nontrivial order in ϵ yields

$$\partial_t p_\xi = \epsilon \langle \boldsymbol{\Phi}^1_{0,\xi}(\boldsymbol{x},\boldsymbol{p}) | \underline{\boldsymbol{D}}_1(\boldsymbol{x}) \Delta \boldsymbol{q}_0 + \nabla \cdot \underline{\boldsymbol{D}}_1(\boldsymbol{x}) \nabla \boldsymbol{q}_0 + \boldsymbol{R}_1 \boldsymbol{q}_0 \rangle. \tag{3.49}$$

The presented argumentation is applicable in a lot of different systems. In optical systems, the phase of the solution generally plays an important role and is naturally influenced by inhomogeneities as well. In this case, for a LS of the form $q_0(\boldsymbol{x}) = |q_0(\boldsymbol{x})| \exp(i\theta)$ the order parameters are $\boldsymbol{c}_0 = \boldsymbol{p}$ and $c_1 = \phi$, and aside from the nondegenerate translational eigenmodes $\phi^1_{0,\xi} = \partial_\xi q_0$ a second type of nondegenerate critical eigenmode having the form $\phi^1_1 = \partial_\phi q_0 = i q_0$ becomes relevant. It is orthogonal to the Goldstone modes so that the dynamics of position and phase do not couple in a low-order approximation and one obtains

$$\begin{aligned} \partial_t p_\xi &= \epsilon \langle \Phi^1_{0,\xi}(\boldsymbol{p},\theta) | I(\boldsymbol{x}) \rangle, \quad \xi = x, y, \ldots, \\ \partial_t \theta &= \epsilon \langle \Phi^1_1(\boldsymbol{p},\theta) | I(\boldsymbol{x}) \rangle, \quad \xi = x, y, \ldots, \end{aligned} \tag{3.50}$$

To the authors knowledge there is currently no treatment of this case in the literature, which may be due to the fact that the projector mode for the angle is hard to find analytically and can only be obtained numerically (e.g by using a shooting method when the asymptotic decay to the ground state is known).

In the experiment, a drift of LSs in gradients was reported in a large number of systems. Examples include semiconductor microresonators and VCSELs [302, 307–309], saturable absorbers in resonator setups [180, 310], liquid crystal light valves [311], single mirror feedback set-ups [3] and oscillons in vibrated granular media [4]. External gradients have been used to trap LSs at well-defined positions to use them or optical

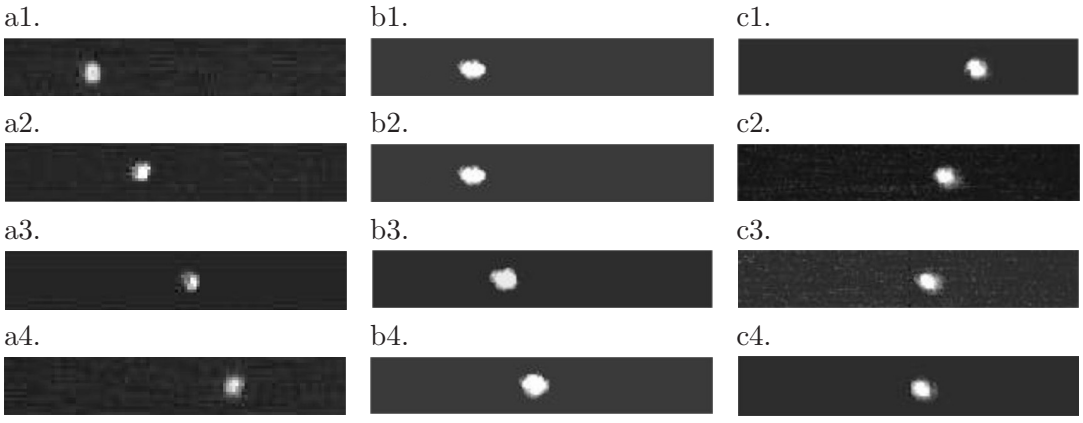

Figure 3.2: Drift of LSs in spatial gradients experimentally observed in pumped optical cavities with saturable absorber. The sequence in a. corresponds to a motion with constant velocity obtained by detuning the resonator mirrors, the time interval between successive images is $\Delta t = 6\,\mathrm{s}$. Sequences b. and c. were obtained by moving one of the resonator lenses creating a trapping site in the middle of the images, here $\Delta t = 3\,\mathrm{s}$. The width of all images corresponds to $l = 6\,\mathrm{mm}$.

data processing and logic operations [308, 309, 312]. The author himself has carried out (unpublished) work in planar gas-discharge systems with high-ohmic barrier in which via external illumination with visible light a checkerboard modulation could be induced in the high-ohmic electrode so that LSs could be trapped in the areas of low resistivity. Furthermore, a local excitation by laser light could be used to guide the individual LSs from one trapping site to another. In Fig. 3.2 we show observations of drifting LSs in a saturable absorber set-up from [180, 302]: the first line shows a sequence of a LS drifting with constant velocity along a gradient just as for the reaction-diffusion example (3.46). The other two lines show trapping events with a trapping site in the center of the images in analogy to (3.47).

Example 2: Drift bifurcation

Our second example deals with a bifurcation from standing to moving LSs. A supercritical realization of a drift bifurcation can be obtained in reaction-diffusion systems like the three-component system (2.26). Here, the transition from standing to moving LSs can be induced by making at least one component slow, for example by increasing the corresponding time constants τ or θ. The first derivation of a reduced description in such systems was done for moving fronts by Bode et al. [278, 303] for a special limiting case (vanishing inhibitor diffusion). Later on an extension to a three component system and LSs was done, again for a special limiting case so that the system could be rewritten as a two-component system with integral coupling [58]. A more general approach was proposed by Moskalenko [313] which however relied on a special decomposition of the linearized operators. In the same way, a description of breathing LSs was derived [314]. Here, we want to use the generally valid approach (3.43) as a starting point for the analysis. Considering the time constants of the reaction-diffusion system as bifurcation parameters, the general system (3.10) takes the more simple form

$$\partial_t \boldsymbol{q} = \underline{\boldsymbol{M}}(\sigma)\boldsymbol{F}(\boldsymbol{q}, \nabla), \tag{3.51}$$

if none of the time constants becomes zero, i.e. the left hand side factorizes into a parameter- and a derivative-dependent part. In the drift bifurcation, the critical eigenmodes $\boldsymbol{\phi}$ appearing in the bifurcation are the generalized eigenmodes of the neutral modes of translation. We hence assume $\boldsymbol{c} = \boldsymbol{p}(T_1, T_2, \ldots)$ (i.e. $\boldsymbol{q}(\boldsymbol{x}, \boldsymbol{c}) = \boldsymbol{q}(\boldsymbol{x} - \boldsymbol{p})$), meaning that the position of the structure changes just on slow timescales. First, we address the case that the stationary state has no special symmetry properties as then only one generalized eigenmode has to be considered. It belongs to a neutral mode in a certain direction ξ, and we define $\boldsymbol{\phi}^1_{0,\xi} := \partial_\xi \boldsymbol{q}_0$ so that the generalized eigenmode is $\boldsymbol{\phi}^2_{0,\xi}$. Both the amplitude α for $\boldsymbol{\phi}^2_{0,\xi}$ and the remainder term $\boldsymbol{r}$ are initially assumed to have a dynamics on all timescales. The eigenvalues of the modes corresponding to the orthogonal directions are assumed to be far enough away from the imaginary axis so that they do not become relevant for the dynamics even when increasing the relevant parameters above the bifurcation point for the critical mode. Then the evolution equation in the

perturbative expansion (3.43) reads

$$\begin{aligned}
&\sum_{l=0}^{\infty} \epsilon^l \partial_{T_l}[\boldsymbol{q}_0 + \epsilon\alpha\boldsymbol{\phi}_{0,\xi}^2 + \epsilon^2\boldsymbol{r}] \\
&= \Big(\underline{\boldsymbol{M}}^0 + \epsilon\underline{\boldsymbol{M}}^1 + \epsilon^2\underline{\boldsymbol{M}}^2\Big)\Big(\boldsymbol{F}(\boldsymbol{q}_0) + \boldsymbol{F}'[\epsilon\alpha\boldsymbol{\phi}_{0,\xi}^2 + \epsilon^2\boldsymbol{r}] \\
&+ \frac{1}{2}\epsilon^2\alpha^2\boldsymbol{F}'' : \boldsymbol{\phi}_{0,\xi}^2 : \boldsymbol{\phi}_{0,\xi}^2 + \frac{1}{6}\epsilon^3\alpha^3\boldsymbol{F}''' : \boldsymbol{\phi}_{0,\xi}^2 : \boldsymbol{\phi}_{0,\xi}^2 : \boldsymbol{\phi}_{0,\xi}^2 + \epsilon^3\alpha\boldsymbol{F}'' : \boldsymbol{\phi}_{0,\xi}^2 : \boldsymbol{r}\Big).
\end{aligned} \tag{3.52}$$

Here, all expressions contributing at least one term up to third order have been taken into account. In particular, we have expanded the matrix of time constants $\underline{\boldsymbol{M}}(\sigma)$ in terms of ϵ, where ϵ is a measure for the distance from the bifurcation point. Generically, one would thus assume $\sigma = \epsilon\hat{\sigma} - \sigma_0$, $\underline{\boldsymbol{M}}^n = \hat{\sigma}^n \partial_\sigma^n \, \underline{\boldsymbol{M}}(\sigma)|_{\sigma=\sigma_0}$. We will return to this aspect in more detail further below.

Evaluating the zeroth order of (3.52) yields the equation for the stationary solution. The first order equation is

$$\begin{aligned}
&-(\partial_{T_1} p_\xi)\boldsymbol{\phi}_{0,\xi}^2 + (\partial_{T_0}\alpha)\boldsymbol{\phi}_{0,\xi}^2 = \alpha\underline{\boldsymbol{M}}_0[\boldsymbol{F}'\boldsymbol{\phi}_{0,\xi}^2 + \underline{\boldsymbol{M}}_1\boldsymbol{F}'\boldsymbol{q}_0] \\
&\Longrightarrow \quad (\partial_{T_1} p_\xi)\boldsymbol{\phi}_{0,\xi}^1 - (\partial_{T_0}\alpha)\boldsymbol{\phi}_{0,\xi}^2 = -\alpha\boldsymbol{\phi}_{0,\xi}^1
\end{aligned} \tag{3.53}$$

From this, using suitable projections we obtain the important result $\partial_{T_0}\alpha = 0$ and hence $\partial_{T_1} p_\xi = -\alpha$. In the second order, we have

$$\begin{aligned}
&-(\partial_{T_2} p_\xi)\boldsymbol{\phi}_{0,\xi}^1 + (\partial_{T_1}\alpha)\boldsymbol{\phi}_{0,\xi}^2 - \alpha(\partial_{T_1} p_\xi)(\partial_\xi\boldsymbol{\phi}_{0,\xi}^2) + \partial_{T_0}\boldsymbol{r} \\
&= \underline{\boldsymbol{M}}_0(\boldsymbol{F}'\boldsymbol{r} + \frac{1}{2}\alpha^2\boldsymbol{F}'' : \boldsymbol{\phi}_{0,\xi}^2 : \boldsymbol{\phi}_{0,\xi}^2) + \alpha\underline{\boldsymbol{M}}_1\boldsymbol{F}'\boldsymbol{\phi}_{0,\xi}^2 + \underline{\boldsymbol{M}}_2\boldsymbol{F}(\boldsymbol{q}_0).
\end{aligned} \tag{3.54}$$

Since $\boldsymbol{p}$ varies only slowly in time, we may use

$$\begin{aligned}
0 &= \partial_{T_0}\langle\boldsymbol{\Phi}_{0,\xi}^2|\boldsymbol{r}\rangle = \langle\partial_{T_0}\boldsymbol{\Phi}_{0,\xi}^2|\boldsymbol{r}\rangle + \langle\boldsymbol{\Phi}_{0,\xi}^2|\partial_{T_0}\boldsymbol{r}\rangle \\
&= -\langle\partial_{T_0}\boldsymbol{p}\cdot\nabla\boldsymbol{\Phi}_{0,\xi}^2|\boldsymbol{r}\rangle + \langle\boldsymbol{\phi}_{0,\xi}^2|\partial_{T_0}\boldsymbol{r}\rangle = \langle\boldsymbol{\Phi}_{0,\xi}^2|\partial_{T_0}\boldsymbol{r}\rangle
\end{aligned} \tag{3.55}$$

to eliminate the last term on the left hand side. The projection of the equation on the suitable modes for the α-component in this case gives us $\partial_{T_1}\alpha = k_1\alpha + k_2\alpha^2$, where we introduced the abbreviations

$$k_1 = \quad \langle\boldsymbol{\Phi}_{0,\xi}^2|\underline{\boldsymbol{M}}_1\boldsymbol{F}'\boldsymbol{\phi}_{0,\xi}^2\rangle, \tag{3.56}$$

$$k_2 = \quad \langle\boldsymbol{\Phi}_{0,\xi}^2|\underline{\boldsymbol{M}}_0\boldsymbol{F}'' : \boldsymbol{\phi}_{0,\xi}^2 : \boldsymbol{\phi}_{0,\xi}^2\rangle + \langle\boldsymbol{\Phi}_{0,\xi}^2|\partial_\xi\boldsymbol{\phi}_{0,\xi}^2\rangle. \tag{3.57}$$

All expressions from (3.55) which do not contribute to (3.56) and (3.57) vanish due to the orthogonality properties of the projector $\boldsymbol{\Phi}_{0,\xi}^2$. After returning to the original

timescales and rescaling $-\epsilon\alpha \to \alpha$ with $\epsilon = \sigma - \sigma_0$, we directly obtain the normal form of the bifurcation which reads

$$\begin{aligned} \partial_t p_\xi &= \alpha \\ \partial_t \alpha &= (\sigma - \sigma_0) k_1 \alpha - k_2 \alpha^2. \end{aligned} \tag{3.58}$$

As we have found a complete description on the timescale T_1, quadratic terms in the scaling of the bifurcation parameter play no role in deriving the normal form of the bifurcation which is of transcritical type. Basically, it is also possible to consider a situation where the critical eigenvalues passing the imaginary axis lie very closely together, however in this situation the scalars will have to be replaced by appropriate tensors.

The result raises the question what happens if the stationary state shows additional symmetries which would for example be the case if we start with a LS showing point symmetry with respect to its center. As a consequence, the coefficient k_2 as defined in (3.57) vanishes for any direction one considers. This makes it necessary to take into account higher-order expressions in ϵ. The first and second order expansions stay the same as above while the third-order equation yields

$$\begin{aligned} &- (\partial_{T_3} p_\xi) \boldsymbol{\phi}^1_{0,\xi} + (\partial_{T_2} \alpha) \boldsymbol{\phi}^2_{0,\xi} - \alpha (\partial_{T_2} p_\xi)(\partial_\xi \boldsymbol{\phi}^2_{0,\xi}) + \partial_{T_1} \boldsymbol{r} \\ &= \alpha^3 \underline{\boldsymbol{M}}_0 (\frac{1}{6} \boldsymbol{F}''' : \boldsymbol{\phi}^2_{0,\xi} : \boldsymbol{\phi}^2_{0,\xi} : \boldsymbol{\phi}^2_{0,\xi} + \alpha \boldsymbol{F}'' : \boldsymbol{\phi}^2_{0,\xi} : \boldsymbol{r}) \\ &+ \underline{\boldsymbol{M}}_1 (\boldsymbol{F}' \boldsymbol{r} + \frac{1}{2} \alpha^2 \boldsymbol{F}'' : \boldsymbol{\phi}^2_{0,\xi} : \boldsymbol{\phi}^2_{0,\xi}) + \alpha \underline{\boldsymbol{M}}_2 \boldsymbol{F}' \boldsymbol{\phi}^2_{0,\xi}. \end{aligned} \tag{3.59}$$

The evolution of p_ξ on the time scale T_2 is obtained from (3.54) using the projector for the neutral eigenmode and the corresponding orthogonality relations,

$$\partial_{T_2} p_\xi = \alpha^2 \langle \boldsymbol{\Phi}^1_{0,\xi} | \partial_\xi \boldsymbol{\phi}^2_{0,\xi} \rangle - \frac{1}{2} \langle \boldsymbol{\Phi}^1_{0,\xi} | \underline{\boldsymbol{M}}_0 \boldsymbol{F}'' : \boldsymbol{\phi}^2_{0,\xi} : \boldsymbol{\phi}^2_{0,\xi} \rangle - \alpha \langle \boldsymbol{\Phi}^1_{0,\xi} | \underline{\boldsymbol{M}}_1 \boldsymbol{F}' : \boldsymbol{\phi}^2_{0,\xi} \rangle \tag{3.60}$$

The first two terms on the right hand side vanish as they correspond to integrations over uneven functions, however the third term does generally not vanish unless $\underline{\boldsymbol{M}}_1$ vanishes. Coming to the evolution of α on the time scale T_2, we find

$$\begin{aligned} \partial_{T_2} \alpha = &\langle \boldsymbol{\Phi}^2_{0,\xi} | \partial_{T_1} \boldsymbol{r} \rangle + \frac{1}{6} \langle \boldsymbol{\Phi}^2_{0,\xi} | \underline{\boldsymbol{M}}_0 \boldsymbol{F}''' : \boldsymbol{\phi}^2_{0,\xi} : \boldsymbol{\phi}^2_{0,\xi} : \boldsymbol{\phi}^2_{0,\xi} \rangle - \alpha \langle \boldsymbol{\Phi}^2_{0,\xi} | \underline{\boldsymbol{M}}_1 \boldsymbol{F}' : \boldsymbol{\phi}^2_{0,\xi} \rangle \\ &+ \alpha \langle \boldsymbol{\Phi}^2_{0,\xi} | \underline{\boldsymbol{M}}_0 \boldsymbol{F}'' : \boldsymbol{\phi}^2_{0,\xi} : \boldsymbol{r} \rangle + \langle \boldsymbol{\Phi}^2_{0,\xi} | \underline{\boldsymbol{M}}_1 \boldsymbol{F}' : \boldsymbol{r} \rangle + \alpha \langle \boldsymbol{\Phi}^2_{0,\xi} | \underline{\boldsymbol{M}}_2 \boldsymbol{F}' : \boldsymbol{\phi}^2_{0,\xi} \rangle \end{aligned} \tag{3.61}$$

The third term on the left hand side of (3.59) does not contribute due to symmetry reasons, and analogously to (3.55) one may derive

$$0 = \partial_{T_1} \langle \boldsymbol{\Phi}^2_{0,\xi} | \boldsymbol{r} \rangle = \alpha \langle \partial_\xi \boldsymbol{\Phi}^2_{0,\xi} | \boldsymbol{r} \rangle + \langle \boldsymbol{\Phi}^2_{0,\xi} | \partial_{T_1} \boldsymbol{r} \rangle \tag{3.62}$$

The remaining problem is to express $\boldsymbol{r}$ by critical modes. To this end, one may reconsider (3.54) and insert the expressions we have derived above:

$$\begin{aligned}&\underline{\boldsymbol{M}}_0\boldsymbol{F}'\boldsymbol{r} - \partial_{T_0}\boldsymbol{r}\\ =&\alpha(\langle\boldsymbol{\Phi}^1_{0,\xi}|\underline{\boldsymbol{M}}_1\boldsymbol{F}' : \boldsymbol{\phi}^2_{0,\xi}\rangle\boldsymbol{\phi}^1_{0,\xi} - \underline{\boldsymbol{M}}_1\boldsymbol{F}' : \boldsymbol{\phi}^2_{0,\xi}) + \alpha^2(\partial_\xi\boldsymbol{\phi}^2_{0,\xi} - \frac{1}{2}\underline{\boldsymbol{M}}_0\boldsymbol{F}'' : \boldsymbol{\phi}^2_{0,\xi} : \boldsymbol{\phi}^2_{0,\xi}).\end{aligned} \tag{3.63}$$

The only chance of solving this equation explicitly is by considering a situation in which $\boldsymbol{r}$ does not depend on T_0. As however $\partial_{T_0}\alpha = \partial_{T_0}p_\xi = 0$ and the remainder term consists of stable modes, one may assume that after a very short time $\boldsymbol{r}$ relaxes from any initial condition to a state in which there is only a dependence on the slower time scales of the dominant modes. In this case, the second term on the left hand side vanishes and one has an inhomogeneous time-independent equation to determine $\boldsymbol{r}$ from stable modes. An important aspect is that when solving (3.63) for $\boldsymbol{r}$ (which can be formally expressed by applying the inverse operator of $\underline{\boldsymbol{M}}_0\boldsymbol{F}'$ to the equation), $\boldsymbol{r}$ can be inserted in (3.61) and thus produces terms in second and third order in α so that the equation does not represent the normal form of the bifurcation (nevertheless the result is correct and contains just terms in p_ξ and α).

One may now try to transform the equation into normal form, but as a more simple solution to the problem one may note that all terms producing quadratic terms vanish if $\underline{\boldsymbol{M}}_1$ vanishes. As $\underline{\boldsymbol{M}}(\sigma)$ is a fixed given function, the only chance of eliminating $\underline{\boldsymbol{M}}_1$ is to change the scaling of the bifurcation parameter from $\sigma = \epsilon\hat{\sigma} - \sigma_0$ to $\sigma = \epsilon^2\hat{\sigma} - \sigma_0$. In this case, the first term in the regular Taylor expansion of $\underline{\boldsymbol{M}}(\sigma)$ is quadratic in ϵ (i.e. $\underline{\boldsymbol{M}}^2 = \hat{\sigma}\partial_\sigma\,\underline{\boldsymbol{M}}(\sigma)|_{\sigma=\sigma_0}$), and $\underline{\boldsymbol{M}}^1$ vanishes as there are only integer powers in a Taylor expansion. With $\boldsymbol{S}$ denoting the solution of (3.63) for $\underline{\boldsymbol{M}}^1$, collecting all terms and performing the same scalings as in the transcritical case the final result is

$$\begin{aligned}\partial_t p_\xi &= \alpha\\ \partial_t\alpha &= (\sigma - \sigma_0)k_1\alpha - k_3|\alpha|^2\alpha,\end{aligned} \tag{3.64}$$

with k_1 according to (3.56) and

$$k_3 = \langle\partial_\xi\boldsymbol{\Phi}^2_{0,\xi}|\boldsymbol{S}\rangle - \frac{1}{6}\langle\boldsymbol{\Phi}^2_{0,\xi}|\underline{\boldsymbol{M}}_0\boldsymbol{N}''' : \boldsymbol{\phi}^2_{0,\xi} : \boldsymbol{\phi}^2_{0,\xi} : \boldsymbol{\phi}^2_{0,\xi}\rangle + \langle\boldsymbol{\Phi}^2_{0,\xi}|\boldsymbol{N}'' : \boldsymbol{\phi}^2_{0,\xi} : \boldsymbol{S}\rangle. \tag{3.65}$$

This result agrees with the findings of Moskalenko [313]. As all directions ξ are equal for a rotationally symmetric structure, one may also replace the scalar variables p_{xi} and α with vector variables $\boldsymbol{p}$ and $\boldsymbol{\alpha}$, respectively.

Looking back at the scaling problem, we may note that when deriving a reduced equation of the general form

$$\partial_t a = \epsilon a + N(a) = c_2a^2 + c_3a^3 + \dots, \tag{3.66}$$

in order form the derivation to remain valid one has to require $\epsilon a \approx N(a)$. Generically $c_2 \neq 0$ and one finds $\epsilon \sim a$ as in the transcritical case. When for symmetry reasons however $c_2 = 0$, the characteristic scaling is $\sqrt{\epsilon} \sim a$.

As we will need a explicitly treatable example when coming to the weak interaction of LSs below, we will make a connection between the general theory and a special case of the concrete system (2.26), namely $d_v = 0$, $\theta = 0$, which was analyzed in [58]. In this case, the three-component system can be transformed into a two-component system with integral coupling, namely

$$\begin{aligned} \partial_t u &= Lu + n(u) \quad -\kappa_3 v, \\ \tau \partial_t v &= \qquad u \qquad\quad -v \end{aligned} \tag{3.67}$$

where we have used the definitions

$$Lu = d_u^2 \Delta u - \int_\Omega G(\boldsymbol{x} - \boldsymbol{x}') u(\boldsymbol{x}') \mathrm{d}^n x' + f'(u_h) u, \tag{3.68}$$

$$n(u) = f(u + u_h) - f(u_h) - f'(u_h) u \tag{3.69}$$

Here, u_h is the homogeneous ground state and G is the Green function for the Laplace operator on the domain under consideration (compare also the explanation in relation to Eq. (2.27)). In the reduced system no time constants vanish any more and explicit expressions for the generalized eigenmodes are available. Furthermore, the system has radially symmetric stationary solutions so that we have to calculate k_1 and k_3. As θ has been fixed in the three-component system, τ must become bifurcation parameter. One may then quickly check that the relevant modes in the spatial direction ξ (except for normalization) are given by

$$\boldsymbol{\phi}^1_{0,\xi} = \begin{pmatrix} \partial_\xi u_0 \\ \partial_\xi u_0 \end{pmatrix}, \qquad \boldsymbol{\phi}^2_{0,\xi} = \begin{pmatrix} 0 \\ -\partial_\xi \frac{u_0}{\kappa_3} \end{pmatrix}, \tag{3.70}$$

$$\boldsymbol{\Phi}^1_{0,\xi} = \begin{pmatrix} \partial_\xi \frac{u_0}{\kappa_3} \\ 0 \end{pmatrix}, \qquad \boldsymbol{\Phi}^2_{0,\xi} = \begin{pmatrix} \partial_\xi u_0 \\ -\partial_\xi u_0 \end{pmatrix}. \tag{3.71}$$

With this expressions and τ_c denoting the value of τ where the bifurcation takes place, according to (3.56) we have

$$k_1 = \frac{\langle \begin{pmatrix} \partial_\xi u_0 \\ -\partial_\xi u_0 \end{pmatrix} | \begin{pmatrix} 0 & 0 \\ 0 & -\frac{1}{\tau_c^2} \end{pmatrix} \begin{pmatrix} 1 & 0 \\ 0 & \tau_c \end{pmatrix} \begin{pmatrix} \partial_\xi u_0 \\ \partial_\xi u_0 \end{pmatrix} \rangle}{\langle \begin{pmatrix} \partial_\xi u_0 \\ -\partial_\xi u_0 \end{pmatrix} | \begin{pmatrix} 0 \\ -\partial_\xi \frac{u_0}{\kappa_3} \end{pmatrix} \rangle} = \kappa_3^2. \tag{3.72}$$

The more complex calculation of k_3 also becomes rather simple as the generalized neutral eigenmode has a zero in its first component, which is related to the fact that a nonlinearity is present only in the u-equation of (3.67). First, Eq. (3.63) can directly be solved, yielding $\boldsymbol{A} = (0, \partial_{\xi\xi} u_0 / \kappa_3^2)$. Furthermore, only the first summand on the r.h.s.

of (3.65) yields a contribution to k_3, the other ones vanish. The result is

$$k_3 = \frac{\langle \begin{pmatrix} \partial_{\xi\xi} u_0 \\ -\partial_{\xi\xi} u_0 \end{pmatrix} | \begin{pmatrix} 0 \\ \partial_{\xi\xi} \frac{u_0}{\kappa_3^2} \end{pmatrix} \rangle}{\langle \begin{pmatrix} \partial_{\xi} u_0 \\ -\partial_{\xi} u_0 \end{pmatrix} | \begin{pmatrix} 0 \\ -\partial_{\xi} \frac{u_0}{\kappa_3} \end{pmatrix} \rangle} = \frac{1}{\kappa_3} \frac{\langle (\partial_{\xi\xi} u_0)^2 \rangle}{\langle (\partial_{\xi} u_0)^2 \rangle}, \tag{3.73}$$

so that combining all expressions yields

$$\begin{aligned} \partial_t \boldsymbol{p} &= \boldsymbol{\alpha} \\ \partial_t \boldsymbol{\alpha} &= (\tau - \tau_c)\kappa_3^2 \boldsymbol{\alpha} + \frac{\langle (\partial_{\xi\xi} u)^2 \rangle}{\kappa_3 \langle u_{1,\xi}^2 \rangle} |\boldsymbol{\alpha}_i|^2 \boldsymbol{\alpha}_i. \end{aligned} \tag{3.74}$$

Note that the central problem for the treatment of (2.26) when going away from the choice $d_v = 0$, $\theta = 0$ lies in the analytical calculation of the generalized eigenmodes. This is related to the fact that the structure of the linearization operator $\boldsymbol{F}'$ greatly simplifies for the special case. On the other hand, independent of the simplification once the eigenmodes are known their equivalents for the adjoint operator $\boldsymbol{F}'^{\dagger}$ can always be given explicitly [96]. Consequently, concrete values for the coefficients in the general case can to be obtained by finding a numerical solution for $\boldsymbol{P}$

Experimentally, LSs traveling with a well-defined velocity have been observed in particular in electric transport systems, for example one-dimensional planar dc-discharges with high-ohmic barrier [32, 144–146] or p-n-p-n semiconductor devices [104, 106, 147, 148]. Other examples arise in chemical systems of reaction-diffusion type, for example as temperature pulses on catalytic surfaces [6, 139–141] or in excitable media filled into thin capillaries [137, 138]. Also examples in optics are known [315]. However, a transition from moving to traveling states was for a long time only known for spatially extended patterns including the Faraday instability [316], cellular flame patterns [317], the printers instability [318] and Rayleigh-Bénard convection [319]. For isolated LSs, to the authors knowledge the only drift bifurcation was observed for rotationally symmetric structures in planar dc and ac gas-discharge systems. Here, the deterministic dynamics is overlayed by strong fluctuations. While we will treat the aspect of fluctuation in much more detail in Sec. 3.4 and the following chapters, at this point we may state that in order to separate deterministic and stochastic parts of the motion of the LSs, the dynamics was generally assumed to be described by a stochastic Langevin equation

$$\partial_t \boldsymbol{p} = \boldsymbol{\alpha}, \qquad \partial_t \boldsymbol{\alpha} = h(\alpha)\frac{\boldsymbol{\alpha}}{\alpha} + R(\alpha)\boldsymbol{\Gamma}(t), \tag{3.75}$$

with $\boldsymbol{\Gamma}(t)$ representing normalized noise forces and unknown functions h and R. Both functions could be determined using stochastic analysis methods based on conditional averages without further assumptions [2, 157, 158], and it turned out that the cubic function (3.64) could always give a satisfying representation of the experimentally obtained values of $h(\alpha)$ in the dc case (compare Fig. 3.3a). In addition, by changing

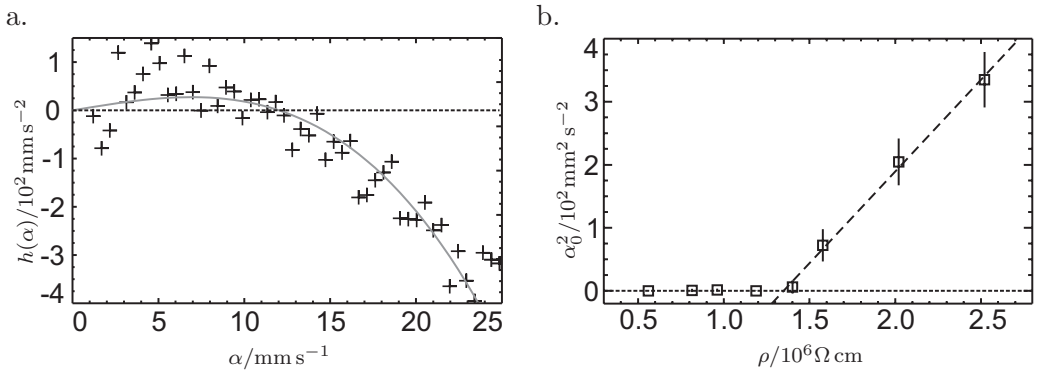

Figure 3.3: a. Experimentally determined function $h(\alpha)$ (compare (3.75)) from the dynamics of isolated LSs in planar dc gas-discharge systems with high-ohmic barrier found via the application of stochastic data analysis methods, the grey line is a fit according to the cubic polynomial from (3.64). b. Drift bifurcation of LS induced by varying the specific resistivity ρ of the semiconductor electrode. The square of the intrinsic velocity α_0 scales linearly with the bifurcation parameter. See [157, 158] for further details and parameters.

several system parameters a bifurcation from intrinsically standing to moving LSs could be induced in which the intrinsic velocity showed the theoretically expected square-root scaling with the bifurcation parameter (Fig. 3.3b). Similar observations were done in the planar ac-driven gas-discharge system except for the fact that no square-root scaling in the bifurcation parameter was found [320].

3.2.3 Normal forms for the dynamics of single LSs

From the above considerations, we have seen how to derive order parameter equations for single LSs which are capable of reflecting the important aspects of the dynamics in many circumstances. By reducing the dynamics to low-dimensional equations, an analysis is strongly facilitated as the number of slow order parameters is generically only small. We want to stress again that each continuous symmetry of a field equation under consideration generates a slow order parameter, independent of the special properties of the system under consideration. In addition, new slow modes can come into play if the system performs a bifurcation.

In low-dimensional systems, there are a number of normal form for supercritical bifurcations, which partly can be found for the dynamics of LSs as well. The most simple possible normal form describes the evolution of the scalar parameter α and reads

$$\partial_t \alpha = (\sigma - \sigma_0)\alpha + h(\alpha) \tag{3.76}$$

with $h(0) = h'(0) = 0$. As above, σ denotes a scalar bifurcation parameter, σ_0 marks the bifurcation point. When no special symmetries are present, the quadratic contribution of $h(\alpha)$ dominates close to the bifurcation point, however when $h(\alpha)$ is an odd function the quadratic contribution vanishes and generically the dominating term is cubic. While the scalar normal form (3.76) is frequently encountered for example for the amplitudes of supercritically generated spatially extended patterns [321], the author is not aware for

any examples concerning dynamic destabilizations of LSs. In contrast, the Hopf normal form

$$\partial_t A = (\sigma - \sigma_0)A + |A|^2 A \tag{3.77}$$

for the amplitude A is frequently found when considering for example breathing LSs and other periodic processes. Note that in neither (3.76) nor (3.77) the critical modes α and A may be given by continuous symmetry parameters. The reason for this is that as the dynamics is equivalent for all choices of the continuous symmetry parameters, the right hand side expressions of (3.76) and (3.77) can not contain these quantities explicitly.

A possible explanation for the fact that (3.76) is typically not encountered for LSs may lie in the fact that when a real eigenvalue passes the origin in a bifurcation, it coincidences with commonly present zero eigenvalues resulting from continuous symmetries. Although theoretically exceptions may be possible for special types of linear operators, in most cases it is found that in this situation the zero eigenvalue becomes degenerate. The corresponding normal form then reads

$$\begin{aligned} \partial_t \alpha_1 &= \alpha_2, \\ \partial_t \alpha_2 &= (\sigma - \sigma_0)\alpha_2 + h(\alpha_2). \end{aligned} \tag{3.78}$$

with h having the same properties as in (3.76). We have discussed a special realization above in the context of drift bifurcations. Basically, an interesting aspect is given by bifurcations of higher co-dimensionality, which is found for example when a drift- and a breathing instability coincidence. Unfortunately, such cases have not been discussed in the literature so far.

3.3 Interaction of structures

Generally, LSs may interact in complex ways involving many degrees of freedom. The concept of order parameters we are currently discussing however relies on the fact that only a few quantities evolve slowly dominating the dynamics of the whole system. In the context of single LSs, in order to derive equations we had to assume that either in the parameter range of interest the changes in the shape of the LSs could be characterized by a few parameters or alternatively and more generally applicable that the deformations are only small compared to the structure itself. Basically, these ideas also apply when making an extension to several interacting LSs. In nonlinear field equations, the influence of one LS on another is based on the fact that the superposition of two solutions generally generates no new solution but induces a dynamic change of the state of the system. A conceptually important case which often allows for an analytical treatment case is that of weak interaction, meaning that the overlap of the structures is so small that they stay essentially preserved in the course of the dynamics and that the change of their shape is again small compared to themselves. This of course excludes processes like generation and annihilation of LSs from the description.

Basically, the above introduced classification according to trial function and projection-based methods can also be applied for interaction processes of LSs. We will thus consider briefly the trial-function based approach before coming to projection-based techniques.

3.3.1 Weak interaction and trial-function methods

For classical soliton equations, inverse scattering transforms were the method of choice to deal with the interaction of LSs. However, when considering perturbed versions of these equations, the direct applicability of inverse scattering mathods is rather limited [322, 323]. One of the first solutions to this problem was proposed by Karpman and Solov'ev [324]. The central idea is that appropriately parameterized trial functions should enter the inverse scattering technique in order to obtain approximate evolution equations for the parameters. As an advantage, it is not necessary to claim that the trial functions always exactly fulfil the evolution equation, examples can be found in [215, 280, 281]. A second approach is to find a Lagrangian or Hamiltonian formulation for the evolution equation, so that the original problem becomes related to a variational principle [282–285]. Typically, a linear superposition of a two or n single localized solutions is inserted into the new evolution equation in order to obtain the order parameter equations. For instance, one may insert a parameterized solution $q_1 + q_2$ into the Hamiltonian $H(q)$ and decompose the result as

$$H(q_1 + q_2) = H(q_1) + H(q_2) + H_{\text{int}}, \tag{3.79}$$

where H_{int} is now the interaction Hamiltonian from which the interaction potential can be determined. Weak dissipation may be taken into account by modifying the trial function in an appropriate way. In this case, in a first approximation only the tails of the LSs are affected, while is reflected for example by oscillations in space. The calculation scheme (3.79) is then applied to the dominant conservative part of the equation [216, 286, 287]. In particular, for large distances of the LSs a repulsive interaction for the purely conservative case may turn to a mixed attractive-repulsive interaction via the dissipative contributions, thereby allowing for the formation of bound states of LSs.

A alternative to the above approach is to use existing integral evolution equations for momentum, energy etc. instead of the Lagrangian evolution equation [39, 288]. Note that all techniques presented here rely on the relation of the evolution of the evolution equation to a classical soliton equation.

3.3.2 Weak interaction and projection methods

In the context of single LSs projection-based methods provide access to systems even if no relation to classical equations exists. The underlying basic strategy remains the same when treating interaction phenomena: dividing the changes in the shape of the structure into fast and slow modes and projecting out the relevant information. For single LSs, the central problem was to carry out projections onto a nonlinear function $\boldsymbol{F}(\boldsymbol{q})$ where $\boldsymbol{q}$ was a sum of modes. For two or more LSs, am aspect of major importance is thus an appropriate decomposition of the nonlinearity acting on the overlapping LSs in order to make a connection to the theory of isolated LSs. In the following, we will only treat "weak interaction" meaning that he overlap of the LSs is not too large and they mainly retain their shape in the course of time. Then, the state of the system differs from the simple superposition of two stationary solutions only in a small function $\boldsymbol{r}$. The goal of

the following section is to develop a decomposition

$$\boldsymbol{F}(\boldsymbol{q}_1 + \boldsymbol{q}_2 + \boldsymbol{r}) = \boldsymbol{F}(\boldsymbol{q}_1) + \boldsymbol{F}(\boldsymbol{q}_2) + \boldsymbol{R} \tag{3.80}$$

where $\boldsymbol{R}$ is again small, and in particular to develop approximate, practically usable expressions for the function $\boldsymbol{R}$. It is then clear that the above results for single LSs can be applied to $\boldsymbol{F}(\boldsymbol{q}_1)$ and $\boldsymbol{F}(\boldsymbol{q}_2)$, and the interaction can be determined by treating $\boldsymbol{R}$.

Compared to a standard expansion, the problem of a decomposition as proposed in (3.80) is that both $\boldsymbol{q}_1$ and $\boldsymbol{q}_2$ have large amplitudes alone at different positions in space. To the authors knowledge, the problem was first dealt with by Elphick et al. who were interested in uniformly traveling pulse trains [289–291]. They proposed a solution motivated by the so-called tight-binding approximation in solid state physics which has afterwards been used by practically all authors dealing with weak interaction and projection methods, examples are given by [58, 59, 62, 217, 293, 294]. The key idea is to use a single unperturbed LS whose dynamics is to be evaluated as starting point and to expand operators applied to perturbed versions of the LS as Taylor expansion. Considering (3.80) and taking $\boldsymbol{q}_1$ as reference solution, the decomposition in this case reads

$$\boldsymbol{F}(\boldsymbol{q}_1 + \boldsymbol{q}_2 + \boldsymbol{r}) = \boldsymbol{F}(\boldsymbol{q}_1) + \boldsymbol{F}'(\boldsymbol{q}_1)[\boldsymbol{q}_2 + \boldsymbol{r}] + \ldots, \tag{3.81}$$

higher orders are commonly not taken into account. The projectors used for the problem are the same as for the isolated LSs. While the use of (3.81) has produced reasonable results (at least when a comparison of full and reduced equations was done, see for example [58]), there are two problems arising. First, the solution around which the operator $\boldsymbol{F}$ is expanded should be large compared to the perturbation so that subsequent terms of the series decrease in size. This certainly holds in the center of $\boldsymbol{q}_1$, but not in between the LSs where $\boldsymbol{q}_1$ and $\boldsymbol{q}_2$ are of equal amplitude. Second, when $\boldsymbol{F}$ becomes linear the interaction terms should vanish in any order of the expansion which is definitely not the case for (3.81).

In order to overcome the problem, we develop a "three-point expansion" as shown in the following. Let us assume that the overlap of the LSs can be described as

$$\boldsymbol{F}(\boldsymbol{q}_1 + \boldsymbol{q}_2) = \boldsymbol{F}(\boldsymbol{q}_1) + \boldsymbol{F}(\boldsymbol{q}_2) - \boldsymbol{F}(\boldsymbol{0}) + O(\epsilon), \tag{3.82}$$

where the smallness parameter ϵ characterizes the weak nonlinear superposition determined by the shape and the distance of the LSs. As the desired expansion should work similar to a classical Taylor expansion, one may symmetrize terms from the Taylor expansion as

$$\begin{aligned}
\boldsymbol{T}_0 &= \boldsymbol{F}(\boldsymbol{q}_1) + \boldsymbol{F}(\boldsymbol{q}_2), \\
\boldsymbol{T}_1 &= \boldsymbol{F}'(\boldsymbol{q}_1)\boldsymbol{q}_2 + \boldsymbol{F}'(\boldsymbol{q}_2)\boldsymbol{q}_1, \\
\boldsymbol{T}_2 &= \frac{1}{2}\boldsymbol{F}''(\boldsymbol{q}_1) : \boldsymbol{q}_2 : \boldsymbol{q}_1 + \frac{1}{2}\boldsymbol{F}''(\boldsymbol{q}_2) : \boldsymbol{q}_1 : \boldsymbol{q}_1,
\end{aligned}$$

etc. Each term in $\boldsymbol{T}_n$ contains either n vectors from $\boldsymbol{q}_1$ or $\boldsymbol{q}_2$. The Tailor expansion of $\boldsymbol{F}(\boldsymbol{q}_1+\boldsymbol{q}_2)$ around $\boldsymbol{0}$, i.e., far from the both LSs, should also contain only symmetrical combinations of $\boldsymbol{q}_1$ or $\boldsymbol{q}_2$. Combining terms containing p fields with $\boldsymbol{q}_1$ and q fields $\boldsymbol{q}_2$ such that $\max(p,q)=n$, we can introduce "correction fields" $\boldsymbol{g}_n$, defined as

$$\begin{aligned}
\boldsymbol{g}_0 &= \boldsymbol{F}(\boldsymbol{0}),\\
\boldsymbol{g}_1 &= \boldsymbol{F}'(\boldsymbol{0})\boldsymbol{q}_1 + \boldsymbol{F}'(\boldsymbol{0})\boldsymbol{q}_2 + \boldsymbol{F}''(\boldsymbol{0}) : \boldsymbol{q}_1 : \boldsymbol{q}_2,\\
\boldsymbol{g}_2 &= \frac{1}{2}\boldsymbol{F}''(\boldsymbol{0}) : \boldsymbol{q}_1 : \boldsymbol{q}_1 + \frac{1}{2}\boldsymbol{F}''(\boldsymbol{0}) : \boldsymbol{q}_2 : \boldsymbol{q}_2 + \frac{1}{2}\boldsymbol{F}'''(\boldsymbol{0}) : \boldsymbol{q}_1 : \boldsymbol{q}_1 : \boldsymbol{q}_2\\
&\quad + \frac{1}{2}\boldsymbol{F}'''(\boldsymbol{0}) : \boldsymbol{q}_2 : \boldsymbol{q}_2 : \boldsymbol{q}_1 + \frac{1}{4}\boldsymbol{F}'''(\boldsymbol{0}) : \boldsymbol{q}_1 : \boldsymbol{q}_1 : \boldsymbol{q}_2 : \boldsymbol{q}_2,
\end{aligned}$$

and so on. With the above results, one finds that in each order of ϵ, the "three-point expansion"

$$\boldsymbol{F}(\boldsymbol{q}_1+\boldsymbol{q}_2) = (\boldsymbol{T}_0-\boldsymbol{g}_0) + \ldots + (\boldsymbol{T}_n-\boldsymbol{g}_n) + O(\epsilon^n) \tag{3.83}$$

is valid everywhere in space. Furthermore, we have a precise error estimation available if perturbation analysis is to be applied.

With (3.83) and the findings for single LSs, we can now write down the order parameter equations for interacting LSs. Using the notation from Eq. (3.22) with the abbreviation

$$\boldsymbol{q}_k(\boldsymbol{x},t) = \boldsymbol{q}_{0k}(\boldsymbol{x}, c_{k1}(t), c_{k2}(t), \ldots) + \boldsymbol{r}_k(\boldsymbol{x}, c_{k1}(t), c_{k2}(t), \ldots), \tag{3.84}$$

we insert the solution $\boldsymbol{q} = \boldsymbol{q}_{01} + \boldsymbol{q}_{02} + \boldsymbol{r}$ into the evolution equation, where we have defined $\boldsymbol{r} = \boldsymbol{r}_1 + \boldsymbol{r}_2$. The uniformly small rest term $\boldsymbol{r}$ can be expressed either through eigenmodes at the "coordinates" $\boldsymbol{c}_1$ or $\boldsymbol{c}_2$. In the first case, we have

$$\begin{aligned}
&-\partial_t \boldsymbol{c}_1 \cdot \nabla_{\boldsymbol{c}_1}\boldsymbol{q}_{01} - \partial_t \boldsymbol{c}_2 \cdot \nabla_{\boldsymbol{c}_2}\boldsymbol{q}_{02} + \sum_i \sum_j^{n(i)} \partial_t \gamma_{i1} \boldsymbol{\phi}_{i1}^j(\boldsymbol{x}, \boldsymbol{c}_1)\\
&= \boldsymbol{F}(\boldsymbol{q}_{01}+\boldsymbol{q}_{02}) + \boldsymbol{F}'(\boldsymbol{q}_{01}+\boldsymbol{q}_{02})\boldsymbol{r} + \ldots,
\end{aligned} \tag{3.85}$$

where the operator $\boldsymbol{F}$ is now expanded around $\boldsymbol{q}_{01}+\boldsymbol{q}_{02}$. On the right hand side, we have now the nonlinear superposition of the two unperturbed localized solutions for which we developed a method of decomposition above, which one may directly insert:

$$\begin{aligned}
&\boldsymbol{F}(\boldsymbol{q}_{01}+\boldsymbol{q}_{02}+\boldsymbol{r}) = \boldsymbol{F}(\boldsymbol{q}_{01}+\boldsymbol{q}_{02}) + \boldsymbol{F}'(\boldsymbol{q}_{01}+\boldsymbol{q}_{02})\boldsymbol{r} + \ldots\\
&= \boldsymbol{F}(\boldsymbol{q}_{01}) + \boldsymbol{F}(\boldsymbol{q}_{02}) + \boldsymbol{F}^I(\boldsymbol{q}_1)\boldsymbol{q}_2 + \boldsymbol{F}^I(\boldsymbol{q}_2)\boldsymbol{q}_1 + \boldsymbol{F}'(\boldsymbol{q}_{01})\boldsymbol{r} + \boldsymbol{F}'(\boldsymbol{q}_{02})\boldsymbol{r} - \boldsymbol{F}'(\boldsymbol{0})\boldsymbol{r} + \ldots
\end{aligned} \tag{3.86}$$

where the first order "interaction operator" $\boldsymbol{F}^I$ is defined via

$$\boldsymbol{F}^I(\boldsymbol{q}_1)\boldsymbol{q}_2 = \boldsymbol{F}'(\boldsymbol{q}_1)\boldsymbol{q}_2 - \boldsymbol{F}'(\boldsymbol{0})\boldsymbol{q}_2 - \frac{1}{2}\boldsymbol{F}''(\boldsymbol{0}) : \boldsymbol{q}_2 : \boldsymbol{q}_2. \tag{3.87}$$

Note that in (3.86), the operators resulting from Fréchet derivatives like $\boldsymbol{F}'(\boldsymbol{q}_{01}+\boldsymbol{q}_{02})$ are expanded the same way as $\boldsymbol{F}$ itself.

We want to illustrate what general results one may expect for the order parameter description of LSs before treating some special examples. To this end, let us assume that we are dealing with a case for which no degenerate eigenvalues appear in the spectrum of $\boldsymbol{F}'(\boldsymbol{q}_{0i})$ (with $i=1,2$) and there is only one critical eigenmode for each LS. The latter is likely to be connected to a continuous symmetry so that $\boldsymbol{q}_{0i}=\boldsymbol{q}_0(\boldsymbol{x},c_i)$. Focussing on the structure $\boldsymbol{q}_1$, one may express $\boldsymbol{r}$ in terms of uncritical eigenmodes belonging to this structure. We thus rewrite (3.86) as

$$\begin{aligned}&\partial_t\boldsymbol{r}+\partial_t c_1\partial_c\boldsymbol{r}(c_1)-\boldsymbol{F}'(\boldsymbol{q}_{01}+\boldsymbol{q}_{02})\boldsymbol{r}\\&=\partial_t\boldsymbol{r}+\partial_t c_1\partial_c\boldsymbol{r}(c_1)-\boldsymbol{F}'(\boldsymbol{q}_{01})\boldsymbol{r}-\boldsymbol{F}'(\boldsymbol{q}_{02})\boldsymbol{r}+\boldsymbol{F}'(\boldsymbol{0})\boldsymbol{r}\\&=+\boldsymbol{F}^I(\boldsymbol{q}_{01})\boldsymbol{q}_{02}+\boldsymbol{F}^I(\boldsymbol{q}_{02})\boldsymbol{q}_{01}-\partial_t c_1\partial_c\boldsymbol{q}_{01}-\partial_t c_2\partial_c\boldsymbol{q}_{02}.\end{aligned}\tag{3.88}$$

According to the Fredholm alternative, the equation is solvable if no resonant terms appear, meaning in particular that the projection of the left hand side onto $\langle\boldsymbol{\Phi}_0^1(c_1)|$ vanishes. As we have note yet made quantitative statements on the weakness of the interaction, we now want to specify that $\partial_t c_2\langle\boldsymbol{\Phi}_0^1(c_1)|\boldsymbol{\phi}_0^1(c_2)\rangle=O(\epsilon^2)$ which can for example be obtained by claiming $\partial_t c_2\sim\epsilon c_2$ and $\boldsymbol{q}_{01}\boldsymbol{q}_{02}\sim\epsilon$. Then, the first order result is

$$\partial_t c_1=\langle\boldsymbol{\Phi}_0^1(c_1)|\boldsymbol{F}^I(\boldsymbol{q}_{01})\boldsymbol{q}_{02}+\boldsymbol{F}^I(\boldsymbol{q}_{02})\boldsymbol{q}_{01}\rangle,\tag{3.89}$$

an analogous result can be obtained for the second LS as well.

Next, we consider the case of degeneracy when a second critical eigenmode for each critical mode appears. Then, the term $\boldsymbol{r}$ does not only consist of uncritical modes and can be written as $\boldsymbol{r}=\alpha_1(t)\boldsymbol{\phi}_0^2(c_1)+\alpha_2(t)\boldsymbol{\phi}_0^2(c_2)+\boldsymbol{R}$ with $\boldsymbol{R}$ now containing only uncritical modes. The argument with which the remainder terms have been eliminated in (3.88) can be extended to generalized eigenmodes [292] and thus be applied to remove terms in $\boldsymbol{R}$. As a result, we find

$$\begin{aligned}&\partial_t c_1+\partial_t c_1\alpha_1\langle\boldsymbol{\Phi}_0^1(c_1)|\partial_c\boldsymbol{\phi}_0^2(c_1)\rangle=\alpha_1+\langle\boldsymbol{\Phi}_0^1(c_1)|\boldsymbol{F}^I(\boldsymbol{q}_{01})\boldsymbol{q}_{02}+\boldsymbol{F}^I(\boldsymbol{q}_{02})\boldsymbol{q}_{01}\rangle,\\&\partial_t\alpha_1+\partial_t c_1\alpha_1\langle\boldsymbol{\Phi}_0^2(c_1)|\partial_c\boldsymbol{\phi}_0^2(c_1)\rangle=\langle\boldsymbol{\Phi}_0^2(c_1)|\boldsymbol{F}^I(\boldsymbol{q}_{01})\boldsymbol{q}_{02}+\boldsymbol{F}^I(\boldsymbol{q}_{02})\boldsymbol{q}_{01}\rangle.\end{aligned}\tag{3.90}$$

Note that in many examples (like the one on the NLS equation below), the product terms on the left-hand side as well as potentially some terms on the right-hand side vanish for symmetry reasons.

Our previous example on the active propagation of LSs shows that in some cases it is necessary to include higher order terms in the perturbation analysis. However, with (3.83) a precise estimate can be given which interaction terms have to be included in the analysis, and the perturbative expansion (3.52) can be generalized accordingly. Generally, the lowest order of the analysis in which interaction terms enter is n, defined by $\boldsymbol{q}_{01}\boldsymbol{q}_{02}\sim\epsilon^n$, so that the distance between the LSs is of essential importance. When the distance between the LSs is large and the interaction term (3.87) enters in the

highest order analyzed, the interaction terms are generally of central force nature. In the opposite case when the distance between the LSs becomes small and the interaction enters in low order, higher order terms may result in a coupling of force terms with other critical modes and hence destroy the central force nature of the interaction. However, as the corresponding terms result from the nonlinear superposition of small perturbations of the first LS with the second one or its perturbations, these contributions are much smaller than the main term.

3.3.3 Examples for interacting LSs

In the following, we will illustrate the general theory of weak interaction on several examples of increasing complexity.

Example 1: Cubic-quintic complex GL equation

In our first example, we consider the interaction of two stationary LSs in the one-dimensional cubic-quintic GL equation

$$\partial_t q = (d_r + id_i)\Delta q + l_r q + (c_r + ic_i)|q|^2 q + (q_r + iq_i)|q|^4 q \tag{3.91}$$

using the above introduced methods. As we need some stationary solutions as starting point and as the LSs are generically oscillating sinusoidally with a frequency ω, we will consider the equation in a co-rotating frame. We treat only stationary solutions with rotational symmetry and no topological charge (see [62] for an example with topological charge), so that the critical modes that have to be considered are the neutral modes in the direction of the connection line between the LSs (which we assume to point along the x-axis) and those corresponding to a phase-shift of the LSs. For reasons of simplicity we will furthermore only consider two equal LSs so that the relative phase difference does not change during interaction. Correspondingly, the only slow order parameter can be chosen to be the x-position $p_{i,x}$ of the LSs.

In order to deal with real operators, we will use a representation of the GL equation in real and imaginary part according to (2.40). The linearization $\boldsymbol{F}'$ of the operator $\boldsymbol{F}$ around a stationary solution (a_1, b_1) is determined then by the 2x2 matrix (F'_{ij}), where the matrix elements are given by

$$\begin{aligned}
F'_{11} &= d_r\partial_{xx} + l_r + c_r(a_1^2 + b_1^2) + 2a_1(c_r a_1 - c_i b_1) \\
&\quad + q_r(a_1^2 + b_1^2)^2 + 4a_1(a_1^2 + b_1^2)(q_r a_1 - c_i b_1), \\
F'_{12} &= -d_i\partial_{xx} + \omega - c_i(a_1^2 + b_1^2) + 2b_1(c_r a_1 - c_i b_1) \\
&\quad - q_i(a_1^2 + b_1^2)^2 + 4b_1(a_1^2 + b_1^2)(q_r a_1 - q_i b_1), \\
F'_{21} &= d_i\partial_{xx} - \omega + c_i(a_1^2 + b_1^2) + 2a_1(c_i a_1 + c_r b_1) \\
&\quad + q_i(a_1^2 + b_1^2)^2 + 4a_1(a_1^2 + b_1^2)(q_i a_1 + q_r b_1), \\
F'_{22} &= d_r\partial_{xx} + l_r + c_r(a_1^2 + b_1^2) + 2b_1(c_i a_1 + c_r b_1) \\
&\quad + q_r(a_1^2 + b_1^2)^2 + 4b_1(a_1^2 + b_1^2)(q_i a_1 + c_r b_1).
\end{aligned} \tag{3.92}$$

For the linearization operator, $\boldsymbol{F}'^{\dagger} = (F'_{ji})$. While the relevant neutral mode $\boldsymbol{\phi}_0^1$ for $\boldsymbol{F}'$ with respect to the LS number 1 are of course given by $(a_{1,x}, b_{1,x})$, it is not possible to give a related analytical expression for the neutral mode of the adjoint operator, which must directly be the correct projector mode as the problem is not degenerated. We will thus calculate it numerically by using a relaxation method, i.e. solving the equation $\partial_t \boldsymbol{\Phi}_0^1 = \boldsymbol{F}'^{\dagger} \boldsymbol{\Phi}_0^1$ for its stationary solution. As last ingredient, we need an expression for the interaction function. With the definition (3.87), one finds

$$\begin{aligned}
&F_a^I(a_1,b_1)[a_2,b_2] = [c_r(a_1^2+b_1^2) + 2a_1(c_r a_1 - c_i b_1) \\
&+ q_r(a_1^2+b_1^2)^2 + 4a_1(a_1^2+b_1^2)(q_r a_1 - q_i b_1)]a_2 \\
&+ [-c_i(a_1^2+b_1^2) + 2b_1(c_r a_1 - c_i b_1) \\
&- q_i(a_1^2+b_1^2)^2 + 4b_1(a_1^2+b_1^2)(q_r a_1 - q_i b_1)]b_2, \\
&F_b^I(a_1,b_1)[a_2,b_2] = [c_r(a_1^2+b_1^2) + 2b_1(c_i a_1 + c_r b_1) \\
&+ q_r(a_1^2+b_1^2)^2 + 4b_1(a_1^2+b_1^2)(q_i a_1 + q_r b_1)]b_2 \\
&+ [c_i(a_1^2+b_1^2) + 2a_1(c_i a_1 + c_r b_1) \\
&+ q_i(a_1^2+b_1^2)^2 + 4a_1(a_1^2+b_1^2)(q_i a_1 + q_r b_1)]a_2.
\end{aligned} \tag{3.93}$$

One may now choose a set of parameters and calculate the reduced equations, which are of the general form

$$\partial_t p_{i,x} = F(|p_i - p_j|)\frac{p_i - p_j}{|p_i - p_j|} \quad \text{with} \quad i,j = 1,2, i \neq j. \tag{3.94}$$

Structurally, this type of interaction law is also encountered for overdamped classical particles. An example for an interaction function in the one-dimensional case is shown in Fig. 3.4a on the left-hand side. As parameters, we have used $d_r = d_i = 0.5$, $l_r = q_r = q_i = -0.1$, $c_r = 0.52$, $c_i = 1$. One may test the correctness of the results by comparing the analytical predictions with simulations of the full GL equation. The positions of the LSs in the full equations can then be defined as corresponding centers of mass of the LS above a certain threshold. As the graph in the right-hand side of Fig. 3.4a shows, there is extremely good agreements of the results for different initial separations. Extending the analysis to more general situations, a relative phase difference of the LSs may be included in the calculation which becomes a second order parameter. This situation was analyzed for very weakly overlapping tails in [217], but no comparison with numerically obtained trajectories was given.

Example 2: Nonlinear Schrödinger equation

Although not a dissipative system, we will take a look at the 1D NLS equation (2.36) using a projection-based method as it shows some interesting properties like Galilean invariance and has a fully analytical solution. Previous works have dealt with this example using inverse scattering techniques. The treatment of the NLS equation can in some sense be considered as a special case of example 1 discussed above which one obtains by choosing almost all parameters as zero, except for $d_i = -1$, $c_i = -1$. We will

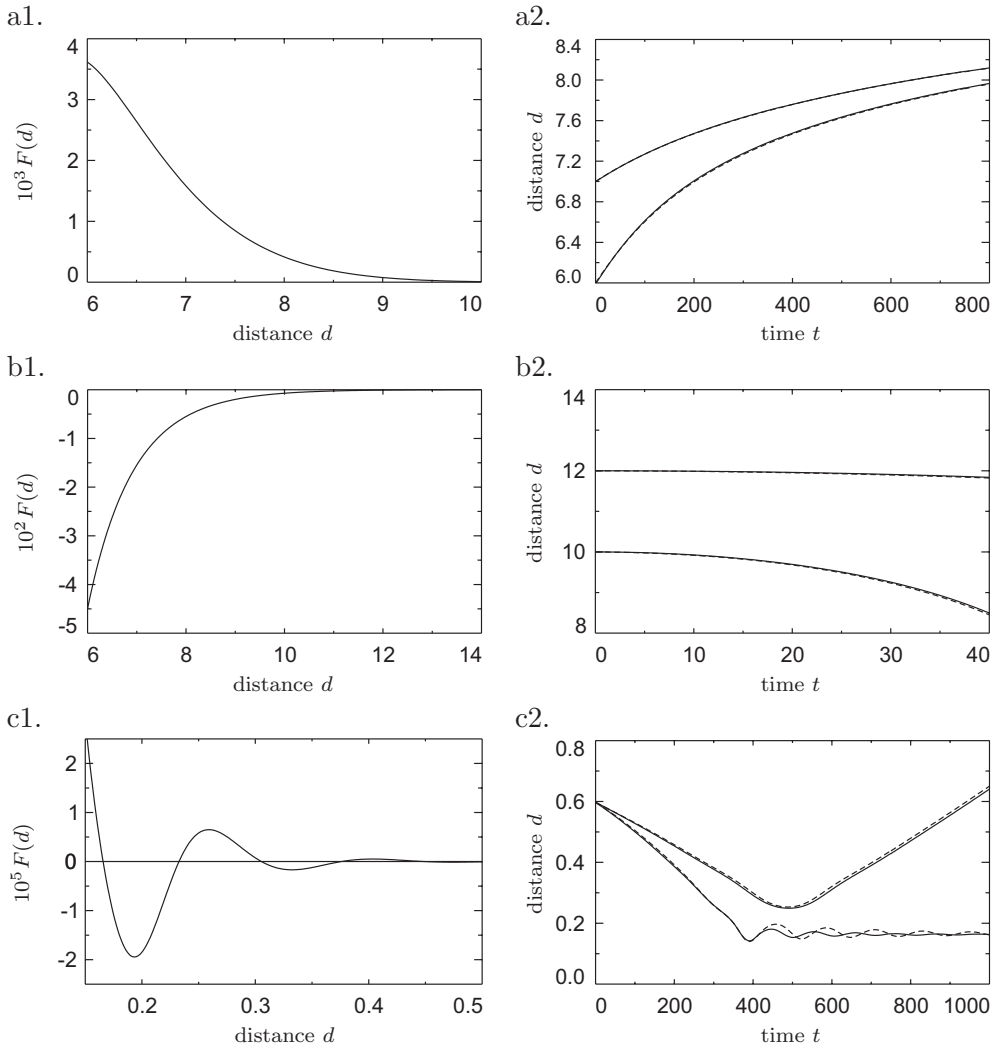

Figure 3.4: Interaction of LSs in the reduced description. The left hand images depict the function $F(d)$ while a comparison of the distance d of two interacting LSs as a function of time according to numerical simulations of the full field equations (solid line) and to the reduced equations (dashed line) is shown on the right. a. Two in-phase LSs in the one-dimensional GL equation for two different initial separations, b. two in-phase LSs in the one-dimensional NLS equation for two different initial separations, c. two LSs in the two-dimensional reaction-diffusion system (2.26) for $\tau = 3.35$ (scattering) and $\tau = 3.375$ (formation of a bound state). For parameters see text.

again consider only the case of interacting LSs with equal phase. The equation has the interesting property that a fully integrable, and in particular an analytical solution for a single LS can be given. To obtain a stationary solution we go to a co-rotating frame, so that one possible representation of a stationary solution at the position p_i is given by the real-valued function $\boldsymbol{q}_i = (\sqrt{2}\,\mathrm{sech}(x - p_i), 0)$ (where we choose a representation in real and imaginary part). Again we will consider only the case of interacting LSs with equal phase. As the NLS does not only have invariances with respect to shifts in position and phase but also Galilean invariance, one may expect a natural degeneracy

of the neutral mode in spite of the stationarity of the LSs. Therefore, the generalized eigenmodes of the neutral modes come into play. As the linearized operator $\boldsymbol{F}'$ greatly simplifies compared to the GL example, one may find the generalized eigenmode by directly solving the equation $\boldsymbol{\phi}_0^1 = \boldsymbol{F}'\boldsymbol{\phi}_0^2$ with $\boldsymbol{\phi}_0^1 = (\sqrt{2}\,\mathrm{sech}(x)\tanh(x), 0)$. The solution reads $\boldsymbol{\phi}_0^2 = (0, -x\tanh(x)/\sqrt{2})$. In addition, the operator $\boldsymbol{F}'$ is antisymmetric, so that one may also find the neutral and generalized eigenmode of the adjoint operator analytically. Except for normalization, one finds that the projectors for the structure $\boldsymbol{q}_i$ are given by $\boldsymbol{\Phi}_0^1 = (-x\tanh(x)/\sqrt{2}, 0)$ and $\boldsymbol{\Phi}_0^2 = (0, \sqrt{2}\,\mathrm{sech}^2(x))$. Evaluating the equations according to the developed formalism yields

$$\begin{aligned} &\partial_t p_i = v_i, \\ &\partial_t v_i = F(|p_i - p_j|)\frac{p_i - p_j}{|p_i - p_j|} \quad \text{with} \quad i, j = 1, 2, i \neq j. \end{aligned} \tag{3.95}$$

This result shows that within the used approximation, the LSs in the NLS behave like classical particles interacting under a central force. The interaction function which one may have expected to be present in the position equation vanishes due to the Galilean invariance of the original equations. For two in-phase LSs, the relevant interaction operator for $F(d)$ in the velocity equation reads $F^I(a_1, b_1)[a_2, b_2] = 3(a_1^2 a_2 + a_1 a_2^2)$ as we have chosen $b_1 = b_2 = 0$, and by inserting the above given expression for the projectors the expression can be given analytically, yielding

$$\begin{aligned} F(d) = 2\,\mathrm{csch}(d)^4 (&24d - 12d\cosh(d) + 12d\cosh(2d) \\ &+ 9\sinh(d) - 18\sinh(2d) + \sinh(3d)). \end{aligned} \tag{3.96}$$

The function is depicted in Fig. 3.4b in the left graph, and the comparison to the full numerical simulation is done in the right graph, again for two different initial separations of the LSs.

Example 3: Reaction-diffusion equation with actively propagating LSs

Our third and most complex example deals with the interaction of LSs with inner degrees of freedom in reaction-diffusion equations. As shown by our second example for isolated LSs, in reaction-diffusion systems one finds supercritical bifurcations from standing to traveling LSs. When several LSs with excited inner degrees of freedom interact, we expect from the general theory that in first order we have a linear superposition of the effects of the inner degrees of freedom and the interaction terms. Although the corresponding equations should be structurally similar to the second example involving the NLS equation, the degeneracy now arises from a bifurcation and not from a Galilean invariance of the system. Depending on the symmetry of the stationary solution, we have shown that for single LSs, one may either expect a normal form given by (3.58) or (3.64). When looking at the concrete example (2.26) in two spatial dimensions, we encounter rotationally symmetric LSs corresponding to the second case. Similar to the GL example we face the problem that it is difficult to calculate some required modes analytically. However, in this case the problem lies in the determination of the

generalized eigenmodes. When the latter are known, the adjoint modes can be given analytically. We have the choice of either calculating the generalized modes numerically or to consider a case where analytical expressions are known. For our model system, the second case is for example given in the parameter limit $d_w \to 0$, $\theta \to 0$.

In [58], the problem was treated using the decomposition (3.81) instead of the more exact decomposition (3.86). After a number of steps, one obtained the final result

$$\begin{aligned}\partial_t \boldsymbol{p}_i &= \boldsymbol{\alpha}_i + F(|\boldsymbol{p}_i - \boldsymbol{p}_j|)/\kappa_3 \frac{\boldsymbol{p}_i - \boldsymbol{p}_j}{|\boldsymbol{p}_i - \boldsymbol{p}_j|}, \\ \partial_t \boldsymbol{\alpha}_i &= (\tau - \tau_c)\kappa_3^2 \boldsymbol{\alpha}_i + \frac{\langle (\partial_{\xi\xi} u_1)^2 \rangle}{\kappa_3 \langle (\partial_\xi u_1)^2 \rangle} |\boldsymbol{\alpha}_i|^2 \boldsymbol{\alpha}_i + F(|\boldsymbol{p}_i - \boldsymbol{p}_j|) \frac{\boldsymbol{p}_i - \boldsymbol{p}_j}{|\boldsymbol{p}_i - \boldsymbol{p}_j|}\end{aligned} \tag{3.97}$$

with τ_c marking the bifurcation point of the drift bifurcation. The results turned out to be rather appropriate to represent the dynamics of the full field equations. The reason for this will be explained in the following. The only nonlinear function in (2.26) appears in the activator equation and reads $f(u) = \lambda u - u^3 + \kappa_1$, furthermore the u-component of the generalized eigenmodes $\boldsymbol{P}$ vanishes for the special case $d_w \to 0$, $\theta \to 0$. With u_h denoting the homogeneous ground state, we have

$$\begin{aligned}&f(u_1 + u_2 + u_h + \epsilon^2 r) \\ &= \lambda u_1 - u_1^3 + \lambda u_2 - u_2^3 - 3u_h^2(u_1 + u_2) - 3u_h(u_1^2 + u_2^2) - 3(u_1^2 u_2 + u_2^2 u_1) - 6u_h u_1 u_2 \\ &+ \epsilon^2 r(\lambda - 3u_h^2 - 6u_h(u_1 + u_2) - 3(u_1^2 + u_2^2) - 6u_1 u_2) - 3\epsilon^4 r^2 (u_h + u_1 + u_2) + \epsilon^6 r^3.\end{aligned} \tag{3.98}$$

This expression is also produced by the general decomposition method (3.86). In contrast, the decomposition (3.81) yields

$$\begin{aligned}&f(u_1 + u_2 + u_h + \epsilon^2 r) = f(u_1 + u_h) + f'(u_1 + u_h)(u_2 + \epsilon^2 r) \\ &= \lambda u_1 - u_1^3 + \lambda u_2 - 3u_h^2(u_1 + u_2) - 3u_h(u_1^2 + u_2^3) - 6u_h u_1 u_2 \\ &- \epsilon^2 r(\lambda - 3u_h^2 - 6u_h u_1 - 3u_1^2).\end{aligned} \tag{3.99}$$

The reason for the good results produced by (3.99) is that when projecting both equations on a projector mode $\langle \Phi_i(u_1)|$ (meaning the projector belongs to the solution u_1) and claiming $u_1 u_2 \sim O(\epsilon^2)$, we find

$$\langle \Phi_i(u_1) | f(u_1 + u_2 + u_h + \epsilon^2 r) - [f(u_1 + u_h) + f'(u_1 + u_h)(u_2 + \epsilon^2 r)] \rangle = O(\epsilon^4). \tag{3.100}$$

As the second example in Sec. 3.2.2.3 has shown that the evaluation must only be performed up to third order, the difference in the results is only a small error of fourth order in ϵ. Thus, the interaction function up to this small error is determined by the first order term interaction operator (3.87), namely

$$F(|\boldsymbol{p}_i - \boldsymbol{p}_j|) = \frac{\langle u_{i,\xi}| - 3(u_i^2 u_j + u_j^2 u_i) - 6u_h u_i u_j \rangle}{\langle u_{1,\xi} | u_{1,\xi} \rangle}, \tag{3.101}$$

For the numerical test in which we consider a head-on collision of two LSs, we choose the other parameters in such a way that the stationary LSs show an oscillatory decay. Correspondingly, the resulting interaction function (Fig. 3.4c) oscillates with distance. In [58] it was suggested to fit this type of interaction law with the analytic expression

$$F(d) = \frac{-d_1}{d^{1/2}} \exp(-d_2 d) \cos(d_3(d - d_4)) \tag{3.102}$$

where the d_i are fit coefficients as this function reflects the decay of Bessel function for large values. As it is not too reasonable to start simulations with different initial separations like in the other examples due to the active propagation of the LSs, instead we vary the intrinsic velocity via the parameter τ. While for small intrinsic velocities resulting in a scattering event of the LSs the agreement is very good, there are some deviations for larger intrinsic velocities, leading to the formation of a bound state. The reason for this is that in the bound state case, the LSs approach each other further than in the other examples we discussed so far. Consequently, higher order correction terms may come into play in this case. Nevertheless, the final state is correctly predicted also by the low-order approximation.

The fact that the complete solution of the u-component can be represented as $u = u_1 + u_2 + u_h + \epsilon^2 r$ is due to the special choice $d_w \to 0$, $\theta \to 0$. For arbitrary parameters, we instead have to use the more general form $u = u_1 + u_2 + u_h + \epsilon(\alpha_1 P_1 + \alpha_2 P_2) + \epsilon^2 r$ with the P_i being the u-components of $\boldsymbol{\phi}_0^2(\boldsymbol{p}_i)$, the generalized neutral eigenmodes of translation for the structure i. With a scaling $u_1 u_2 \sim O(\epsilon^2)$, terms with P_i couple to the unperturbed structure u_j in third order in ϵ, thus breaking the central force nature of the interaction as previously mentioned above. In order to avoid this in the general case, one has to claim $u_1 u_2 \sim O(\epsilon^n)$ with $n > 2$, implying that the derivation would hold only for larger distances. Using the general decomposition (3.86) however theoretically leads to correct results in arbitrary order of ϵ (for the GL and NLS examples above, it was even possible to claim $u_1 u_2 \sim \epsilon$).

In experimental systems, weak interaction processes manifest themselves in various ways. The perhaps most significant one is the formation of bound states consisting of two or several LSs, which can for example be found for current filaments in planar gas-discharges of both dc [171, 172, 325–327] and ac type [1, 328], oscillons in granular media and colloidal suspensions [4, 329, 330], electrical networks [331], chemical pulses [137, 138], liquid crystal light valves [332–334], saturable absorbers [204] or semiconductor microresonators [308, 335]. In a number of systems, typical lock-in distances could be connected to oscillatory tails of the LSs [3, 311, 328, 336, 337]. The only direct measurement of an interaction law was up to now carried out in planar dc gas-discharge systems [173]. Here, the individual LSs propagate under the combined action of intrinsic drive, interaction and the influence of noise (Fig.3.5a). Furthermore, it is found that bound states are possible and may exist over a longer period of time before breaking up (Fig.3.5b). In order to determine an interaction law from experimental data a phenomenological extension of the Langevin equation (3.75) in the form

$$\partial_t \boldsymbol{p}_i = \boldsymbol{\alpha}_i, \qquad \partial_t \boldsymbol{\alpha}_i = h(\alpha_i)\frac{\boldsymbol{\alpha}_i}{\alpha_i} + \sum_{i \neq j} F(d_{ij})\frac{\boldsymbol{d}_{ij}}{d_{ij}} + R(\alpha_i)\boldsymbol{\Gamma}_i(t) \tag{3.103}$$

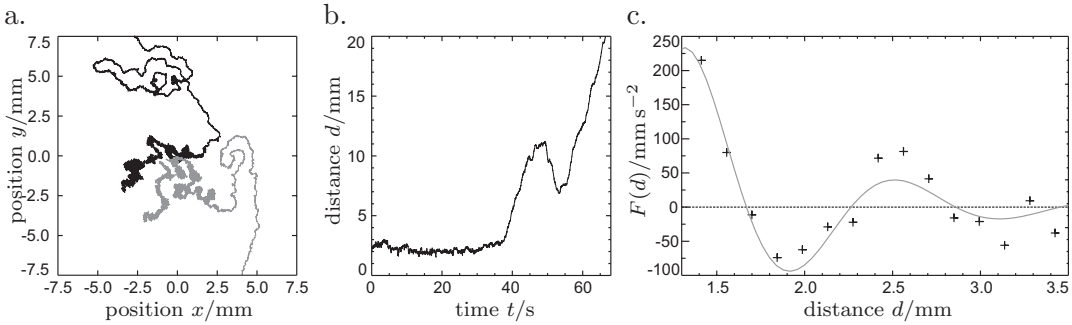

Figure 3.5: Trajectories (a.) and time evolution of the distance (b.) for two interacting LSs in planar dc gas-discharge systems propagating under the influence of noise. The LSs form a bound state over about 35 s before the molecules break up. c. Typical example for an interaction law found with the analysis method described in the text, the grey line is a fit according to (3.102). See [173] for further details.

was proposed whose deterministic part has the same form as (3.97) if in the latter system the coupling in the $\boldsymbol{p}$-equation is neglected. Using means of stochastic data analysis the interaction function $F(d)$ could be determined from experimental data in several cases for the interaction of two LSs, a characteristic example is depicted in Fig.3.5c. The results can be well represented by the theoretically proposed oscillating function (3.102). In those cases in which oscillatory tails could be seen, stable lock-in distances were found to coincidence with a constructive overlap of the tails. Neglecting potential interaction functions in the p_i-equation of (3.103) is necessary to access the experimental data as only position and velocity are measurable quantities. In the next chapter we will discuss in more detail the influence of different coupling structures for actively propagating and interacting LSs, however we may already state here that if only two LSs are considered, in many examples the coupling in the $\boldsymbol{p}$-equation has only minor influence.

3.3.4 Symmetries, dynamics and interaction processes

Considering particle concepts for example in classical Newton mechanics, many important concepts are closely connected to the structure of the underlying equations. Terms like energy, momentum, angular momentum etc which today have become extremely intuitive for most physicists arise as conserved quantities via the corresponding force balance equations.

Turning to self-organized LSs, we find ordinary differential equations for a small number of slowly varying quantities. When position and velocity appear as order parameters, the structure of the reduced equations formally shows strong parallels to classical Newton equations. One may therefore consider the latter as manifestation of the particle-like nature of the LSs. Of course, when comparing the structure of the reduced equations with classical particle equations, potential similarities arise on a mathematical, not a physical level. This means that while the phenomenology of the dynamics may be similar or equal to a classical situation, a comparison of physical mechanisms is usually not possible (ideas like mass for example do not exist for LSs).

While a systematic classification of the behavior of LSs according the properties of the underlying field equation is missing so far, our considerations already allow for some

interesting statements. Generically, systems in which LSs exist will have only translational and rotational invariance. Different examples have shown that for a rotationally symmetric stationary solution sufficiently far below a bifurcation point, only the position will appear as symmetry-induced order parameter, so that in the presence of small inhomogeneities and neighboring LSs, the system will be determined by equations of the form

$$\partial_t \boldsymbol{p}_i = \boldsymbol{f}(\boldsymbol{p}_i) + \boldsymbol{g}(\boldsymbol{p}_i - \boldsymbol{p}_j). \tag{3.104}$$

Here, $\boldsymbol{f}$ reflects the influence of inhomogeneities and $\boldsymbol{g}$ accounts for weak interaction. This expression formally corresponds to the equation for interacting, overdamped Newtonian particles moving in an external potential. In our example on the classical NLS equation translational invariance together with Galilean invariance for two interacting LSs with equal phase results in the structure

$$\begin{aligned} \partial_t \boldsymbol{p}_i &= \boldsymbol{v}_i [+\boldsymbol{f}_1(\boldsymbol{p}_i)], \\ \partial_t \boldsymbol{v}_i &= [\boldsymbol{f}_2(\boldsymbol{p}_i)] + \boldsymbol{g}(\boldsymbol{p}_i - \boldsymbol{p}_j), \end{aligned} \tag{3.105}$$

due to a natural degeneracy of the eigenvalues. The resulting behavior then directly corresponds to what one would expect for classical particles. The Galilean invariance of the field equation is reflected by the same property of the reduced equation. Weak inhomogeneities may break the Galilean invariance and thus result in the terms put in angular brackets. Finally, our example on LSs in reaction-diffusion systems has shown that entirely "unclassical" behavior can be found in the form of active propagation with the general form

$$\begin{aligned} \partial_t \boldsymbol{p}_i &= \boldsymbol{v}_i + \boldsymbol{f}_1(\boldsymbol{p}_i) + \boldsymbol{g}_1(\boldsymbol{p}_i - \boldsymbol{p}_j), \\ \partial_t \boldsymbol{v}_i &= \boldsymbol{h}(\boldsymbol{v}_i) + \boldsymbol{f}_2(\boldsymbol{p}_i) + \boldsymbol{g}_2(\boldsymbol{p}_i - \boldsymbol{p}_j). \end{aligned} \tag{3.106}$$

While the coupled set of two first order equations (3.106) reflects some "inert" behavior of the LSs, the latter is due to an additional inner degree of freedom that is excited in a bifurcation. In more detail, the inner degree of freedom with a slow time constant couples to the neutral modes responsible for the translation of the structure (one first-order ODE), and the inner degree of freedom is excited by itself (resulting in a second first-order ODE). In the long-time limit the dynamics of isolated LSs will thus not be determined by the initial conditions (for example the initial velocity), but by the inner degrees of freedom. The resulting type of dynamics is totally untypical for classical particles where no inner degrees of freedom are considered or where they are at least decoupled from propagation. We have seen that the active propagation (3.106) arises from a degeneracy of eigenvalues in the bifurcation point. In the non-degenerate case, a Hopf bifurcation to for example a breathing structures is generic. In a codimension-two point or further above a codimension-one point, there can also be a coaction of traveling and breathing.

Looking at the structure of the equations (3.104) - (3.106), one may give a rough estimate of typical dynamical phenomena that can occur in the considered situation

	Eq. (3.104)	Eq. (3.105)	Eq. (3.106)
propagation	no	arbitrary velocity	fixed velocity
repulsion	yes	yes	yes
pinning	yes	yes	yes
lock-in	yes	yes	yes
scattering	no	yes	yes
oscillating molecules	no	yes	yes
rotating molecules	no	yes	yes
reaction to perturbation (long-time limit)	ch. of position	ch. of direction and velocity	ch. of direction

Table 3.2: Overview on possible dynamical phenomena for LSs described by the equations (3.104) - (3.106).

(Table 3.2). In the case of stationary LSs, the overdamped motion puts strong restriction on the dynamics. In the long time-limit, the structures can not perform a motion with a finite velocity, the only change to induce a shift of the position is by local inhomogeneities or perturbations. Furthermore, even in the latter case there can be no oscillations around potential resting points due to for example a trapping inhomogeneity. Consequently, without interaction a potential trapping site will definitely trap a LS that comes close enough. In systems with Galilean invariance, one may basically encounter all phenomena that are known for classical particles as long as the order parameter approximation is valid. In particular, each LS may have a different velocity in the long-time limit, and perturbations may change these velocities continuously. While spatial inhomogeneities break the Galilean invariance of the system and consequently also of the underlying field equations, for small perturbations their influence manifests in the field equations as additional additive space-dependent terms. In this way, the system gets a hybrid character between classical and overdamped motion, whether one type of dynamics dominates depends on the type of system. The active propagation basically allows for most of the classical dynamical phenomena to occur as well as the particles show some "inert" behavior due to their inner degree of freedom. Nevertheless, the coupling structure of the equations is generally more complex and the active propagation only allows for one absolute velocity of isolated LSs in the long time limit. We will discuss the new features of this kind of dynamics in more detail in the next chapter.

While it is not too difficult to systematically classify the possible types of dynamics when only the "standard" symmetries (translation, rotation, Galilean) are present, the situation is currently not as clear for hidden symmetries like invariance with respect to phase shifts, scaling transformations etc. While the above presented projection techniques are technically capable of dealing with this problem, it is likely that group theoretic methods have to be applied to give a general classification. Last but not least, even when it is possible to calculate analytically or numerically the functions in (3.104) - (3.106) as well as other order parameter equations, an understanding of their nature is essentially connected to the specific mechanisms in the underlying system.

3.4 Stochastic and fluctuating systems

3.4.1 General theory

In many physical systems noise is present and affects the dynamics of LS (see for example [157, 158, 320] as well as Fig. 3.5). In order to account for these effects, one may either extend the above derived order parameter equations in a phenomenological way or introduce noise terms already on the level of the underlying field equations. Depending on the system, sources of noise may be thermal fluctuations, fast generation processes, coupled heat-baths, external radiation etc. In the following, we want to explore how noisy processes in the field equations influence the dynamics of LSs on the level of order parameter equations. A potential way of modeling the influence of noise is by extending the field equations (3.10) to

$$\partial_t \boldsymbol{q} = \boldsymbol{F}(\boldsymbol{q}, \nabla, \boldsymbol{\sigma}) \longrightarrow \partial_t \boldsymbol{q} = \boldsymbol{F}(\boldsymbol{q}, \nabla, \boldsymbol{\sigma}) + \underline{\boldsymbol{M}}(\boldsymbol{q})\, \boldsymbol{\Gamma}(\boldsymbol{x}, t). \tag{3.107}$$

where $\underline{\boldsymbol{M}} = m_\eta(\boldsymbol{q})\delta_{\eta\mu}$ is a diagonal matrix with noise amplitudes as entries and $\boldsymbol{\Gamma}$ is a vector with normalized noise forces (η and μ represent the components of $\boldsymbol{q}$). The statistical properties of the noise forces are essential for the dynamics of the equation. In order to do an analytical calculation, we will assume that the noise forces have vanishing mean, are Gaussian distributed and are δ-correlated in space and time, i.e.

$$\Big\langle \Gamma_\eta(\boldsymbol{x}, t)\Gamma_\mu(\boldsymbol{x}', t') \Big\rangle_E = 2\delta_{\eta\mu}\delta(\boldsymbol{x} - \boldsymbol{x}')\delta(t - t'), \tag{3.108}$$

where the brackets with index E denote the ensemble average. Furthermore, the noise amplitudes are assumed to be so small that the action of the fluctuations does not endanger the integrity of the LS, for example by annihilation or generation of other LSs. An analysis of the latter type of processes is for example given in [338].

The stochastic generalization given by Eq. (3.107) implies that the "amplitudes" c_i, and γ_j appearing in the eigenmode decomposition become random variables because they are subjected to fluctuating forces. In detail, in the stochastic case Eq. (3.23) becomes

$$-\partial_t \boldsymbol{c} \cdot \nabla_{\boldsymbol{c}}[\boldsymbol{q}_0 + \tilde{\boldsymbol{q}}] + \frac{\partial}{\partial_t}\tilde{\boldsymbol{q}} = \boldsymbol{F}(\boldsymbol{q}) + \underline{\boldsymbol{M}}(\boldsymbol{q})\, \boldsymbol{\Gamma}. \tag{3.109}$$

Projecting on the individual eigenmodes as in the deterministic case, we obtain in the non-degenerate case

$$\partial_t \gamma_i + \cdot \sum_k \partial_t c_k \gamma_k \langle \boldsymbol{\Phi}_i^1 | \partial_{c_k} \boldsymbol{\phi}_k^1 \rangle = \lambda_i \gamma_i + \langle \boldsymbol{\Phi}_i^1 | \boldsymbol{N}(\boldsymbol{q}) \rangle + \langle \boldsymbol{\Phi}_i^1 | \underline{\boldsymbol{M}}(\boldsymbol{q}) \boldsymbol{\Gamma} \rangle, \tag{3.110}$$

the generalizations for the c_i and the degenerate case should be obvious.

Let us start with a single LS and the most simple case that we are far below any bifurcation points, meaning that the dynamics only has to be considered on very slow

time scales. Considering only translational invariance, the only critical modes are associated with the position and the amplitudes of all other modes relax to zero. The corresponding terms drop out of (3.110), and we obtain

$$\partial_t p_\xi = \langle \mathbf{\Phi}^1_{0,\xi} | \underline{\boldsymbol{M}}(\boldsymbol{q}_0) \mathbf{\Gamma} \rangle. \tag{3.111}$$

Physically this means that at each instant the structure experiences a deformation by noise which instantaneously relaxes so that only a neutral displacement remains. The result agrees with results reported in earlier works for propagating kinks in bistable one-component reaction-diffusion systems [339] and should be generic for arbitrary types of systems.

In a next step, we may exemplarily consider a situation where a neutral generalized eigenmode influences the dynamics. Looking at the perturbation analysis carried out in our second example in Sec. 3.2.2.3, we have seen that different time scales come into play in this situation. In particular, as we see from Eqns. (3.53) and (3.54) on the time scale T_1 of the perturbation analysis uncritical modes already appear, however without influencing the dynamics. We thus have to develop a way to treat the fluctuations for the non-critical modes. The difference between deterministic and stochastic case is that the stochastic generalizations of the deterministic equations contain additional terms $\zeta_{i,nc}$ defined as

$$\zeta_{i,nc}(t) = \langle \mathbf{\Phi}^1_i | \underline{\boldsymbol{M}}(\boldsymbol{q})\, \mathbf{\Gamma}(t) \rangle. \tag{3.112}$$

Distinguishing between fast and slow deterministic modes (with amplitudes β_k and α_i, respectively), we may again try to express the amplitudes β_k of the non-critical modes in terms of the amplitudes α_i. Taking the fluctuating contributions $\zeta_{i,nc}$ into account, we obtain relations of the form

$$\beta_k = h_k(\boldsymbol{\alpha}) + W_k(\boldsymbol{\alpha}, \zeta_{k,nc}). \tag{3.113}$$

The fluctuating contributions of the non-critical modes, however, can usually be neglected because they are small with respect to the fluctuating contributions of the critical modes [340, 341]. Neglecting the terms W_k in Eq. (3.113), we can eliminate the non-critical modes in the amplitude equations of the critical modes just as in the deterministic case. Furthermore, we again make the approximation $\underline{\boldsymbol{M}}(\boldsymbol{q}) \approx \underline{\boldsymbol{M}}(\boldsymbol{q}_0)$. Then, we obtain in the non-degenerate case

$$\partial_t \alpha_i = g_i(\boldsymbol{\alpha}) + \langle \mathbf{\Phi}^1_i | \underline{\boldsymbol{M}}(\boldsymbol{q}_0)\, \mathbf{\Gamma} \rangle \tag{3.114}$$

with the g_i being the same functions as in the deterministic case.

For the drift bifurcation, the same idea can be applied. As a generalization of (3.111) in the presence of a generalized eigenmode one thus finds

$$\partial_t p_\xi = f_\xi(\boldsymbol{\alpha}) + \langle \mathbf{\Phi}^1_{0,\xi} | \underline{\boldsymbol{M}}(\boldsymbol{q}_0)\, \mathbf{\Gamma} \rangle \tag{3.115}$$

with $f_\xi(\boldsymbol{\alpha}) = \langle \boldsymbol{\Phi}^1_{0,\xi} | \boldsymbol{F}(\boldsymbol{q}) \rangle$ under the above approximations. Equations for the components of $\boldsymbol{\alpha}$ are obtained in an analogous way with the help of suitable projectors $\boldsymbol{\Phi}^2_{0,\xi}$. In sum, we have shown that in the stochastic case we need to add particular fluctuating components to the deterministic relations given for example by Eq. (3.34). The resulting stochastic evolution equations for $\boldsymbol{p}$ and $\boldsymbol{\alpha}$ in our above example written in vector notation read

$$\begin{aligned} \partial_t \boldsymbol{p} &= \boldsymbol{\alpha} + \boldsymbol{\Phi}^1_{0,\xi} | \underline{\boldsymbol{M}}(\boldsymbol{q}_0)\, \boldsymbol{\Gamma}(\boldsymbol{x},t) \rangle, \\ \partial_t \boldsymbol{\alpha} &= \boldsymbol{g}(\boldsymbol{\alpha}) + \langle \boldsymbol{\Phi}^2_{0,\xi} | \underline{\boldsymbol{M}}(\boldsymbol{q}_0)\, \boldsymbol{\Gamma}(\boldsymbol{x},t) \rangle, \end{aligned} \tag{3.116}$$

showing that in general, all order parameters will be influenced by the noise in the system.

In order to explore the properties of the noise terms in more detail, we calculate the first and second moment of the noise forces componentwise. In the following equations, the indexes ξ and χ denote spatial directions (i.e. mutually orthogonal modes), and as above, η and μ denote the individual components of the occurring modes. Also, in order to improve the overview, we will denote the scalar product by an index $\boldsymbol{x}$ in order to distinguish it from the ensemble average, which is as before denoted with the index E. For the first moment, one finds

$$\Big\langle \langle (\boldsymbol{\Phi}^1_{0,\xi})_\eta | m_\eta(\boldsymbol{q}_0)\, \Gamma_\eta(\boldsymbol{x},t) \rangle_{\boldsymbol{x}} \Big\rangle_E = \int\limits_\Omega m_\eta(\boldsymbol{q}_0) G_{P,\xi,\eta} \Big\langle \Gamma_\eta(\boldsymbol{x},t) \Big\rangle_E \mathrm{d}^n x = 0. \tag{3.117}$$

The second moment yields the relation

$$\begin{aligned} & \Big\langle \langle (\boldsymbol{\Phi}^1_{0,\xi})_\eta (\boldsymbol{x} - \boldsymbol{p}(t)) | m_\eta(\boldsymbol{q}_0(\boldsymbol{x} - \boldsymbol{p}(t)))\, \Gamma_\eta(\boldsymbol{x},t) \rangle_{\boldsymbol{x}} \\ & \times \langle (\boldsymbol{\Phi}^1_{0,\chi})_\mu (\boldsymbol{x}' - \boldsymbol{p}(t')) | m_\mu(\boldsymbol{q}_0(\boldsymbol{x}' - \boldsymbol{p}(t')))\, \Gamma_\mu((\boldsymbol{x}'),t') \rangle_{\boldsymbol{x}'} \Big\rangle_E \\ = & \int\limits_\Omega \int\limits_\Omega m_\eta(\boldsymbol{q}_0(\boldsymbol{x} - \boldsymbol{p}(t))) m_\mu(\boldsymbol{q}_0(\boldsymbol{x}' - \boldsymbol{p}(t'))) (\boldsymbol{\Phi}^1_{0,\xi})_\eta (\boldsymbol{x} - \boldsymbol{p}(t))\, (\boldsymbol{\Phi}^1_{0,\chi})_\mu (\boldsymbol{x}' - \boldsymbol{p}(t')) \\ & \times \Big\langle \Gamma_\eta(\boldsymbol{x},t) \Gamma_\mu(\boldsymbol{x}',t') \Big\rangle_E \mathrm{d}^n x\, \mathrm{d}^n x' \\ = & \; 2 \int\limits_\Omega \int\limits_\Omega m_\eta(\boldsymbol{q}_0(\boldsymbol{x} - \boldsymbol{p}(t))) m_\mu(\boldsymbol{q}_0(\boldsymbol{x}' - \boldsymbol{p}(t'))) (\boldsymbol{\Phi}^1_{0,\xi})_\eta (\boldsymbol{x} - \boldsymbol{p}(t)) (\boldsymbol{\Phi}^1_{0,\chi})_\mu (\boldsymbol{x}' - \boldsymbol{p}(t)) \\ & \times \delta(\boldsymbol{x} - \boldsymbol{x}') \delta(t - t')\, \mathrm{d}^n x\, \mathrm{d}^n x' \\ = & \; 2 \langle m^2_\eta(\boldsymbol{q}_0) (\boldsymbol{\Phi}^1_{0,\xi})^2_\eta \rangle_{\boldsymbol{x}} \delta_{\eta\mu} \delta_{\xi\chi} \delta(t - t'). \end{aligned} \tag{3.118}$$

An analogous result is obtained for the projections on the other critical modes. This shows that the projections keep the property of being δ-correlated in time. However, analogously to (3.118) one may calculate the correlations of the noise forces obtained using different projectors and thereby show that the noise forces in the equations for the different order parameters obtained according to (3.114) are not necessarily independent

of each other (unlike the noise forces in the different components in the original field equation). Considering for example additive noise in the field equations, the coefficient m_η can be drawn out of the integral in (3.118), and one sees that the correlation for different noise terms only vanishes if the projectors are orthogonal.

The extension of regular field equations by stochastic terms may generally bring in a wide range of different timescales affecting all modes. In order to overcome this problem, we have neglected the fluctuating forces $\zeta_{i,nc}$ that act on the amplitudes of non-critical modes. That is, we have put the expressions W_k in Eq. (3.113) equal to zero because the noise amplitudes of these fluctuating forces are usually much smaller than the noise amplitudes of the fluctuating forces related to the critical modes. Nevertheless, these weakly interacting fluctuating forces can also affect the amplitude dynamics of the critical modes. The quality of the approximation thus essentially depends on the properties of the linearization spectrum and the time scales for which the reduced equations are derived. Generally, the results are the better the slower the time scale on which the reduced equations are to hold and the larger the gap between the eigenvalues belonging to critical and non-critical modes.

In order to explicitly account for the impacts of the fluctuating forces $\zeta_{i,nc}$, one generally has two options. First, one may try to derive analytical expressions for W_k (for examples see [340, 341]). If we substitute such an analytical expression into $\boldsymbol{q}$, we will see that $\boldsymbol{q}$ depends on the fluctuating components $\zeta_{i,nc}$: $\boldsymbol{q}(\boldsymbol{\alpha},\boldsymbol{\beta}) \rightarrow \boldsymbol{q}(\boldsymbol{\alpha},\{\zeta_{i,nc}\})$. As a result, the Langevin equations for the α_i and β_i will in any case involve multiplicative noise terms. Another origin of multiplicative noise may be higher order corrections to our approximation $\underline{\boldsymbol{M}}(\boldsymbol{q}) \approx \underline{\boldsymbol{M}}(\boldsymbol{q}_0)$ we made above. As an alternative to this approach, the impact of a particular fluctuating forces $\zeta_{i,nc}$ can be examined by adding the corresponding amplitude β_i to the set of critical modes. Accordingly, the amplitude vector $\boldsymbol{\alpha}$ would read $\boldsymbol{\alpha} = (\alpha_1,\ldots,\alpha_M,\beta_i)$. This second approach will yield additive noise Langevin equations if additive noise is considered in the field equation. Comparing the two approaches, we see that multiplicative noise terms can arise due to projections from higher dimensional phase spaces to lower dimensional ones. This finding is in line with our notion about the origin of multiplicative noise sources [342]. Multiplicative noise forces originate from fluctuating parameters which in more comprehensive descriptions would satisfy additive noise Langevin equations.

Looking at the case where degenerate eigenvalues connected to propagation come into play, we find that the general form of the order parameter equations for propagating LSs in noisy field equations is more complex than the frequently used phenomenologically introduced form for active Brownian particles. The latter is mostly introduced on a phenomenological basis. While a rigorous approach is possible when a Hamilton function can be set up for the system [343], no general approach has been available for dissipative field equations for which actively propagating localized solutions are observed.

3.4.2 Noise correlations in the order parameter equations

Particle-like behavior under the influence of noise is known to exist in the form of Brownian motion of particles since the experimental investigations by Brown and Brongniart in 1827 and the fundamental theoretical works by Bachelier [344], Smoluchowski [345] and Einstein [346]. In its simplest form, the basis of modeling of Brownian motion is

given by the Langevin equation

$$\partial_t \boldsymbol{p} = \boldsymbol{\alpha}, \quad \partial_t \boldsymbol{\alpha} = -\gamma \boldsymbol{\alpha} + R\boldsymbol{\Gamma}(t), \tag{3.119}$$

describing the acceleration $\dot{\boldsymbol{\alpha}}$ of a Brownian particle as the superposition of a deterministic part $-\gamma\boldsymbol{\alpha}$ with damping coefficient γ and a stochastic part with additive noise forces which in most theoretical works are assumed to be δ-correlated. The physical motivation for using an equation of the form (3.119) can be manifold. In order to describe the motion of microscopic particles, one had to assume frequent collisions of a single particle with neighboring particles, leading to both deterministic and stochastic parts in the equation. The stochastic part is also frequently motivated by a coupled heat bath [347], where the noise amplitudes are considered as a measure of the temperature. In many situations, Eq. (3.119) can be validated by tracing Brownian particles and analyzing the corresponding distribution functions. In addition, many systems allow for a rigorous derivation of Eq. (3.119) from basic mechanical equations using standard statistical techniques. Comparing (3.119) to (3.116), aside from generalized deterministic functions $\boldsymbol{f}$ and $\boldsymbol{g}$ we find noise forces in both components which may even be correlated.

Many recent investigations deal with phenomenological extensions of Eq. (3.119), which are often of the form

$$\partial_t \boldsymbol{p}_i = \boldsymbol{\alpha}_i, \quad \partial_t \boldsymbol{\alpha}_i = \boldsymbol{g}(\boldsymbol{\alpha}_i) + \sum_{i \neq j} \boldsymbol{F}(\boldsymbol{d}_{ij}) + \underline{\boldsymbol{R}}(\boldsymbol{\alpha}_i)\boldsymbol{\Gamma}_i(t). \tag{3.120}$$

Eq. (3.120) describes the motion of a Brownian particle with index i and a generalized deterministic part under a force F caused by other Brownian particles with index $j \neq i$, where $\boldsymbol{d}_{ij}$ is given by $\boldsymbol{x}_i - \boldsymbol{x}_j$ and the $\boldsymbol{\Gamma}_i$ are statistically independent Langevin forces. A frequent choice of $\boldsymbol{g}(\boldsymbol{\alpha})$ is given by $\boldsymbol{g}(\boldsymbol{\alpha}) = k_1\boldsymbol{\alpha} - k_3|\boldsymbol{\alpha}|^2\boldsymbol{\alpha}$ leading to *active Brownian motion*, which is a phenomenological model for the dynamics of self-propelled objects. Types of Eq. (3.120) are encountered when modeling grains in dusty plasmas [348], myosin head on actin filaments [349, 350], swarms of fishes and daphnia [351], traffic flow [352] and even sociological systems [353]. For this choice of $\boldsymbol{g}(\boldsymbol{\alpha})$ we also have a strong connection to the intrinsic dynamics of LSs we have derived in the previous sections when considering the dynamics of an isolated LS.

In the following, our goal is to explore the influence of driving both components $\boldsymbol{p}$ and $\boldsymbol{\alpha}$ with noise as found in the previous section and compare the findings to the phenomenological model of active Brownian motion. When considering only the $\boldsymbol{\alpha}$-equation which is independent of $\boldsymbol{p}$, Eqns. (3.116) and (3.120) for a single particle and additive noise (meaning $\underline{\boldsymbol{R}}(\boldsymbol{\alpha}) = R$) are almost equal. For this equation alone a few properties can still be given analytically with standard means [354], for example the stationary solution of the Fokker-Planck equation which reads

$$P(\boldsymbol{\alpha}) = N \exp\Big(\frac{1}{R^2}(\frac{k_1}{2}\alpha^2 - \frac{k_3}{4}\alpha^4)\Big). \tag{3.121}$$

Due to the nonlinearity of the equation however, many interesting quantities are rather difficult to obtain analytically. Therefore, in order to explore the influence of noise in

several coupled equations in a first step we will consider the linear equation

$$\begin{aligned}\partial_t p &= \alpha + R_p(s\Gamma_p(t) + \sqrt{1-s^2}\Gamma_\alpha(t)),\\ \partial_t \alpha &= -k_1\alpha + R_\alpha \mathbf{\Gamma}_\alpha(t)\end{aligned} \tag{3.122}$$

with $s \in [0,1]$. It may be considered as a model for an active particle below a drift bifurcation in the limit of small particle velocities so that nonlinear terms in α can be neglected. The second equation exactly corresponds to (3.119) while the first equation contains two driving terms. The noise forces Γ_p and Γ_α are assumed to be uncorrelated, so that for $s = 0$, both components are driven independently. In contrast, for $s = 1$ the driving in both components is equal. For classical Brownian motion, it is well known that the mean squared displacement of a particle as a function of time scales linearly with the latter for sufficiently large times [354]. In the following, we will show analytically how the mean squared displacement (in one spatial dimension) behaves for the extension (3.122). As a starting point, we integrate the first equation of (3.122) in time to obtain

$$\begin{aligned}
&\langle (p(t)-p(0))^2\rangle\\
=\ &\langle \int_0^t \partial_t p(t_1)\,\mathrm{d}t_1 \int_0^t \partial_t p(t_2)\,\mathrm{d}t_2\rangle\\
=\ &\langle \int_0^t\int_0^t [\alpha(t_1) + R_p(s\Gamma_p(t_1) + s'\Gamma_\alpha(t_1))][\alpha(t_2) + R_p(s\Gamma_p(t_2) + s'\Gamma_\alpha(t_2))]\,\mathrm{d}t_1\mathrm{d}t_2\rangle\\
=\ &\langle \int_0^t\int_0^t [\alpha(t_1)\alpha(t_2) + R_p\alpha(t_1)[s\Gamma_p(t_2) + s'\Gamma_\alpha(t_2)] + R_p\alpha(t_2)[s\Gamma_p(t_1) + s'\Gamma_\alpha(t_1)]\\
&+R_p^2(s^2\Gamma_p(t_1)\Gamma_p(t_2) + s'^2\Gamma_\alpha(t_1)\Gamma_\alpha(t_2) + 2ss'\Gamma_p(t_1)\Gamma_\alpha(t_2))]\,\mathrm{d}t_1\mathrm{d}t_2\rangle\\
=\ &\int_0^t\int_0^t \langle\alpha(t_1)\alpha(t_2)\rangle\,\mathrm{d}t_1\mathrm{d}t_2 + 2R_p\int_0^t\int_0^t \langle\alpha(t_1)[s\Gamma_p(t_2) + s'\Gamma_\alpha(t_2)]\rangle\,\mathrm{d}t_1\mathrm{d}t_2\\
&+\int_0^t\int_0^t \langle R_p^2(s^2\Gamma_p(t_1)\Gamma_p(t_2) + s'^2\Gamma_\alpha(t_1)\Gamma_\alpha(t_2))\rangle\,\mathrm{d}t_1\mathrm{d}t_2\\
=\ &I_1 + I_2 + I_3.
\end{aligned} \tag{3.123}$$

Here, we have introduced the abbreviation $s' = \sqrt{1-s^2}$ and exploited the fact that Γ_p and Γ_α are assumed to be uncorrelated. In the following, we will evaluate the three integral expressions I_i, $i = 1,2,3$ as defined in the last line of (3.123). The first one is encountered also in the context of classical Brownian particles and can be solved by

inserting the second equation of (3.122) (compare also [354]):

$$\begin{aligned}
I_1 &= \int_0^t\int_0^t \langle [\alpha(0)e^{k_1 t_1} + R_\alpha \int_0^{t_1} e^{k_1(t_1-t_1')}\Gamma_\alpha(t_1')\,\mathrm{d}t_1'] \\
&\quad \times [\alpha(0)e^{k_1 t_2} + R_\alpha \int_0^{t_2} e^{k_1(t_2-t_2')}\Gamma_\alpha(t_2')\,\mathrm{d}t_2']\rangle\,\mathrm{d}t_1\mathrm{d}t_2 \\
&= \int_0^t\int_0^t [\alpha(0)^2 e^{-k_1(t_1+t_2)} + 2R_\alpha^2 \int_0^{t_1}\int_0^{t_2} e^{-k_1(t_1+t_2-t_1'-t_2')}\delta(t_1'-t_2')\,\mathrm{d}t_1'\mathrm{d}t_2']\mathrm{d}t_1\mathrm{d}t_2 \\
&= \int_0^t\int_0^t [\alpha(0)^2 e^{-k_1(t_1+t_2)} + \frac{R_\alpha^2}{k_1}(e^{-k_1|t_1-t_2|} - e^{-k_1(t_1+t_2)})]\,\mathrm{d}t_1\mathrm{d}t_2 \\
&= (\alpha(0)^2 - \frac{R_\alpha^2}{k_1})\frac{(1-e^{-k_1 t})^2}{k_1^2} + 2\frac{R_\alpha^2}{k_1^2}t + 2\frac{R_\alpha^2}{k_1^3}(1-e^{-k_1 t}) \stackrel{t\to\infty}{\longrightarrow} 2\frac{R_\alpha^2}{k_1^2}t
\end{aligned} \tag{3.124}$$

The second integral describes the driving via the noise correlation:

$$\begin{aligned}
I_2 &= 2\int_0^t\int_0^t \langle [\alpha(0)e^{-k_1 t_1} + R_\alpha \int_0^{t_1} e^{-k_1(t_1-t_1')}\Gamma_\alpha(t_1')\,\mathrm{d}t_1'][R_p(s\Gamma_p(t_2) + s'\Gamma_\alpha(t_2))]\rangle\,\mathrm{d}t_1\mathrm{d}t_2 \\
&= 2\int_0^t\int_0^t \langle \alpha(0)e^{-k_1 t} R_p[s\Gamma_p(t_2) + s'\Gamma_\alpha(t_2)] + R_p R_\alpha \int_0^{t_1} e^{-k_1(t_1-t_1')} s\Gamma_p(t_2)\Gamma_\alpha(t_1')\,\mathrm{d}t_1' \\
&\quad + R_p R_\alpha \int_0^{t_1} e^{-k_1(t_1-t_1')} s'\Gamma_\alpha(t_2)\Gamma_\alpha(t_1')\,\mathrm{d}t_1'\rangle\,\mathrm{d}t_1\mathrm{d}t_2 \\
&= 4R_p R_\alpha s' \int_0^t\int_0^t\int_0^{t_1} e^{-k_1(t_1-t_1')}\delta(t_2-t_1')\,\mathrm{d}t_1'\mathrm{d}t_1\mathrm{d}t_2 \\
&= 4R_p R_\alpha s' \int_0^t\int_0^t e^{-k_1(t_1-t_2)}\Theta(t_1-t_2)\,\mathrm{d}t_1\mathrm{d}t_2 = \frac{4R_p R_\alpha s'}{k_1}\int_0^t (1-e^{-k_1 t_1})\,\mathrm{d}t_1 \\
&= \frac{4R_p R_\alpha s'}{k_1}(t - \frac{1-e^{-k_1 t}}{k_1}) \stackrel{t\to\infty}{\longrightarrow} \frac{4R_p R_\alpha s'}{k_1}t.
\end{aligned} \tag{3.125}$$

The last integral is the most simple to evaluate and reads

$$I_3 = R_p^2 \int_0^t\int_0^t (s^2\delta(t_1-t_2) + s'^2\delta(t_1-t_2))\,\mathrm{d}t_1\mathrm{d}t_2 = 2R_p^2 t \tag{3.126}$$

As final result, we may state that when for large times the initial conditions play no role any longer, the mean squared displacement behaves as

$$\langle (p(t)-p(0))^2 \approx 2(\frac{R_\alpha^2}{k_1^2}+\frac{2R_pR_\alpha\sqrt{1-s^2}}{k_1}+R_p^2)t. \tag{3.127}$$

This shows that we have three contributions to the displacement: the noisy driving in the p- and α-component and an additional term monotonously increasing in strength when the noise forces in the components become more correlated.

In a next step, we will have a look at the case

$$\begin{aligned}\partial_t p &= \alpha + R_p(s\Gamma_p(t)+\sqrt{1-s^2}\Gamma_\alpha(t)),\\ \partial_t \alpha &= k_1\alpha - k_3|\alpha|^2\alpha + R_\alpha \mathbf{\Gamma}_\alpha(t).\end{aligned} \tag{3.128}$$

The nonlinearity in the second equation poses severe problems for the analytical calculation of a number of quantities, so that we have to rely on numerical calculations for many of the following results. To this end, we will use a standard explicit discrete stochastic integration of (3.128) (compare [354]) given by

$$\begin{aligned}p(t+\Delta t) &= p(t)+\Delta t\alpha(t)+\sqrt{\Delta t}R_p(s\Gamma_p(t)+\sqrt{1-s^2}\Gamma_\alpha(t)),\\ \alpha(t+\Delta t) &= \alpha(t)+\Delta t(k_1\alpha(t)-k_3|\alpha(t)|^2\alpha(t))+\sqrt{\Delta t}R_\alpha\mathbf{\Gamma}_\alpha(t).\end{aligned} \tag{3.129}$$

When using the parameters of Fig. 3.4c ($k_1 \approx 0.001$, $k_3 \approx 6500$, $F(d)$ as in Fig. 3.4c) a characteristic time scale of the dynamics is $T_1 = 100 - 1000$. The time step of the simulations is chosen as $T_2 = 0.01$. Varying this time step by an order of magnitude without does not change the results, showing that this choice is reasonable.

The first quantity of interest is the average mean squared value of α given by the second equation, i.e.

$$\langle \alpha^2 \rangle = \frac{\int_0^\infty \alpha^2 P(\alpha)\,\mathrm{d}\alpha}{\int_0^\infty P(\alpha)\,\mathrm{d}\alpha} \tag{3.130}$$

with $P(\alpha)$ according to (3.121). While an analytical solution is basically possible, it has a rather complicated form (involving several error functions) so that we fix k_1 and k_3 and look at the mean squared value of α as a function of R (Fig. 3.6a). We see that for vanishing noise amplitudes the average value coincidences with the intrinsic velocity and then first goes down with increasing noise amplitude. Here, the PDF of α widens from a δ-peak and in average shifts to smaller values of α. There is a noise value where the mean squared velocity takes a minimum value before monotonously re-increasing. Here, the fluctuating parts starts dominating the dynamics and only the cubic damping of the intrinsic driving remains relevant.

To investigate the dependence of the mean squared displacement for $R_p = 0$ (classical active Brownian motion) and selected values of R_α, we choose an initial condition $\alpha(0) =$

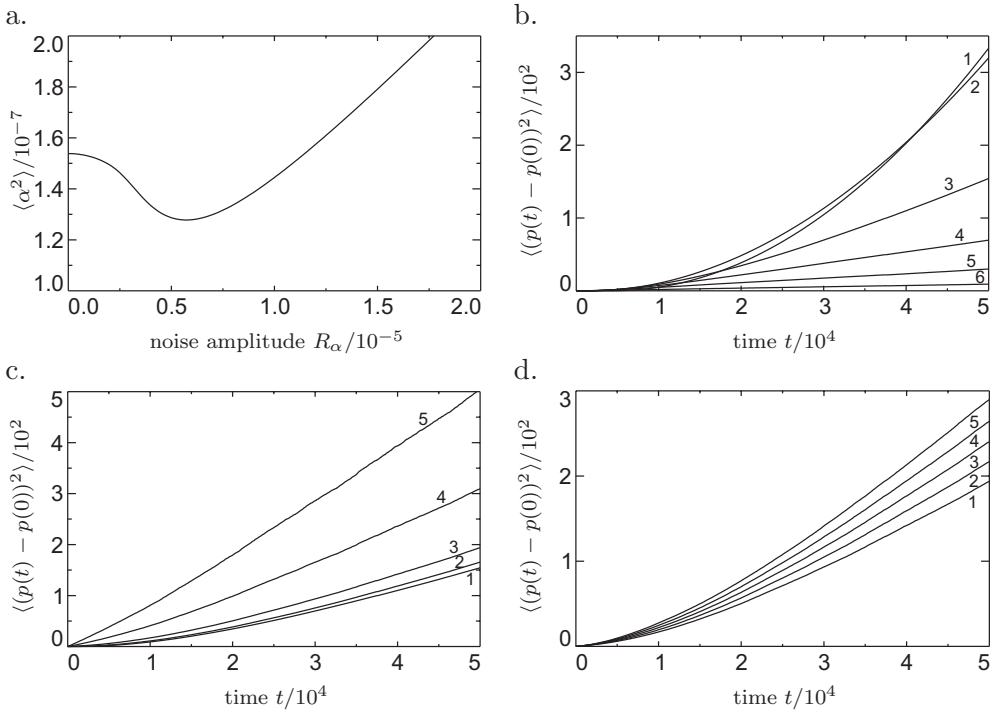

Figure 3.6: Ensemble averages for the evolution equation (3.128). a. Expectation value of α^2 as a function of R_α according to (3.130). b. Average mean squared displacement for $R_p = 0$ and $R_\alpha = 10^{-7}$ (1.), $1.5 \cdot 10^{-6}$ (2.), $4.5 \cdot 10^{-6}$ (3.), $6 \cdot 10^{-6}$ (4.), $9 \cdot 10^{-6}$ (5.), $5 \cdot 10^{-5}$ (6.). c. Average mean squared displacement for $R_\alpha = 4.5 \cdot 10^{-6}$, $s = 0$ and $R_p = 5 \cdot 10^{-3}$ (1.), $R_p = \cdot 10^{-2}$ (2.), $R_p = 2 \cdot 10^{-2}$ (3.), $R_p = 4 \cdot 10^{-2}$ (3.), $R_p = 6 \cdot 10^{-2}$ (6.). d. c. Average mean squared displacement for $R_\alpha = 4.5 \cdot 10^{-6}$, $R_p = 2 \cdot 10^{-2}$ and $s = 0$ (1.), $s = 0.25$ (2.), $s = 0.5$ (3.), $s = 0.75$ (4.) and $s = 1$ (5.). The last three figures have been obtained by simulating 10000 ensemble members with $\alpha(0) = 0$, time step $\Delta t = 0.01$.

0 and simulate 10000 realizations of the stochastic process using (3.129) with the above time step. A closer inspection shows that the initial conditions influence the dynamics for about $\Delta T = 1000$ so that the total time for the simulation is taken as $T = 50000$, the results are shown in Fig. 3.6b. For $R_\alpha \approx 0$ we see a square scaling which directly results from a constant velocity stabilized by intrinsic propagation. Increasing the noise amplitude now first reflects the findings for the mean squared velocity: the mean squared velocity goes down and the square scaling turns into a linear scaling, the intermediate curves can be represented by power laws with powers monotonically going from 2 to 1. A surprising property can be found for high noise amplitudes: although the mean squared velocity according to (3.130) re-increases for large noise amplitudes, the mean squared displacements continues to monotonically decrease in strength. Even if the noise amplitude exceeds the minimum of Fig. 3.6a by one or several orders of magnitude. The findings however are not in direct contradiction as (3.130) is the stationary solution of the Fokker-Planck equation belonging to the second equation of (3.129) and does not consider that the direction of motion can be reversed when the noise amplitudes are high enough. Together with the cubic damping for high velocities, this process results in a strong variation of the current velocity and a very small net displacement.

Next, we will look at the effect of an additional driving in the p-component, first for $s = 0$. To this end, we choose a fixed value of $R_\alpha = 4.5 \cdot 10^{-6}$ corresponding to curve 3 in Fig. 3.6b so that in the α-equation the intrinsic drive still plays a significant role. Again 10000 ensemble members have been simulated for selected values of R_p and $s = 0$ (Fig. 3.6c). In our treatment of the linear case (see Eq. (3.123)) we have found an uncorrelated driving in the p- and α-components results in two contributions to the displacement (above termed I_1 and I_3). The details of the derivation indicate that we should expect the term I_3 to be the same in the nonlinear case as well. Indeed, subtracting the curve for $R_p = 0$ from the curves for $R_p > 0$ depicted in Fig. 3.6b, we find (data not shown) that the difference curves grow linear in time with a slope $\lambda = R_p^2$ just as predicted by (3.126).

The last simulation (Fig. 3.6d) deals with the influence of correlated driving. For $R_\alpha = 4.5 \cdot 10^{-6}$ and $R_p = 2 \cdot 10^{-2}$ with increasing s the displacement grows in strength. The same result can be found also for other values of R_p and R_α. Unfortunately we have no analytical prediction for the dependence of the curves on s, however the simulations show that the dependence is not linear as for Eq. (3.122).

We want to remark that to the authors knowledge, there are no closed analytic expressions for the mean-squared displacement in the case of active propagation so far. While we have treated only the one-dimensional case, in two or more dimensions the situation is different as while the intrinsic driving also stabilizes a certain value of the absolute velocity, the direction of propagation represents a neutral manifold. Thus, for the case that the propagation velocity stays constant and noise changes only the direction of propagation, there are analytical estimates for the mean-squared displacement by introducing an effective angular diffusion constant in the description via the Fokker-Planck equation [355, 356].

Chapter 4

Many-body Systems

In the last chapter, we have seen how the infinite-dimensional field equations describing LSs could be reduced to finite-dimensional ODEs for relevant slow quantities like positions, velocities and inner degrees of freedom. This level of description has three big advantages. First, it reveals strong formal similarities to the equations encountered in classical mechanics when position or velocity appear as relevant order parameters, thus representing a manifestation of the particle image on a mathematical basis. Second, an analytical and numerical treatment of complex processes involving many LSs is easier than in the infinite-dimensional system and for large particle numbers on long time scales even essentially enables a practical access. Third, the dynamic evolution of the ODEs is much easier to understand intuitively.

Once the reduced equations have been derived for a given field equation, they can be considered rather independently of the underlying field description whose properties are only reflected by the structures of the ODEs and the coefficients in the equations. In the spirit of universal properties of LSs, the goal of this chapter is therefore not to explore the properties of a fixed type of reduced system belonging to one special field equation. Instead, we want to explore how the interplay of different mechanisms in the reduced equations produced various dynamical many-body phenomena and what differences arise for example in the dynamics of active and classical Newton particles.

Motivated from our findings from the last chapter, as a starting point we may consider a general evolution equation of the form

$$\begin{aligned} \dot{\boldsymbol{p}}_i &= \boldsymbol{\alpha}_i + \sum_{j\neq i} \boldsymbol{F}_1(\boldsymbol{p}_j - \boldsymbol{p}_i) + R_1 \boldsymbol{\Gamma}_{i,1}(t), \\ \dot{\boldsymbol{\alpha}}_i &= k_1 \boldsymbol{\alpha}_i - k_3 |\boldsymbol{\alpha}_i|^2 \boldsymbol{\alpha}_i + \sum_{j\neq i} \boldsymbol{F}_2(\boldsymbol{p}_j - \boldsymbol{p}_i) + R_2 \boldsymbol{\Gamma}_{i,2}(t). \end{aligned} \tag{4.1}$$

Here, the indices i and j denote the different LSs. Eq. (4.1) contains many of the different reduced equations discussed previously. For $\boldsymbol{F}_1 = \boldsymbol{0}$, $k_1 = k_3 = R_1 = R_2 = 0$, we have Newton equations for the dynamics of classical particles and LSs in the translationally invariant NLS equation. With $\boldsymbol{F}_1 = \boldsymbol{0}$, $R_1 = 0$ we obtain the prototype equations commonly to as a phenomenological model for active Brownian motion [357], for example in the context of dusty plasmas [348], myosin heads on actin filaments [349, 350], swarms of fishes and daphnia [351], traffic flow [352] and even sociological systems [353]. The

choice $R_1 = R_2 = 0$ yields the deterministic motion of LSs in reaction-diffusion systems we derived above. The system (4.1) provides our "workbench" for this chapter. We will vary one or several coefficients and "switch on and off" different terms in order to explore the action of the individual constituents of the system.

All parameters together with the functions $\boldsymbol{F}_1$ and $\boldsymbol{F}_2$ and the properties of the noise forces $\boldsymbol{\Gamma}_{1,2}(t)$ produce a very high-dimensional parameter space although some parameters can be eliminated by renormalizing the variables. While many of our analytic statements on two-particle interaction below do not depend on a special choice of the above quantities, for numerical simulations we have to choose fixed values at least for some quantities. The most important choice is related to the interaction function. We have seen in Fig. 3.4 that attractive, repulsive as well as mixed types of short-ranged interaction forces are possible. Furthermore, in the literature also long-ranged interactions have been considered in the context of active Brownian particles [358]. In the following, we will mainly considered mixed attractive-repulsive interactions as bound states are generic for the latter. In some sense, the mixed-type interaction can be considered prototypical not only for LSs but can be found in a similar form also for classical particles with van-der-Waals-like types of interaction typically associated with a Morse or Lennard-Jones potential.

A good choice for an oscillatory interaction function is given by the function depicted in Fig. 3.4c which we derived rigorously from a reaction-diffusion system. Aside from representing a realistic example, the interaction function has the advantage that the analytic fitting function (3.101) is available. However, the function was obtained for weakly interacting LSs and thus holds only above a certain minimal distance. In the original field equations, an approach of two LSs to a smaller distance potentially results in events like fusion, generation etc which we can not account for in our current consideration on the basis of ODEs. While we therefore generally try to choose the other system parameters in such a way that the distances stay above the critical minimal distance, a further approach can not always be avoided. Unfortunately, for the fitting function (3.101) we have $F(d) \to 0$ for $d \to 0$, i.e. an additional lock-in distance at the origin. To ensure that the LSs do not lock in at this point, we extend our analytical fitting function (3.101) as

$$F(d) = \begin{cases} \frac{-d_1}{d^{1/2}} \exp(-d_2 d) \cos(d_3(d-d_4)) & \text{for } d > d_4 - \frac{\pi}{d_3} \\ \frac{d_1}{d^{1/2}} \exp(-d_2 d) & \text{otherwise} \end{cases} . \tag{4.2}$$

In this way, the function is essentially the same as before in the range where the original derivation is valid and becomes strongly repulsive for small distances as $F(d) \sim d^{-1/2}$ for $d \to 0$. We want to state (data not shown here) that the numerical results are always strongly similar for different extensions of (3.101) as long as the interaction is purely repulsive for small d.

4.1 Non-fluctuating systems

In the first half of this chapter, we explore deterministic dynamics that are obtained by choosing $R_1 = R_2 = 0$ in (4.1). We will first consider a number of dynamical phenomena involving only two LSs (bound states, oscillation, rotation) and their dependence on

two central aspects. First, we want to compare classical Newton particles with active particles under similar conditions. Second, we want to find out how a more complex coupling structure with $F_1(d) \neq 0$ which is not encountered for classical particles alters the dynamical properties. Later on, we turn to processes involving larger numbers of LSs.

4.1.1 Analytic considerations in one-dimensional systems

Case 1: Starting with two LSs in one spatial dimension, we first consider the "classic" Newtonian case determined by the evolution equation

$$\dot{p}_i = \alpha_i, \quad \dot{\alpha}_i = F_2(p_j - p_i). \tag{4.3}$$

Under the transformations $d_- = p_2 - p_1$, $d_+ = (p_2 + p_1)/2$ the equation turns into

$$\ddot{d}_- = 2F_2(d_-), \quad \ddot{d}_+ = 0. \tag{4.4}$$

This reflects the well-known result that under central force interaction, the center of mass of two particles propagates unperturbed while the central force influences the relative distance. One may thus consider (4.4) as an equation of motion for an undamped single particle in the potential $V(d)$, where the latter is the negative antiderivative of $F_2(d)$. In particular, it is well possible that when $F_2(d)$ oscillates with distance, the particle undergoes a periodic oscillation in one of the potential valleys if the initial conditions are appropriate. The minima of the potential $V(d)$ correspond to stable fixed points of $F(d)$.

Case 2: In a next step, we will consider the extension

$$\dot{p}_i = \alpha_i + F_1(p_j - p_i), \quad \dot{\alpha}_i = F_2(p_j - p_i), \tag{4.5}$$

which has no direct mechanical counterpart, but helps clarifying the influence of the extended coupling structure in more complex situations. Going again to central coordinates, one finds

$$\ddot{d}_- = 2F_2(d_-) + 2F_1'(d_-)\dot{d}_-, \quad \ddot{d}_+ = 0. \tag{4.6}$$

Using the image of a single particle in the potential $V(d)$ as above, we now encounter a position-dependent change of the velocity determined by $F_1'(d)$. Motivated by our findings for reaction-diffusion equations, we may consider in particular $F_1 \sim F_2$. Looking at an oscillation in the potential valley around a point d_0 for this particular case, we have $F_1'(d_0) < 0$ when the fixed point is stable. Thus, the oscillation is damped for small oscillation amplitudes and d_- will converge to d_0. Consequently, for the special choice of the "force functions" a uniformly propagating stationary molecule of LSs is preferred with respect to an oscillating cluster. For other choices of $F_1(d)$ and $F_2(d)$, this statement is generally not valid.

Case 3: In order to explore the interplay of active propagation and interaction, we will now analyze

$$\dot{p}_i = \alpha_i, \quad \dot{\alpha}_i = k_1\alpha_i - k_3|\alpha_i|^2\alpha_i + F_2(p_j - p_i). \tag{4.7}$$

In spite of the nonlinearity in the equation it is again reasonable to transform (4.7) into central coordinates. As a result, we have

$$\begin{aligned} \ddot{d}_- &= k_1\dot{d}_- - k_3\dot{d}_-(\frac{1}{4}\dot{d}_-^2 + 3\dot{d}_+^2) + 2F_2(d_-), \\ \ddot{d}_+ &= k_1\dot{d}_+ - k_3\dot{d}_+(\frac{3}{4}\dot{d}_-^2 + \dot{d}_+^2). \end{aligned} \tag{4.8}$$

The possible dynamics in the four-dimensional phase space of (4.8) is already quite complicated. Let us therefore consider first the second equation alone. For fixed d_-, it has fixed points characterized by $\dot{d}_{+,0}^2 = (k_1 - k_3\frac{3}{2}\dot{d}_-^2)/b$, which can either be zero or two symmetric finite values. As $\dot{d}_-^2$ is always positive, the dynamics is such that the system tries to converge against one of the fixed points which can however move to other values in the course of time if the restriction of fixed d_- is dropped. If $\dot{d}_{+,0}$ manages to reach zero at $t = t_0$ (which holds for example if $a < b\frac{3}{2}\dot{d}_-^2$ for a sufficiently long time interval) the acceleration of the center vanishes for all $t > t_0$ so that the center stays at rest arbitrarily long afterwards. In contrast, for a finite $\dot{d}_{+,0}$ this does not hold as changes in $\dot{d}_-$ modify the position of the fixed point.

Let us point out two particularly relevant scenarios in combination with the first equation. If the dynamics is such that the initial separation d_- is close to a stable fixed point d_0 of $F_2(d)$ with $|\dot{d}_+| \gg |\dot{d}_-|$ close to $\dot{d}_{+,0}$, $\dot{d}_-$ converges to zero because of the large cubic damping rate, and d_- converges to d_0, marking a stable stationary state independent of $\dot{d}_+$. In this case, the second equation can be solved directly, and in the long-time limit one arrives at $\dot{d}_+^2 = k_1/k_3$. In other words, if the LSs start with a configuration close enough to a moving bound state, in the long-time limit one obtains the latter propagating with the intrinsic velocity of the single LSs.

The second scenario we are interested in occurs when initially the center of the LSs is close to resting and the LSs approach each other. In this case, $|\dot{d}_+| \ll |\dot{d}_-|$, and as discussed above $\dot{d}_{+,0}$ is likely to take the stable fixed point zero. Then, the first equation in (4.8) can be interpreted as an equation of motion for a single active particle at the position d_- in a potential given by $2V(d_-)$. It is intuitively not clear whether in this situation the particle will oscillate, perform a chaotic type of motion, escape from the potential or come to rest. We therefore choose a suitable representation of the problem by decomposing it into a conservative and a dissipative part. Introducing the "impulse" and "position" variables $q' = d_-$ and $p' = \dot{d}_-$, for $\dot{d}_+ = 0$ the system (4.8) can be rewritten as

$$\begin{aligned} \dot{q}' &= \frac{\partial H(q',p')}{\partial p'}, \qquad \dot{p}' = -\frac{\partial H(q',p')}{\partial q'} + k(p')\frac{\partial H(q',p')}{\partial p'} \\ \text{with} \quad H(q',p') &= \frac{p'^2}{2} + 2V(q'), \qquad k(p') = k_1 - \frac{k_3}{4}|p'|^2. \end{aligned} \tag{4.9}$$

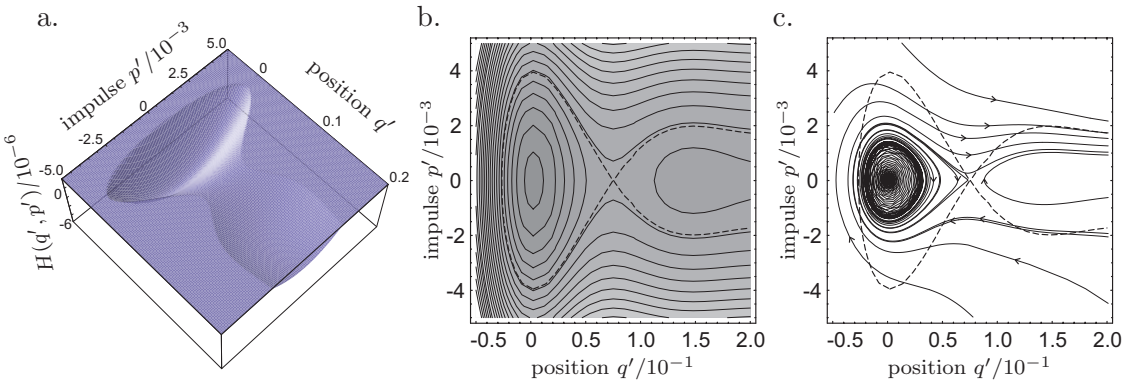

Figure 4.1: Three-dimensional (a.) and contour plot (b.) of the Hamiltonian $H(q', p')$ according to (4.9) with the interaction function depicted in Fig. 3.4c. The contour lines correspond to the sets $A(E)$ defined in the text, the special contour line $A(E_{\max})$ for the valley on the left is marked by a thicker dashed line. The last figure (c.) shows trajectories defined by (4.9) with $k_1 = 2.4 \cdot 10^{-4}$, $k_3 = 6500$, indicating the existence of a limit cycle.

We note that $k(0) > 0$ and that there is a $p'_0 = 2\sqrt{k_1/k_3}$ so that $k(p') < 0$ for $p' > p_0$. Looking at the time evolution of the Hamiltonian, a direct calculation using the definitions in (4.9) shows that

$$\begin{aligned} \dot{H} &= p'\dot{p}' + 2\frac{\partial V(q')}{\partial q'}\dot{q}' \\ &= p'\Big(-\frac{\partial H}{\partial q'} + k(p')\frac{\partial H}{\partial p'}\Big) + 2\frac{\partial V(q')}{\partial q'}p' \\ &= -2\frac{\partial V(q')}{\partial q'}p' + 2\frac{\partial V(q')}{\partial q'}p' + k(p')\frac{\partial H}{\partial p'}p' \\ &= k(p')\Big(\frac{\partial H}{\partial p'}\Big)^2. \end{aligned} \tag{4.10}$$

After this generally valid calculation, let is now come to the case of oscillatory particle interaction where $V(q')$ must have at least one valley as the interaction function has one stable fixed point, which we without loss of generality assume to be located at $q' = 0$. In this case which can mathematically be expressed by the fact that there is an environment $U_\epsilon(q' = 0)$ in which $q'\frac{\partial V(q')}{\partial q'} > 0$, $H(q', p')$ also forms a two-dimensional valley close to the origin (compare Fig. 4.1a). One may thus define energy contour lines $A(E) = \{(q', p')|H(q', p') = E\}$ which do not intersect close to the origin due to the above arguments (Fig. 4.1b). Defining $C(E) = \{(q', p')|H(q', p') < E\}$, $C(E_1) \subset C(E_2)$ for $E_1 < E_2$ holds close to the origin. For realistic situations, the interaction force decays with distance, and thus there is a maximal $E_{\max}$ marking the lowest point in the "valley rim" of $H(q', p')$ for which the above statements hold. In the origin $k(0) > 0$. This means that when the particle rests inside the potential minimum, a slight perturbation leads to an increase of the Hamiltonian. The dissipative effects are thus so strong that they can overcompensate the transformation from kinetic into potential energy.

A problem that occurs in our context is that the function k is just dependent on p', and we know that this value can not overcome p'_0. Unfortunately, there is no explicit

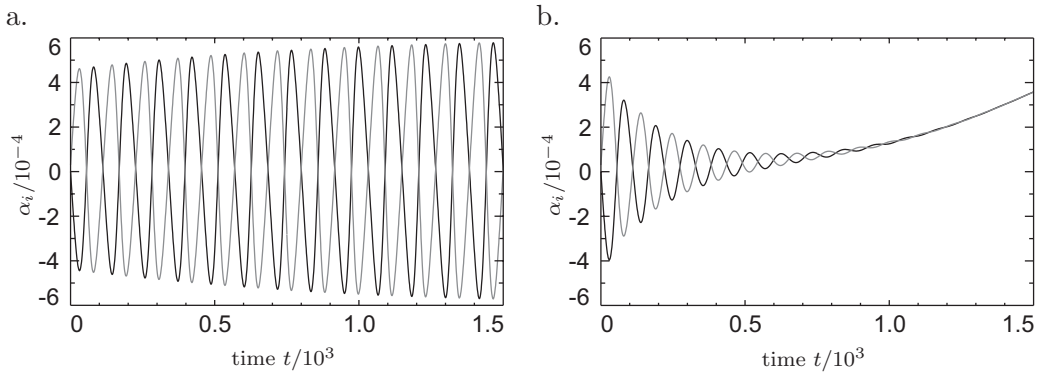

Figure 4.2: Oscillating and propagating bound states of two LSs. a. Time evolution of the variables α_i, $i = 1, 2$ (black and grey lines) according to (4.7) with an interaction function $F_2(d) = 0$, $F_2(d) = F(d)$ with $F(d)$ as in Fig. 3.4c, an initial separation $d_- = 0.18$, $k_1 = 2.4{\cdot}10^{-3}$, $k_3 = 6500$ and $\alpha_1(0) = 0$, $\alpha_2(0) = 3 \cdot 10^{-5}$. The result is the formation of a stable oscillating molecule. b. The same situation and initial conditions, this time with $F_1(d) = F(d)/0.3$. The outcome is the formation of a propagating bound state.

bound on q' so that one has to rely on a phase space plot of the dynamics given by (4.9) so prove the existence of a stable limit cycle in the Hamilton valley (see Fig. 4.1c). It is noteworthy to point out that for an equation of the form

$$\partial_t p = \alpha + \boldsymbol{F}_1(p), \quad \partial_t \alpha = k_1\alpha - k_3|\alpha|^2\alpha + \boldsymbol{F}_2(p), \tag{4.11}$$

which describes a single active particle interacting with a spatial inhomogeneity (compare Eq. (3.106)) it is also possible to find a Hamiltonian formulation similar to (4.9) in which the function k dependent on both p' and q'. In this case, there is a closed contour line with $H = E_b$ for which $k(p', q') = 0$ and where $k < 0$ in a region outside the area marked by this contour line. If in such a case the parameters are such that $E_b < E_{\max}$ a particle starting in $C(E_b)$ is confined by the energy line $A(E_b)$, and we thus know that we have a confined two-dimensional dynamics inside $C(E_{\max})$ with an (single) unstable fixed point inside the Poincaré-Bendixon theorem can be applied [359], saying that the dynamics will converge against a stable limit cycle. The corresponding calculation is rather lengthy and shall not be carried out at this point, but can be found in detail in [360].

Case 4: We now consider the dynamic equation

$$\dot{p}_i = \alpha_i + F_1(p_j - p_i), \quad \dot{\alpha}_i = k_1\alpha_i - k_3|\alpha_i|^2\alpha_i + F_2(p_j - p_i) \tag{4.12}$$

which reflects the deterministic evolution of intrinsically propagating and interacting LSs in reaction-diffusion systems. Compared to case 3, the more complex coupling structure makes analytical statements much more difficult. We want to stress however one central point. It is clear that (4.12) represents a hybrid case of (4.5) and (4.7). For the former equation, we have seen that the oscillations are suppressed if $F_1(d) \sim F_2(d)$ while for the latter an oscillating state is generic for appropriate initial conditions as given above. A

number of numerical simulations confirms that the double coupling structure in (4.12) also suppresses oscillations in spite of the active propagation of the individual LSs. This is visualized in Fig. 4.2. Here we simulate the evolution of two LSs with almost vanishing initial values of α. To break the symmetry of the initial conditions, the initial values of α are given an extremely small difference. Fig. 4.2a shows the evolution of the α-component for case 3 discussed above. As analytically predicted, both LSs are accelerated by the interaction force and form a molecule with a center at rest and the individual particles performing antiphase oscillations. In Fig. 4.2b we use the same conditions except for a change of the coupling structure ($F_1(d) = F_2(d)/0.3$). The result is that the extremely small difference in the initial velocities is sufficient to break the symmetry of the long-time solution so that the LSs form a bound state propagating in a direction determined by the initial conditions with the mutual distance of the LSs relaxing to a constant value.

In the course of this chapter we will see that the above observations are essential for explaining a variety of phenomena involving the dynamics of large numbers of LSs.

4.1.2 Analytic considerations in two-dimensional systems

From our one-dimensional examples, we have already obtained some information on bound, uniformly propagating and oscillating states. Generalizing the equations of motion to two spatial dimensions, the dynamics may become significantly more complex due to the different topology of the two-dimensional space. As our interest lies particularly on long-time solutions, we will only have a look at bound states without oscillations. In two-dimensional space, these states do not necessarily have to propagating uniformly along a line with a fixed distance vector, but instead it is also possible that two LSs form a rotating pair. For a closer look on this issue, we will again use the hierarchy of systems from above.

Case 1: The two-dimensional generalization of (4.3) leads to

$$\ddot{\boldsymbol{d}}_- = 2F_2(d_-)\frac{\boldsymbol{d}_-}{d_-}, \quad \ddot{\boldsymbol{d}}_+ = \boldsymbol{0}. \tag{4.13}$$

where $\boldsymbol{d}_- = \boldsymbol{p}_2 - \boldsymbol{p}_1$, $\boldsymbol{d}_+ = (\boldsymbol{p}_2 + \boldsymbol{p}_1)/2$. This problem which effectively corresponds to the motion of a single particle under a central force potential is well known in classical mechanics for example for the motion of planets, and thus the solution is straightforward. Both energy E and angular momentum $\boldsymbol{L}$ defined by

$$E = \frac{\dot{d}_-^2}{2} + \frac{L^2}{2d_-^2} + 2V(d_-), \quad \boldsymbol{L} = \boldsymbol{d}_- \times \dot{\boldsymbol{d}}_-, \tag{4.14}$$

are conserved, and thus the problem can be described by the motion of a single particle in the effective potential

$$V_{\text{eff}}(d_-) = \frac{L^2}{2d_-^2} + 2V(d_-). \tag{4.15}$$

This is illustrated for two different values of L in Fig. 4.3a, again with the oscillatory interaction function from Fig. 3.4c. The initial conditions determine the conserved value

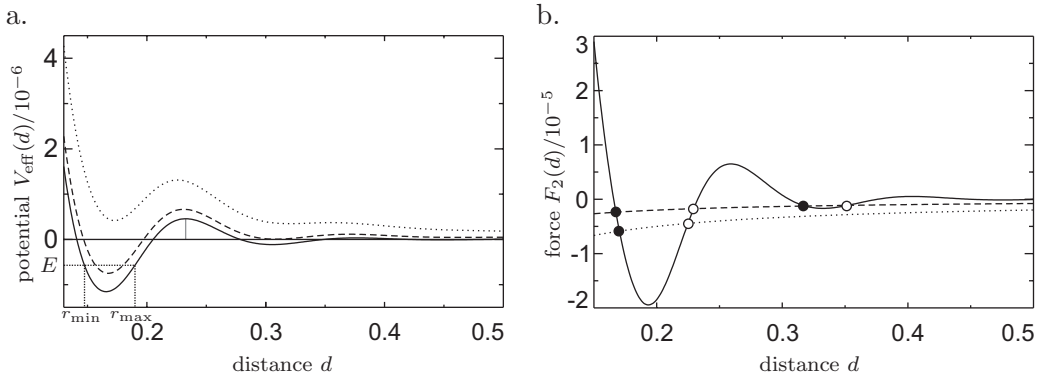

Figure 4.3: Bound rotating states of LSs in two dimensions. a. Effective potential $V_{\text{eff}}(d)$ according to (4.14) with the interaction function from Fig. 3.4c and the three cases $L = 0$ (solid line), $L = 1.5 \cdot 10^{-4}$ (dashed line) and $L = 3 \cdot 10^{-4}$ (dotted line). For a given total energy E and an angular momentum L, the distance can oscillate between $r_{\min}$ and $r_{\max}$ if the initial conditions lie inside a potential valley. b. Formal compensation of the interaction force $F(d)$ (solid line) by the formal centrifugal forces as given by the first case in (4.26). The latter are depicted for $k_1/k_3 = 2 \cdot 10^{-7}$ (dashed line) and $k_1/k_3 = 5 \cdot 10^{-7}$ (dotted line), leading to different numbers of stable and instable fixed points.

of L and thus also the point whether $V_{\text{eff}}(d_-)$ has local minima or not. When the initial conditions are chosen in such a way that the particle starts inside a potential valley and the energy does not exceed the local boundaries of the valley, the particle oscillates inside the valley between two radii $r_{\min}$ and $r_{\max}$, meaning that returning to the two-particle image, the particles form a rotating state with a distance varying periodically in time. In order to stabilize a constant radius, the energy has to be chosen such that it takes directly the value of a local potential minimum, the initial radius of course has to match this choice as well. Note that due to the first term on the right-hand side of (4.15), the constant radii will not directly correspond to stable lock-in points of the interaction force.

Case 2: Considering the case

$$\dot{\boldsymbol{p}}_i = \boldsymbol{\alpha}_i + F_1(|\boldsymbol{p}_j - \boldsymbol{p}_i|)\frac{\boldsymbol{p}_j - \boldsymbol{p}_i}{|\boldsymbol{p}_j - \boldsymbol{p}_i|}, \quad \dot{\boldsymbol{\alpha}}_i = F_2(|\boldsymbol{p}_j - \boldsymbol{p}_i|)\frac{\boldsymbol{p}_j - \boldsymbol{p}_i}{|\boldsymbol{p}_j - \boldsymbol{p}_i|}, \tag{4.16}$$

the energy arguments used in the first case can not be applied directly. Following an idea proposed by Moskalenko [313], we will thus introduce the four variables $s_1 = |\boldsymbol{p}_2 - \boldsymbol{p}_1|^2$, $s_2 = |\boldsymbol{\alpha}_2 + \boldsymbol{\alpha}_1|^2/4$, $s_3 = |\boldsymbol{\alpha}_2 - \boldsymbol{\alpha}_1|^2$ and $s_4 = (\boldsymbol{p}_2 - \boldsymbol{p}_1) \cdot (\boldsymbol{\alpha}_2 - \boldsymbol{\alpha}_1)$, furthermore we introduce $f_i(s_1) = F_i(|\boldsymbol{p}_j - \boldsymbol{p}_i|)/|\boldsymbol{p}_j - \boldsymbol{p}_i|$. This helps in producing a certain analogy to the one-dimensional case. To reduce the dimensionality of the whole problem, one may assume that in a stationary state, both LSs are equal in the sense that $\alpha_1 = \alpha_2$. Then, (4.16) simplifies to

$$\begin{aligned} \dot{s}_1 &= 2s_4 + 4f_1(s_1)s_1, \\ \dot{s}_3 &= 4f_2(s_1)s_4, \\ \dot{s}_4 &= s_3 + 2f_1(s_1)s_4 + 2f_2(s_1)s_1. \end{aligned} \tag{4.17}$$

As we are only interested in stationary solutions, we directly see from the second equation that either $f_2(s_1) = 0$ or $s_4 = 0$. The first case leads to $s_3 + 2f_1(s_1)s_4 = 0$ while the second case implies $f_1(s_1) = 0$, $s_3 + 2f_2(s_1)s_1 = 0$. For arbitrary functions f_1 and f_2, either of the relations can generally be fulfilled. However, $f_1 \sim f_2$ directly leads to $s_3 = 0$, implying that the LSs propagate in parallel so that no rotating molecule is possible.

Case 3: With the above introduced abbreviations, our next case

$$\dot{\boldsymbol{p}}_i = \boldsymbol{\alpha}_i, \quad \dot{\boldsymbol{\alpha}}_i = k_1\boldsymbol{\alpha}_i - k_3|\boldsymbol{\alpha}_i|^2\boldsymbol{\alpha}_i + F_2(|\boldsymbol{p}_j - \boldsymbol{p}_i|)\frac{\boldsymbol{p}_j - \boldsymbol{p}_i}{|\boldsymbol{p}_j - \boldsymbol{p}_i|}, \tag{4.18}$$

can be transformed into

$$\begin{aligned}
\dot{s}_1 &= 2s_4, \\
\dot{s}_2 &= 8k_1 s_2 - 2k_3(4s_2 + s_3)s_2, \\
\dot{s}_3 &= 2k_1 s_3 - \frac{k_3}{2}(4s_2 + s_3)s_3 + 4f_2(s_1)s_4, \\
\dot{s}_4 &= s_3 + k_1 s_4 - \frac{k_3}{4}(4s_2 + s_3)s_4 + 2f_2(s_1)s_1.
\end{aligned} \tag{4.19}$$

This directly tells us $s_4 = 0$ in the stationary state, so that (4.19) simplifies to

$$\begin{aligned}
0 &= 8k_1 s_2 - 2k_3(4s_2 + s_3)s_2, \\
0 &= 2k_1 s_3 - \frac{k_3}{2}(4s_2 + s_3)s_3, \\
0 &= s_3 + 2f_2(s_1)s_1.
\end{aligned} \tag{4.20}$$

As we want to avoid parallel propagation we claim $s_3 \neq 0$, so that we can conclude

$$4s_2 + s_3 = 4\frac{k_1}{k_3}, \qquad f_2(s_1) = -2\frac{\frac{k_1}{k_3} - s_2}{s_1}. \tag{4.21}$$

This basically allows for a whole number of possible combinations of s_1, s_2 and s_4. However, numerical simulations (data not shown) indicate that starting from arbitrary initial conditions generically either a propagating state or a state with $s_2 = 0$, i.e. a molecule with a resting center, is formed. The reason for this is similar to the one-dimensional counterpart discussed above: for $\alpha_1 = \alpha_2$, the second equation in (4.19) shows that once s_2 vanishes during the dynamical evolution, it remains zero independent of the evolution of the other variables. The statements remains valid also if the strict equality of the α_i is softened up, which is confirmed by an analysis of the full equation (4.18).

Case 4: The most complicated scenario is given by the structure

$$\dot{\boldsymbol{p}}_i = \boldsymbol{\alpha}_i + F_1(|\boldsymbol{p}_j - \boldsymbol{p}_i|)\frac{\boldsymbol{p}_j - \boldsymbol{p}_i}{|\boldsymbol{p}_j - \boldsymbol{p}_i|}, \quad \dot{\boldsymbol{\alpha}}_i = k_1\boldsymbol{\alpha}_i - k_3|\boldsymbol{\alpha}_i|^2\boldsymbol{\alpha}_i + F_2(|\boldsymbol{p}_j - \boldsymbol{p}_i|)\frac{\boldsymbol{p}_j - \boldsymbol{p}_i}{|\boldsymbol{p}_j - \boldsymbol{p}_i|}, \tag{4.22}$$

which under the above assumptions is equivalent to

$$\begin{aligned}
\dot{s}_1 &= 2s_4 + 4f_1(s_1)s_1,\\
\dot{s}_2 &= 8k_1 s_2 - 2k_3(4s_2 + s_3)s_2,\\
\dot{s}_3 &= 2k_1 s_3 - \frac{k_3}{2}(4s_2 + s_3)s_3 + 4f_2(s_1)s_4,\\
\dot{s}_4 &= s_3 + 2f_1(s_1)s_4 + k_1 s_4 - \frac{k_3}{4}(4s_2 + s_3)s_4 + 2f_2(s_1)s_1.
\end{aligned} \tag{4.23}$$

As in case 3, the second equation for $s_2 \neq 0$ implies $4s_2 + s_3 = 4\frac{k_1}{k_3}$, from which we conclude $f_2(s_1)s_4 = 0$. Assuming $s_4 = 0$, one may subsequently derive that all s_i are except s_1 are zero, which is physically senseless. Therefore, $f_2(s_1) = 0$. For arbitrary f_1 this yields the relation $s_1 s_3 = s_4^2$ which together with the first equation gives a number of stationary solutions. For the special case $f_1 \sim f_2$ however, we again find $s_3 = s_4 = 0$ meaning that no rotating states exist. As a consequence, we drop our first assumption and consider $s_2 = 0$, i.e. antiparallel vectors $\boldsymbol{\alpha}_i(t)$. This of course simplifies the last two equations of the system (4.23). However, in order to produce a result comparable to case 3, we have to make further assumptions of the relation of $f_1(s_1)$ and $f_2(s_1)$, namely $f_1 = f_2$. Then the third and fourth equation can be recombined yielding

$$\begin{aligned}
0 &= s_4 + 2f_2(s_1)s_1,\\
0 &= (s_3 - s_4)(2k_1 - 2 - \frac{k_3}{2}s_3),\\
0 &= 2k_1 s_3 - \frac{k_3}{2}s_3^2 + 4f_2(s_1)s_4.
\end{aligned} \tag{4.24}$$

For small k_1, because of $s_3 > 0$ the second relation of (4.24) implies $s_3 = s_4$. The final form is thus

$$s_3 = s_4 = -2f_2(s_1)s_1, \quad f_2(s_1) = -2\frac{\frac{k_1}{k_3}}{\frac{4}{k_3} + s_1}. \tag{4.25}$$

Comparing the results for the different cases, we can draw the following conclusion. Generally, there are different possible rotating states depending on the interaction functions. While the double coupling structure with $F_1 \sim F_2$ forbids rotating states in case 2, the additional action of active propagation re-enables their existence. While in the single-coupling case with active propagation the velocity is perpendicular to the line connecting the LSs ($s_4 = 0$), this condition is not necessary for the double-coupling case. On the other hand, at least for $F_1 = F_2$ the center of the structures must rest in the latter case, while this condition in not necessary in the first case. As a potentially surprising fact, we find that a central condition for the stable bound states with $s_2 = 0$ in both cases is the balance of two forces reading

$$F_2(d) = -2\frac{\frac{k_1}{k_3}}{d} \quad \text{and} \quad F_2(d) = -2\frac{\frac{k_1}{k_3}}{\frac{4}{k_3 d} + d}, \tag{4.26}$$

for single and double coupling, respectively. An illustration of this balance in the first case is given in Fig. 4.3b, reminding of the balance of centrifugal and attracting forces that can also be derived from the classical consideration of case 1 when considering a force instead of an energy balance (compare (4.14)). The second case is qualitatively extremely similar.

4.1.3 Numerical calculations in two-dimensional systems

We now turn to systems with larger numbers of particles. In this context, the expression "large" refers to particle numbers around 100 and not around 10^{23} as frequently considered for classical systems in the thermodynamical limit. The reason for this choice is not only of practical nature, but related to the fact that the number of LSs that can possibly be generated in experimental systems does usually not exceed 100. Even if larger numbers could be generated, the latter would lie far below the numbers considered in the thermodynamical limit. Like in classical mechanics, analytic statements for the "microscopic" dynamics of than more three particles can hardly be obtained, so that we will have to rely mainly on numerical calculations. However, the above discussion of two-particle interactions provides a basic for understanding important parts of the many-particle dynamics.

As we deal with deterministic systems of coupled ODEs in the following, we will use a standard fourth-order Runge-Kutta scheme in the numerical simulations. The central algorithms were implemented by M. Röttger, details can be found in [361]. In the latter work, details proving the efficiency of the used methods were given, so the central concern at this point remains the choice of adequate time steps for the chosen parameter values. Most investigations use the same parameters as in Sec. 3.4.2 so unless otherwise stated we keep the time step of the simulations at $\Delta T_1 = 0.01$. Discrete time derivatives are determined on a time scale $T_2 = 10$. Both T_1 and T_2 can be varied (in particular increased) by an order of magnitude without changing the results, however we stick to the above choice to be capable of keeping the same time scale when it comes to the simulation of stochastic Langevin equations further below, where in particular the choice of T_2 is a more delicate matter.

4.1.3.1 Free propagation

One of the conceptually most simple situations to consider is the free and unbounded motion of many particles. Our goal in this case is to compare the characteristics of the dynamics for classical particles and different realizations of active particles. A first step towards an exploration of this subject was done by Röttger who conducted simulations of the double coupling case [361]. In the following numerical simulations, we want to keep a fixed average particle density. To this end, we consider a squared area of size 4×4 with periodic boundary conditions and 81 particles. In all simulations, the interaction function $F_2(d)$ is that given by Fig. 3.4c either in the classic, single or double coupled version, and in the latter case we choose $F_1(d) = F_2(d)/0.3$ which corresponds to the rigorous derivation from the reaction-diffusion field equations. As initial condition, all particles are equally distributed by arranging them on a square grid. The initial separation of the particles is so large that they do not feel the forces caused by the other particles when the simulation starts. Furthermore, the initial velocities of the individual

particles are chosen randomly in such a way that all propagation angles are equally probable while the absolute velocity is equally distributed in an interval $[0, 2\alpha_0]$ so that the average velocity is α_0.

For classical particles the initial conditions determine the global energy and momentum which remain conserved in time. The question whether two particles can approach to a certain distance can be answered by energy arguments: let us assume that only two particles collide, then a transformation to center-of-mass coordinates (compare (4.13)) shows that the motion can be described by the dynamics of a single particle in the effective potential (4.15). When two particles approach from a large distance, a potential locking event can only take place when the kinetic energy of the single particle in the reduced description is high enough to cross the potential barriers caused by the oscillating interaction function. The energy is minimal for a central collision and takes the value $E_{\min}$ for the angular momentum $L = 0$, indicated by a grey line in Fig. 4.3a.

In the following, we will consider two situations. In the first one, $\alpha_0 = 3 \cdot 10^{-4}$ so that when two particles collide with velocity α_0 in a central collision, for the energy of the reduced particle we have $E_r \approx 0.4 E_{\min}$. In the second situation, we have $\alpha_0 = 1.52 \cdot 10^{-3}$, resulting in $E_r \approx 10 E_{\min}$. For these choices, only two of the theoretically infinitely many lock-in positions of the interaction function are of practical relevance due to the exponential decay of the interaction strength. Looking at the case $\alpha_0 = 3 \cdot 10^{-4}$, shortly after the start of the simulation we first see a stage in which the particles remain essentially isolated and perform various collisions leading to thermalization (a snapshot of the dynamics is shown in Fig. 4.4a1). Concerning the plot, we have to give a number of explanations: the size of the circle representing a particle is chosen such that the diameter corresponds to the smallest possible stable lock-in distance for the interaction function (4.2). The color is a measure for the current value of α, the smallest value taken during the whole simulation corresponds to pure blue and the largest value to pure red (see [361] for details). The color scale goes via green for intermediate values, pure green corresponds to α_0. Comparing Fig. 4.4a1 to a2 which is taken significantly later, the colors already indicate that thermalization has changed the velocity spectrum, in particular, there are some very fast LSs in the tail of the corresponding distribution. These particles have enough energy to reach overcome the repulsive interaction of other LSs and reach stable lock-in distances. When during the collision a sufficient amount of impulse is transferred the collision partners, the energy of the LS may become so small that it can not leave the trapping potential. This leads to the formation of larger clusters as indicated by a black circle in the second figure. Generally, we find a flowing equilibrium between clusters and single LSs with the properties of a classical liquid state.

When the overall kinetic energy is increased, it is easier for particles to approach each other up to close distances, however, trapping also becomes more difficult as the particles have more energy available to leave the trapping potential. An increase of α_0 to $1.52 \cdot 10^{-3}$ has some directly visible consequences for the dynamics (Fig. 4.4b). Again, after a short transient in which the particles thermalize (Fig. 4.4b1) a flowing equilibrium is reached (Fig. 4.4b2). Compared to $\alpha_0 = 3 \cdot 10^{-4}$, the number of larger clusters has strongly decreased to almost zero in the long-time limit as two colliding particles almost always separate instantly after a collision. The reason for this is that even after thermalization, the kinetic energy of the particles is in most cases larger than the energy needed to leave the trapping potential. Consequently, the state shown in

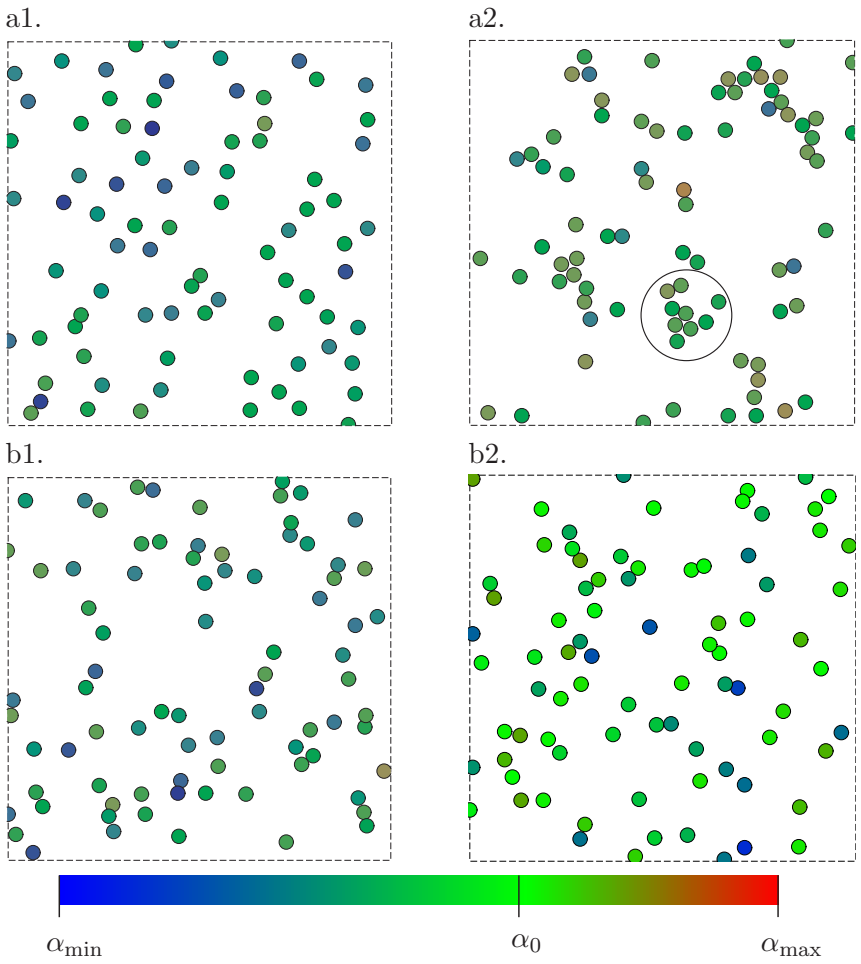

Figure 4.4: Free propagation of Newton particles with an oscillatory type of interaction function. a. Dynamics of 81 "classical" particles on the domain $\Omega = [-2, 2] \times [-2, 2]$ with periodic boundary conditions, an interaction function $F_2(d)$ as shown in Fig. 3.4c and initial conditions as given in the text for $\alpha_0 = 3 \cdot 10^{-4}$ at times $t = 8400$ (a1) and $t = 42000$ (a2). The large circle indicates a transient bound complexes of several particles. b. Corresponding sequence for $\alpha_0 = 1.52 \cdot 10^{-3}$, also for $t = 8400$ (b1) and $t = 42000$ (b2).

Fig. 4.4b has all properties of a gaseous phase.

Considering now the case of active propagation, we may again distinguish between the prototype model with single coupling in the velocity component or the double coupling derived from the dynamics of LSs in reaction-diffusion systems. Both cases turn out to be basically equivalent in their long-time behavior for high intrinsic velocities while some differences arise for low intrinsic velocities. Over a large range of parameters, the motion can essentially be characterized by the quantity α_0 which now is defined as the intrinsic particle velocity $(k_1/k_3)^{1/2}$ although of course the exact results depend on k_1 and k_3 individually. All absolute particle velocities quickly converge to this value if the initial separation of the particles is large enough.

For the single-coupling case, we choose the same values of α_0 as in the classical case via the choice $k_3 = 6500$ as well as $k_1 = 0.0006$ and $k_1 = 0.015$, respectively. In both

cases, the long-time behavior of the system is completely different from the classical case. For small intrinsic velocity (Fig. 4.5a), in the long time limit most particles lock in at the second smallest possible lock-in distance with respect to their nearest neighbors. However, due to the chosen particle density and the rather weak interaction strength at this distance the whole structures is not rigid. Instead, the particles oscillate around their equilibrium positions and the cluster experiences permanent deformations. In summary, although the cluster shows the long-ranged correlations typical for a solid, the state is "elastic" and experiences permanent changes of its structures. The situation becomes different when going to larger values of α_0. While we have experienced the formation of a gaseous state for classical propagation, in the active propagation case we find that the particles quickly lock in at the smallest possible distance and form a number of smaller clusters (Fig. 4.5b1) which finally collide and merge into one large cluster (Fig. 4.5b2) with a very rigid structure. In this state, all LSs propagate with the intrinsic velocity in the same direction. One should note that for a large cluster it is

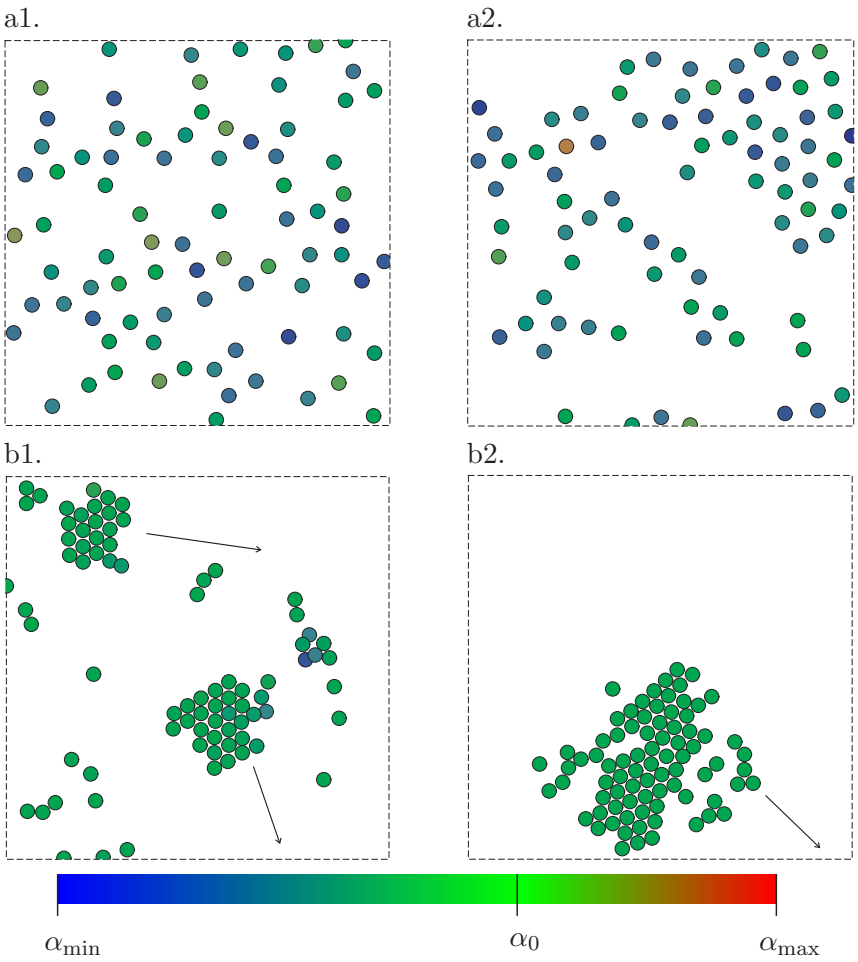

Figure 4.5: a. Dynamics of 81 active single-coupled particles with $\alpha_0 = 3 \cdot 10^{-4}$ realized by the choice $k_1 = 0.0006$ and $k_3 = 6500$. All other conditions are as in Fig. 4.4. b. The same situation with $k_1 = 0.015$, resulting in $\alpha_0 = 1.52 \cdot 10^{-3}$.

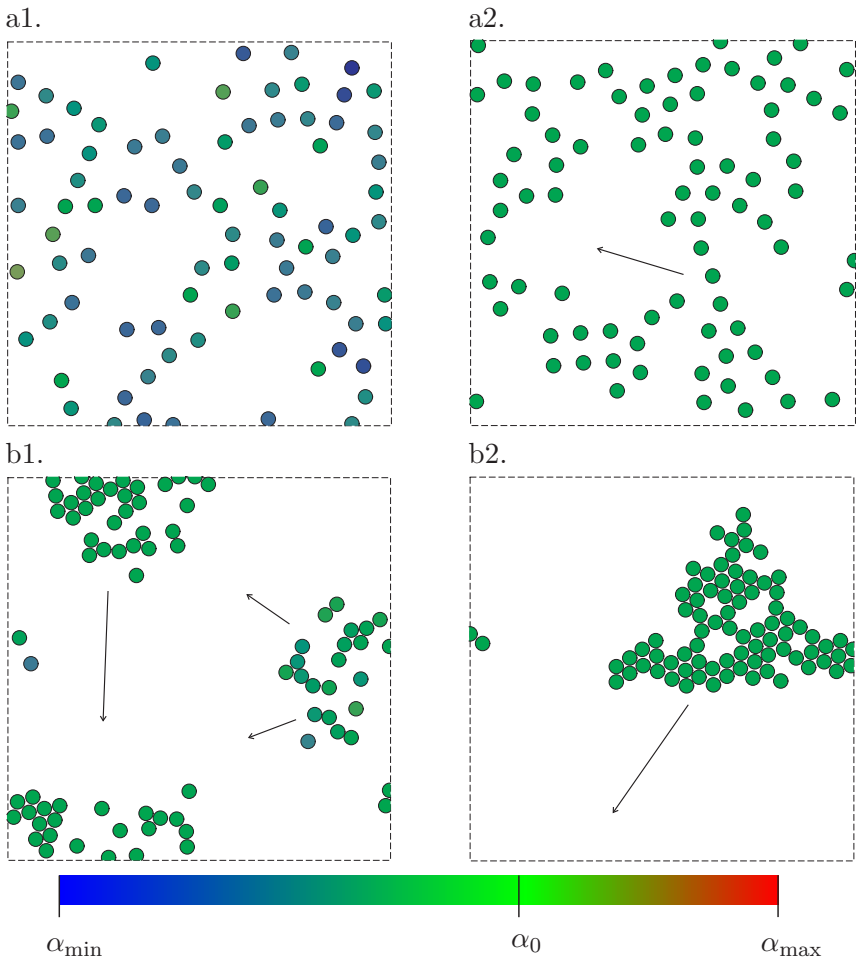

Figure 4.6: a. Dynamics of 81 active double-coupled particles with $F_1(d) = F_2(d)/0.3$, all other conditions as given in Fig. 4.5a and b.

easier to "absorb" smaller clusters than for a smaller one because its spatial extension sterically hinders the particles from re-escaping after a collision.

A central difference between classical dynamics and active propagation is that in the classical case, the particles can change their velocity only due to interaction, and energy and impulse are conserved. In the active case, both quantities are not conserved, and two rather independent mechanisms are available to change the velocity. Thus when two active particles are at a stable lock-in distance, the cluster can reach the intrinsic velocity without a change of this distance and without the necessity of the presence of other LSs to which energy and momentum have to be transferred to reduce these quantities for itself.

Fig. 4.6 corresponds to Fig. 4.5 except that the double coupling structure was used (with $F_1(d) = F_2(d)/0.3$ as found for the reaction-diffusion example). Here we see that for a given intrinsic velocity the same lock-in distances as in the single-coupling case are preferred. However, while for large α_0 the dynamics is principally the same, for the case of small intrinsic velocities a difference arises: the individual LSs do not oscillate around

their equilibrium positions in the long-time limit, but instead the cluster propagates uniformly with its intrinsic velocity. This finding is directly connected to our analytical considerations in Sec. 4.1.1. Here, we have found that while the single-coupling state prefers oscillating states under many circumstances, the double-coupling dampens these oscillations and causes a uniform propagation (compare also Fig. 4.2).

4.1.3.2 Confined motion

Under randomly chosen initial conditions, the unconfined propagation of active particles typically with oscillatory interaction leads to the formation of one large cluster independent of how the equations are coupled. Another interesting scenario can be constructed by looking at experiments in planar ac gas-discharge systems in which many LSs are confined in a domain of circular shape [362]. In this case, it was found that the LSs arrange on an almost hexagonal grid and perform a collective rotational motion around the center of the domain. It is very likely that the phenomenon is due to active motion combined with a mixed attractive-repulsive interaction law. This is supported by the fact that for a given geometry and fixed parameters, in the experiment exactly one value for the absolute angular velocity can be observed. Furthermore, stable co-rotating defects in the hexagonal structure have been found, which do not match the assumption of a purely repulsive interaction between the LSs as encountered for example for Coulomb crystals [363]. We want to clarify whether the experimental observations can be reproduced by the reduced equations we have been discussing so far. While the active propagation of single LSs in the mentioned ac gas-discharge systems has been verified and quantitatively measured [320], unfortunately there are currently no measurements on interaction laws. A complete set of parameters both for single and interacting LSs is available for planar dc gas-discharge systems ([157, 173], compare also Fig. 3.5), but in these systems no rotational motion was observed as it was not possible to generate enough LSs due to experimental limitations.

To overcome this problem, we choose the parameter set for the dc case. The parameters are obtained via stochastic analysis methods for which a coupling structure with an interaction force only in the $\boldsymbol{\alpha}$-component was assumed (termed case 3 above). It was shown [173] that the experimentally obtained interaction force could be well represented using the analytical interaction function (4.2) originally derived for reaction-diffusion systems. This is not too surprising as the function reflects the decay of Bessel functions for large arguments, the latter typically appearing in the context of describing the superposition of exponentially decaying oscillatory tails. The parameters characterizing the interaction are taken as $d_1 = 1386$, $d_2 = 1.2167$, $d_3 = 5.27957$ and $d_4 = -1.604$ exclusively in this section. A direct connection to experimental data can be obtained by taking all units as multiples of millimeters and seconds. In the experiments, the domain in which the LSs propagate is confined by a mechanical spacer which the LSs can not penetrate. We will model this confinement by a repulsive force which vanishes inside a circular domain and quickly increases in strength outside. Shifting the center of the domain to the origin, the additional force can be conveniently expressed in polar coordinates as

$$\boldsymbol{F}_{\mathrm{sp}}(r) = \begin{cases} \mathbf{0} & \text{for } r < r_0 \\ c(r - r_0)^2 \boldsymbol{e}_\theta & \text{for } r \geq r_0 \end{cases} . \tag{4.27}$$

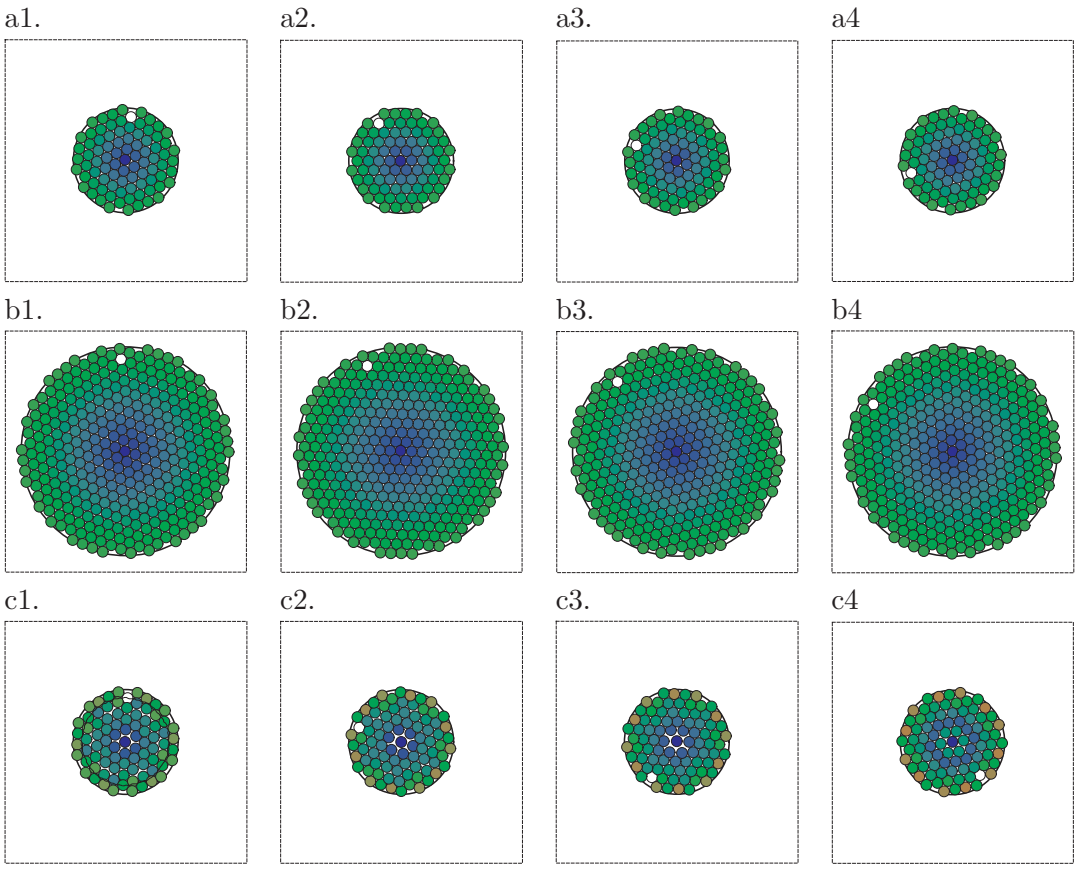

Figure 4.7: Rotation of a hexagonal cluster of active particles ($k_1 = 0.8$, $k_3 = -0.042$) with $c = 200$ as described in the text. a. Simulation with small spacer radius $r_0 = 4$. The snapshots were taken at $t = 8, 9, 10$ and 11 from (a1 to a4). The color-coding corresponds to that used in Fig. 4.5, one LSs was marked in white to indicate the course of the dynamics. b. The same sequence as in a., however with $r_0 = 16$. c. Repetition of the simulation in a. with a higher intrinsic velocity ($k_1 = 2$) producing oscillations of the cluster. This is also indicted by the particle trajectory for one rotation plotted in the first figure.

With this choice, the repulsing force by the spacer is always directed to the origin. For setting the repulsion strength c, we have to state that in the experiment, the intrinsic velocities of the particles lie between $v = 0$ and $v = 20$. By choosing $c = 200$, the LSs can hardly penetrate the circular boundary defined by $r = r_0$. Finally, the parameters for the active propagation are taken as $k_1 = 0.8$, $k_3 = -0.042$ so that $\alpha_0 = 4.36$. Noise which is always present in the experiment is neglected in the current investigation. We will see that most experimental observations are reproduced also without noise.

As we change the parameters in the functions significantly with respect to our previous investigations (which is exclusively done in this section), we have to rethink our consideration on the time step used for the numerical simulation. Consequently, the simulation time step is decreased to $\Delta T_1 = 5 \cdot 10^{-5}$ while the ratio of T_1 and T_2 is kept the same as before. To determine the initial conditions for the simulation, we note that in the experiment the LSs are arranged on a almost hexagonal grid which is typical

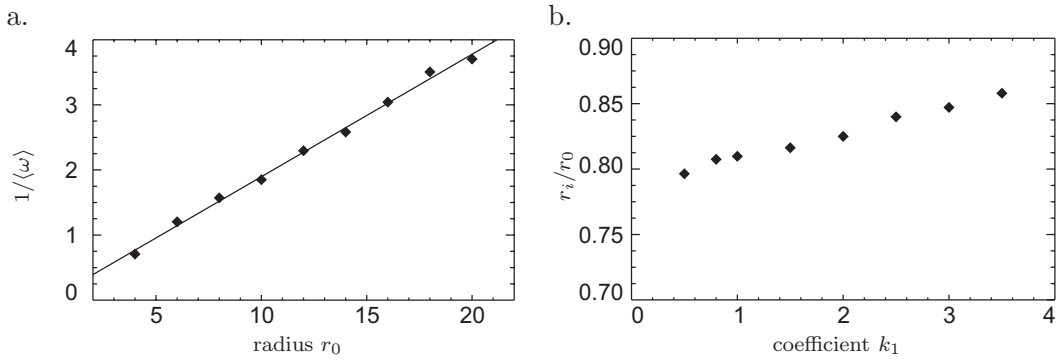

Figure 4.8: Detailed analysis of rotating particle clusters. a. Dependence of the reciprocal averaged rotational velocity $\langle\omega\rangle$ on the radius r_0 for the parameters used in Figs. 4.7a and b showing a linear dependence. b. Ratio r_i/r_0 for different values of the coefficient k_1 determined for $r_0 = 10$.

for attractive-repulsive interaction functions like (4.2) because the most dense stable arrangement in which the LSs are positioned on stable lock-in points of the interaction force caused by their neighbors is just the hexagonal one. We thus create a hexagonal grid with the lock-in distances of nearest neighbors just corresponding to the smallest stable fixed point of (4.2). One LS is positioned in the origin, and only those members of the grid for which $r \leq r_0$ are kept. As initial velocity, we take an already rotating state via $\alpha_x = \alpha_0 p_y/r_0$, $\alpha_y = -\alpha_0 p_x/r_0$.

Numerical simulations have been carried out for different r_0 ranging from $r_0 = 4$ to $r_0 = 20$. Qualitatively the dynamics is similar in all cases, as can be seen from Fig. 4.7a and b for $r_0 = 8$ and $r_0 = 16$. For the above choice of parameters, the interaction forces are strong enough to keep the LSs close to their equilibrium positions to that the whole hexagonal arrangements of clusters rotates as one solid body. The colors indicate that for all radii of the domain, those LSs which are close to the boundary of the domain move with their equilibrium velocity. This of course directly implies that the LSs closer to the origin must on average move with a velocity smaller than the intrinsic one, which can also be seem from the figures. An interesting point is given by the fact that with the special initial conditions given above, the cluster can even perform a stable rotation for $c = 0$, i.e. without a confining area. The same rotating motion can also be induced using random initial conditions, which however now requires a confining area to cause the initial transient process to develop in the correct way.

Before coming to some quantitative investigations, we briefly want to address the point what happens when the intrinsic velocity is increased, for example via a change of the coefficient k_1. For $k_1 \approx 2$, the overall motion is still dominated by rotation, while in particular the inner LSs begin conducting oscillations around their equilibrium positions, which is shown in Fig. 4.7c using again $r_0 = 8$ as in Fig. 4.7a. The LSs close to the boundary are less affected, however their dynamics shows small oscillations as well (see for example the trajectory plotted in Fig. 4.7c1). A further increase of the intrinsic velocity increases the strength of the fluctuations, and the rotational motion of the cluster is superimposed with a breathing-like dynamics in radial direction. Finally, when the intrinsic velocity becomes too high the LSs can overcome the forces keeping

them near their equilibrium position and the solid structure decays to a ring-like one.

In the following, we are interested in the rotating structure for small intrinsic velocities such that the rotating state is essentially isotropic with respect to its center. In Fig. 4.8a, we investigate the dependence of the time-averaged rotation velocity $\langle\omega\rangle$ of the cluster around the origin (which is rather well-defined for the state under consideration and determined in the time interval shown in Fig. 4.7) as a function of the radius r_0. The figure shows that in a good approximation $\langle\omega\rangle \sim 1/r_0$. From this dependence, one may directly estimate that the ratio r_i/r_0 with r_i denoting the radius for which the LSs propagate with the intrinsic velocity α_0 is more or less independent of r_0. We may thus take a fixed radius $r_0 = 10$ and look at the values of r_i/r_0 as a function of α_0 by varying the coefficient k_1. The results are shown in Fig. 4.8b. For the whole range of velocities is which a stable rotation can be observed, the ratio r_i/r_0 lies slightly above 0.8, meaning that only those LSs close to the outer boundary of the structure move faster than the intrinsic velocity. It should however be kept in mind that on the one hand, the number of structures propagating with a given velocity increases linearly with the distance r from the origin and that on the other hand, the "torque" on the cluster caused by the particles becomes larger with increasing radius. A closer look on Fig. 4.8b reveals that the ratio r_i/r_0 slightly increases with increasing intrinsic velocity. A rather intuitive explanation for this can be given by considering that the LSs remain exactly on their equilibrium positions only when the cluster is at rest or when the interaction strength becomes extremely large. During rotation, the particles experience "centrifugal forces" that increase their distance from the center of rotation. With all particles increasing their distance to the origin due to this effect the more the higher the intrinsic velocity, the ratio r_i/r_0 must naturally increase as well.

Another point we want to address is the rotation of structures with defects which is also observed in the experiments. Basically, one may state that over a large range of radii r_0, one may remove one or several LSs from the cluster and still observe a rather regular rotational motion. A central aspect in this context is that removing LSs generally breaks the discrete rotational symmetry of the system and produces a shift of the center of mass of the cluster, which will cause the latter to change its position during the dynamical evolution. Furthermore, replacing LSs by defects generally weakens the

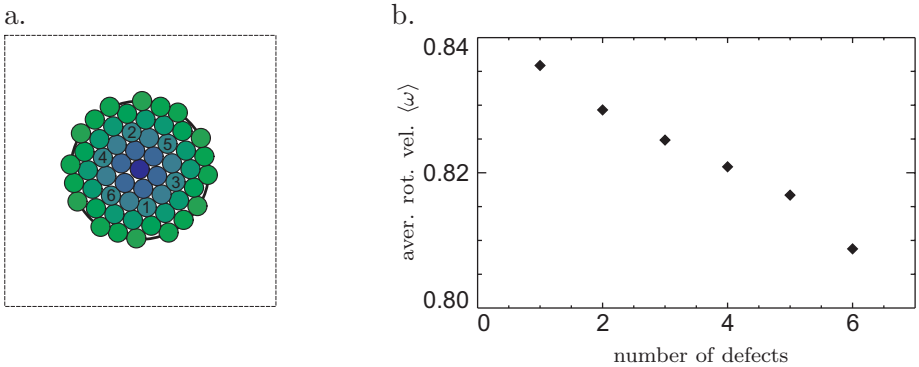

Figure 4.9: a. Rotating cluster for $r_0 = 6$ with all other parameters as given in Fig. 4.7a. The numbers indicate the sequence in which the particles are taken away to create defects. b. Average angular velocity of the cluster depending on the number of defects.

forces with which the LSs are kept at their positions so that oscillations of the cluster become more likely. All these effects may influence the rotational motion in a rather complex way. In order to get reasonable quantitative statements on the motion with defects, we choose the case $r_0 = 6$ where the cluster is small enough to see a clear effect. We conduct a number of simulations in which up to 6 LSs propagating with a velocity slower than the intrinsic one are removed from the cluster (the sequence is shown in Fig. 4.9a). The resulting average angular velocities are shown in Fig. 4.9b, showing a monotonous decrease of the velocity the more particles are taken away.

There are two likely mechanisms to explain the observations which may act simultaneously in the analyzed case. First, the rotational velocity of the cluster is a balance between those LSs in the inside of the cluster which propagate slower than the intrinsic velocity and thus try to accelerate and those at the boundary which propagate too fast and thus try to decelerate. When taking away LSs that are trying to accelerate the cluster, those decelerating become more dominant and can thus reduce the overall angular velocity of the cluster. Second, the more LSs are taken away, the weaker the forces that keep the remaining particles at their equilibrium positions. Thus oscillations as those shown in Fig. 4.7c occur even for small intrinsic velocities and (although small in amplitude) may reduce the mean angular velocity. In order to eliminate the second effect in future works, potentially a modification of the interaction function stiffening the cluster structure may be helpful.

As a last point, we want to briefly comment on rotating structures for classical particles. When the rotational velocity is low and the interaction forces can essentially keep the particles on their equilibrium positions, the structure can be assigned a moment of inertia and standard textbook techniques can be applied for the treatment of rotational motion. In particular, for appropriate initial conditions any rotational velocity can be realized. For random initial velocities, the cluster can still perform a rotational motion which is accompanied by a bouncing motion in the trapping potential as numerical investigations can prove (data not shown). As our main motivation for the consideration of confined motion were experimental observations of active particles, we do not want to go into more detail on this point here.

4.1.3.3 Excitation and switching fronts

Above, we have seen an example for many actively propagating LSs forming one more or less rigid body. In a good approximation, the rotating state could be considered as stationary because the absolute velocities of the LSs remained constant after the decay of initial transients. Although the particles were propagating intrinsically, the behavior of the cluster showed a number of similarities with solids consisting of classical particles like molecules or ions. For classical particles in lattice arrangements, it is long known that they can conduct characteristic types of oscillations around their lattice positions and localized excitations with particle-like properties like phonons can arise. It is thus interesting to ask how excitations and perturbations spread and potentially disperse in active media.

In order to determine an appropriate setting to investigate the spreading of excitations in extended clusters, we may recall that in [361] the central collision of two quadratic clusters of 11×11 LSs in the double-coupling case for one intrinsic velocity and a hexagonal arrangement was analyzed. Here, it was found that the clusters were

compressed during collision and that this compression occurred on a timescale faster than that of the intrinsic propagation. In the following, motivated by these findings we want to use the presented scenario to produce excitations in clusters. A genuine advantage of letting two clusters collide is that the clusters can be arranged in such a way that they are initially in a stable equilibrium. As due to the size of the cluster in [361] the velocity of the excitation was likely to be influenced by boundary effects, we extend the cluster to 9×100 particles and a symmetric arrangement with respect to the initial direction of propagation (Fig. 4.10a). The latter point ensures that in a central collision with a second cluster excitations propagate mainly in this direction, which is not necessarily the case when using an asymmetrical cluster as in [361].

In the following simulations, we switch back to the interaction functions used in Sec. 4.1.3.1, the range of velocities and the time steps for the simulations are adapted accordingly. In the simulation, the initial velocity of all particles is the same and corresponds to the intrinsic one in the case of active propagation so that the whole cluster moves to the right retaining its shape in the course of time. To save simulation time, instead if simulating two clusters the whole structure is placed into a rectangular domain with no-flux Neumann boundary conditions. In this way, the cluster propagates homogeneously until its front end comes close to the right boundary of the domain. The collision with the boundary is then equivalent with a mirror cluster which is reflected at the boundary.

For low intrinsic velocities (which we will consider exclusively in the following), the particles in the front of the moving solid are forced to stop abruptly when colliding with the boundary while those further away from the collision zone do not yet feel the collision due to the short-ranged interactions. As a result, they continue their motion to the boundary, resulting in a compression of the solid with respect to its initial shape. Due to the repulsive interaction for small particle distances, the following particles have to lower their velocity as well and eventually come to a stop, triggering a whole compression front to run through the cluster along its main axis. The direction of motion is essentially determined by the symmetry of the cluster, fronts in any direction can be generated by choosing appropriate asymmetric clusters.

The whole compression process is visualized in the sequence of images shown in Fig. 4.10a. The initial state in green shows that the cluster is in equilibrium. The second image was taken directly after the cluster hit the boundary showing the initial phase of the compression wave which moves through the cluster with almost constant velocity. When reaching the end of the cluster, the particles of the very end have the possibility of reversing their direction without being obstructed by other particles. Once they switch direction, their intrinsic drive stabilizes propagation opposite to the initial direction. The particles pull their neighbors with them, and as the effect is enhanced by the intrinsic drive of the particles, a second front, this time of decompressing type, runs to the cluster from left to right. When reaching the right end, the intrinsic drive co-acting with the pulling particles is strong enough to detach the whole cluster from the wall. The whole state then converges to equilibrium with some additional quickly decaying fronts running to the cluster.

In order to see how the particles behave in the compressed state, we have chosen two particles (marked in white in Fig. 4.10a) whose α_x-component we plot as a function of time in Fig. 4.10b. The black vertical lines in the figure indicate where the snapshots have been taken. It becomes clear that in the compressed state, the particles are not

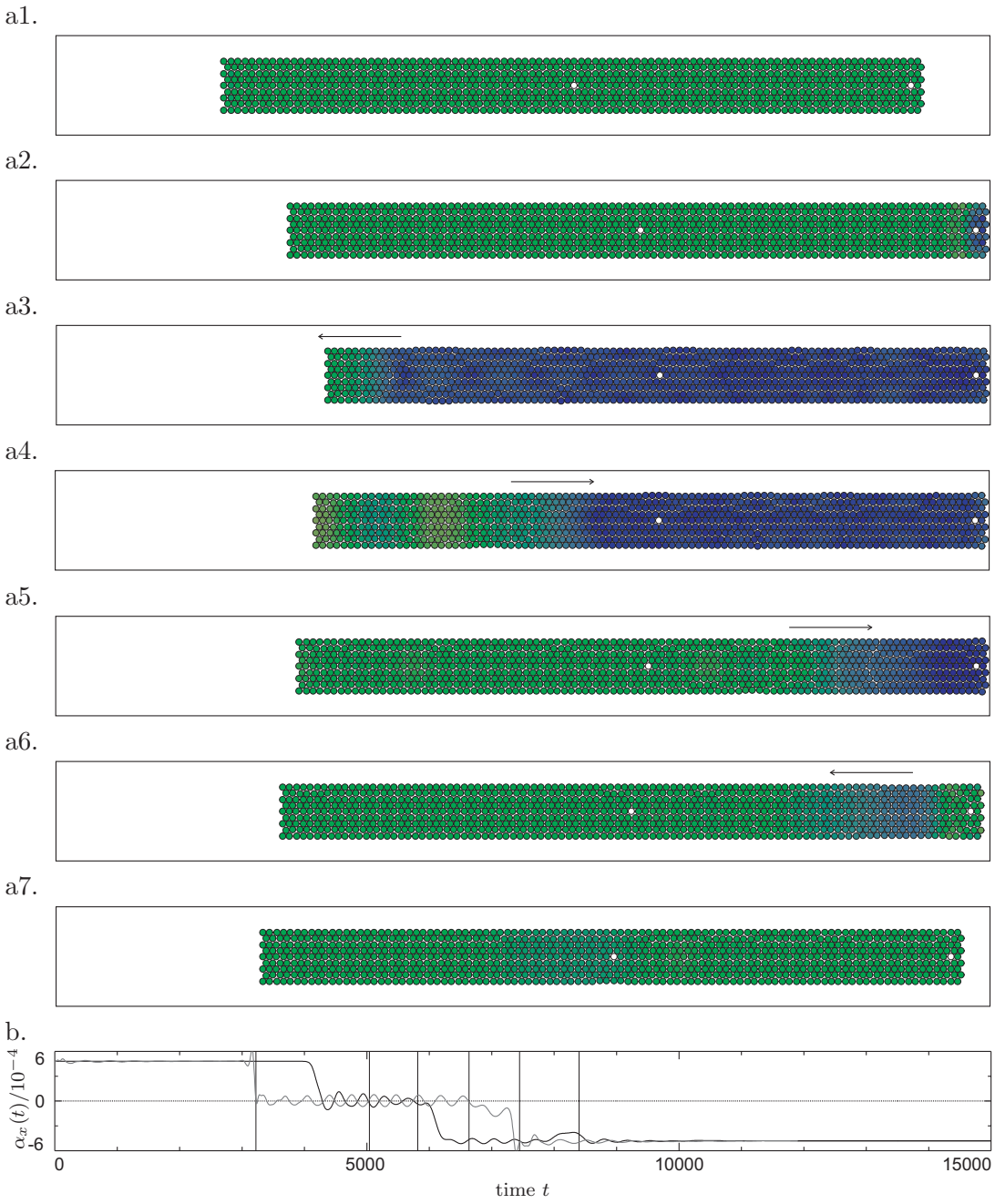

Figure 4.10: Compression fronts in clusters of active particles. a. Collision of a cluster of 9×100 LSs with the boundary of the domain $\Omega = [-4, 18] \times [-0.4, 2]$. The color of each LS marks the current absolute value of the corresponding inner degree of freedom $\boldsymbol{\alpha}$ as in the previous figures. Times the snapshots are taken are 1: 0, 2: 3222, 3: 5040, 4: 5814, 5: 6636, 6: 7446, 7: 8400. b. x-component of the $\boldsymbol{\alpha}$-vector as a function of time for the two LSs in the center and on the right of the cluster are marked with white color(grey line central LS, black line right LS). The vertical black lines indicate the times used in a. Parameters: $k_1 = 0.0015$, all others as in Fig. 4.6.

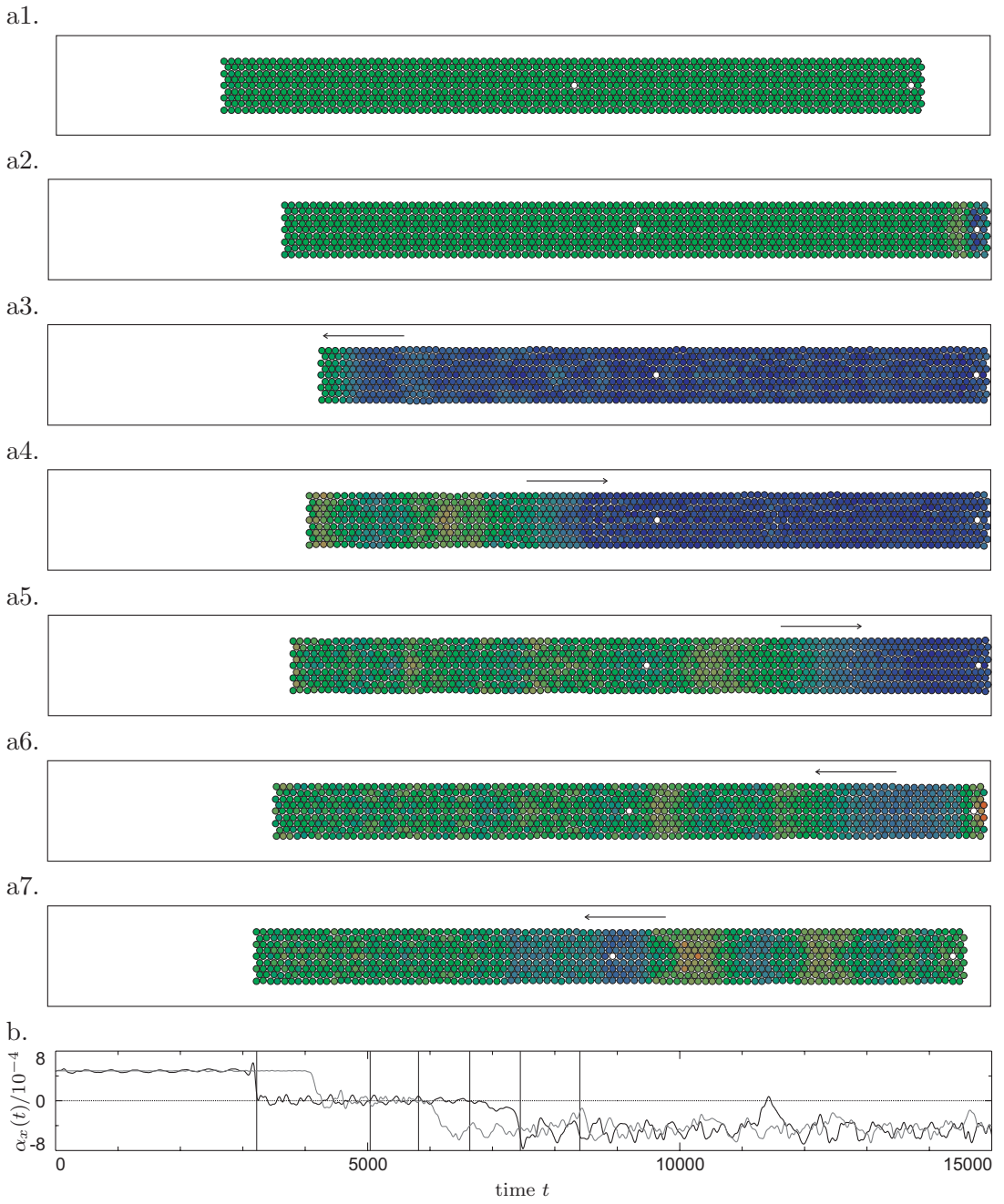

Figure 4.11: Repetition of the simulation of Fig. 4.10 with an underlying classical particle dynamics, all other conditions (in particular α_0) are the same.

at rest but perform an almost periodical oscillatory type of motion. Furthermore, the frequency of the oscillation increases with increasing compression of the cluster.

Following the above observations, one may ask two questions. First, how would classical particles and active particles with single coupling behave in the same situation and second, how does the choice of the intrinsic velocity influence the dynamics. Starting

with the first question, one may conduct a simulation with the same initial conditions as in Fig. 4.10, however with the other types of particle dynamics. The results for classical particles are shown in Fig. 4.11. On first glance, the behavior after the collision with the wall seems similar. As for symmetry reasons the overall energy has to be conserved during the collision with the mirror cluster, most of the kinetic energy of the individual particles is transferred into potential energy and the cluster produces a compression front as well. An important observation which we will discuss in more detail below is that the velocity with which the front propagates through the cluster is lower than in the case shown in Fig. 4.6. Second, there is also a decompression front following the compression front which can also be explained with the conservation of the total energy. During the collision process, the cluster exchanges its overall momentum with the wall (or its mirror cluster) and the direction of propagation is reversed.

At this point, more significant differences to Fig. 4.6 become visible. In the latter case, there is a strong mechanism that dampens out oscillations and other fluctuations, forcing the cluster to take its equilibrium state in the long-time limit. In the classical case however, the compression and decompression fronts which propagate much faster than the particles themselves are not damped out. Instead their propagation leads to a propagating localized state of low velocities inside a high-velocity state which disperses very slowly in the course of time. The dynamics of this state inside the cluster causes the whole cluster to move to the left performing a caterpillar-like type of movement: while the center of the cluster moves, the structure almost periodically contracts and expands. This becomes also visible when looking at the velocities of the two particles again marked in white. In the compressed state, compared to the actively propagating case the particles are practically at rest as all kinetic energy has been depleted. However, once decompression sets in, the velocity varies approximately between a vanishing and the negative initial velocity on a characteristic time scale. Looking at the case of single coupling, one basically finds the phenomenology of the double-coupling case. However, the velocities of the compression and decompression fronts are lower.

Turning now to the question how the choice of the initial or intrinsic velocity affects the dynamics of the cluster, we may briefly sum up a number of observations. Basically, a compression front followed by a decompression front is observed in all cases. They differ however in a number of attributes like their shape, their velocity and the behavior of the particles in the compressed state. For very small velocities, the cluster does not detach from the wall when the decompression front reaches the right end. In contrast, for very high velocities individual particles may leave their lattice positions during the collision, causing a strong deformation of the cluster at the collision site. Here, a number of symmetry-breaking instabilities are observed. For all velocities between these two extremes, the cluster eventually returns to the equilibrium state in the case of active propagation independent of whether a coupling between the particles is present in the $\boldsymbol{p}$ component or not. In the classical case, various forms of oscillations are observed after the collision.

Of all properties described above, we want to discuss only one in more detail: the velocity with which the longitudinal excitation of the collision spreads through the cluster, conceptually corresponding to some kind of "sound velocity". As the propagation velocity is constant in a relatively good approximation, one may take the time T for the propagation of the front through the cluster as a reciprocal measure for the average velocity. It can be estimated from velocity curves like those depicted in Figs. 4.10b and

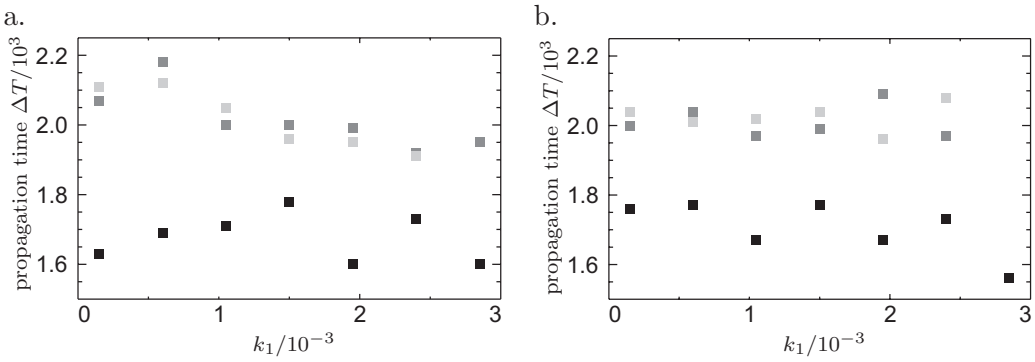

Figure 4.12: Velocities of compression and decompression fronts. a. Propagation time T for compression fronts as exemplarily depicted in Fig. 4.10 to pass through the whole cluster as a function of the driving parameter k_1 in the case of double coupling (black points) and single coupling (dark grey points). All other conditions correspond to Fig. 4.10. The light grey points correspond to the classical case where for a given value of k_1 the initial velocity of the cluster was chosen to correspond to the intrinsic velocity in the case of active propagation. b. The same plot as in a. for the decompression front following the compression front.

4.11b for particles at the ends of the cluster although a certain uncertainty remains as it is not always clear how to precisely define the moment when the excitation arrives at the point of interest. The reason why we do not define a velocity associated with T is that it is not entirely clear which length scale has to be taken into account due to the contraction of the cluster.

Fig. 4.12a shows the results for the compression front in the double-coupling, the single coupling and the classical case as discussed above. The values are shown as a function of the driving parameter k_1 controlling the active propagation while keeping all other parameters fixed. In the case of classical Newton equations an initial velocity of the particles was chosen that corresponds to the intrinsic velocity for the given value of k_3 in the case of active propagation. As central result, one may state that for a given dynamics equation with fixed interaction functions, the front velocity does not significantly depend on the velocity with which the cluster has been propagating before the collision (the potential error of each measurement lies in the region of $\Delta T = 100$). Furthermore, the cases of classical dynamics and active propagation with coupling only in the α-component practically coincide. In contrast, for the interaction function in both components the propagation of the compression front through the cluster takes about 15 % less time. As the compression front is followed by a decompression front which can again be associated a characteristic propagation time, in Fig. 4.12b we plot the latter again as a function of k_1. Here some data points are missing as in particular for high velocities the decompression is overlaid by oscillations so strongly that the determination of the propagation time is not possible. Within the error of the determination, we find quantitatively the same results as for the compression front.

Analyzing the above results, one may state that for the Galilean-invariant system of classical Newton equations, one may transform the system to a moving frame, showing that the situation of a uniformly cluster colliding with its mirror image is equivalent to a resting cluster which is excited on one side with a short local compression pulse. In this terminology, the velocity with which the cluster moves in the resting frame

determines the properties of the excitation in the co-moving frame. It is then not too surprising that the velocity with which the excitation front spreads is independent of the excitation as it is known that the latter for classical solids depends only on the material parameters density and compression module. This statement holds of course only if in the stationary frame the velocity of the propagating cluster is smaller than the "sound velocity" which is true for the case considered above. Adding active propagation to the dynamic equations breaks the Galilean invariance of the system. Nevertheless, at least for the chosen parameters obviously the results are not essentially influenced. It is likely that the particles are coupled so stiffly that the velocity relaxes to a value close to zero on a time scale so short that the active propagation can not significantly contribute to the dynamics. When the coupling structure of the equations is changed via an additional force term in the position equation, the front velocity becomes larger. This is due to the proportionality of the forces in both components as the action of the force in the $\boldsymbol{\alpha}$-component is enhanced.

4.2 Fluctuating systems

In recent years, a good amount of work has been invested in exploring the dynamics of many particles under the influence of noise, in particular for the previously introduced active Brownian particles (compare Sec. 3.4.2). We have seen that the general evolution equation (4.1) together with possible correlations in the noise forces has extremely many degrees of freedom and contains the standard models for active Brownian particles as special case. In order to have the possibility of comparing our results with most other works of the current literature, we will not consider the Langevin equations with noise forces in both components as derived in Sec. 3.4 but instead look at the system

$$\begin{aligned} \dot{\boldsymbol{p}}_i &= \boldsymbol{\alpha}_i + \sum_{i \neq j} \boldsymbol{F}_1(\boldsymbol{d}_{ij}), \\ \dot{\boldsymbol{\alpha}}_i &= k_1 \boldsymbol{\alpha} - k_3 |\boldsymbol{\alpha}|^2 \boldsymbol{\alpha} + \sum_{i \neq j} \boldsymbol{F}_2(\boldsymbol{d}_{ij}) + R_{\boldsymbol{\alpha}} \boldsymbol{\Gamma}_i(t), \end{aligned} \tag{4.28}$$

which corresponds to (3.120) in the case of active propagation and additive noise for $\boldsymbol{F}_1 = \boldsymbol{F}_2 = 0$. In most of the following investigations, we will vary the intrinsic velocity via the parameter k_1 and the fluctuation strength given by $R_{\boldsymbol{\alpha}}$, furthermore we will look at the influence of the force term $\boldsymbol{F}_1$. A comparison with classical particles in this case is not reasonable as the noise forces correspond to a permanent energy input into the system that has to be compensated by a dissipative mechanism for high particle velocities to prevent the system from diverging [364]. Such a mechanism is only present if $k_1 < 0$ or $k_3 < 0$.

4.2.1 Numerical considerations in two-dimensional systems

For evolution equations with noisy contributions it is basically clear that in contrast to the deterministic case any quantitative consideration may involve only statistical statements, for example on distribution functions or moments. To obtain the latter for systems involving active propagation, in recent years there have been attempts to

apply techniques of statistical mechanics to noisy canonical-dissipative systems as introduced for a special deterministic case in Sec. 4.1.1. The central idea is to solve the Fokker-Planck equation belonging to the Langevin equation (4.28) in order to obtain the corresponding probability distribution function. To this end, one may try to rewrite (3.120) as

$$\begin{aligned} \partial_t q_i &= \frac{\partial H}{\partial p_i}, \\ \partial_t p_i &= -\frac{\partial H}{\partial q_i} - k(H)\frac{\partial H}{\partial p_i} + R(H)\mathbf{\Gamma}_i(t), \end{aligned} \tag{4.29}$$

(compare (4.9)) with an appropriately chosen Hamiltonian whose properties facilitate solving the Fokker-Planck equation, the latter reading

$$\partial_t P + \sum_i \Big(p_i \frac{\partial P}{\partial q_i} - \frac{\partial H}{\partial p_i}\frac{\partial P}{\partial p_i} \Big) = \sum_i \frac{\partial}{\partial p_i}\Big(k(H)P + \frac{1}{2}R^2(H)\frac{\partial P}{\partial p_i} \Big) \tag{4.30}$$

for this special case [365]. Unfortunately, analytic solutions are only available in special cases, for example when considering a single particle in a potential [366], linearly coupled particles in one-dimensional systems under special symmetry assumptions [367] or when coupling between the individual particles is neglected [365]. Otherwise, one usually has to resort to numerical simulations which is in the spirit of the methods we used above for many particles in the deterministic case.

4.2.1.1 Bound state of two active Brownian particles

Similar to our considerations on deterministic motion, we will start with only very few active particles. As we have already produced a number of results for single particles in Sec. 3.4.2, the next case of higher complexity is thus given by a bound state of two LSs under the influence of noise as it it depicted for an experimental system in Fig. 3.5. We will study this case using the parameters of Sec. 4.1.3.1 varying the parameters k_1 (thereby changing the intrinsic velocity) and $R_{\boldsymbol{\alpha}}$ (the noise amplitude). Both parameters are kept low enough to ensure that the bound state stays preserved in the course of time. In order to characterize the dynamics of the state of interest, we look at two quantities: the velocity of the center of mass of the cluster, i.e. $v = \partial_t(\boldsymbol{p}_1 + \boldsymbol{p}_2)/2$, as a measure for the translational motion and the angular velocity ω of the cluster with respect to its current center. The latter is defined in the following way: a system of polar coordinates is moved along with the center of mass so that the position of one fixed LS can be given by a radius r and an angle θ in this coordinate frame. The angular velocity is then defined as the temporal derivative of θ. As white noise forces are nowhere differentiable, velocity and other quantities involving time derivatives are defined via a first order finite difference scheme.

A technical issue we have to address before starting is the correct choice of time steps for the numerical simulation and the determination of time-derivative expressions. In the noise-free case where we have used a standard Runge-Kutta scheme to integrate

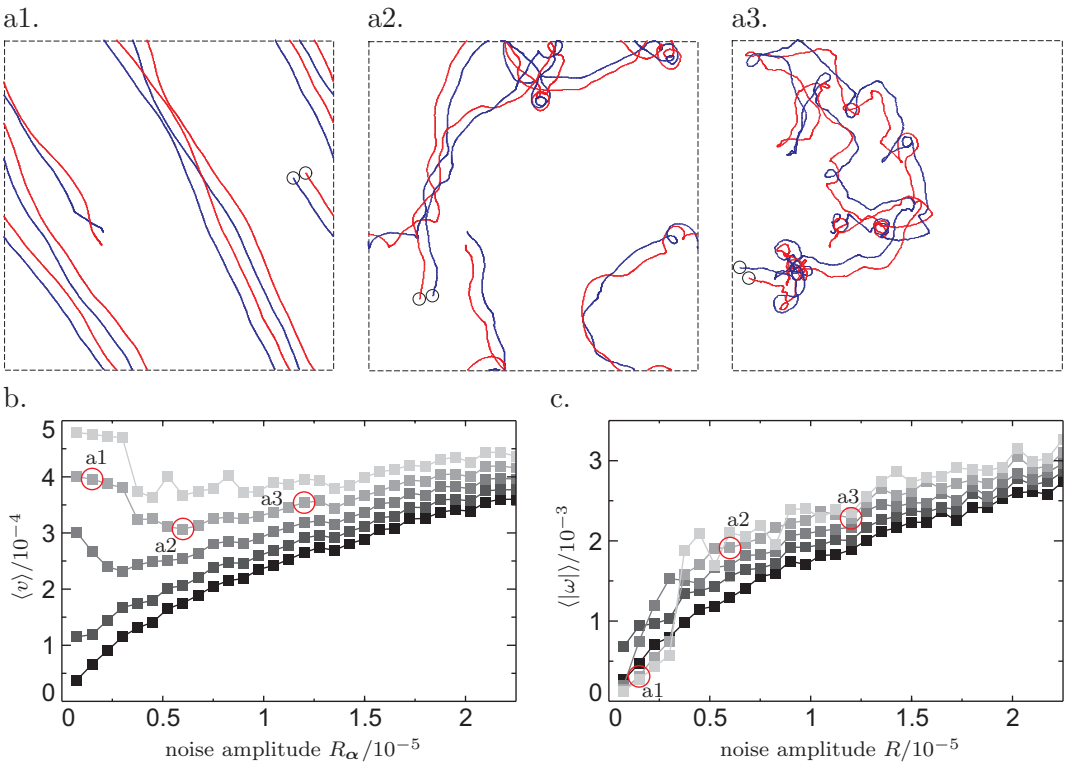

Figure 4.13: Dynamics of a two-particle molecule in the double-coupling case. a. Trajectories of two active particles forming a bound state shown over a time interval $\Delta T = 50000$ for $k_1 = 1.05 \cdot 10^{-3}$ and $k_3 = 6500$ resulting in the intrinsic velocity $\alpha_0 = 1.05 \cdot 10^{-4}$ and noise amplitudes of $R_{\boldsymbol{\alpha}} = 0.15 \cdot 10^{-5}$ (a1), $0.6 \cdot 10^{-5}$ (a2) and $1.2 \cdot 10^{-5}$ (a3). b. Average velocity of the center of the cluster as a function of $R_{\boldsymbol{\alpha}}$ and α_0. The α_0-dependence is visualized using curves with different grey scales, from dark to light grey they correspond to $k_3 = 6500$ and $k_1 = -0.3 \cdot 10^{-3}$, $0.15 \cdot 10^{-3}$, $0.6 \cdot 10^{-3}$, $1.05 \cdot 10^{-3}$ and $1.5 \cdot 10^{-3}$. Each point was determined over a total averaging period of $\Delta t = 5 \cdot 10^5$. c. Average absolute angular velocity of the cluster with respect to its center shown using the same coloring and conditions as in b.

numerically the differential equations, the trajectories are smooth and the determination of discrete derivatives poses no significant problems as long as the time step T_2 for the discrete time derivatives is also small enough, but larger than the time step T_1 of the numeric integration. The simulation of Langevin equations is performed using the standard forward stochastic integration scheme given by (3.129). For the following results, we again use the algorithm implemented by Röttger [361] or appropriate modifications. As the characteristic time scale for the chosen parameters in the deterministic counterpart lies in the order of $100 - 1000$, we keep a time step on the order of $T_1 = 0.01$ for the simulations (as in the Runge-Kutta case). It can be ensured by a variation of T_1 that the results are statistically independent of this variation. In order to determine time derivatives, we also choose the intermediate time scale $T_2 \approx 1000\, T_1$ as before in the Runge-Kutta case. A closer inspection shows that in the presence of noise, this time scale is the smallest one on which the dynamics is due to both deterministic and stochastic parts. A variation of T_2 by an order of magnitude quantitatively changes the results for average time derivatives by about 20 % but does not cause qualitative

changes.

We start with the double coupling structure of the reduced equations which turns out to produce results more simple to understand than the single-coupling case. Two LSs are positioned at an initial distance for which a stable molecule is possible in the case of vanishing initial velocity. The intrinsic velocity is varied between zero (corresponding to a purely damping effect of the deterministic velocity-dependent part) and medium values. Fig. 4.13a depicts trajectories of the two LSs recorded for $\alpha_0 = 4 \cdot 10^{-4}$ and noise amplitudes of $R_{\boldsymbol{\alpha}} = 1.5 \cdot 10^{-6}$, $6 \cdot 10^{-6}$ and $12 \cdot 10^{-6}$. For very low noise amplitudes (Fig. 4.13a1), the constituents of the molecule are almost at rest while the center propagates with intrinsic velocity. The weak noise forces can affect the dynamics to a significant extent only on a slow time-scale and induce gradual changes in the direction of propagation and the orientation of the molecule. With increasing strength of the fluctuations, their influence on the motion of the molecule becomes more dominant (Fig. 4.13a2). Aside from changing the main direction of motion, one may recognize that from time to time the fluctuations switch the system from an essentially propagating to an essentially rotating state in which the center of the molecule is at rest. The same fluctuations may however have the opposite effect and perturb the rotational motion in favor of a translational one. Even higher fluctuations increase the number of events in which the system switches to rotational motion at a given time (Fig. 4.13a3).

With the above observations in mind, we can now come to the discussion of the quantitative results depicted in Fig. 4.13b and c. To produce the figures, very long series of trajectories for every parameter combination have been produced over an interval $\Delta T = 5 \cdot 10^5$ and the time-averaged velocities and angular velocities have been determined. It is assumed that for the Markov process, the ensemble average can be replaced by a time average. For negative k_1 (black curves), without noise the molecule can neither propagate nor rotate on long time-scales. The fluctuations drive both types of dynamics as the molecules move closely along the neutral manifold defined by a free motion of the center together with a fixed distance of the particles. Consequently, the average values of both v and ω increase monotonically with increasing fluctuation strength. When

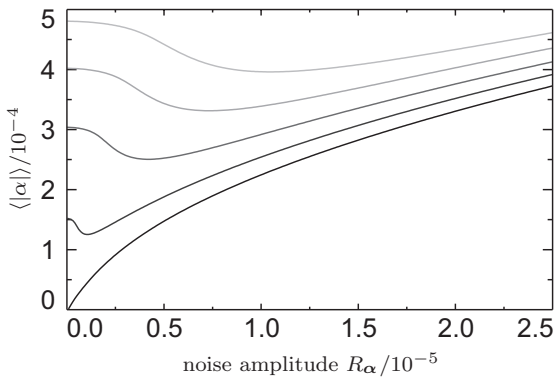

Figure 4.14: Expectation values of $|\alpha|$ for a single active Brownian particle in the one-dimensional case calculated analogously to (3.130) for different intrinsic velocities as a function of the noise amplitude $R_{\boldsymbol{\alpha}}$. The choice of parameters for the active propagation corresponds to Fig. 4.13 (meaning $k_3 = 6500$ and $k_1 = -0.3 \cdot 10^{-3}$, $0.15 \cdot 10^{-3}$, $0.6 \cdot 10^{-3}$, $1.05 \cdot 10^{-3}$ and $1.5 \cdot 10^{-3}$) which is also indicated by the grey-scale color coding of the different lines.

the parameter k_1 is now increased above the drift bifurcation point, for vanishing noise amplitudes the cluster generically propagates as a whole with its intrinsic velocity. Fluctuations can now induce a slow rotational motion of the cluster or even cause the system to temporally switch to a purely rotating state. We may compare our findings for the average absolute velocity v with the expectation value of $|\alpha|$ in the one-dimensional case which can be calculated analytically as in (3.130) for the same parameters that have been used in the two-dimensional simulation. The corresponding curves are shown in Fig. 4.14, and one immediately recognizes a strong quantitative agreement to Fig. 4.13b.

The agreement of the curves allows for a number of conclusions. A single actively propagating particle in two dimensions has a dynamically stabilized velocity, yet a neutral manifold given by the direction of propagation. When combining two LSs to a molecule, the interaction force alone produces a one-dimensional neutral manifold (the orientation of the molecule). If the LSs move in opposite directions, this may produce a rotational motion along this manifold consistent with the neutral manifold of the single-particle motion. If the propagation direction is the same however, a state is stabilized in which the direction of propagation is perpendicular to the connecting axis between the LSs. As Fig. 4.13a1 shows, this state is preferably taken for small noise intensities. As we have previously shown that the double coupling structure strongly suppresses antiphase oscillations along the connecting axis of the LSs (and a closer inspection indeed shows that the distance between the LSs undergoes weak fluctuations), the essential effect we see in the velocity curve is the perturbations of the noise caused in the main direction of propagation. For higher noise amplitudes, the system can switch between the rotating and the propagating state, and a closer inspection shows that for high noise amplitudes we can estimate that typically $\langle|\omega|\rangle d_0/2 \approx \langle v\rangle/2$ with d_0 denoting the equilibrium distance. This reflects the observation that about half the time the molecule performs a rather uniform propagation that then switches to a rotating state. In summary, the analogy to a single particle in one dimension results from the suppression of oscillations along the connecting line of the LSs.

In a next step, we may ask whether there are any differences in the dynamics when considering the single-coupling case with $F_1 = 0$. The answer depends slightly on the point of view. For many initial conditions, the system evolves to a state that is rather similar to that observed for the same parameters in the double coupling case in the sense that the averaged characteristic quantities like center and angular velocity show a qualitatively similar dependence on the noise amplitude. An example is shown in Fig. 4.15a1 which is rather equivalent to Fig. 4.13a1. A closer look however shows that the curves for $\langle v\rangle$ to not agree quantitatively in particular for low to intermediate noise amplitudes and generally take smaller values in the single-coupling case. The most likely reason for the observation of this effect is the lack of suppression of antiphase oscillations along the connecting line of the LS. The pure oscillations in one spatial dimension correspond to a resting center of the LSs in the absence of noise, so that even in two dimensions and in coaction with other mechanisms a reduced velocity of the center can be expected.

The most significant difference to the double coupling case however does not lie in the above quantitative difference of the expectation values for the average velocity, but in the fact that for the case of double-coupling virtually all initial conditions converge to a state with the same statistical properties. This marks the central difference in the single coupling case in particular for high intrinsic velocities. As we see in Figs. 4.15b

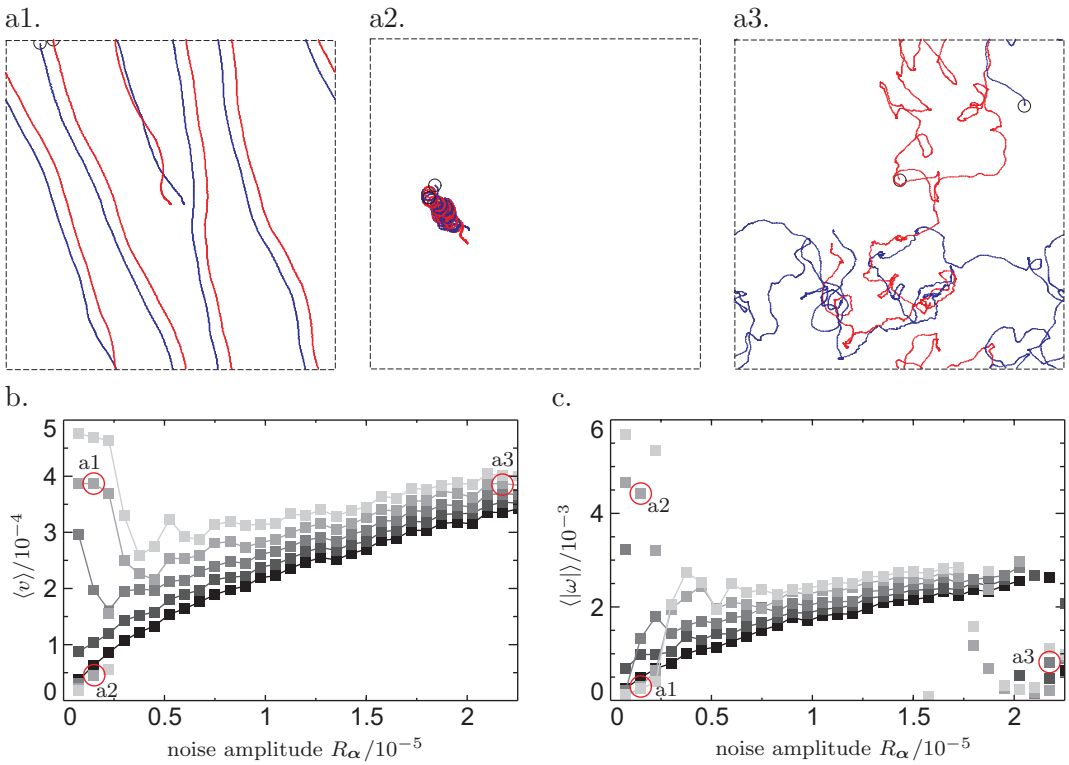

Figure 4.15: Dynamics of a two-particle molecule in the single-coupling case. a. Trajectories of the bound state shown over a time interval $\Delta T = 50000$ for the parameters marked by red circles in b and c. b. Average velocity of the center of the cluster as a function of R_α and α_0, the coloring, conditions and parameters corresponds to Fig. 4.13. Note that unlike the results in the latter figure, the state of the system can depend on the initial conditions (compare the red circles, for explanations see text). c. Average absolute angular velocity of the cluster with respect to its center shown using the same coloring as in b.

and 4.15c, there are some parameter values for which two values of the velocities are depicted. One state generally is the equivalent to the curves in Fig. 4.13 while the other lies far away from it. The reason for this is the existence of two "noisy attractors". To explain this term, let us consider for example the situation with $a = 0.00105$ for a small noise amplitude $R = 1.5 \cdot 10^{-6}$. There are two possible states for this choice of parameters which are highlighted in Fig. 4.15b and c using red circles. Typical trajectories corresponding to the two states are shown in Figs. 4.15a1 and a2 explaining the different possible states. Certain initial conditions lead to an extremely stable rotational motion of the two particles (a1). The weak noise amplitudes can displace the center only very slowly in this situation. As a result, the angular velocity is rather high while the center is almost at rest. Other initial conditions lead to a state (a2) which is equivalent to that depicted in Fig. 4.13a1. A second type of deviation from the expected curves arises for very high noise amplitudes (Fig. 4.15a3). Here, it turns out that the molecule breaks up after being bound over a certain period. In conclusion, we may state that comparing the single- and double coupling situation basically produces the same dynamics for certain initial conditions with two differences: the double-coupling with noise favors a propagating with respect to a rotating state and stabilizes the bound state as it suppresses

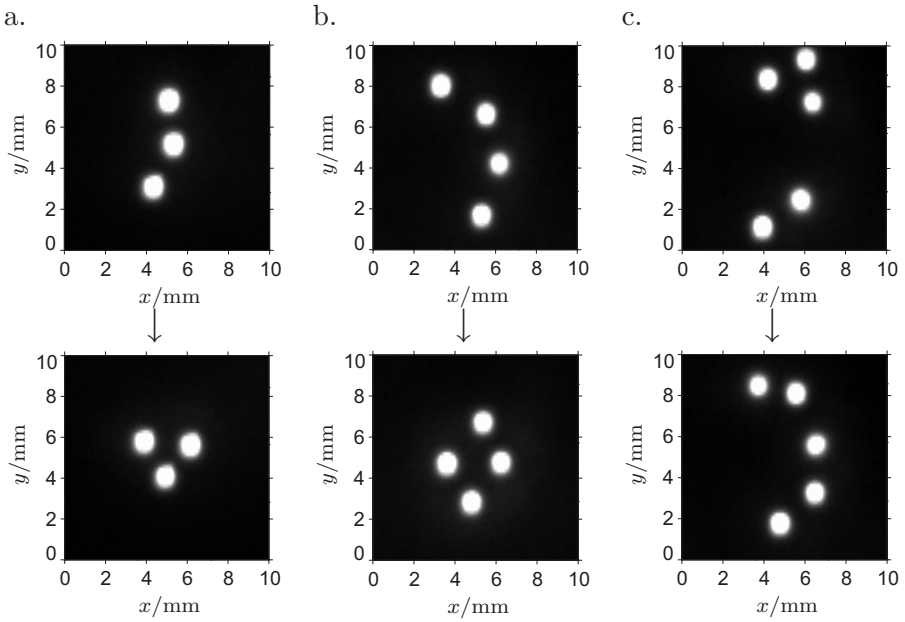

Figure 4.16: Typical clusters of a. three, b. four and c. five LSs observed in a planar dc gas-discharge system indicating with high-ohmic barrier. One may observe a change of the configurations in the course of time due to fluctuations and intrinsic dynamics (from upper to lower row). For details see [2].

oscillations.

Further investigations on active particles under the influence of noise may take into account the interaction of three or more particles. This situation is also found in experimental systems like planar gas-discharge systems (Fig. 4.16). In particular, one finds that there are several stable conformations in which the LSs arrange over and extended interval of time (like the triangular and the stretched cluster depicted in Fig. 4.16a) and that fluctuations may then induce switching processes between the different states.

4.2.1.2 Bound state of many active Brownian particles

As in the deterministic case, one may look at the dynamics of many LSs instead of only two. For a long time, there has been interest in the collective motion of "classical" random walkers and diffusion-limited aggregation [368], for example as description for the growth of neurons [369] or the generation of rough surfaces [370]. In recent times, this topic has been expanded to active Brownian motion to describe the motion of swarms [351, 371–373] and interesting new processes like noise-induced transitions have been observed [358]. Most investigations have been performed for long-ranged interactions, either to simplify calculations or to keep the swarms of active particles localized. The short-ranged interactions appearing in the context of LSs in this context may produce a number of differences compared to the long-ranged case.

When many particles are on a domain, it makes sense to ask for both bound and unbound states as similar to large ensembles of classical particles, noise may induce the breaking and generation of clusters leading to a characteristic flowing equilibrium. In a

first step however, we want to investigate the dynamics of a single large cluster for noise amplitudes low enough that the integrity of the cluster remains preserved in the course of time. This restriction allows for a comparison with the two-particle case above. We will again use 81 active particles for the simulation. They are initially arranged on a hexagonal grid with an equilibrium distance as previously encountered for the investigations on compression fronts above, the cluster itself is of square shape. Similar to the two-particle case, the velocity of the center of the cluster as well as the average absolute angular velocity with respect to the center should represent reasonable quantities to characterize the dynamics. Furthermore, we use exactly the same parameters and constants as in Figs. 4.13 and 4.15, the results for double- and single coupling are shown in Fig. 4.17.

In the figure, we see that in contrast to the case of two active particles, the curves look rather different in the two cases. For the double-coupling scenario, the mean velocity of the cluster for vanishing noise amplitudes corresponds to the intrinsic velocity and then decreases monotonically with increasing noise amplitudes until the cluster loses its integrity and breaks up (Fig. 4.17b1). This is different from the case of two active particles where the initial decrease is quickly followed by a re-increase. The angular velocity grows almost linearly with the noise amplitude (Fig. 4.17b2). For the single-coupling case, the situation is completely different. Generically, the average velocity of the cluster is far below the intrinsic velocity, even for very small noise amplitudes and independent of the intrinsic velocity itself (Fig. 4.17c1). It grows monotonically with increasing noise amplitude at a small rate. On the other hand, the angular velocity of the cluster is generally higher, in particular for small noise amplitudes (Fig. 4.17c2). An important aspect that has to be pointed out is that for small noise amplitudes and sufficiently high intrinsic velocities, in both single- and double-coupling case there are some initial conditions in which behavior different from the generic dynamics is observed. Concerning this scenario, for the double-coupling case we may find the typical behavior of the single-coupling case (if the initial velocity of the LSs is close to zero) and vice versa (if the initial velocity of the LSs is high and uniformly directed), some examples are marked in the figures by red circles. The "bistability region" is larger the higher the intrinsic velocity.

To find an explanation for the observed behavior, we have a look at particle trajectories in the bistable region for the single-coupling case. Extending our domain to $[-8, 8] \times [-8, 8]$ (which does not influence the results due to periodic boundary conditions) and plotting trajectories of two particles at opposite ends of the cluster offers a way to facilitate a comparison with the two-particle case (Figs. 4.13 and 4.15). In Fig. 4.17a1 we see that the (ungeneric) case of a high velocity of the center is comparable with the two-particle case. The cluster propagates almost uniformly in one direction, and the fluctuations induce a slow variation in the angular orientation. In Fig. 4.17a2 we see the generic situation for the single-coupling case. The main part of the motion of the individual particles is an oscillation in the "potential" generated by the neighboring particles. This effect is much stronger than in the two-particle case as except at the boundaries, each LS is now surrounded by 6 nearest neighbors. As a consequence, the net displacement of the cluster in the course of time is very small. A look at the average absolute angular velocity shows already rather high values for small noise amplitudes. This is however no consequence of a persistent rotational motion like in the two-particle case, but rather due to a rocking motion of the whole cluster that permanently expe-

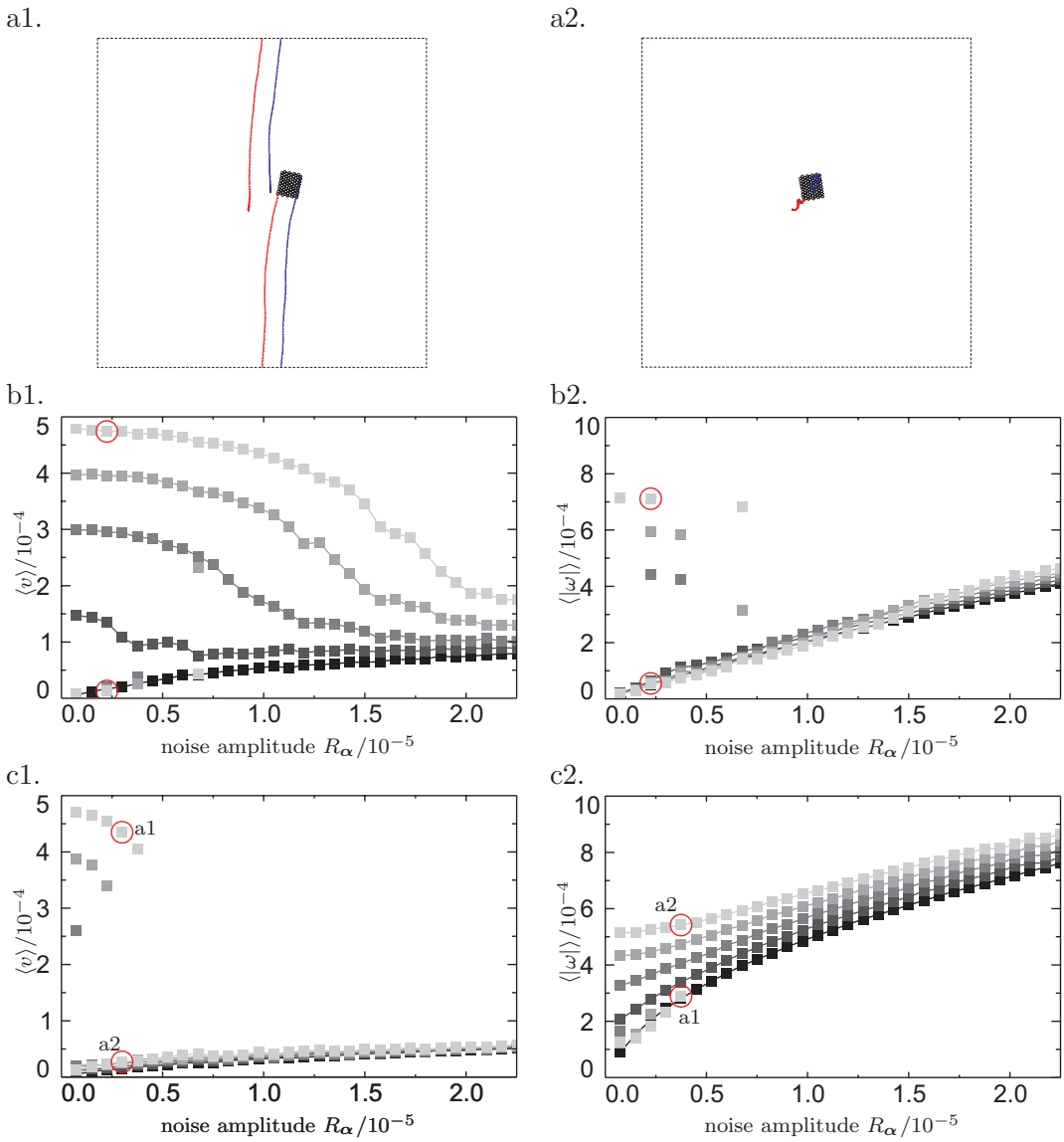

Figure 4.17: Dynamics of a single stable cluster of 81 actively propagating LSs for the single and double-coupling case of the underlying equations. a. Trajectories of the bound state shown over a time interval $\Delta T = 50000$ on the domain $[-8, 8] \times [-8, 8]$ and periodic boundary conditions for the parameters marked by red circles in c. (single coupling case). b. Average velocity of the center of the cluster (b1) and average absolute angular velocity (b2) with respect to its center as a function of R and α_0 in the double-coupling case, the coloring, conditions and parameters corresponds to Fig. 4.13. c. The same quantities as in b. plotted for the single-coupling case.

riences changes of its shape so that the angular velocity frequently changes sign. The statement stay valid when going to large noise amplitude: while the product $\langle |\omega| \rangle d_c/2$ with d_c denoting the average diameter of the cluster take values close to α_0, the "effective" velocity of the LSs at the boundary of the cluster considered on long time scales is an order of magnitude lower.

In the double-coupling case, due to the large number of neighbors for each individual

LS there is a strong suppression of cluster oscillations. The noise amplitude R_α at which for higher intrinsic velocities a local minimum of $\langle v \rangle$ is reached is about three times as high as in the case of a two-particle molecule, which coincides with the fact that the interaction force experienced by LSs in the bulk is trice as high. The values for the average angular velocity are rather small for small noise amplitudes which can again be explained by the suppression of cluster oscillations. For high noise amplitudes, the angular velocity takes about half the value compared to the single-coupling case. Again, this effect is not due to a persistent motion on a long time scale but to fast changes on short time scales.

With the above findings and our analytic investigations for two particles, we can now give a complete characterization of the possible dynamics. The intrinsic motion causes an inert behavior of the active particle that tries to produce a uniform propagation of particle clusters. If only two particles are present, the oscillatory interaction generates a stable lock-in distance, however a neutral manifold is given by the angular orientation of the molecule. Noise causes a displacement of the cluster and in parallel a drift along the neutral manifold corresponding to a rotational motion. The velocity of the center quickly drops with increasing noise amplitude because a rotational motion along a neutral manifold can easily be induced. Qualitatively and quantitatively a possible coupling in the position equation plays no essential role although for single coupling an atypical purely rotational motion is possible. Turning to many particles, the LSs inside a large cluster are trapped in potential generated by six nearest neighbors so that no neutral manifold of rotation exists any more. The cluster may now propagate as a whole or the individual particles may oscillate in the trapping potential. From our considerations on two LSs we have learned that a coupling function in the position equation which has stable fixed points at the same positions as the coupling function in the velocity equation suppresses oscillations. Hence it is natural that the generic state in the double-coupling case is the one moving with intrinsic velocity. The decrease in the center velocity with increasing fluctuations is now not primarily due to a rotational motion of the cluster, but due to the fact that the oscillations drive the LSs into an oscillating state that is not favored by the deterministic dynamics. For the single-coupling case, the oscillating state generally is the favored one, so that the oscillations are just amplified by the presence of noise.

4.2.1.3 "Phase transitions"

Up to now, we have only considered bound states of either two or many actively propagating LSs. When looking at classical Brownian motion, one way to derive the underlying Langevin equations is considering a system of damped coupled particles in an external heat bath. With this in mind, the noise amplitude R in the Langevin equations is sometimes also considered as a measure for the temperature of the external heat bath [347]. For classical particles with a thermodynamically well defined temperature it is known that large ensembles of particles can change their state of aggregation in different types of phase transitions with characteristic properties. In this section, we are interested in the analogue of these transitions for actively propagating particles.

We may start in an elementary phenomenological fashion by taking a number of LSs with the same conditions already used above several times and look at typical states of the system for noise amplitudes so high that the particles stop arranging in just one large

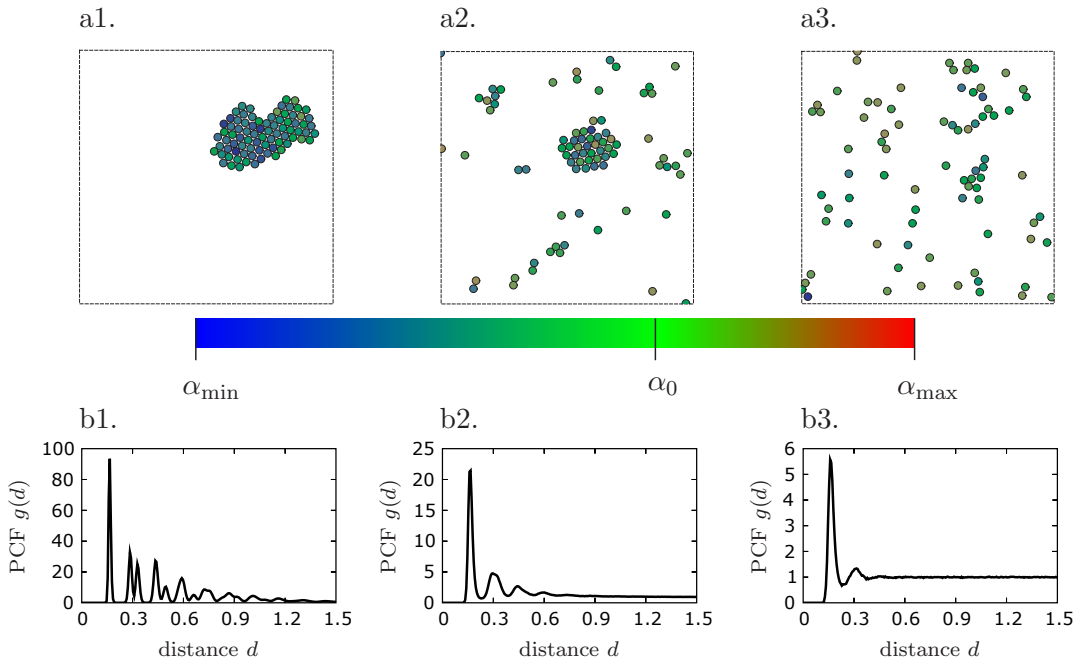

Figure 4.18: Snapshot of the particle distribution at $t = 2.5 \cdot 10^5$ and pair correlation function $g(d)$ for $k_1 = 2.4 \cdot 10^{-3}$, $k_3 = 6500$ and (a1, b1) $R_{\boldsymbol{\alpha}} = 3 \cdot 10^{-5}$, (a2, b2) $R_{\boldsymbol{\alpha}} = 6 \cdot 10^{-5}$, (a3, b3) $R_{\boldsymbol{\alpha}} = 9 \cdot 10^{-5}$.

cluster. We will start with the double-coupling structure of the underlying equations. Compared to the analysis of a single large cluster, we will this time use a range of larger intrinsic velocities for reasons that will become obvious in the following. Figs. 4.18a1-a3 show snapshots of typical states of the system for $k_1 = 0.0042$ and noise amplitudes of $R_{\boldsymbol{\alpha}} = 3 \cdot 10^{-5}$, $6 \cdot 10^{-5}$ and $9 \cdot 10^{-5}$. They were taken after a long simulation time so that the resulting state can be considered as independent of the initial conditions. The first image corresponds again to one large solid which generically forms for virtually all initial conditions at small noise amplitudes. Directly above the corresponding value of the noise amplitude, the cluster starts to decay into several smaller ones, a typical state is depicted in the second image. These smaller clusters are accompanied by a number of isolated LSs. Single or several LS may attach or detach from the clusters so that a dynamical equilibrium is formed. With increasing noise amplitudes, the average cluster size decays (third image) until on average most LSs are isolated. This observation has qualitative similarities with the dynamics of classical particles under an increase of their mean kinetic energy (compare Fig. 4.4).

It is intuitively rather obvious that the state of aggregation changes in the sequence depicted in Fig. 4.18a. A central criterion is that for low noise amplitudes, there is a homogeneous state of high particle density, while for very high noise amplitudes there is again a homogeneous state of low particle density. It is thus interesting to ask about the nature of the transition between these states. To this end, we first have to review some basic points on phase transitions in systems with classical particles. Commonly, the idea of phase transitions is discussed in systems of classical particles with particle

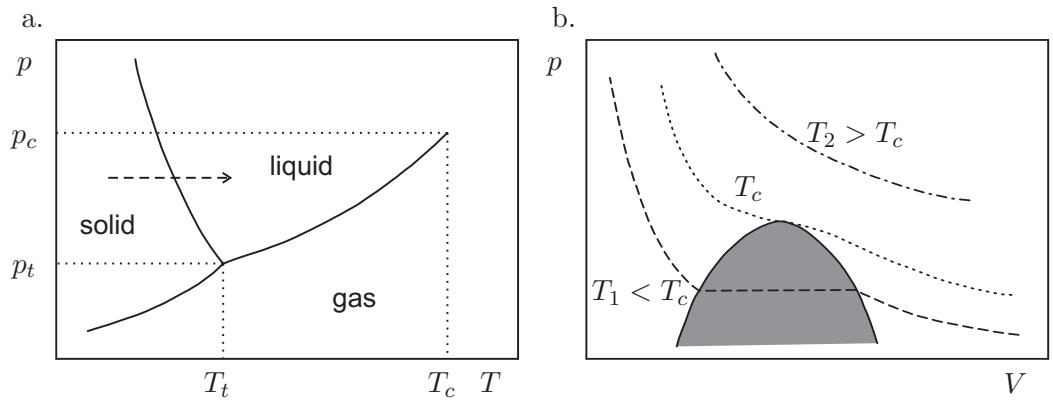

Figure 4.19: Schematic illustration of phase transitions for ensembles of classical particles. a. Phase diagram for water in the plane spanned by pressure p and temperature T, the indices t and c mark the triple and the critical point, respectively. b. Phase diagram for a liquid-gas transition of a real gas in the plane spanned by pressure p and volume V. They grey area marks a region in which gaseous and liquid phase can coexist. For $T_2 > T_c$, no distinction between the phases is possible.

numbers in the order of $N = 10^{23}$, allowing for statements in the "thermodynamical limit". A phase is defined as a macroscopically homogeneous state characterized by properties like density, magnetization, crystalline stricture, dipole moment etc. A phase transition is then defined as a bifurcation in which the system changes from one to a second phase which differ in at least one of the characteristic properties. If two or more phases coexist, the number of particles in the phase boundary is so small that it can be neglected.

According to the classical definition by Ehrenfest [374], transitions between different phases can be classified via the free energy of the system. Changing the temperature of the system, one or several derivatives of the free energy generally show a discontinuity in the transition point with the lowest order showing this property determining the order of the phase transition. Also more modern definitions of phase transitions rely on the existence of an energy functional: in first order transitions, investing a certain amount of latent heat the system switches from one state to the other via mixed state regimes in which both phases exist. Second order transitions have no latent heat and are of continuous type as there is only an infinitesimal difference on the properties of the different states at the transition point.

Let us look at two classical examples for phase transitions. The first one arises in the $p-T$ phase diagram of water, where depending on the parameters either isolated gaseous, liquid and solid states as well as mixed states may exist (Fig. 4.19a). Increasing for example the temperature for fixed pressure (dashed line), one may cross the coexistence line of solid and liquid state, thereby inducing a first order phase transition as there is a large discrepancy in density between liquid and solid state. A typical $p-V$ phase diagram for a liquid-gas transition is shown in Fig. 4.19b. Following the dashed line marking a constant temperature T_1, one goes from a region of liquid state through an extended region of two coexisting phases to a purely gaseous state in a first-order transition. The dotted line at the critical temperature T_C marks the critical temperature above which gaseous and liquid state cannot be distinguished. Following the line, at the transition

point between gas and liquid there is only an infinitesimal difference in the macroscopic properties of the phases, and one has a second-order transition. Close to the transition point, several characteristic quantities like the correlation length d_c commonly show a power law scaling

$$d_c(T) \sim (T - T_c)^{\mu} \tag{4.31}$$

with a universal exponent μ. For higher temperature $T_2 > T_c$ (dash-dotted line), no transition takes place.

A problem arising in the theoretical treatment of phase transitions and the relation to LSs is the transitions are characterized by an irregular behavior (discontinuities, singularities) of the corresponding thermodynamical potentials. For LSs however, the concepts of energy, latent heat and thermodynamic potentials etc have no meaning. Another obstacle arises as we are interested in describing ensembles of LSs with particle numbers usually between 10 and 100 (in extreme cases potentially up to 1000). One should be aware that also classical particle ensembles of this size may have properties significantly different from those in the thermodynamic limit [375–377].

Given the above problems, we may ask whether the transitions as shown in Fig. 4.18 share at least some common properties of classical phase transitions. In his work [361], Röttger analyzed the dynamics of active particles under the influence of noise and proposed to use two characteristic quantities to characterize the states of interest. The first one is the spatial pair correlation function [378], defined in two spatial dimensions as

$$g(d) = \frac{N}{d} \left\langle \sum_i \sum_{j \neq i} \delta(d - d_{ij}) \right\rangle . \tag{4.32}$$

Here, d_{ij} is the distance between the LSs i and j, N is a normalization factor and the brackets denote a suitable average (usually the ensemble average, we will again use a temporal average). While long-ranged correlations reflect the long-ranged order of a solid state, short-ranged correlations reflect the characteristics of fluids or gases. The characteristic length on which (4.32) decays to a constant (meaning that no correlations are present for larger distances d) is defined as correlation length d_c. In practice, the evaluation of the average in (4.32) is carried out by counting the occurring values of the distance in terms of a histogram. Note that (4.32) is different from the expression in Röttger's work as he did not carry out the division by the distance d in front of the average. In addition, the correlation function is only evaluated for values of d that do not exceed half the length of the active area to avoid problems with infinite numbers of mirror particles occurring for periodic boundary conditions. Last but not least, the area below the distribution is normalized to one in the analyzed range of distances. Some works prefer a normalization such that $g(d) \to 1$ for $d \to \infty$, which however is not always possible in our case when considering purely solid states where $g(d) \to 0$ due to the finite number of particles considered (see below).

For the application of (4.32), after starting the simulation the data in an initial period of $\Delta t_0 = 10^5$ were ignored in order to ensure that the state of the system was (statistically) independent of the initial conditions. The remaining simulation of length $\Delta t_1 = 7 \cdot 10^5$ was evaluated by analyzing successive snapshots with a time interval $\Delta t_1 =$

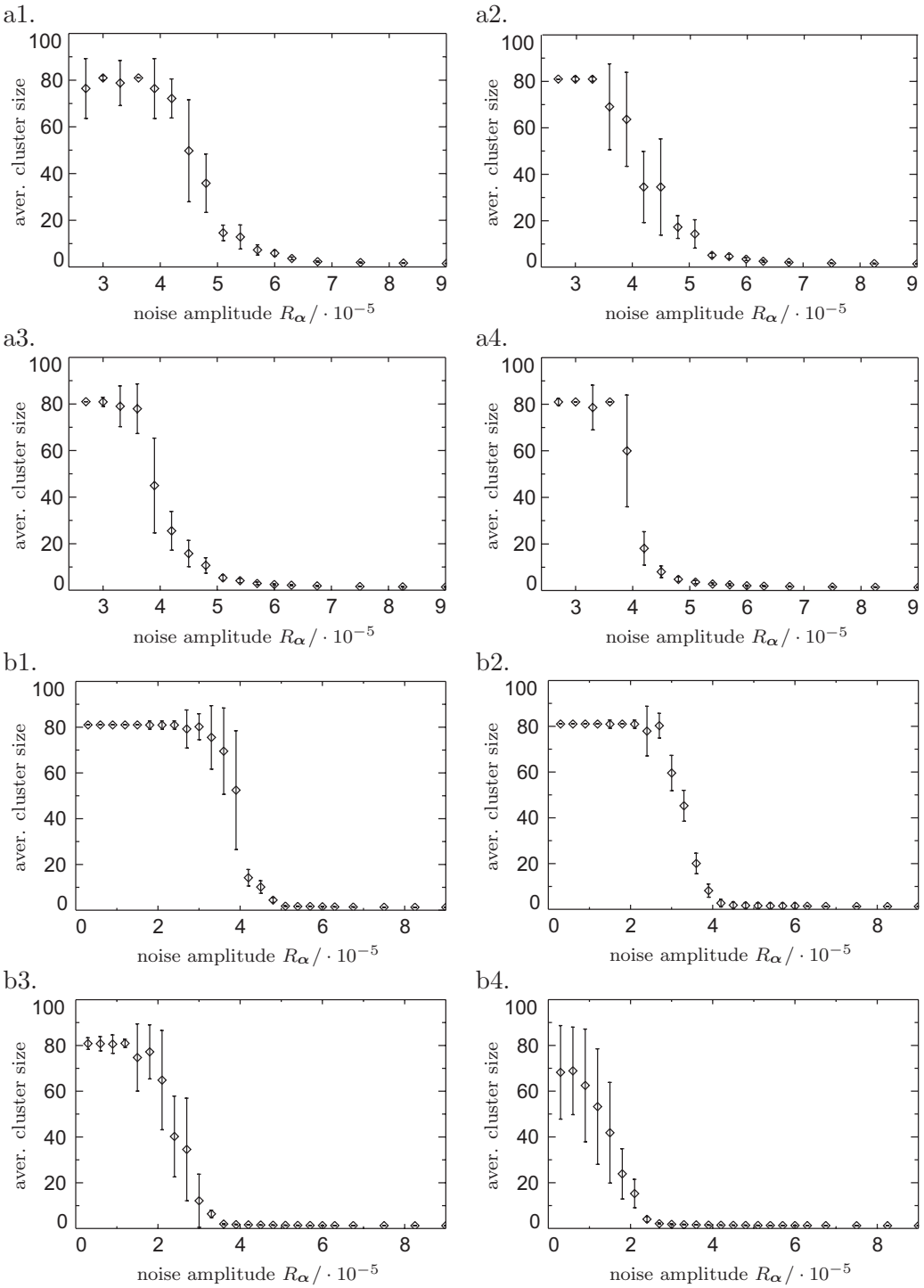

Figure 4.20: Decay of large clusters due to noise. a. Average cluster size and its variance (error bars) depending on $R_{\boldsymbol{\alpha}}$ in the double-coupling case for different values of $k_1 a$ (a1. $k_1 = 0.6 \cdot 10^{-3}$, a2. $k_1 = 2.4 \cdot 10^{-3}$, a3. $k_1 = 4.2 \cdot 10^{-3}$, a4. $k_1 = 6.0 \cdot 10^{-3}$) obtained from a simulation over a total time interval of $\Delta t = 8 \cdot 10^5$. The data contributing to the averaged expressions have been taken after an initial interval of $\Delta t_0 = 10^5$ to ensure that the initial conditions have no influence on the outcome. b. Repetition of the investigations performed in a. for the single-coupling case with $F_1(d) = 0$ with otherwise the same conditions.

2000 in between, the results are shown in Fig. 4.18b. The multi-peaked distribution in b1 clearly indicates that we are dealing with a solid state, the decay of the function for large distances is essentially due to the limited area and the chosen particle density. The increase of the noise amplitude then leads to a decay of the long ranged correlations. The correlation function in b2 is typical for a liquid state which is characterized by small clusters and isolated particles. Here only a short-ranged correlation remains. The third state is not entirely easy to classify. While the short-ranged correlations have decayed further and mainly only one nearest-neighbor peak remains, the state has properties that could be attributed either to a liquid or a gaseous state (compare for example [379, 380] for examples with classical particles).

Röttger's second suggestion was to look at the size of the two largest connected clusters in the system as a function of time, where a cluster is defined as a particle compound in which all cluster members have another member to whom its distance does not exceed a critical value d_c. For the interaction function under consideration, it turns out that a reasonable choice is given by $d_c = 1.15 d_0$ where d_0 is the first stable lock-in distance. With this all LSs can be uniquely assigned to one cluster. Different from Röttger's original idea, we will look at the mean size of all clusters present in the system and characterize the properties of the flowing equilibrium by the corresponding variance in time. The results of this analysis is depicted in Fig. 4.20a for different intrinsic velocities ($k_1 = 0.6 \cdot 10^{-3}$, $2.4 \cdot 10^{-3}$, $4.2 \cdot 10^{-3}$, and $6.0 \cdot 10^{-3}$) and noise amplitudes $R_{\boldsymbol{\alpha}}$. For small noise amplitudes, all figures show a plateau region with almost vanishing variance. Here, we have a completely solid, crystalline state with only one cluster. In the opposite case of very high noise amplitudes, the average cluster size takes values closely above one, again with very small variance. Here, most LSs are on average isolated while some are bound in small clusters for short time intervals.

Let us now look at the transition between the two states. First, the stability of the solid state increases with increasing coefficient k_1 (i.e. increasing intrinsic velocity), which is clear from the above discussed fact that the intrinsic drive to restore particle velocities to the equilibrium velocity is stronger if k_1 is increased and also from the fact that the average velocities are higher themselves. Note that this effect has no counterpart in the field of classical particles. Once a sufficient noise threshold for the breakup of the cluster has been reached, the average cluster size decreases monotonically with the noise amplitude. Here, it turns out that the decrease becomes steeper when the intrinsic velocity is increased: while the decay takes place over a noise amplitude interval of more than $\Delta R = 3 \cdot 10^{-6}$ at $k_1 = 0.6 \cdot 10^{-3}$, the corresponding interval at $k_1 = 6.0 \cdot 10^{-3}$ has a width smaller than $\Delta R = 10^{-6}$. For very high noise amplitudes, almost no clusters of LSs are present in the system any more (due to the finite particle density, there is also a finite probability for the LSs to come close to each other, however the average period of existence for a cluster is very small).

Let us now look at the single coupling case with $F_1(d) = 0$ and re-perform the investigation with the same parameters (Fig. 4.20b). We have extended the displayed range of noise amplitudes up to lower values. For small intrinsic velocities, we again have a stable plateau at small noise amplitudes corresponding to a solid state. The results also have a quantitative similarity to the double-coupling case. Significant changes however can be observed for larger noise amplitudes. The region in which the solid state exists becomes smaller, and for $k_1 = 6.0 \cdot 10^{-3}$ the cluster starts decaying even for the smallest noise amplitudes so that no purely solid state exists in this case.

In order to get more insight into the dynamics for the different situation, we have to consider other characteristic quantities as well. For classical Brownian particles, it is common to look at the mean squared kinetic energy $E = \langle v^2/2 \rangle$ although the system is not conservative in nature. Motivated by the analogy to our system, we may look at this quantity as well as the velocity is an important dynamical property. Figs. 4.21a and b show the dependence of the mean squared velocity on the noise amplitude for the different intrinsic velocities already used above in the double- and single coupling case after the system has reached a flowing equilibrium. In either figure, the results for small noise amplitudes reflect the findings of Sec. 4.2.1.2. Looking first at the double-coupling case, we see that at small intrinsic velocities ($k_1 = 2.4 \cdot 10^{-3}$ and $4.2 \cdot 10^{-3}$) the velocity curves increase monotonically and approach a linear shape at high noise amplitudes of $R_{\boldsymbol{\alpha}} \approx 8 \cdot 10^{-5}$. For higher intrinsic velocities, one may recognize three regions of characteristic scaling: one in which the slope of the curve decreases, one region of re-increasing with nonlinear scaling and one region of linear scaling. Interestingly, the curve in the first two regions can be represented by power laws of the form

$$\langle v^2 \rangle(R) = a|R_{\boldsymbol{\alpha}} - R_c|^{\mu} \tag{4.33}$$

as is indicated exemplarily indicated by grey lines in Figs. 4.21, however the fit coefficients a, R_c and μ all vary for the different curves and also for the first and second region.

It is important to realize that the noise amplitude for which the slope of the curves changes from negative to positive values coincidences with the value where the solid structure starts breaking up into smaller substructures. In Fig. 4.13 we have seen that for smaller clusters or isolated LSs, in the corresponding range of noise amplitudes an increase of the mean squared velocity can be expected. For very high noise amplitudes, most LSs are isolated, and we find a linear scaling similar to Fig. 3.128 for isolated structures.

For the single-coupling case, as expected from Fig.4.17b the mean squared velocity increases monotonously with the noise amplitude. For high noise amplitudes the scaling of all curves becomes linear with the same slope (but not the same offset) as in the double coupling counterpart. For lower noise amplitudes, the dynamics is essentially dominated by oscillations of the individual LSs around their equilibrium positions until the cluster starts to decay, and again power law fits according to (4.33) can be used to represent the data in a satisfying way (exemplarily indicated by a grey line in Fig.4.17b). Unfortunately, also in this case no universal exponents are found.

An interesting point is given by the question of the dependence of the observed phenomena on the particle number. To explore this point, we choose $k_1 = 6.0 \cdot 10^{-3}$, the double coupling case and increase the particle number to 1225 while the domain size is increased to $[-9.72, 9.72] \times [-9.72, 9.72]$ (in this way, the average particle density stays the same as in the simulations with 81 particles). By reducing the overall simulation time to $4 \cdot 10^5$ and increasing the time step to $\Delta T_1 = 0.05$, on a single processor the time for each run takes about one week. In this way, 15 simulations for different noise amplitudes have been carried out. Two central results may be given. First, the noise amplitude necessary to break up the solid state grows about 50 % compared to the situation with 81 particles. A possible reason for this observation is that by increasing

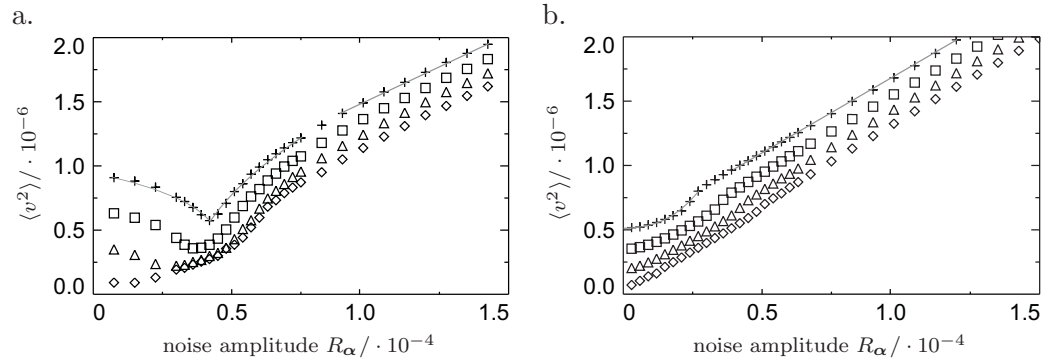

Figure 4.21: Evolution of moments during cluster decay. a. Average mean squared velocity of the LSs depending on $R_{\boldsymbol{\alpha}}$ for different values of k_1 (diamonds: $k_1 = 0.6 \cdot 10^{-3}$, triangles: $k_1 = 2.4 \cdot 10^{-3}$, squares: $k_1 = 4.2 \cdot 10^{-3}$, crosses: $k_1 = 6.0 \cdot 10^{-3}$) in the double-coupling case. b. The same quantities for the single-coupling case.

the particle number by an order of magnitude, in the solid state the ratio of LSs in the bulk compared to those in the cluster boundaries greatly increases. As a separation from the cluster is facilitated for LSs at the boundaries, the threshold for breakup may be smaller for smaller clusters.

A second important observation is that when the cluster size is increased, qualitatively the behavior of the system remains the same, implying in particular a finite transition region in which two states of aggregation coexist. We visualize this result with three correlation functions for low, medium and high noise amplitudes that we have obtained the same way we did for 81 particles. Fig. 4.22a shows the correlation function of a solid state. One observes a plateau of oscillations of almost equal amplitude up to $d \approx 3$ where the correlation function starts to decay. The correlation function in the transition region (Fig. 4.22b) has two characteristic parts: a very high first peak resulting from the collision of isolated LSs and then a number of much lower peaks with a characteristic decay caused by several larger clusters simultaneously present in the system. Going to very high noise amplitudes, only the first peak survives, indicating an almost gaseous

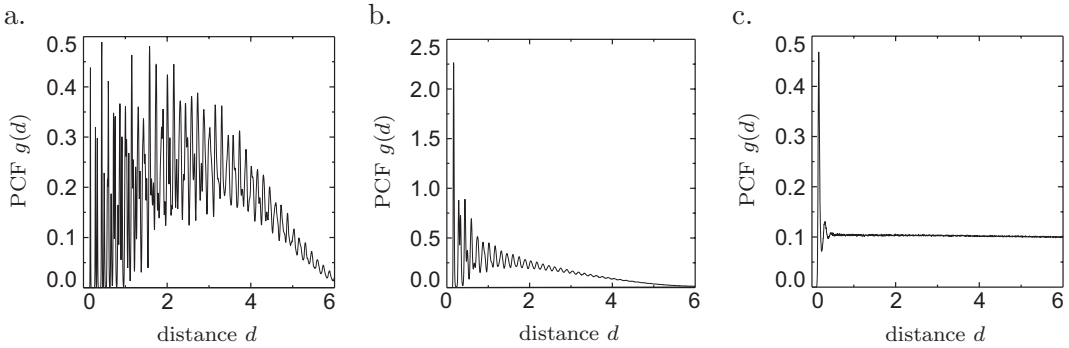

Figure 4.22: Pair correlation functions for a transition from a solid-like phase (a.) over a mixed state (b.) to a liquid-like phase (c.) in a large ensemble of 1225 particles. Parameters: $k_1 = 6.0 \cdot 10^{-3}$, active area $[-9.72, 9.72] \times [-9.72, 9.72]$, all other conditions as in Fig. 4.18.

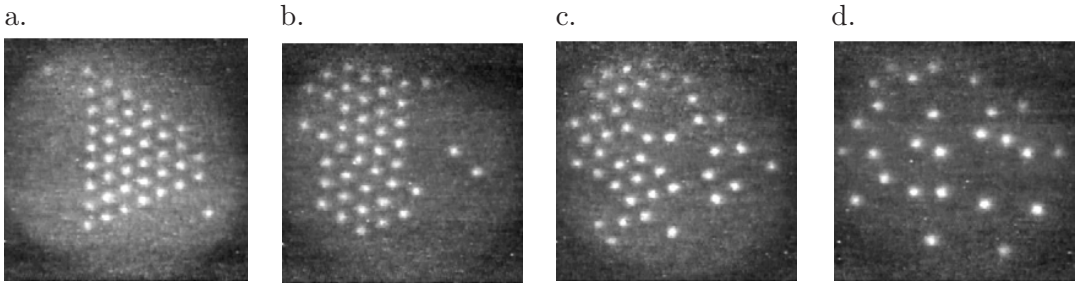

Figure 4.23: Snapshots showing the dynamics of many LSs in a planar dc gas-discharge system with high-ohmic barrier on a active area of diameter $D = 20\,\mathrm{mm}$. The sequence a-d corresponds to a transition from a solid-like to a gas-like state induced by decreasing the specific resistivity of the semiconductor electrode. For details see [172].

state.

As a conclusion to our findings, we may state that increasing the noise amplitudes for a given intrinsic particle dynamics, one always observed a transition from a solid-like to a liquid or gas-like state of aggregation, accompanied by an extended region of coexistence between the two states. In this state, one may clearly distinguish the individual phases for example according to their densities. Universal scaling laws as typically encountered near critical points could not be determined so far although some properties individually scale with power laws. In this sense, one may see a certain analogy to the first-order transition of classical particles shown in Fig. 4.19b. In future investigations, one could try to apply more criteria characterizing the individual phases (compare for example [381, 382]) to get a better image of the nature of the transition.

In the experiment, different states of aggregation of LSs could be observed for example in planar dc gas-discharge systems with high-ohmic barrier. Here, around 50 LSs can coexist in the discharge plane. For high values of the semiconductor resistivity, a solid states forms which preserved in the course of time (Fig. 4.23a). Decreasing the resistivity leads to individual LSs to separate from the cluster (Fig. 4.23b) and then to a transition to a gas-like state (Figs. 4.23c and d). During the process, the particle number decreases as there are collisions which lead to annihilation of one or several LSs. A likely explanation for the observations is given by Fig. 3.3b, showing that the intrinsic velocity may increase when the semiconductor resistivity is lowered. A comparison with Fig. 4.20 then indeed shows that increasing the intrinsic velocity may induce the desired transition. Unfortunately, there are currently no investigations on the question of how the individual parameters in the gas-discharge system influence the fluctuating forces in the system.

There as several other experimental systems capable of carrying a sufficient number of LSs to show many-body dynamics, however, the observation of different states of aggregation has not been reported for potentially different reasons. A promising candidate to find the desired type of dynamics are planar ac gas-discharge systems showing many phenomenological similarities to their dc counterpart. While it is even easier to generate many LSs in this kind of system, up to now mostly solid arrangements have been found. When the density of the LSs was lowered, a collision of two structures often led to fusion or annihilation [320, 383]. Nonetheless, many interesting many-particle phenomena have

been found in this system as well. Theoretically also generation and annihilation events could be accounted for in the Langevin equations by dynamically changing the number of equations according to the phenomena of interest. As an example, a generation could be described by adding a particle with random initial velocity and a position sufficiently far away from the other particles. Also optical systems allow for the observation of many LSs. In set-ups involving liquid crystal light valves, many LSs with oscillatory tails may form and interact in a characteristic way during a short transient phase after their generation, however quickly afterwards the particles become pinned and stationary [311, 312, 384]. Here, the LSs are likely to show no intrinsic propagation and the noise in the system is to weak to overcome pinning effects in the system. Nonetheless, as noisy dynamics has been at least mentioned for a number of other optical systems, it is likely that in optical systems many-particle phenomena will be considered in the future as well. A third type of system that is likely to show the desired type of dynamics are vibrated granular media and colloidal suspensions [4, 330].

Chapter 5

Excursion to biology: the dynamics of cells

Throughout this work, we have dealt with LSs in different types of inanimate systems. Starting from field equations, it was possible to derive reduced equations by methods of adiabatic elimination, which in turn could be used to deal with large ensembles of LSs. In this way, taking the field equations as a fundamental starting point we have developed a certain hierarchy of increasingly complex processes.

We have already mentioned that aside from the above kind of LSs, other types of "structures with particle-like properties" can be encountered in the field of research on complex systems. Many of them arise in the field of biology or life sciences in general, examples are given by cells, swarms of birds, fish, ants, pedestrians or cars. One the one hand, the interest in such structures matches one of the declared long-time goals of researchers working on the field of nonlinear dynamics and self-organization: the application of the knowledge obtained during research in the field of life sciences. However, while some authors have almost euphorically claimed to be able to describe biological patterns such as animal fur coatings with theoretical models (see the book of Murray [385] for a good example), some care has to be taken.

One of the primary problems is that for the systems considered for example in biology the dynamics is significantly more complex than in physical systems. Biochemical processes usually involve large cycles of slow and complexly coupled reactions. Often, an exact knowledge of important steps is extremely difficult to acquire, also because quantitative reproducibility in the experimental works is a problematic issue. As a consequence, the methodology in biology is different from that in physics. There are generically no first principle approaches (i.e. models developed from first principle equations which can be compared to the experiment), but instead the system under consideration is first only described at most on a qualitative (yet non-mathematical) level. In particular, one may try to see correlations between different processes, which may then lead to a rough image of the complex connection between them. Up to now, the number of attempts to overcome these problems is rather low (see for example [386–389]).

In this chapter, we make an excursion to the field of biology and explore some details of the dynamics of living cells. From a general point of view, cells certainly show many properties as we have encountered them for LSs in inanimate systems: they are solitary, very robust with respect to perturbations, have (many) active internal degrees of freedom

and show dynamics and interaction phenomena. On the other hand, the similarities arise only on a purely phenomenological level and have no theoretical background on the basis of model considerations etc. Among other things, we will see that model-free analysis methods allow to find a self-consistent description of cell motion on the basis of stochastic differential equations.

5.1 Cells as particle-like structures

Cells have a fundamental role for biological systems as they can be considered as "building blocks" for structures of higher complexity. Similar to the way of proceeding in physical systems, there are certain prototype systems on which systematic research is carried out in order to transfer the obtained knowledge to other systems. For eukaryotic cells, such a prototype system is given by the social ameba Dictyostelium discoideum [390], which is in particular well established for the investigation of cell motility and chemotaxis [391–396]. While the first term refers to the undirected and stochastic motion of isolated cells, the latter is defined as the ability of cells to perform a partly directed motion along chemical gradients. Chemotaxis plays an essential role for the developmental cycle of Dictyostelium [397]: in a hostile environment in which only a low amount of nutrients is available, single starving Dictyostelium cells are able to emit pulses of cyclic adenosine 3′,5′-monophosphate (cAMP) for which other cells develop receptors during the starvation process. The receptors arranged over the cell body give the cell directional information about the gradient of the signal, and with each cell moving in the direction of the cAMP signals, an aggregation phase sets in during which large numbers of cells arranges on a rotating spiral [390]. This marks the beginning of a differentiation phase: the spiral evolves to a slug-like structure which rises into the vertical to a fruiting body. While the cells forming the stalk die, the tip emits new spores forming isolated cells, so that the cells in the tip reproduce their genetic information.

While each phase in the life cycle of Dictyostelium shows a lot of interesting properties, in the following we are only interested in the directed and undirected motion of isolated cells.

5.2 Experimental techniques

In current research on Dictyostelium, there is a certain gap in development: while the last decade has witnessed a rapid advance in deciphering the molecular pathways that govern the directional response of a cell to chemoattracting agents [397, 398], the overall picture that links the molecular details of intracellular signaling to the macroscopic movement of cells is only beginning to emerge. One important reason for this is that in order to obtain reliable and reproducible experimental results, precisely controlled and tunable environments are required. Compared to similar problems in physical set-ups, living organisms are even more sensitive to external influences of all kinds.

Basically, there are a number of demands an experimental set-up for the investigation of isolated cells has to fulfill. First, cells are usually of a typical size of some micrometers, so that microscopical technique must be applied for data acquisition with which the set-up has to be compatible. Second, spatial homogeneity is very important. Third, cells may release different chemicals from their body, thereby altering their environment. A

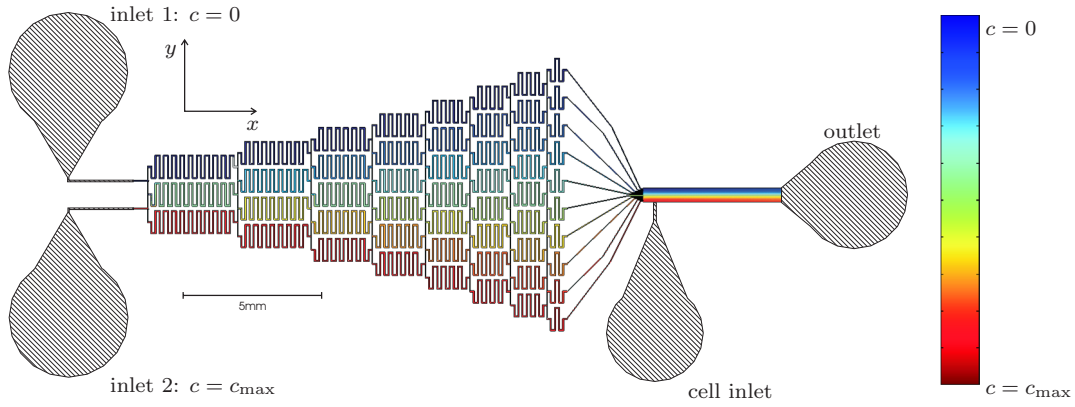

Figure 5.1: Original layout of the microfluidic device used to produce linear gradients, consisting of three inlets, an outlet, a mixing cascade and the main observation channel. The color coding corresponds to numerical simulations of Eqns. (5.1) and (5.2) with parameters and boundary conditions as given in the text, illustrating the functionality of the device.

good set-up should therefore be capable of quickly removing such perturbations. Last, when experiments in chemical gradients are to be carried out, concentration profiles should be possible to produce with a given precision on a time scale fast with respect to the characteristic scales of the cell motion. In the typical chemotaxis assays, concentration profiles are established by diffusion from a chemical source through porous media or a small gap to a sink [399–405]. In most cases, the concentration profile is established slowly and continues to change over time. One notable exception is the design by Fisher et al [401] where temporally stable gradients were established by running solutions of different concentrations through semipermeable fibers embedded in an agarose gel.

All of these chambers have the disadvantage that they do not allow the removal of any chemicals released by the cells themselves. The above problems can be avoided by using microfluidic devices which combine a number of features that make them optimally suited for the study of chemotactic behavior. Aside from allowing a precise manipulation of the concentration profile [406–408] and reducing the transition time to establish a stable linear gradient to the order of a few seconds or less, microfluidic devices can also control the concentration of substances released by the cells themselves and thus replace a dynamically changing concentration distribution with an externally controllable chemical environment. So far, microfluidic devices have been applied to the migration of neutrophils [409], bacteria [410], and cancer cells [411]. In the following investigations, microfluidic techniques are used to study Dictyostelium chemotaxis in spatially linear and temporally stable cAMP gradients.

The device we use consists of two basic parts. The first one is a pyramidal mixing cascade with two inlets whose layout is to scale depicted in Fig. 5.1. The channels have a common height $h = 50\,\mu$m. Solutions of minimal (zero) and maximal ($c_{\max}$) cAMP concentrations are introduced into the device using an automated syringe pumping system through the inlets. The flow velocity through the cascade with a velocity so low that the fluid flow stays always laminar. At each bifurcation in the network, the flow is parted into an upper and a lower branch and diffusively mixed with the flow from the neighboring channels. In this way, from two incoming channels with the concentrations

c_1 and c_2 three new channels with the concentrations c_1, $(c_1 + c_2)/2$ and c_2 are created at each bifurcation. This produces well defined concentration steps with high precision before all branches are finally merged in a single channel making up the second part of the device. It has dimensions of $50\,\mu\text{m} \times 525\,\mu\text{m} \times 5000\,\mu\text{m}$. When the individual channels are merged in the main channel, diffusion turns the fine concentration steps into a linear gradient perpendicular to the direction of the flow.

While we do not want to go into too many details on the production of the device (see e.g [412] for this issue), we quickly recall some basic steps. Photolithographic techniques are used to produce a relief of the network on top of a silicon wafer. A photoresistive coating is spun onto the waver and soft-baked before a photomask with the layout of the device is placed onto the layer and illuminated with ultraviolet light. The coating is then hard-baked, and the substrate is chemically removed where the photoresist has not been exposed to UV light. The master waver with the relief thus represents a positive image of the device. The network is produced by pouring PDMS (polydimethylsiloxane), a silicon-based organic polymer onto the waver, which hardens in the course of time and turns from a viscous liquid to an elastic solid. The PDMS strip with the negative image can then be removed. To finish the device, the bottom of the strip is sealed with a glass coverslip after activating the PDMS surface in a plasma cleaner. In- and outlets for different fluids are produced by drilling small holes through the PDMS strip and connecting them via plastic hoses. The inflow rates through the hoses can be precisely controlled by syringe pumps.

In order to illustrate the mechanism and to assure the functionality of the device, one may numerically find the concentration profiles inside the device by first solving the three-dimensional incompressible Navier-Stokes equation

$$\partial_t \boldsymbol{u} + (\boldsymbol{u} \cdot \nabla)\boldsymbol{u} = -\frac{1}{\rho}\nabla p + \nu \Delta \boldsymbol{u}, \quad \nabla \cdot \boldsymbol{u} = 0, \tag{5.1}$$

where $\boldsymbol{u}$ is the fluid velocity, p is the pressure ρ is the density of the fluid and ν is the kinematic viscosity. The parameters were taken for water ($\rho = 10^{-12}\,\text{g}\,\mu\text{m}^{-3}$, $\nu = 10^6\,\mu\text{m}^2\,\text{s}^{-1}$), and as boundary conditions a constant inflow velocity ($u = 3250\,\mu\text{m}\,\text{s}^{-1}$) as well as a vanishing pressure at the outflow were used, all other boundaries have no-slip conditions. With the stationary solution $\boldsymbol{u}$, one may then solve the convection-diffusion equation

$$\partial_t c = D\Delta c - \boldsymbol{u} \cdot \nabla c + R(c), \tag{5.2}$$

where c is the concentration of cAMP, D the cAMP diffusivity in water (assumed to be $D = 400\,\mu\text{m}^2\,\text{s}^{-1}$ according to [413]) and R is the local reaction rate which was set to zero in a first step. As boundary conditions, fixed concentrations were given at the inflow, at the outflow a purely convective flux was assumed and all other walls were supposed to have no-flux (i.e. isolating) boundary conditions. The result in Fig. 5.1 shows that for the given parameters the mixing cascade quickly generated the desired concentration values at the each bifurcation. Fig. 5.2 shows a slice through the three-dimensional concentration profiles at the beginning and the end of the main channel averaged over the channel height as black lines, confirming that an almost linear gradient develops about $d = 100\,\mu\text{m}$ away from the channel wall where the concentration is almost constant and

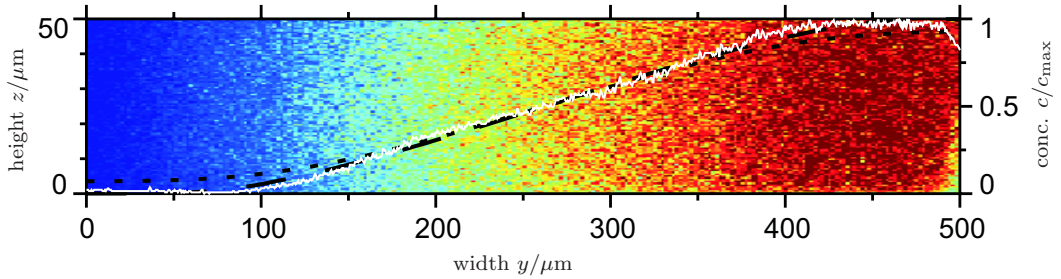

Figure 5.2: Slice cut through the concentration profile the main channel of the device depicted in Fig. 5.1. The colored background (bottom and left scale) shows the results of spatially resolved 2-photon microscopy (scale as in Fig. 5.1), and the white line (bottom and right scale) corresponds to the density averaged over the height coordinate. The solid and dashed black line show the corresponding quantity at the beginning and the end of the channel obtained by three-dimensional numeric simulations of Eqns. (5.1) and (5.2) with parameters as given in the text.

that the flow velocity is high enough that the gradient is not washed out by diffusion over the length of the channel. The numerically obtained results can even be compared directly with experiments. To this end, one may use fluorescein instead of cAMP in the device whose concentration can be measured in the three-dimensional space by 2-photon imaging techniques. The resulting slice cut through the concentration distribution at the beginning of the channel is displayed in Fig. 5.2 as colored background, and the concentration averaged over the channel height is shown as white line, showing very good agreement with the numerical results.

Before presenting the experimental results, we want to point out one more important aspect that has been completely neglected in works on cells in microfluidic devices so far. It is rather intuitively clear that in order to provide a stable gradient over the length of the channel, the fluid velocity must be so high that a diffusive decay of the gradient is prevented, presenting a lower bound for suitable flow velocities. An upper bound is certainly given by the premise that the flow should not cause mechanical deformations of the cells. There is however another effect which lowers this upper bound even further, at least for the analysis of chemotaxis. To understand this effect, let us assume the cell as a small, impenetrable obstacle in the fluid flow on the bottom of the device. As the fluid is incompressible, during their transition along the obstacle small fluid elements undergo a strong change in velocity. In particular, numerical investigations show that the part of the fluid which gets very close to the cell surface comes from a very small volume element in front of the cell. This means that in the absence of diffusion, a concentration gradient convectively transported to the cell will not reach its surface due to the formation of a special boundary layer. Of course, further away from the cell the concentration profile is not influenced by the obstacle. In order for the cell to "feel" the concentration gradient, it is thus necessary that the concentration profile is transferred diffusively into the boundary layer before the flow has passed the obstacle. In other words, the ratio of convective and diffusive transport, expressed by the dimensionless Péclet number $\mathrm{Pe} = Lu/D$ where L is a typical scale (for example the diameter of the cell) must lie in an appropriate range.

A further illustration is given in Fig. 5.3. Here, a semisphere of diameter $L = 15\,\mu$m

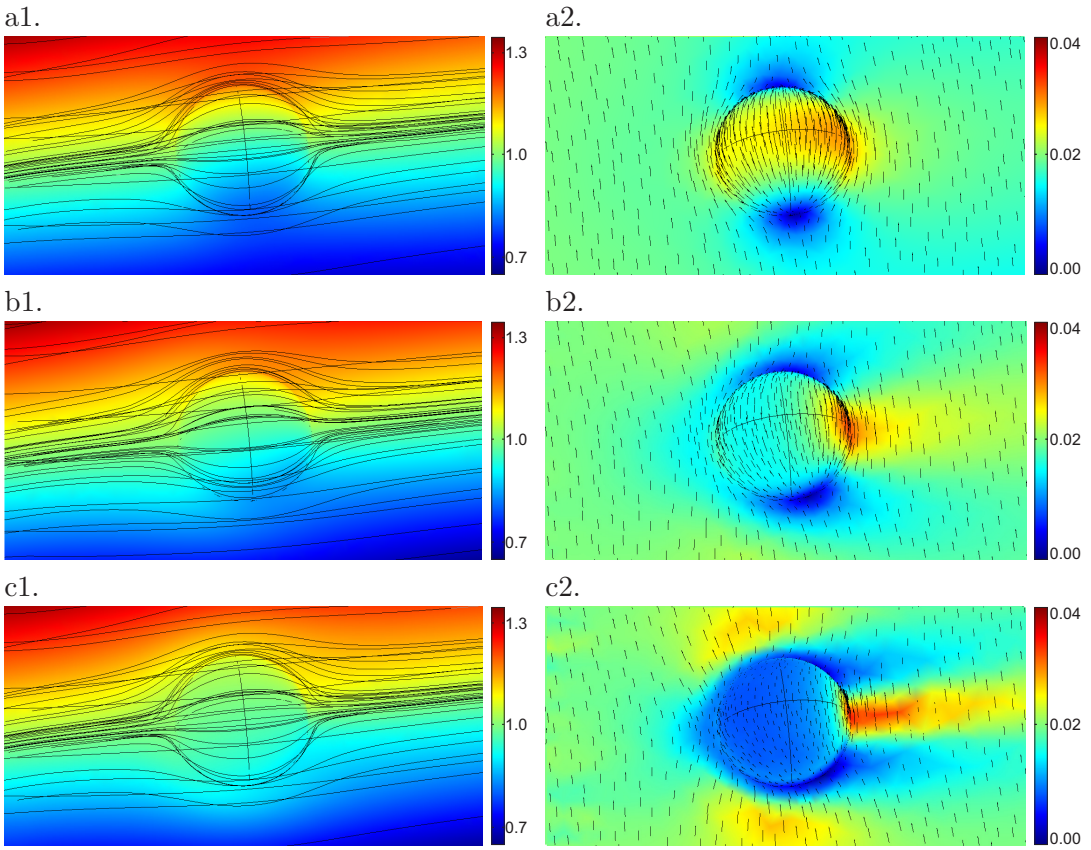

Figure 5.3: Numerical simulations of Eqns. (5.1) and (5.2) showing the shielding of the cell surface from external gradients at high flow velocities. The left figures show the fluid flow around a semi-spherical obstacle for different flow velocities in the form of flow lines and the corresponding concentration profile on the cell and wall surfaces resulting from an an initially linear profile on the left. The right hand side shows the absolute value of the gradient locally tangent to the surface and its direction in the form of small arrows. The Péclet numbers are a. $\mathrm{Pe} = 2$, b. $\mathrm{Pe} = 20$ and c. $\mathrm{Pe} = 200$. For further explanations see text.

was placed on the bottom of the channel in the main device and numerical calculations for the flow and concentration profiles were carried out for different inflow velocities. The simulations for Fig. 5.3a was carried out for $\mathrm{Pe} = 2$. A flow enters the cell from the left and leaves the cell at the right, as also indicated by the black streamlines. It transports in a linear concentration gradient perpendicular to the main flow direction whose value on the surface of the channel and the cell are color-coded in Fig. 5.3a1. In order so see whether the "correct" value of the gradient arrives at the cell, the absolute value of the gradient tangent to the surface is displayed color-coded in a2, the corresponding gradient direction is indicated by small black arrows. As one may see, the deviations from the ideal value (which is 0.02 in our case and shown as a green color) are not too large and lie around 10 to 15 percent. However, additional simulations shows that the gradient decays by diffusion over the total channel length of $l = 5\,\mathrm{mm}$, so that the flow velocity is too small in (a.). Figs. 5.3b and c show essentially the same content as before, however with Péclet numbers of 20 and 200. It turns out that for

the intermediate flow velocity there is the gradient on the cell surface takes the desired value almost everywhere and the gradient can persist over the full channel length. At high flow velocities the above-described shielding effect sets in, so that there is almost no gradient on the cell surface. In additional simulations, the inside of the cell was modeled as a sink by choosing $R(c) = -\gamma c$ with different values of γ under the constraint of a continuous connection of the concentration profile inside and outside, but it was found that the results were not influenced by this modification in a significant way.

In conclusion, the numerical simulations show that sufficient care has to be taken in the choice of the parameters for the experiment. With this preparations, all of the following experiments were carried out in such a way that the above perquisites are met. In order to assure equal initial conditions in each experiment, the following protocol for cell preparation was used: AX3-derived strain WF38 Dictyostelium cells, which express a green fluorescent protein fused to the pleckstrin-homology (PH) domain of the cytosolic regulator of adenylyl cyclase (CRAC), were grown in shaking suspension of HL5 nutrient solution (56 mM glucose, 10 g/l peptic peptone, 5 g/l yeast extract, 2.5 mM Na_2HPO_4, 2.6 mM KH_2PO_4, penicillin, streptomycin, gentamycin, pH 6.5) and renewed from frozen stock every four weeks. For all experiments, 2 ml of cell suspension at $2 \cdot 10^6$ cells/ml were concentrated by centrifugation at 100 g for $\Delta t = 20$ s. The supernatant was removed and the cells were resuspended, loaded into the main channel, and allowed to settle and attach to the bottom glass coverslip for half an hour. Care was taken to avoid the formation of cell clusters and uneven distributions throughout the loading process. After a four hour period of development in slowly running buffer solution (5 mM Na_2HPO_4, 5 mM KH_2PO_4, 2 mM $MgSO_4$ and 0.2 mM $CaCl_2$, pH 6.2, flow speed of about $u = 320$ mm/s) in which the cells were able to signal each other, a cAMP concentration profile was established in the main channel within $\Delta t = 30$ s.

For each experiment, the cellular dynamics was recorded for the first hour following the establishment of the gradient in a region close to the inlet of the main channel using an inverted wide field Olympus IX-71 microscope coupled to a Qimaging Retiga EXI firewire CCD camera. We used a 10x dry objective to capture the whole width of the channel in a 1360x1036 pixel frame. Unless otherwise noted, images were taken at intervals of 30 seconds. The trajectories of cells were extracted from the experimental data using the following procedure: the phase-contrast information was transformed into intensity information by applying a Sobel edge detection, followed by a blurring of the individual images. The centers of the cells were then identified as the centers of connected regions with intensity above a given threshold. From the positions in the individual frames, two-dimensional trajectories were determined using a nearest-neighbor particle tracking algorithm. The quality of this procedure was checked by comparing with manually obtained tracks.

5.3 Directed and undirected motion

5.3.1 Experimental results

A first series of experiments has been performed with two spatially homogeneous cAMP concentration of $c = 0$ nM and $c = 100$ nM as well as with gradients between zero and different maximal levels of cAMP concentration from $c_{\max} = 10^{-3}$ nM to $c_{\max} = 10^4$ nM in steps of one order of magnitude. With the gradient extending over $d = 300\,\mu$m, the

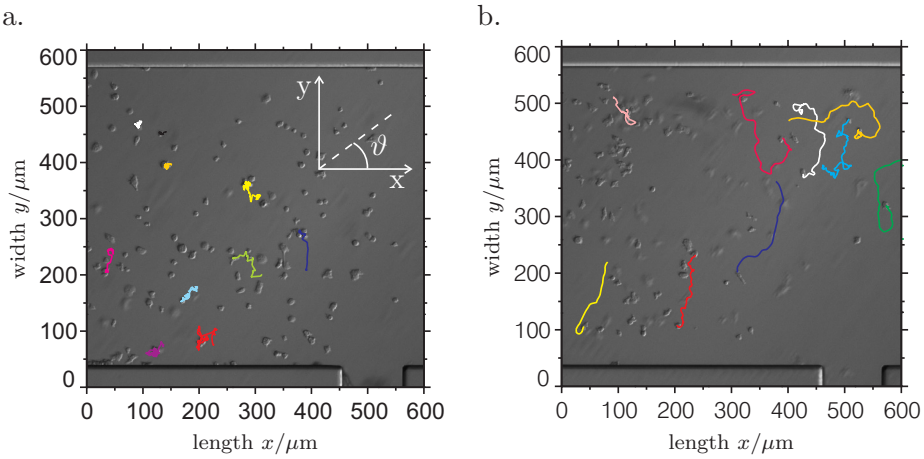

Figure 5.4: Phase contrast images of the initial cell distribution for experiments in buffer solution (a.) and a gradient with $\nabla c = 0.033\,\mathrm{nM}/\mu\mathrm{m}$ (b). The dynamical evolution is indicated by cell tracks which were obtained using an automated tracking algorithm as described in the text and correspond to time intervals of approximately half an hour.

latter corresponds to values from $\nabla c = 3.3 \cdot 10^{-6}$ to $33\,\mathrm{nM}/\mu\mathrm{m}$. For each experiment a new gradient device was produced and the correct gradient steepness was verified by measurement of the fluorescence from a small amount of fluorescein in the solution. Due to the high precision of the microfabrication process, different devices had equal performance.

In the absence of cAMP, the cells are generally not at rest, but perform a random type of motion. Fig. 5.4a shows typical trajectories determined using the above described computer algorithm. The average cell velocity for this case can be determined as $v = 4.19\,\mu\mathrm{m/min}$. The histograms of the velocity components v_x and v_y are symmetric with respect to the origin and the propagation angles (defined in Fig. 5.4a) are practically uniformly distributed, as shown in Figs. 5.5a1 and a2, respectively. As no preferred direction can be observed, it is confirmed that cell motion is not influenced by flow-induced shear forces in the set-up. In a similar manner, cells have been examined at a 100 nM homogeneous cAMP concentration. A slightly higher average velocity of $v = 4.19\,\mu\mathrm{m/min}$ has been observed and again the propagation angles were isotropically distributed. In order to understand the details of the observed random walk and the slightly different average velocities at varied constant cAMP concentrations, one may use stochastic analysis techniques to which we will turn below in Sec. 5.4.

Considering now the gradient case, a directional response can be found when the gradient steepness exceeded a threshold value of $\nabla c = 10^{-3}\,\mathrm{nM}/\mu\mathrm{m}$, below a similar behavior to the non-gradient case is found. Typical cell tracks for the former case are depicted in Fig. 5.4b for $\nabla c = 0.033\,\mathrm{nm}/\mu\mathrm{m}$. The distribution of velocity components and propagation angles are shown in Figs. 5.5b1 and b2. While the v_x distribution is similar to the non-gradient case, the v_y distribution is strongly skewed into the direction of the gradient. The angular distribution exhibits a pronounced peak at $\theta = 90°$ corresponding to the direction of the gradient. From the distributions it becomes clear that although there is a net propagation of the cells in the direction of the gradient, there are strong stochastic deviations which sometimes even lead to phases of motion against the

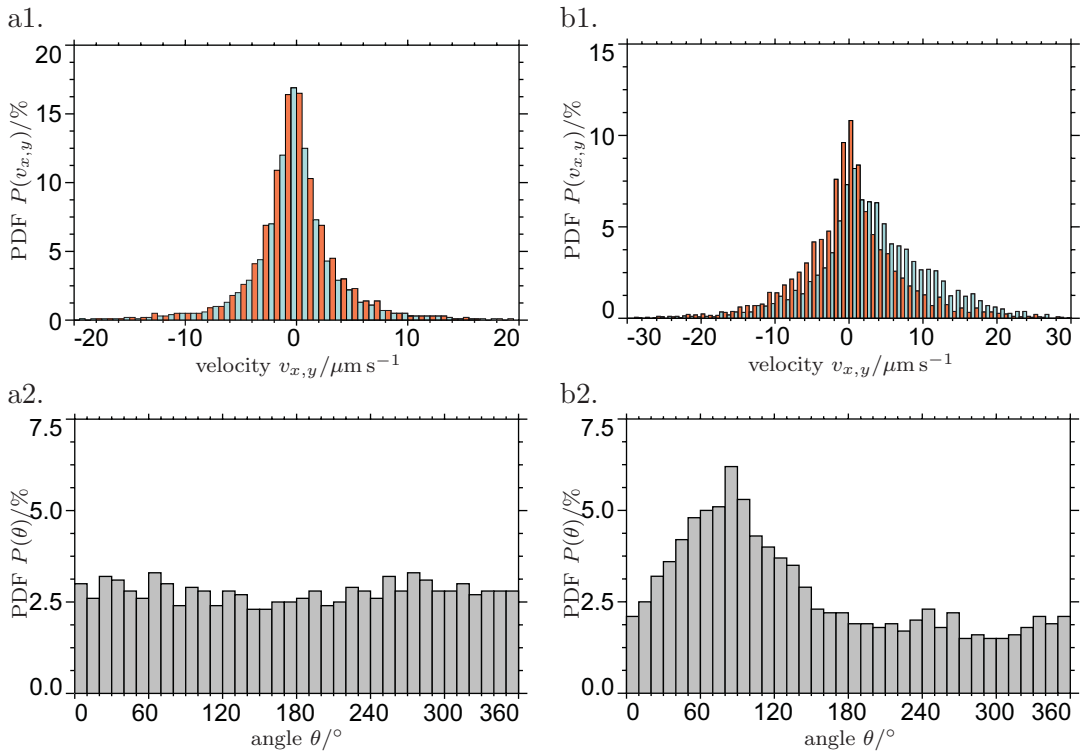

Figure 5.5: Experimentally obtained histograms of for the velocity components v_x (red) and v_y (blue) as well for the propagation angle θ for the trajectories depicted in defined in Fig. 5.4 with corresponding letters.

gradient. To give an overview of the parameter dependency, the results for the average v_x and v_y velocities as well as the average motility as a function of concentration gra-

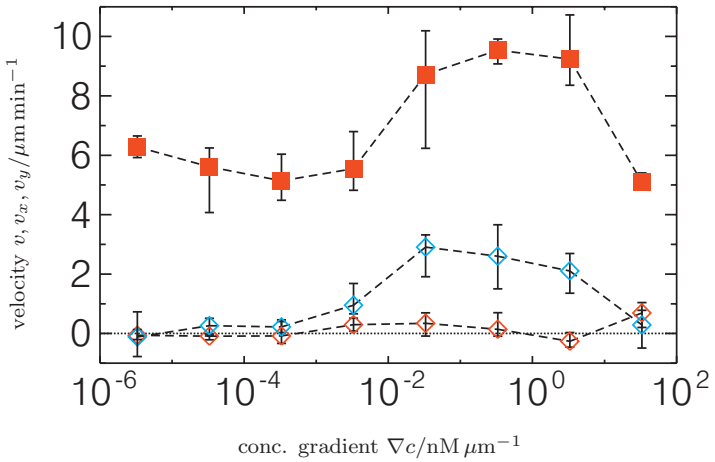

Figure 5.6: Average velocity components v_x (red diamonds), v_y (chemotactic velocity, blue diamonds) as well as absolute velocity (squares) measured for different cAMP gradients. The bars indicate the spread in velocities (see text).

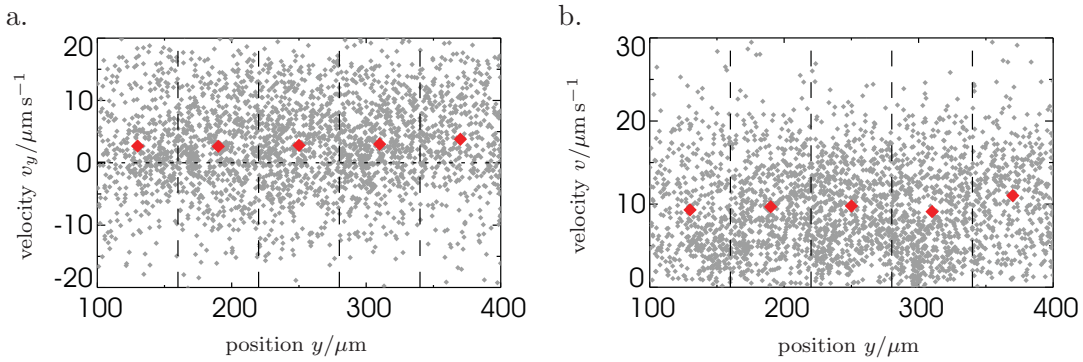

Figure 5.7: Scatter plot of experimentally measured velocity values for v_y (a.) and v (b.) depending on the position in the cAMP gradient for the example case $\nabla c = 3.3\,\mathrm{nM}/\mu\mathrm{m}$. The red dots mark the average values taken in the five bins separated by vertical dashed lines.

dients are summarized in Fig. 5.6. The velocity component v_y averaged in time is also referred to as chemotactic velocity as it characterizes the net migration of cells against the external gradient. The figure also provides error bars, however, in this special case they do not reflect the variance of the velocity distributions which are very large due to the stochastic nature of the dynamics. Instead, the region of the linear gradient has been divided into five equal bins and the cell dynamics was evaluated separately within each bin (Fig. 5.7). The bars then indicate the range of mean velocity values obtained by this binning procedure.

Above a threshold of $\nabla c = 10^{-3}\,\mathrm{nM}/\mu\mathrm{m}$, both motility and chemotactic velocity increase significantly with increasing gradient. For concentration gradients above $\nabla c = 10^{-1}\,\mathrm{nM}/\mu\mathrm{m}$, motility and chemotactic velocity then become approximately independent of the gradient. Note that the average motility for these gradients ($v \approx 9\,\mu\mathrm{m/min}$) is comparable to the motility observed in cells that had been developed to peak motility by external pulsing of cAMP [414–416]. Thus, cells developed in our microfluidic device are at a similar developmental stage as cells developed using traditional pulsing techniques. For even higher gradients, i.e. $\nabla c > 3.3\,\mathrm{nM}/\mu\mathrm{m}$, both quantities decay rapidly to the sub-threshold values.

5.3.2 Conclusions for directed motion

From the above data, two main conclusions can be drawn. First, as indicated in Fig. 5.7 and confirmed via an analysis of the scatter plots for other gradients, the absolute level of local cAMP concentration seems to have no influence on the chemotactic velocity, except in regions of very low or very high cAMP concentrations. Directed motion appears to be determined by the absolute steepness of the gradient only.

Second, as a function of the cAMP gradient, four characteristic situations can be clearly distinguished (compare Fig. 5.6). In the subthreshold regime below $10^{-3}\,\mathrm{nM}/\mu\mathrm{m}$, no directed motion can be observed. It is highly probable that in this regime, too few cAMP molecules hit the receptors in order to generate a signal in the cell.

At the threshold for directed motion, the gradient takes a value of $\Delta c = 3.3 \times 10^{-3}\,\mathrm{nM}/\mu\mathrm{m}$, spanned from zero to $c_{\max} = 10\,\mathrm{nM}$. In the following, we will estimate how many cAMP receptors are sending signals to the cell when the cells travels through

the gradient. One has to be aware that as explained in Sec. 5.2, the transport of cAMP molecules is both determined by fluid flow and diffusion. The following consideration will show that at the above mentioned threshold, chemical equilibrium in cAMP concentration is well established, but that for higher values, unbinding processes at the receptors may be transport limited. Very close to the cell, transport occurs only by diffusion due to the vanishing flow velocity on the cell surface. The thickness δ_D of the corresponding diffusion boundary layer is given by $\delta_D \approx \delta_U \mathrm{Sc}^{-1/3}$, where δ_U is the thickness of the viscous boundary layer and Sc is the Schmidt number, given by the ratio of kinematic viscosity ν and cAMP diffusivity D [417]. Inserting the values also used in the FEM simulation, one finds $\mathrm{Sc} \approx 2500$. In the estimation of the viscous boundary layer thickness, the geometry of the cell plays a role. In the most simple approximation, $\delta_U = \mathrm{Re}^{-1/2} L$, where L is the characteristic length of the cell (we assume $L = 7.5\,\mu\mathrm{m}$), and $\mathrm{Re} = \mu L/D$ is the Reynolds number. Hence one finds $\delta_U = 110\,\mu\mathrm{m}$ and $\delta_D = 8.3\,\mu\mathrm{m}$.

Knowing the length on which diffusion dominates, it is possible to estimate whether binding and unbinding processes to cAMP receptors are reaction or transport limited via the Damköhler number Da, which gives the ratio of reaction and diffusion velocities. The latter is readily obtained by the term $D/\delta_D \approx 50\,\mu\mathrm{m\,s}^{-1}$. The first number can be obtained by assuming Langmuir chemisorption kinetics, where the attachment and detachment of cAMP molecules to the corresponding receptors is described by on and off reaction rates. These are given by $R_{\mathrm{on}} = k_{\mathrm{on}} c(1-\theta)n$ and $R_{\mathrm{off}} = k_{\mathrm{off}}\theta n$, where k_{on} and k_{off} are the on and off rate constants, $\theta = \frac{c}{c+k_{\mathrm{off}}/k_{\mathrm{on}}}$ is the receptor occupancy relative to its maximum value, c is the cAMP concentration and n is the surface number density of cAMP receptors. In equilibrium, i.e $R_{\mathrm{on}} = R_{\mathrm{off}}$, we have

$$\theta = \frac{c}{c + K_d} \tag{5.3}$$

where $K_d = k_{\mathrm{off}}/k_{\mathrm{on}}$. Some authors report the existence of several kinetic receptor forms of cAR1 having different affinity and possibly different density [418, 419], however in order to simplify the argumentation we will assume a spherical cell with $N = 77000$ uniformly distributed receptors [420], an off rate of $k_{\mathrm{off}} \approx 1\,\mathrm{s}^{-1}$ [421] and an intermediate value of $K_d \approx 100\,\mathrm{nM}$. As the reaction velocity is obtained from the reaction rate by dividing by c [417], all necessary values are known, resulting in $\mathrm{Da}_{\mathrm{on}} \approx 0.03(1-\theta)$ and $\mathrm{Da}_{\mathrm{off}} \approx 7\theta$. This shows that while binding is always close to being reaction controlled, the unbinding can become transport limited for higher concentrations. However, at the threshold of directed motion $\mathrm{Da}_{\mathrm{off}} \approx 0.04$, i.e. that there is an equilibrium between flowing bulk and surface cAMP concentration.

If $\mathrm{Da}_{\mathrm{off}}$ is small enough for a given cAMP concentration, chemical equilibrium is achieved and it is easy to estimate the relative receptor density θ from (5.3). This is particularly useful when comparing the signals generated at the front and the rear of a cell migrating in a given cAMP gradient. To this end, we will assume that at the threshold concentration, a cell of length $l_c = 2L$ with receptors uniformly distributed on its surface is in the middle of the gradient. In this case, the concentration at the rear end of the cell is $c_{\mathrm{r}} = 0.475\,\mathrm{nM}$, while the concentration at the front end is $c_{\mathrm{f}} = 0.525\,\mathrm{nM}$. From Eq. (5.3) it then follows that the corresponding relative site occupancies are $\theta_{\mathrm{r}} = 0.473\,\%$ and $\theta_{\mathrm{r}} = 0.522\,\%$ (compare also Table 5.1). Assuming that

$c_{\max} = 2c$ (nM)	θ_r (%)	$\theta_r \tilde{N}$	θ_f (%)	$\theta_f \tilde{N}$	$(\theta_f - \theta_r)\tilde{N}$
0.01	0.005	1	0.005	1	0
0.1	0.048	12	0.052	13	1
1	0.473	118	0.522	131	13
10	4.535	1134	4.988	1247	113
100	32.203	8051	34.426	8607	556
1000	82.609	20652	85	21000	348
10000	97.938	24485	98.131	24533	48

Table 5.1: Occupancy rates and numbers for the receptor cAR1 at front and rear of a cell in the middle of the gradient as well as difference in occupancy as a function of maximum cAMP concentration according to Eq. (5.3) using $K_d = 100\,\mathrm{nM}$.

of the $N = 77000$ receptors, the cell has $\tilde{N} = 25000$ binding sites available on both front and rear, the number of occupied sites in equilibrium would be 118 versus 131. The same calculation can be done at other positions in the gradient. One finds that while the absolute number of occupied receptors may change from about zero to more than 250, the difference of occupied receptors at front and back is always the same. This observation should be compared to the fact that the chemotactic velocity was found to be dependent on the absolute value of the gradient, but not on the concentration itself.

Finally, one may ask what the maximum possible flow-enhanced diffusive flux to the cell surface may be. An upper bound can be found by assuming that the cell is exposed to cAMP for the first time, meaning that the concentration adjacent to the surface is zero and the concentration in the bulk is c_0. In this case, the diffusive flux is given by Dc_0/δ_D [417]. With the above flow conditions and $c_0 = 0.5\,\mathrm{nM}$ at the threshold for directed motion, multiplying the resulting flux by the area of the hemispherical cell yields that 5000 cAMP molecules per second hit each cell. This would correspond to 0.07 cAMP molecules per receptor and second. Assuming a processing time of at most minutes (for example comparable to the period of cAMP waves during aggregation [390]), this suggests that the initial response requires high amplification of a chemical signal subject to shot noise.

In the directional regime, the chemotactic velocity increases with increasing cAMP gradient. The cAMP transport remains reaction limited, and the absolute difference in receptor occupancy at front and rear of the cells increases. For steep cAMP gradients, a plateau regime is entered. Choosing $\mathrm{Da}_{\mathrm{off}} = 1$ shows that the beginning of the plateau region coincides with the cAMP desorption becoming transport limited. As at the same time, the absorption of cAMP molecules stays diffusion limited, one may assume that the receptor occupancies are actually higher that the values in Table 5.1 based on a chemical equilibrium.

In extremely high gradients, one observes a complete loss of any directional response, where the behavior corresponds to the dynamical state observed in the subthreshold regime. As this phenomenon occurs for concentration values of about $c = 5\,\mu\mathrm{M}$, one may use (5.3) to find a lower bound for the receptor occupancy in this case (Table 5.1). The calculation shows that while the difference in the number of occupied receptors is larger than at the threshold for directed motion, at least 98 % of all sites are occupied on average. As steep gradients correspond to high local chemoattractant concentrations

over large parts of the channel, an easy way to explain the cells' loss of directional motion is to assume that the receptors on the cell surfaces get completely saturated, preventing the cells from sensing any cAMP gradient at all. One should however be aware that other authors have proposed that at high cAMP concentrations, on overall desensibilization of cAMP receptors may occur (through alteration in binding properties or covalent modification, compare for example [418]), which may also play a role.

The above considerations raise two important questions: first, how long does it take a cell to measure the occupancy of its receptors in order to eliminate the influence of noise and large offsets, and second, how can a small difference in receptor occupancy lead to a strongly amplified downstream response? The small numbers suggest that stochastic effects on the shot-noise level play a role in chemotactic gradient sensing. However, most current models are based on continuum approximations [389, 422] and the development of a stochastic approach is only beginning to emerge [423].

Last but not least, the findings can be compared with those of other authors in different set-ups. The observed directional response for gradients steeper than $\nabla c = 10^{-3}\,\mathrm{nM}/\mu\mathrm{m}$ is in excellent agreement with the value of $\nabla c = 3.6 \cdot 10^{-3}\,\mathrm{nM}/\mu\mathrm{m}$ reported by Mato et al. [424]. The maximum chemotactic response between $\nabla c = 0.01$ and $0.1\,\mathrm{nM}/\mu\mathrm{m}$ matches the observation by Varnum and Soll [425] who found a maximal chemotactic velocity at $\nabla c = 0.01\,\mathrm{nM}/\mu\mathrm{m}$. A similar value of $\nabla c = 0.05\,\mathrm{nM}/\mu\mathrm{m}$was also reported by Vicker et al. [426]. The rapid decrease in chemotactic velocity for steep gradients, i.e. high cAMP concentrations, was also reported by Varnum and Soll [425]. For shallow gradients however, our results do not agree with the data of Varnum and Soll, who observed a constant level of high motility also for small cAMP concentrations. This can be explained by the differences in the experimental setup. Most of the previous work was carried out in gradient chambers where concentration profiles build up through pure diffusion. Waste products and chemical signals secreted by the cells can accumulate inside these chambers. In a microfluidic device, the effect of waste products and mutual signaling between cells is significantly decreased due to a continuous fluid flow. This leads to different results in the regime of low cAMP concentrations. Fisher et al. [401] have minimized the effect of secreted substances by using appropriate mutants. For comparison, we have translated our data into accuracy of chemotaxis [401, 427] (data not shown). The maximal chemotactic response occurs for similar gradient values Fig. 5 in [401]. However, Fisher et al. report a continuous increase in chemotactic motion with increasing gradient, while we observed a pronounced lower threshold at $\nabla c = 10^{-3}\,\mathrm{nM}/\mu\mathrm{m}$.

5.4 Stochastic motion of cells

With the above experiments, we have been able give an answer to the question how the effective chemotactic motion of cells is connected to the chemical gradient in the system. However, we have also seen that both for directed and indirected motion the dynamics is accompanied by a random walk type of dynamics. From this, two further questions arise: first, what is the nature of the random motion and second, is the latter influenced by cAMP or at the variations observed for example in the average velocity for constant cAMP concentrations just accidental?

Looking at the general state of research, one may remark that a number of elaborate

models of bacterial motility have been developed, see for example [428] and references therein. Much less is known about the migratory dynamics of eukaryotic cells. In most cases, they are modeled as persistent random walkers that are described by an Ornstein-Uhlenbeck process with additional persistence in the direction of motion [429, 430]. This concept has been successfully applied to describe the motile behavior in various higher organisms [431–433]. In recent years, an increasing number of cases was reported that could not be described by the concept of a persistent random walker [434]. In particular, exponential [435] and Tsallis' distributions [436, 437] were observed in contrast to the Gaussian velocity distribution that is expected for an Ornstein-Uhlenbeck process. Also, Lévy walk models have been proposed to account for ballistic dispersion of migrating amebas [438].

The basic reason for the many different types of models and descriptions lies in fact that as common for biological systems, there are generally no first principle models available so that most models are motivated by a phenomenological similarity with the experimental observations. Nevertheless, from our experience with LSs in inanimate systems it seems reasonable to assume that a low-dimensional model with only few order parameters may be suitable to deal with this situation as well even if the order parameters are introduced on a phenomenological level. For the largest part of the commonly used models, a number of different characteristic quantities can be analytically calculated, the latter including moments, velocity distributions, autocorrelation functions and other statistical measures that can also be derived from experimental time-lapse observations of motile cells. As practically all models have been proposed on a phenomenological level, generally no a-priori statements on the magnitude of the parameters appearing in the models can be given from first-principle considerations. Therefore, typically the quantities of interest are fitted to the experimental results and it is checked whether a good and contradiction-free representation can be obtained. A central problem of this approach however is that qualitatively different models may produce similar distributions or other characteristic quantities so that is often hard to decide which model is more suitable to reflect the experimental observations.

5.4.1 Stochastic analysis

In the following, we will approach the above problem using model-free analysis methods, restricting us to the non-gradient case in this work. To provide an experimental basis, a series of experiments was performed with undeveloped cells as well as developed cells in buffer solution and constant cAMP concentrations of $c = 10\,\mathrm{nM}$ and $c = 100\,\mathrm{nM}$. Using a automatized movable microscope state, instead of one a sequence of five images of the channel could be taken, thereby greatly increasing the amount of available data points. Last but not least, the image acquisition interval was decreased to values up to 5 seconds in some of the experiments. Fig. 5.8a shows a typical trajectory of a single cell obtained at the corresponding high acquisition rate of $f = 0.2/\mathrm{s}$. A first visual inspection shows that one may distinguish two "modes" of motion. On the one hand, there are time intervals in which the cell performs a rather erratic motion while the net propagation is only rather small. On the other hand, there are phases in which the motion seems rather directed and the cell changes position in an almost jump-like manner. While this may give a first indication that the motion is not of classical Brownian type, one may consider the PDF for example for the velocity component v_x (Fig. 5.8b). As it is well

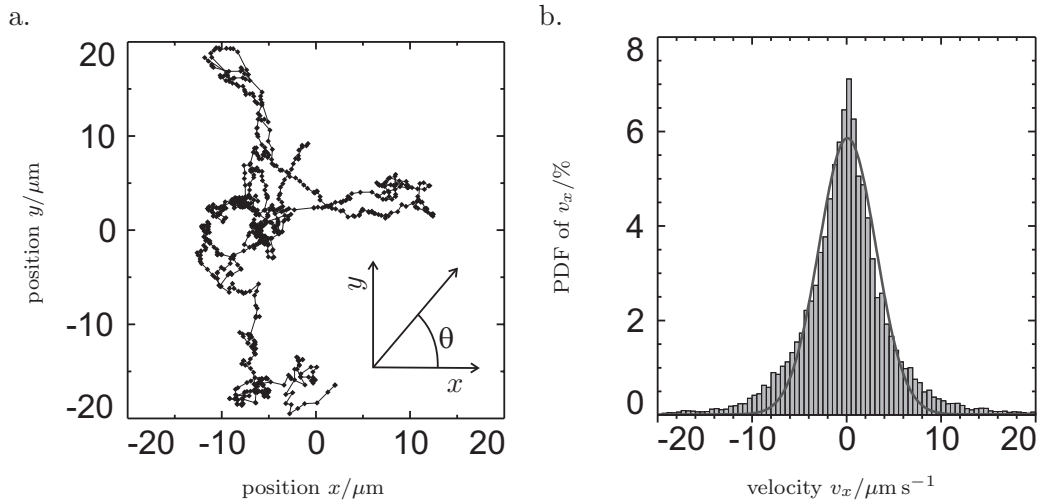

Figure 5.8: Random motion if Dictyostelium cells in isotropic environments. a. Trajectory of the center of a cell performing a random type of motion at a constant cAMP concentration of 10 nM. Each dot corresponds to a step of $\Delta t = 5$ s. b. Corresponding velocity distribution of the v_x component for several cells and Gaussian fit.

known, for Brownian motion each velocity component should individually be Gaussian distributed. A fit to the PDF however shows that while an approximate correspondence is given for low velocities, the tails of the distribution are much too fat to fit the Gaussian prediction.

Instead of postulating an extended model producing heavy-tailed distributions, we will use a stochastic analysis methods that could already be successfully applied in the context of investigating the stochastic dynamics of current filaments in planar gas-discharge systems [96, 157, 158, 173, 320]. While details are given in the literature, we will repeat the basic steps for completeness. As a minimum conjecture, we can expect that there are both deterministic and stochastic contributions to the movement of a cell. A generally applicable approach is given by assuming an underlying Langevin-type equation of the form

$$\dot{\boldsymbol{v}} = \boldsymbol{h}(\boldsymbol{v}) + \underline{\boldsymbol{R}}(\boldsymbol{v})\,\boldsymbol{\Gamma}(t), \tag{5.4}$$

for the velocity $\boldsymbol{v}(t)$ of the center of the moving structure [340, 354]. Here, $\boldsymbol{h}(\boldsymbol{v})$ denotes the deterministic and $\underline{\boldsymbol{R}}(\boldsymbol{v})\,\boldsymbol{\Gamma}(t)$ the stochastic part of motion. The latter contains normalized noise forces $\boldsymbol{\Gamma}(t)$ for which the correlation time should decay fast with respect to the time scale of the average cell velocity so that one may ideally assume white noise,

$$\langle \Gamma_i(t) \rangle = 0, \quad \langle \Gamma_i(t)\Gamma_j(t') \rangle = \delta_{ij}\delta(t-t'). \tag{5.5}$$

The approach assumes that no interaction occurs with other cells, which is a good approximation if the loading density in the microfluidic channel is not too high so that collision events are rare. Then, the general functions $\boldsymbol{h}$ and $\underline{\boldsymbol{R}}$ can be determined from a trajectory $\boldsymbol{v}(t)$ that is a solution of (5.4) without any further assumptions on their

shape using conditional averages:

$$h_i(\boldsymbol{v}_0) = \lim_{\Delta t\to 0}\frac{1}{\Delta t}\,\langle v_i(t+\Delta t)-v_i(t)\rangle|_{\boldsymbol{v}(t)=\boldsymbol{v}_0}\,, \tag{5.6}$$

$$R_{ki}(\boldsymbol{v}_0)R_{kj}(\boldsymbol{v}_0) = \frac{1}{2}\lim_{\Delta t\to 0}\frac{1}{\Delta t}\langle (v_i(t+\Delta t)-v_i(t)) \times (v_j(t+\Delta t)-v_j(t))^T\rangle\big|_{\boldsymbol{v}(t)=\boldsymbol{v}_0}\,. \tag{5.7}$$

Here, the Langevin equation in the case of multiplicative noise is interpreted according ti Itô, otherwise spurious drift terms have to be considered in (5.6). As explained in [157], taking a finite time-step Δt in the above equations changes the results on the analysis, however, decreasing the time-step further and further usually causes a continuous convergence to the correct result. As in the practical data analysis also only a finite amount of data points is available, the exact conditional average is replaced by a binning procedure during which the space of the random variables is divided into small bins, yielding

$$h_i(\boldsymbol{v}_0) \approx \frac{1}{\Delta t}\,\langle v_i(t+\Delta t)-v_i(t)\rangle|_{\boldsymbol{v}(t)\approx\boldsymbol{v}_0}\,, \tag{5.8}$$

$$R_{ki}(\boldsymbol{v}_0)R_{kj}(\boldsymbol{v}_0) \approx \frac{1}{2\Delta t}\,\langle (v_i(t+\Delta t)-v_i(t)(v_j(t+\Delta t)-v_j(t))^T\rangle\big|_{\boldsymbol{v}(t)\approx\boldsymbol{v}_0}\,. \tag{5.9}$$

An additional problem in real-life applications arises from the fact that the claim of white noise (5.5) can never exactly be fulfilled. Therefore, the approximation of white noise is only valid on sufficiently long time-scales, but does not hold for very short time-scales. Correlations in the fluctuating forces destroy the validity of (5.6) and (5.7) and cause typically a characteristic divergence of the conditional averages if the time-step comes into the range of the noise correlation time. Consequently, the time-step has to be chosen in such a way that it is as small as possible but larger than the correlation time of the fluctuating forces.

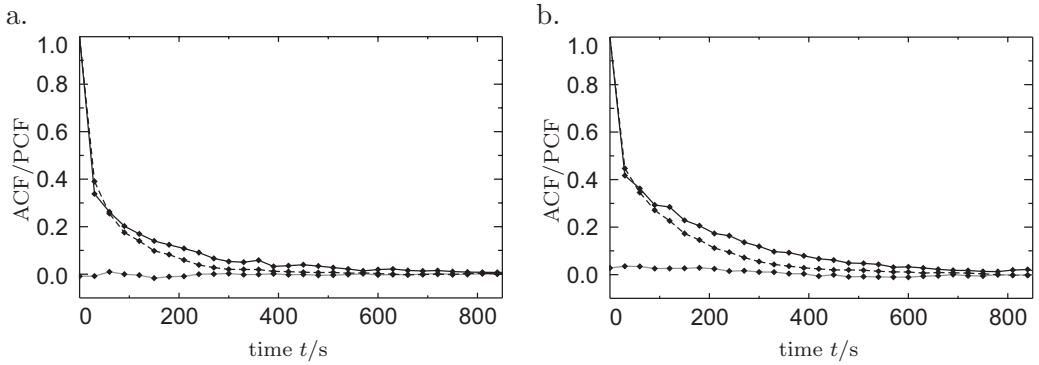

Figure 5.9: Auto- and cross correlation functions for cells in development buffer (a.) and after two hours of exposure to cAMP with $c = 10\,\mathrm{nM}$ (b.). The solid and dashed black lines correspond to autocorrelation functions of v_x and v_y, respectively, while the grey line marks the v_x-v_y cross correlation function.

For the concrete analysis of the experimental call tracks, one may first consider the fact that great care has been taken for the spatially homogeneous preparation of the experiments. In a next step, one may check the above assumptions on correlation times by first looking at auto- and cross correlation functions of the experimentally measured velocity time series. While in the periods where a strongly erratic motion is observed the correlation even between successive steps is very small, the correlation functions for the whole velocity series shows a strong decay for short times followed by a slow decay over about ten minutes, as shown for the cases of buffer solution and a constant cAMP concentration of $c = 10\,\mathrm{nM}$ in Fig. 5.9a and b, respectively. One has to be aware that the correlation curves arise from a coaction of deterministic and stochastic dynamics and thus do not allow for a direct conclusion about the correlation time of the noise forces alone. Motivated by the above findings, we will start with the assumption that (5.4) is approximately valid on a time scale of $\Delta t = 30\,\mathrm{s}$. Evaluating the experimental trajectories using (5.6) and (5.7) (data not shows) reveals within the precision of the averaging procedure that the general Langevin equation (5.4) is isotropic in velocity space, meaning that it can be simplified to

$$\dot{\boldsymbol{v}} = h(v)\,\frac{\boldsymbol{v}}{v} + R(v)\,\boldsymbol{\Gamma}(t). \tag{5.10}$$

While for the deterministic part this also directly follows from symmetry arguments, it should be pointed out that the dependence $R(v)$ couples the velocity components v_x and v_y so that they are no longer independent. However, as we will discuss below this coupling does not only produce self-consistent results, but also matches the mechanism for cell propagation. As the relevant functions are now one-dimensional, the conditional average based analysis also can be executed in a quasi one-dimensional way [157, 173] yielding

$$h(v_0) \approx \left\langle \frac{(\boldsymbol{v}(t+\Delta t) - \boldsymbol{v}(t))}{\Delta t} \cdot \frac{\boldsymbol{v}(t)}{v(t)} \right\rangle \Bigg|_{|\boldsymbol{v}(t)|\approx v_0} \tag{5.11}$$

and

$$R(v_0) \approx \left\langle \frac{(v_x(t+\Delta t) - v_x(t))^2 + (v_y(t+\Delta t) - v_y(t))^2}{4\Delta t} \right\rangle \Bigg|_{|\boldsymbol{v}(t)|\approx v_0}. \tag{5.12}$$

All results we will present and discuss in the following have been obtained via the one-dimensional analysis as the resolution is generally much better than for the two-dimensional analysis.

In order to analyze and compare the cell dynamics in different environments, a series of experiments was performed in the following way. After inserting the cells into the channel the latter have been exposed to a flow of buffer solution for one hour. Afterwards, the environment of interest was created in the channel, which typically took less than 30 seconds to build up. The cell motion was then recorded for several hours. For the data evaluation, the data were binned into intervals of one hour and all data sets were analyzed individually. As it turns out, the dynamics is qualitatively similar in all analyzed cases (Figs. 5.10 and 5.11). As for classical Brownian motion, in the deterministic part of

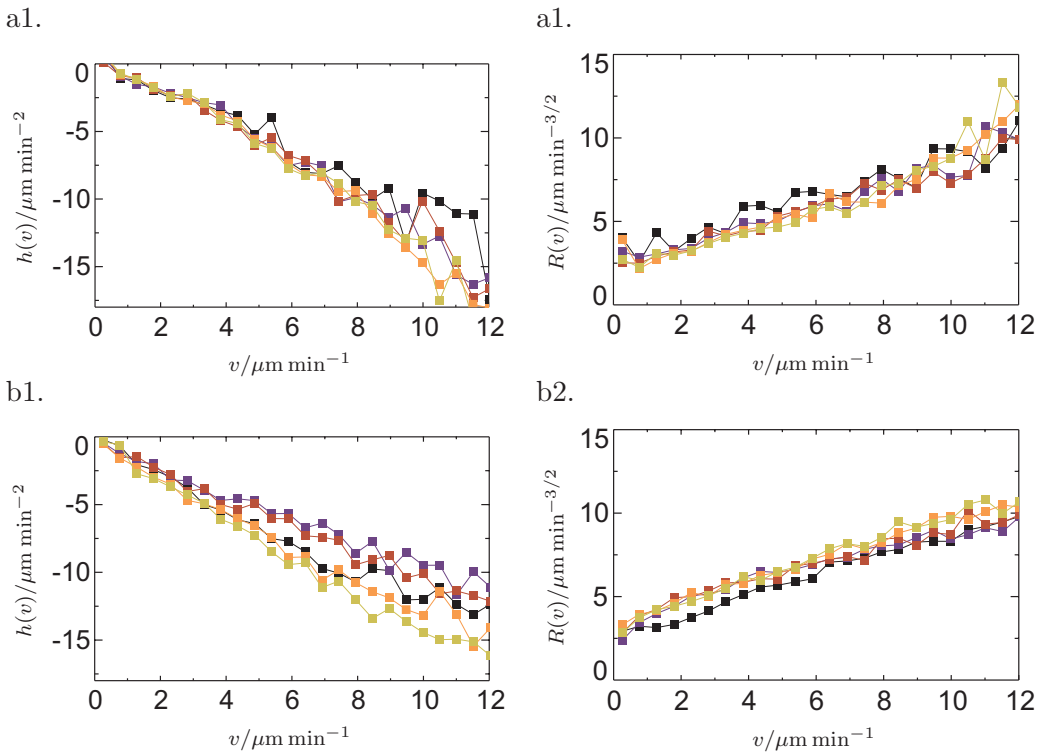

Figure 5.10: Deterministic and stochastic contributions to the cell motion estimated using Eqs. (5.11) and (5.12) for cells in development buffer (a1 and a1) and 10 nM of cAMP (b1 and b2). Color coding: black = pre-exposure time in development buffer, blue = first hour, red = second hour, orange = third hour, yellow = fourth hour.

the dynamics the acceleration is almost proportional to the velocity with a negative proportionality constant. The difference to classical Brownian dynamics must thus lie in the stochastic part. Indeed, there is no constant noise amplitude (i.e. additive noise), instead $R(v)$ increases strongly with increasing velocity (i.e. multiplicative noise). Again, there is an almost linear slope of the curve. Several further comments on the figures can be made. First, one may test the dependence of the results on the time step Δt. To this end, for several cases the latter was varied from $\Delta t = 10\,\mathrm{s}$ to $\Delta t = 120\,\mathrm{s}$. The results show no significant dependence on the time step, indicating that as discussed above the time step is small enough to obtain a good convergence to the ideal "Markov" result and that the noise correlation time lies below 10 s. Second, the averaging process is rather good for velocities of $v < 12.5\,\mu\mathrm{m/min}$ and still of acceptable quality up to $v < 25\,\mu\mathrm{m/min}$, for higher velocities the convergence towards the correct result is not complete due to the limited number of data points. Unfortunately, it is difficult to give a measure for the local convergence of the averaging procedure in each bin as the individual distributions are of non-standard type (like Gaussian, Poisson etc) and thus no analytic expressions for the error of the mean value are known.

Turning now to more details on the concrete results and the influence of different environments, Fig. 5.10 shows both functions $h(v)$ and $R(v)$ for developed cells during a 1-hour exposure to development buffer followed a. by another exposure to development

buffer and b. by an exposure to cAMP ($c = 10\,\mathrm{nM}$) for the same time. The results are displayed only for $v < 12.5\,\mu\mathrm{m/min}$ where very good convergence could be achieved. The analysis shows that during a permanent exposure to development buffer, there is no long-term change in the dynamic behavior of the cells, allowing for the conclusion that no fatiguing or other processes take place inside the cells that affect its motion. A slightly different situation is encountered however when the cell is exposed to cAMP. Before the exposure, a comparison of Figs. 5.10a and b shows that the dynamical behavior of the cells is quantitatively the same in both experiments. After the exposure, the noise amplitude still remains the same independent of the exposure to cAMP. In the deterministic part of the dynamics, there is however a certain change. Directly after the exposure to cAMP, the deterministic damping decreases about 15 %, which in coaction with the unaltered fluctuating part leads to an increased motility of the cell. In the course of time however, the cell seem to adapt to its new environment, so that the damping re-increases until reaching its original value after about three hours. The trend even continues and the damping rate exceeds its original value, making the cell effectively slower compared to the buffer solution case.

Carrying out the same analysis in a cAMP environment with a concentration $c = 100\,\mathrm{nM}$ and for undeveloped cells, as for the development buffer case no change in the course of time was observed. This raises the question whether the changes in the 10 nM cases are statistically significant or just an artifact due to a lack of convergence. To clarify this question, a second series of analogue experiments was carried out. While the results for undeveloped cells, 0 nM and 100 nM were found to be the same as in the first experiment, in the 10 nM case again a variation was found, however only about half as large as in the case depicted in Fig. 5.10b. This makes it rather difficult to decide whether there is a slow change due to an adaption to stimulating chemicals in the course of time or not.

As with the available amount of data question of the time-dependence is difficult to clarify, in the following we will assume that no time-dependence is present and use

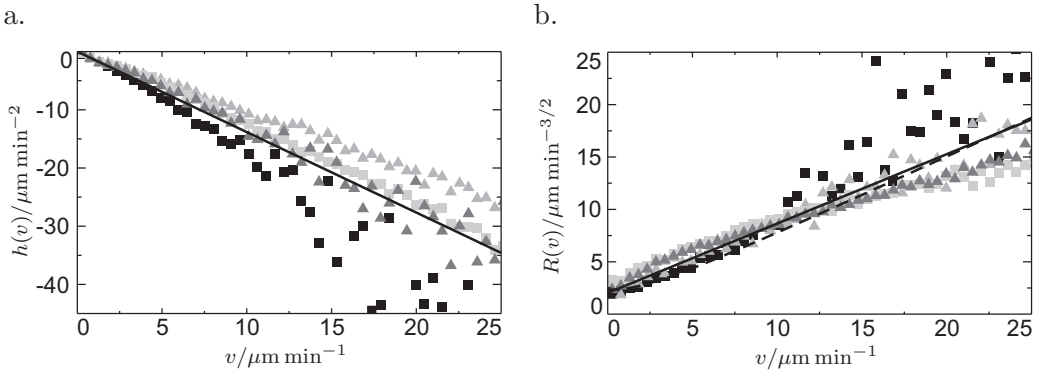

Figure 5.11: a. Deterministic and b. stochastic contributions to the cell motion estimated using Eqns. (5.11) and (5.12) for undeveloped cells (black squares) as well as developed cells in 0 nM cAMP (dark grey triangles), 10 nM cAMP (medium grey triangles) and 100 nM cAMP (light grey squares). The 0 nM case was fitted with the expressions given in the text yielding $\alpha = 2.027$, $\beta = 0.662$, $\gamma = 1.383$, $\eta = 5.3687$, $\mu = 0.55263$, in b. the solid line is the Lévy and the dashed line is the Tsallis fit.

all available data for a given chemical environment in a single analysis to improve the resolution for higher velocity values up to $v = 25\,\mu$m/min. Fig. 5.11 shows the deterministic and stochastic part for the four analyzed cases. As a result, we find that the noise amplitude as a function of velocity is quantitatively the same in all cases. In the damping rate however, there is a clear difference that is statistically significant in any case. Compared to the dynamics of developed cells without cAMP stimulation, the damping for the undeveloped cells is about 50 % higher. The results of 0 nM cAMP and 100 nM cAMP practically coincidence. Last but not least, cells which are stimulated with 10 nM cAMP are most motile as their damping rate is about 30 to 40 % lower than in the development buffer environment.

With the above model-free analysis, we have basically obtained a complete characterization of the cell motion in a stochastic sense, and all relevant quantities like moments and correlations can be calculated. Before coming to a discussion of the results on a biological level, we want to make a connection to other models which as explained above tend to derive results on the bases of distribution functions and other related quantities. Following the stochastic analysis, it seems reasonable to fit the parameter-free estimates with analytic expressions $h(v) = -\gamma v$ and $R(v) = \alpha + \beta v$ where the coefficients may depend on the environment and on time. As the latter dependence is extremely slow, it can be neglected on the typical time scale of the cell motion. One may now ask what form the corresponding stationary velocity PDF is. As it is rather well-known [340, 354], for each Langevin equation a unique evolution equation for the velocity PDF can be derived, which is referred to as Fokker-Planck equation in the Markov case. Identifying the functions in the Langevin equations with the first and second Kramers-Moyal coefficients of the Fokker-Planck equation, the latter reads

$$\partial_t P(v_x, v_y) = -\partial_{v_i}(D_i^1(v_x, v_y)P(v_x, v_y)) + \partial^2_{v_i v_j}(D_{ij}^2(v_x, v_y)P(v_x, v_y)) \tag{5.13}$$

with $i, j = x, y$, $D_i^1(v_x, v_y) = -\gamma v_i$ and $D_{ij}^2(v_x, v_y) = \delta_{ij}(\alpha + \beta\sqrt{v_x^2 + v_y^2})^2$. Eq. (5.13) can be rewritten as a continuity equation for the probability density flux:

$$\partial_t P(v_x, v_y) = -\partial_{v_i} j_i \quad \text{with} \quad j_i = -\gamma v_i P - \partial_{v_i}(\alpha + \beta v)^2 P. \tag{5.14}$$

With the isotropy in phase space, the stationary solution should be isotropic as well, i.e. $P_{\mathrm{st}}(v_x, v_y) = P_{\mathrm{st}}(v, \theta) = P_{\mathrm{st}}(v)$. As boundary conditions, we have the natural condition $P_{\mathrm{st}}(v) \to 0$ and $\partial_{v_i} P_{\mathrm{st}}(v) \to 0$ for $v \to \infty$. Via (5.14), one may directly conclude $j_i = 0$ in the stationary case. In order to solve the second equation in (5.14) with vanishing j_i, one may introduce $G(v) = (\alpha + \beta v)P_{\mathrm{st}}$ (compare for example [354]). This yields the new evolution equation

$$\partial_{v_i} G(v) + \frac{\gamma v_i}{(\alpha + \beta v)^2} G(v) = \partial_v G(v) + \frac{\gamma v}{(\alpha + \beta v)^2} G(v) = 0. \tag{5.15}$$

The latter equality holds as $\partial_{v_i} G = \partial_v G \partial v_i v = \partial_v G v_i / v$. This ODE is now easy to solve, and the solution reads

$$G(v) = G_0\Big(\int_v \gamma \exp\Big(\frac{v'}{(\alpha + \beta v')^2}\Big)\,\mathrm{d}v'\Big). \tag{5.16}$$

As a consequence, one directly finds

$$\begin{aligned} P_{\mathrm{st}}(v) &= \frac{N_0}{(\alpha+\beta v)^2}\Big(\int\limits_v \gamma \exp(\frac{v'}{(\alpha+\beta v')^2})\,\mathrm{d}v'\Big) \\ &= \frac{N_0}{(\alpha+\beta v)^{2+\gamma/\beta^2}} \exp\Big(-\frac{\alpha\gamma}{\beta^2(\alpha+\beta v)}\Big). \end{aligned} \tag{5.17}$$

From (5.17) we can directly see that

$$\begin{aligned} \partial_{v_i}(\alpha+\beta v)^2 P_{\mathrm{st}}(v) &= -\frac{N_0\gamma v}{(\alpha+\beta v)^2}\Big(\int\limits_v \gamma \exp(\frac{v'}{(\alpha+\beta v')^2})\,\mathrm{d}v'\Big)\partial_{v_i} v \\ &= \frac{N_0\gamma v_i}{(\alpha+\beta v)^2}\Big(\int\limits_v \gamma \exp(\frac{v'}{(\alpha+\beta v')^2})\,\mathrm{d}v'\Big) \\ &= -\gamma v_i P_{\mathrm{st}}(v). \end{aligned} \tag{5.18}$$

meaning that $j_i = 0$ so that the correct solution of (5.14) is indeed given by (5.17). It is interesting to discuss the limiting cases of small and large velocity given by $\alpha \gg \beta v$ and $\alpha \ll \beta v$, respectively. In the first case, the PDF from (5.17) turns into

$$P_{\mathrm{st}}(v) \approx N_1 \exp\Big(-\frac{\gamma v^2}{2\alpha^2}\Big). \tag{5.19}$$

This is the Gaussian distribution one would expect for classical Brownian motion, which should be intuitively clear as the multiplicative noise is almost additive for small velocities. Consequently, under these conditions the Langevin equation describes an Ornstein-Uhlenbeck process leading to (5.19). In the opposite case of high velocities, the exponential is close to unity, yielding the power law

$$P_{\mathrm{st}}(v) \approx N_2 v^{-2-\gamma/\beta^2}. \tag{5.20}$$

As there are no first principle considerations which could be applied the find the velocity PDF of the cells (and thus demand the functions h and R to be fitted by linear functions), some works suggest [436, 437] that the random motion could be determined by a Tsallis statistics [439–441]. The central idea here is that the system tries to maximize the generalized entropy

$$S_q = \frac{\int P^q(\boldsymbol{v})\,\mathrm{d}\boldsymbol{v} - 1}{1-q} \tag{5.21}$$

where q is a measure for the non-extensivity of the system of interest. It can be shown that the most simple way of producing a stationary distribution which maximizes (5.21) via a Langevin equation is by substituting the linear expression for the noise amplitude

from above by the expression $R^2(v) = \eta + \mu v^2$. Analogously to our calculation (5.15)-(5.18), one may quickly check that

$$P_{\rm st}(v) = N_3(\eta + \mu v^2)^{1+\gamma/(2\mu)}. \tag{5.22}$$

The asymptotics for this solution are rather similar to (5.17): for $\eta \gg \mu v^2$ we have

$$P_{\rm st}(v) \approx N_4 \exp\Big(-\frac{\gamma v^2}{2\eta}\Big) \tag{5.23}$$

and the case $\eta \ll \mu v^2$ yielding again a power law

$$P_{\rm st}(v) \approx N_5 v^{-2-\gamma/\mu}. \tag{5.24}$$

Note in particular that the definition (5.21) implies that the exponent $1+\gamma/(2\mu)$ should correspond to $1/(1-q)$, which is equivalent to $q = \gamma/(\gamma + 2\mu)$.

To test the self-consistence of the stochastic analysis and to check which fit matches better the experimental data, we may for example consider the case of cells in development buffer and fit the different analytic functions $h(v)$ and $R(v)$ to the experimental curves from Fig. 5.11. The resulting curves have been added to the figure to facilitate a comparison with the measured data points (the fit coefficients are given in the figure caption). While both curves yield an acceptable representation of the experimental data, a slightly better coincidence is obtained for a linear fit of the noise amplitude (solid line). As the distribution $P_{\rm st}(v, \theta)$ should not depend on the angular coordinate due to the isotropy of the phase space, we may furthermore improve the experimental determination of $P_{\rm st}(v)$ by considering the integral distribution over the angular coordinate, i.e.

$$\tilde{P}_{\rm st}(v) = \int_0^{2\pi} P_{\rm st}(v, \theta)\, {\rm d}\theta. \tag{5.25}$$

Fig. 5.12a shows this distribution as well as the analytic predictions (5.17) and (5.22) with the fit coefficients from the stochastic analysis in linear representation. Although velocity values up to $v = 25\,\mu$m/min have been used to find the fit coefficients, it turns out reasonable to compare the velocity PDFs up to the maximal measured values of $v \approx 37.5\,\mu$m/min. Both linear and Tsallis curve basically reproduce the experimentally measured PDF, there are however some deviations for small velocities to to $5\,\mu$m/min. The latter are larger for the linear and smaller for the Tsallis fit. As the values of the PDF are rather small for high velocities, it is worth looking at the tail of the distribution in a double-logarithmic plot (Fig. 5.12b). As expected from theoretical predictions, the tail of the PDF forms a straight line in the representation, corresponding to a power law. One may see that for the given case, the linear fit of the noise amplitude produces a better coincidence with the measured data than the Tsallis prediction. The coefficient q as a measure for the non-extensivity of the system can be estimated to be $q = 0.56$.

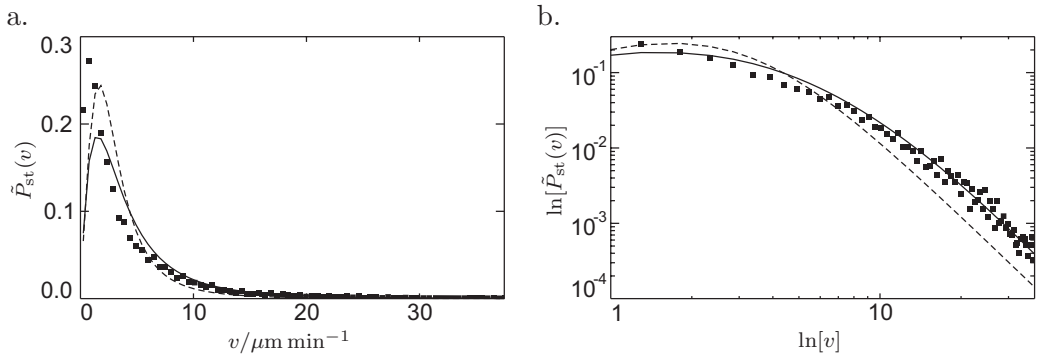

Figure 5.12: Comparison of experimental measured velocity PDFs and prediction of the stochastic analysis. a. Experimentally measured stationary velocity PDF $\tilde{P}_{\rm st}(v)$ as defined in (5.25) for cells in development buffer and fit according to Eqns. (5.17) (solid line) and (5.22) (dashed line) using the fit coefficients given in Fig. 5.11. b. The same data in double-logarithmic plot.

Results for the PDF similar to the above shown ones can also be found for the other chemical environments under investigation. Deviations from the theoretical predictions occur in particular for very small velocity values. Basically, this may have two potential reasons. On the one hand, there may be some additional effects for small velocities that are not included in the Langevin equation set up above. On the other hand, a velocity of $v = 5\,\mu$m/min corresponds to a displacement of two pixels in one frame. As the experimental images shown in Fig. 5.4 have been taken with a total resolution of approximately 400 pixels, an error of 1 pixel per frame in the determination of the cell position may easily result from the tracking algorithm. This "measurement noise" may play a role in particular for small cell velocities.

5.4.2 Discussion of the results

The above stochastic analysis has revealed that Dictyostelium cells in environments of constant cAMP concentration propagate according to a damped type of motion overlayed by multiplicative fluctuations. This reflects the qualitative properties of the observed random walks. We have seen that in certain phases, the motion is rather erratic and confined to a small region of space. In this state, the velocity is low and the dynamics is essentially of Brownian type. When accidentally the velocity becomes high enough via the fluctuations, the noise amplitude rises strongly as well. This may induce a short phase of "jump-like" dynamics in which a rather directed type of motion is observed. The cell can thereby change its position before the velocity becomes again so low that the dynamics switches back to a Brownian type. This kind of motion belongs to the class of Lévy walks [442, 443] and offers several advantages compared for example to pure Brownian motion from an evolutionary point of view. It has been pointed out that Lévy walks are an efficient search algorithm [444] and have been proposed as a model for motion of soil amebas [438] and as search flight patterns of albatrosses [445]. The Tsallis approach proposed by some other authors [436, 437] can also be used to find consistent results with the stochastic analysis and leads to similar statistics as the linear representation of the multiplicative noise. In this context it is important to recall

that Tsallis statistics was originally developed as a thermodynamical approach to fractal systems [439] and has re-interpreted more recently in terms of superstatistical systems [446].

Shenderov and Sheetz have developed a detailed model of Dictyostelium discoideum locomotion based on the observation of inversely correlated periods of turning and movement [447]. While the overall shape of our velocity PDFs is similar to their result, in the above presented case better agreement with the experimental data for large velocities is found, which can be attributed to the presence of multiplicative noise. Moreover we have not included any specific model assumptions to derive the stochastic equations of motion and thus assume that our approach can be readily applied to other cellular systems. For example, in their study of human keratinocytes and fibroblasts, Selmeczi et al. also employed conditional averaging for the analysis of their data [434]. However, they did not exploit the connection to the Kramers-Moyal coefficients of the corresponding Fokker-Plack equation, which can be used to directly obtain the velocity PDF without any further assumptions.

With respect to the investigations carried out in this work, one may point out that we have encountered the Langevin equations obtained by stochastic data analysis methods for cells also in the context of self-organized LSs. Although we have artificially introduced the velocity of the cells as phenomenological order parameter to characterize the dynamics, it is astonishing that formally very similar results are found. In physical systems, usually two types of noisy dynamics are distinguished. On the one hand, there is classical Brownian motion which can be considered as passive in the sense that the action of external mechanisms drives the particle under consideration which would otherwise either be at rest. The other scenario is active Brownian motion where the passive deterministic motion turns to intrinsic, dynamically stabilized motion which is superimposed by noise [351, 373]. The existence of both phenomena for LSs was proven experimentally using the above introduced methods of conditional averages (compare Fig. 3.3 and the related remarks). According to this classification, the dynamics of the cells of passive type. Note however that the noisy contributions to cell motion do not arise from thermodynamic fluctuations caused by external heat baths or other cells as expected in the classical Brownian problem. They are generated by the cells themselves so that the movement may still be considered "active" in a biological sense. Detailed observations of eukaryotic cells have shown that the individual cell, capable of changing its shape in the course of time, extends a membrane process named lamellipodium which is driven by the polymerization of actin [390]. The perpetual formation and retraction of pseudopodia can be interpreted as a disordered walking motion.

While details of the connection between the determined Langevin equation and the biological processes inside the cell have to be clarified in future works, a number of implications arise as immediate consequences of the above observations. Only the damping of the cells seems to be affected by cAMP. This indicates that two different mechanisms may be responsible for damping and propulsion. One may speculate that while the noisy part of the dynamics is due to pseudopodia, damping is caused by the limitations of potential cell body deformations. A potential adaption to the presence to cAMP in the course of time occurs for those cAMP concentrations for which an onset of directed motion has been observed. Finally, the stochastic analysis technique in future works may be extended to include directed motion in gradients.

Chapter 6

Conclusions and outlook

6.1 Summary of the work

Self-organized LSs can be observed in a large variety of different experimental systems and have received a significant amount of theoretical interest in the last decade. There are two important reasons for the fascination caused by these objects. One the one hand, although being spatially extended objects theoretically described by field variables, LSs show many particle-like properties like robustness with respect to perturbations, propagation, scattering, bound states and other complex interaction phenomena. A number of potential applications has been suggested, for example in the context of information transmission and the realization of logic operations [308, 312, 384]. On the other hand, the formation of LSs seems to be a rather universal phenomena. While the individual systems capable of showing LSs come from various branches of physics and are very different in nature (one may for example mention optics, gas-discharges, chemical systems, granular media or semiconductors), the phenomenology of the particle-like behavior is always similar. Many researchers consider understanding the physical systems as a first step in accomplishing the long-time goal of investigating complex systems in biology and life sciences in general.

A significant amount of research has been carried out to investigate the details of pattern formation in the individual fields, however up to now the aspect of explaining the common features of the individual systems has only been addressed rather sparsely. A potential reason for this may be the fact that even in the individual fields, there is often a lack of understanding concerning illustrative mechanisms. To approach the above problems, in this work we have dealt with four complexes of questions, each corresponding to one of the foregoing main chapters.

The first one (Chap. 2) has focussed on the mechanisms responsible for the stabilization and dynamics of LSs in a number of system classes. The relevance of these mechanisms is due to the fact that LSs are generally generated subcritically and no normal form theory for the system equations is available up to now. This reflects the current situation in the field of nonlinear PDEs in general: unlike in the field of linear PDEs where to large extents a systematic classification of the behavior of the PDEs according to a few characteristic properties (like the parabolic, hyperbolic or elliptic nature of the equations) can be given, for most nonlinear problems only a toolbox-like collection of techniques is available. In the chapter, we have treated reaction-diffusion,

Ginzburg-Landau and Swift-Hohenberg equations and have found common mechanisms like front-locking, dynamic stabilization due to various forms of transport and interaction processes as a consequence of nonlinear superposition and spatial coupling which appear in a similar form in all types of systems. Also more specific mechanisms responsible for different instabilities of stationary LSs like propagation and breathing have been discussed.

The results of the first chapter have shown that on the basis of field equations alone the particle-like dynamics of LSs and their universal properties can not be understood in a satisfying way as there are still large discrepancies in the nature of the individual systems. A key approach to deal with this issue is given by the concept of slowly varying order parameters representing the basis for reducing the field equations to ODEs by techniques of adiabatic elimination. In Chap. 3 we have presented different ways of deriving the reduced equations. For isolated LSs, we have discussed drift in gradients as well as propagating and breathing destabilizations. Furthermore, a new decomposition method was developed to treat nonlinear operators acting on many LSs, allowing for a rigorous treatment of many interacting LSs. Here, we have dealt with examples of reaction-diffusion, Ginzburg-Landau and nonlinear Schrödinger type. We have pointed out that slow modes can either be connected to continuous symmetries or bifurcations and presented a number of example cases, indicating that a knowledge of the system symmetries alone offers a great deal of information on the possible structure of the reduced particle description. In addition, also the influence of fluctuation field for the dynamics of LSs was discussed and a connection to classical Brownian motion was made.

A great advantage of the reduced description is the possibility to treat the dynamics of large ensembles of LSs on long time scales which would be impossible on the level of the field equations due to limitations in current computational methods. This topic has been dealt with in Chap. 4 which is divided into three parts. In the first one, we have carried out analytic considerations on the dynamics of two interacting structures and compared the properties of actively propagating and interacting LSs with that of classical Newton particles. While larger numbers of LSs can only be treated numerically, the analytic considerations reveal a number of important aspects helping to understand the more complicated cases. The second part focussed on the deterministic dynamics of lager numbers of LSs (i.e. without the influence of fluctuations). Here we have found strong clustering tendencies for active propagation as well as compression fronts and rotational motion in confined spaces. Taking fluctuations into account, a number of other phenomena may arise which include noise induced transitions and the existence of different states of aggregation similar to classical many-particle systems.

In the last chapter (Chap. 5), we have made an excursion to the field of life sciences and investigated the dynamics of Dictyostelium discoideum cells which represent a prototype organism in biology. As reproducibility of experimental observations is much more difficult to obtain in animate systems, microfluidic devices have been used to provide a well-controllable environment in which the reaction of the cells to chemical stimuli with cyclic adenosine-mono-phosphate (cAMP) could be investigated. In chemical gradients, a directed motion of the cells (chemotaxis) can be found, and a threshold concentration for the onset of this phenomenon was observed. A complete quantitative description of the cell dynamics in isotropic environments could be obtained by applying methods of stochastic data analysis, using the velocity of the cells as phenomenological order parameter. Thereby it was found that the cells perform random Lévy walks

and that stimulation with cAMP affects only the deterministic part of the cell motion. Furthermore, the application of the analysis shows that although for cells generally no description on the level of field equations is available, the dynamics on coarse spatial and temporal case strongly resembles that of LSs propagating under the influence of noise.

6.2 Open questions and further progress

Investigating mechanisms explaining the formation and dynamics of LSs, we have focussed on three rather frequently encountered classes of systems. Each of the systems is closely related to a number of different experimental systems. While we have compared our theoretical finding with experimental results whenever possible, a general problem in research on LSs is that often such a comparison is lacking in the literature. Furthermore, while models of the GL and SH type are argued to reflect the properties of various types of systems, a rigorous derivation from first-principle considerations is often not carried out. An important, yet time-consuming task would be to apply the knowledge gained in this and related works to models designed for specific experiments, thereby allow for a more systematic comparison of theory and experiment. A second challenge that is far from being accomplished is to find mechanisms in systems with nonlinear spatial coupling terms as frequently encountered in hydrodynamics and electrical transport systems.

Our considerations on reducing the equations for the dynamic evolution of LSs to ODEs have shown that the structure of the reduced equations typically is essentially connected to the symmetries of the underlying field equations. While we have considered single and interacting structures in systems with generic types of symmetries (translation, rotation, Galilean), an important next step would lie in a systematic classification using methods of group theory. In particular, the role of hidden symmetries like phase shifts of solutions and their coupling to the generic symmetries should be looked upon in more detail.

The dynamical properties of larger ensembles of LSs, possibly in the presence of noise, has only been considered rather rarely up to now. The motivation to study for example the interaction of active Brownian particles currently rather arises from problems encountered in life sciences like swarming of fish or pedestrians. The topic is of particular interest as there exists a great amount of knowledge in the field of classical particle ensembles. As many theoretical methods are related to the concept of energy however, they can no longer be applied when looking at LSs. Nonetheless, there are both similarities and unknown new phenomena whose treatment may demand the development of new statistic methods.

In the field of physics, works that later on have been considered as particularly important have in many cases either allowed for general and widely applicable statements or lead to potential applications. An interest in the universal properties of LSs thus puts a particular emphasis on the first point. Concerning the second one, up to now the number of applications realized in the field of self-organization and LSs is rather limited (one possibility are LSs in optics for data processing). Here, a great change for many interesting potential discoveries may arise.

Bibliography

[1] E. Ammelt, D. Schweng, and H.-G. Purwins. Spatio-Temporal Pattern Formation in a Lateral High-Frequency Glow Discharge System. *Phys. Lett. A*, 179, 348–354, 1993.

[2] H. U. Bödeker. Dynamik und Wechselwirkung dissipativer Solitonen in einer planaren Gleichspannungs-Gasentladung. Master's thesis, Institut für Angewandte Physik, Westfälische Wilhelms-Universität Münster, 2003.

[3] B. Schäpers, M. Feldmann, T. Ackemann, and W. Lange. Interaction of Localized Structures in an Optical Pattern-formation System. *Phys. Rev. Lett.*, 85(4), 748–751, 2000.

[4] P. B. Umbanhowar, F. Melo, and H. L. Swinney. Localized excitations in a vertically vibrated granular layer. *Nature*, 382(6594), 793–796, 1996.

[5] A. L. Hodgkin and A. F. Huxley. A quantitative description of membrane current and its application to conduction and excitation in nerve. *J. Physiol.*, 117(4), 500–544, 1952.

[6] H. H. Rotermund, S. Jakubith, A. von Oertzen, and G. Ertl. Solitons in a surface reaction. *Phys. Rev. Lett.*, 66(23), 3083–3086, 1991.

[7] G. Ahlers. Experiments with pattern-forming systems. *Physica D*, 51(1-3), 421–443, 1991.

[8] K. M. Mayer, J. Parisi, and R. P. Huebener. Imaging of self-generated multifilamentary current patterns in GaAs. *Z. Phys. B.*, 71(2), 171–178, 1988.

[9] M. Faraday. On the forms and states assumed by fluids in contact with vibrating elastic surfaces. *Philos. Trans. Royal Soc. London*, 121(1-4), 319–340, 1831.

[10] J. S. Russell. Report on Waves. In *Report of the fourteenth meeting of the British Association for the Advancement of Science. York 1844*, pages 311–390, London, 1845.

[11] J. W. Rayleigh. On waves. *Philosoph. Mag.*, 1(5), 257–279, 1876.

[12] J. Boussinesq. Théorie de l'intumescence liquide appelée onde solitaire ou de translation, se propageant dans un canal rectangulaire. *Comp. Rend. Acad. Sc. Paris*, 72, 755–759, 1871.

[13] D. J. Korteweg and H. de Vries. On the change of form of long waves advancing in a rectangular channel, and on a new type of stationary waves. *Philos. Mag.*, 39, 422–443, 1895.

[14] W. Ostwald. Periodische Erscheinungen bei der Auflösung des Chroms in Säuren. *Z. Phys. Chem.*, 35, 33–76, 1900.

[15] O. Lehmann. Gasentladungen in weiten Gefässen. *Ann. Phys.*, 4(7), 1–28, 1902.

[16] J. Nagumo, S. Arimoto, and S. Yoshizawa. An active pulse transmissin line simulating nerve axon. *Proc. Inst. Radio Engin. Electr.*, 50, 2061–2070, 1962.

[17] N. J. Zabusky and M. D. Kruskal. Interactions of solitons in a collisionless plasma and the recurrence of initial states. *Phys. Rev. Lett.*, 15, 240–243, 1965.

[18] V. E. Zakharov and A. B. Shabat. Exact theory of 2-dimensional self-focusing and one-dimensional self-modulation of waves in nonlinear media. *Sov. Phys. JETP*, 34(1), 62–69, 1972.

[19] W. A. Strauss. Existence of solitary waves in higher dimensions. *Comm. Math. Phys.*, 55(2), 149–162, 1977.

[20] A. M. Turing. The chemical basis of morphogenesis. *Philos. Trans. Royal Soc. B*, 237, 37–72, 1952.

[21] M. Krupa, B. Sandstede, and P. Szmolyan. Korteweg-deVries Equation and Generalizations. 5. Uniqueness And Nonexistence Of Polynomial Conservation Laws. *J. Math. Phys.*, 11(3), 952–960, 1970.

[22] A. M. Barnett and H. A. Jensen. Observation of Current Filaments in Semi-Insulating GaAs. *Appl. Phys. Lett.*, 12(10), 341–342, 1968.

[23] C. N. Berglund. Thermal filaments in Vanadium dioxide. *IEEE Transact. Electron Dev.*, 16(5), 432–437, 1969.

[24] A. M. Barnett. Filament Formation. In R. K. Williardson and A. C. Beer, editors, *Semiconductors and Semimetals*, volume 6, pages 141–200. Academic Press, New York, 1970.

[25] M. Remoissenet. *Waves Called Solitons: Concepts and Experiments*. Springer, Berlin, 3. edition, 1999.

[26] H. Baumann, R. Symanczyk, C. Radehaus, H.-G. Purwins, and D. Jäger. Properties of Solitary Current Filaments in Silicon Pin Diodes. *Phys. Lett. A*, 123, 421–424, 1987.

[27] U. Rau, J. Peinke, J. Parisi, and R. P. Huebener. Switching behavior of current filaments in p-germanium connected in parallel. *Z. Phys. B.*, 71(3), 305–310, 1988.

[28] A. Brandl, M. Volcker, and W. Prettl. Reconstruction of the spatial structure of current filaments in n-GaAs in a magnetic field. *Appl. Phys. Lett.*, 55(3), 238–240, 1989.

[29] H. Willebrand, C. Radehaus, F.-J. Niedernostheide, R. Dohmen, and H.-G. Purwins. Observation of Solitary Filaments and Spatially Periodic Patterns in a DC Gas-Discharge System. *Phys. Lett. A*, 149, 131–138, 1990.

[30] Y. S. Kivshar and B. A. Malomed. Dynamics of solitons in nearly integrable systems. *Rev. Mod. Phys.*, 61(4), 763–915, 1989.

[31] V. I. Tetviashvili. Multidimensional and dissipative solitons. *Physica D*, 3(1-2), 329–334, 1981.

[32] M. Bode and H.-G. Purwins. Pattern formation in reaction-diffusion systems – dissipative solitons in physical systems. *Physica D*, 86, 53–63, 1995.

[33] C. I. Christov and M. G. Velarde. Dissipative Solitons. *Physica D*, 86, 323–347, 1995.

[34] N. Akhmediev and A. Ankiewicz. *Dissipative Solitons.* Lecture Notes in Physics. Springer, Berlin, 2005.

[35] D. Ruelle. Small Random Perturbations of Dynamical Systems and the Definition of Attractors. *Comm. Math. Phys.*, 82(1), 138–151, 1981.

[36] J. Milnor. On the Concept of Attractor. *Comm. Math. Phys.*, 99(2), 177–195, 1985.

[37] R. FitzHugh. Impulses and physiological states in theoretical models of nerve membrane. *Biophys. J.*, 1, 445, 1961.

[38] C. P. Schenk, M. Or-Guil, M. Bode, and H.-G. Purwins. Interacting pulses in three-component reaction-diffusion-systems on two-dimensional domains. *Phys. Rev. Lett.*, 78, 3781–3783, 1997.

[39] N. N. Akhmediev, A. Ankiewicz, and J. M. Soto-Crespo. Multisoliton Solutions of the Complex Ginzburg-Landau Equation. *Phys. Rev. Lett.*, 79(21), 4047–4050, 1997.

[40] H. Sakaguchi. Motion of pulses and vortices in the cubic-quintic complex Ginzburg-Landau equation without viscosity. *Physica D*, 210, 128–148, 2005.

[41] M. Or-Guil, M. Bode, C. P. Schenk, and H.-G. Purwins. Spot bifurcations in three-component reaction-diffusion systems: The onset of propagation. *Phys. Rev. E*, 57(6), 6432–6437, 1998.

[42] A. J. Scroggie, J. M. McSloy, and W. J. Firth. Self-propelled cavity solitons in semiconductor microcavities. *Phys. Rev. E*, 66, 036607, 2002.

[43] G. L. Lamb Jr. *Elements of Soliton Theory.* Wiley Interscience, New York, 1980.

[44] V. G. Makhankov. *Soliton Phenomenology.* Kluwer Academic Publishers, Norwell, 1990.

[45] D. E. Edmundson and R. H. Enns. Fully three-dimensional collisions of bistable light bullets. *Opt. Lett.*, 18(19), 1609–1611, 1993.

[46] D. E. Edmundson and R. H. Enns. Particlelike nature of colliding three-dimensional optical solitons. *Phys. Rev. A*, 51(3), 2491–2498, 1995.

[47] V. V. Steblina, Y. S. Kivshar, and A. V. Buryak. Scattering and spiraling of solitons in a bulk quadratic medium. *Opt. Lett.*, 23(3), 156–158, 1998.

[48] G. Fibich and B. Ilan. Optical light bullets in a pure Kerr medium. *Opt. Lett.*, 29(8), 887–889, 2004.

[49] D. E. Edmundson and R. H. Enns. Robust bistable light bullets. *Opt. Lett.*, 17(8), 586–588, 1992.

[50] A. S. Desyatnikov and Y. S. Kivshar. Rotating optical soliton clusters. *Phys. Rev. Lett.*, 88(5), 053901, 2002.

[51] L.-C. Crasovan, Y. V. Kartashov, D. Mihalache, L. Torner, Y. S: Kivshar, and V. M. Pérez-García. Soliton "molecules": Robust clusters of spatiotemporal optical solitons. *Phys. Rev. E*, 67, 046610, 2003.

[52] M. Suzuki, T. Ohta, M. Mimura, and H. Sakaguchi. Breathing and wiggling motions in three-species laterally inhibitory systems. *Phys. Rev. E*, 52(4), 3645–3655, 1995.

[53] H. Sakaguchi and B. A. Malomed. Breathing and randomly walking pulses in a semilinear Ginzburg-Landau system. *Physica D*, 147, 273–282, 2000.

[54] Y. Nishiura, T. Teramoto, and K.-I. Ueda. Scattering of travelling spots in dissipative systems. *Chaos*, 15(047509), 2005.

[55] H.-G. Purwins, H. U. Bödeker, and A. W. Liehr. Dissipative Solitons in Reaction-Diffusion Systems. In N. Akhmediev and A. Ankiewicz, editors, *Dissipative Solitons, Lectures Notes in Physics*, Berlin, 2005. Springer.

[56] J. Kosek and M. Marek. Collision-stable waves in excitable reaction-diffusion systems. *Phys. Rev. Lett.*, 74(11), 2134–2137, 1995.

[57] H. Sakaguchi and H. R. Brandt. Localized patterns for the quintic complex Swift-Hohenberg equation. *Physica D*, 117, 95–105, 1998.

[58] M. Bode, A. W. Liehr, C. P. Schenk, and H.-G. Purwins. Interaction of Dissipative Solitons: Particle-like Behaviour of Localized Structures in a Three-Component Reaction-Diffusion System. *Physica D*, 161, 45–66, 2002.

[59] A. G. Vladimirov, J. M. McSloy, D. V. Skryabin, and W. J. Firth. Two-dimensional clusters of solitary structures in driven optical cavities. *Phys. Rev. E*, 65(046606), 1–11, 2002.

[60] A. S. Desyatnikov and Y. S. Kivshar. Spatial optical solitons and soliton clustes carrying an angular momentum. *J. Opt. B*, 4, S58–S65, 2002.

[61] S. Gatz and J. Herrmann. Soliton propagation and soliton collision in double-doped fibers with a non-Kerr-like nonlinear refractive-index change. *Opt. Lett.*, 17(7), 484–486, 1992.

[62] D. V. Skryabin and A. G. Vladimirov. Vortex induced rotation of clusters of well localized states in the complex Ginzburg-Landau equation. *Phys. Rev. Lett.*, 89(4), 044101, 2002.

[63] N. N. Rosanov, S. V. Fedorov, and A. N. Shatsev. Two-dimensional laser soliton complexes with weak, strong and mixed coupling. *Appl. Phys. B*, 81(7), 937–943, 2005.

[64] W. H. Press, B. P. Flannery, S. A. Teukolsky, and W. T. Vetterling. *Numerical Recipes in C. The Art of Scientific Computing. Second Edition*. Cambridge University Press, Cambridge, 1996.

[65] K. J. Lee, W. D. McCormick, Q. Ouyang, and H. L. Swinney. Pattern Formation by Interacting Chemical Fronts. *Science*, 261, 192–194, 1993.

[66] O. Jensen, V. O. Pannbacker, E. Mosekilde, G. Dewel, and P. Borckmans. Localized structures and front propagation in the Lengyer-Epstein model. *Phys. Rev. E*, 50(2), 736–749, 1994.

[67] D. Haim, G. Li, Q. Ouyang, W. D. Mccormick, H. L. Swinney, A. Hagberg, and E. Meron. Breathing spots in a reaction-diffusion system. *Phys. Rev. Lett.*, 77(1), 190–193, 1996.

[68] V. K. Vanag and I. R. Epstein. Pattern formation in a tunable medium: The Belousov-Zhabotinsky reaction in an aerosol OT microemulsion. *Phys. Rev. Lett.*, 87(22), 228301, 2001.

[69] V. K. Vanag and I. R. Epstein. Stationary and Oscillatory Localized Patterns, and Subcritical Bifurcations. *Phys. Rev. Lett.*, 92(12), 128301, 2004.

[70] P. K. Maini, K. J. Painter, and N. P. Chau. Spatial pattern formation in chemical and biological systems. *J. Chem. Soc. Faraday Trans.*, 93, 3601–3610, 1997.

[71] Y. A. Astrov. Phase transition in an ensemble of dissipative solitons of a Turing system. *Phys. Rev. E*, 67, 035203, 2003.

[72] V. I. Nekorkin and V. B. Kazantsev. Autowaves and solitons in a three-component reaction-diffusion system. *Int. J. Bif. Chaos*, 12(11), 2421–2433, 2002.

[73] O. Descalzi, Y. Hayase, and H. R. Brand. Analytical approach to localized structures in a simple reaction-diffusion system. *Phys. Rev. E*, 69, 026121, 2004.

[74] P. C. Fife. *Mathematical Aspects of Reacting and Diffusing Systems*, volume 28 of *Lecture Notes in Biomathematics*. Springer, Berlin, 1979.

[75] A. S. Mikhailov. *Foundations of Synergetics I. Distributed Active Systems*, volume 51 of *Springer Series in Synergetics*. Springer, Berlin, 1990.

[76] B. S. Kerner and V. V. Osipov. *Autosolitons. A New Approach to Problems of Self-Organization and Turbulence*, volume 61 of *Fundamental Theories of Physics*. Kluwer Academic Publishers, Dordrecht, 1994.

[77] J. Smoller. *Shock Waves and Reaction Diffusion Equations*. Springer, New York, 2 edition, 1994.

[78] U. Middya, M. Sheintuch, M. D. Graham, and D. Luss. Patterns of temperature pulses on electrically heated catalytic ribbons. *Physica D*, 63(3-4), 393–409, 1993.

[79] U. Middya, M. D. Graham, D. Luss, and M. Sheintuch. Pattern selection in controlled reaction-diffusion systems. *J. Chem. Phys.*, 98(4), 2823–2836, 1993.

[80] H.-G. Purwins and C. Radehaus. Pattern Formation on Analogue Parallel Networks. In H. Haken, editor, *Neural and Synergetic Computers*, volume 42, pages 137–154. Springer Series in Synergetics, 1988.

[81] H.-G. Purwins, C. Radehaus, T. Dirksmeyer, R. Dohmen, R. Schmeling, and H. Willebrand. Application of the Activator Inhibitor Principle to Physical Systems. *Phys. Lett. A*, 136, 480–484, 1989.

[82] T. Dirksmeyer, R.Schmeling, J. Berkemeier, and H.-G. Purwins. Experiments on the Formation of Stationary Spatial Structures on a Network of Coupled Electrical Oscillators. In D. Walgraef and N. M. Ghoniem, editors, *Proceedings of the NATO Advanced Study Institute on Patterns, Defects and Materials Instabilities Cargése, France, September 4 - 15, 1989*, volume 183 of *NATO ASI series : Series E, Applied sciences*, pages 91–107, Dordrecht, 1990. Kluwer.

[83] A. Wacker and E. Schöll. Spiking in an activator-inhibitor model for elements with S-shaped negative differential conductivity. *Z. Phys. B*, 93(4), 431–436, 1994.

[84] F.-J. Niedernostheide, H.-J. Schulze, S. Bose, A. Wacker, and e. Schöll. Spiking in semiconductor device: experiments and comparison with a model. *Phys. Rev. E*, 54(2), 1253–1260, 1996.

[85] M. Meixner, P. Rodin, E. Schöll, and A. Wacker. Lateral current density fronts in globally coupled bistable semiconductors with S- or Z-shaped current voltage characteristics. *Europ. Phys. J. B*, 13(1), 157–168, 2000.

[86] S. Amiranashvili, S. V. Gurevich, and H.-G. Purwins. Ionization fronts in planar dc discharge systems with high-ohmic electrode. *Phys. Rev. E*, 71, 066404, 2005.

[87] K. J. Lee and H. L. Swinney. Lamellar structures and self-replicating spots in a reaction-diffusion system. *Phys. Rev. E*, 51(3), 1899–1915, 1995.

[88] V. V. Osipov and C. B. Muratov. Ultrafast traveling spike autosolitons in reaction-diffusion systems. *Phys. Rev. Lett.*, 75(2), 338–41, 1995.

[89] G. Nicolis and I. Prigogine. *Self-Organization in Nonequlibrium Systems*. Wiley, New York, 1997.

[90] T. Kolokolnikov, T. Erneux, and J. Wei. Mesa-type patterns in the one-dimensional Brusselator and their stability. *Physica D*, 214(1), 63–77, 2006.

[91] G. Bogdiogov and H. Engel. Oscillatory Dispersion and Coexisiting Stable Pulse Trains in an Excitable Medium. *Phys. Rev. Lett.*, 90(14), 148302, 2003.

[92] V. S. Zykov and K. Showalter. Wave Front Interaction Model of Stabilized Propagating Wave Segments. *Phys. Rev. Lett.*, 94, 068302, 2005.

[93] V. K. Vanag and I. R. Epstein. Dash waves in a reaction-diffusion system. *Phys. Rev. Lett.*, 90(9), 098301, 2003.

[94] J. E. Pearson. Complex Patterns in a Simple System. *Science*, 261(9), 189–192, 1993.

[95] Y. Nishiura, T. Teramoto, and K.-I. Ueda. Scattering and separators in dissipative systems. *Phys. Rev. E*, 67(056210), 2003.

[96] S. V. Gurevich, H. U. Bödeker, A. S. Moskalenko, A. W. Liehr, and H.-G. Purwins. Drift Bifurcation of Dissipative Solitons due to a Change of Shape: Experiment and Theory. *Physica D*, 199(1-2), 115–128, 2003.

[97] C. P. Schenk, P. Schütz, M. Bode, and H.-G. Purwins. Interaction of self-organized quasiparticles in a two-dimensional reaction-diffusion-system: The formation of molecules. *Phys. Rev. E*, 57(6), 6480–6486, 1998.

[98] A. S. Moskalenko, A. W. Liehr, and H.-G. Purwins. Rotational bifurcation of localized dissipative structures. *Europhy. Lett.*, 63(3), 361–367, 2003.

[99] A. Ito and T. Ohta. Self-organization in an excitable reaction-diffusion system. III. Motionless localized versus propagating-pulse solutions. *Phys. Rev. A*, 45(12), 8374–8382, 1992.

[100] T. Ohta, M. Mimura, and R. Kobayashi. Higher-dimensional localized patterns in excitable media. *Physica D*, 34(1-2), 115–144, 1989.

[101] H. Hempel, I. Schebesch, and L. Schimansky-Geier. Travelling pulses in reaction-diffusion systems under global constraints. *Europ. Phys. J. B*, 2(3), 399–407, 1998.

[102] S. Kawaguchi and M. Mimura. Collision of Travelling Waves in a Reaction-Diffusion System with Global Coupling Effect. *SIAM J. Appl. Math.*, 59(3), 920–941, 1999.

[103] E. P. Zemskov, V. S. Zykov, K. Kassner, and S. C. Mller. Stability of traveling fronts in a piecewise-linear reactiondiffusion system. *Nonlinearity*, 13, 2063–2076, 2000.

[104] F.-J. Niedernostheide, M. Arps, R. Dohmen, H. Willebrand, and H.-G. Purwins. Spatial and Spatio-Temporal Patterns in pnpn Semiconductor Devices. *Phys. stat. sol. b*, 172, 249, 1992.

[105] F.-J. Niedernostheide, M. Ardes, M. Or-Guil, and H.-G. Purwins. Spatiotemporal Behaviour of Localized Current Filaments in p-n-p-n Diodes: Numerical Calculations and Comparison with Experimental Results. *Phys. Rev. B*, 49, 7370–7384, 1994.

[106] E. Schöll, F. J. Niedernostheide, J. Parisi, W. Prettl, and H.-G. Purwins. Formation of Spatio-Temporal Structures in Semiconductors. In F. H. Busse and S. C. Müller, editors, *Evolution of Spontaneous Structures in Dissipative Continuous Systems*, pages 446–494. Springer, Berlin, 1998.

[107] P. Rodin. Theory of traveling filaments in bistable semiconductor structures. *Phys. Rev. B*, 69, 045307, 2004.

[108] P. Rodin. Onset of thermally driven self-motion of a current filemant in a bistable semiconductor structure. *Phys. Rev. B*, 71, 085309, 2005.

[109] E. S. Lobanova and F. I. Ataullakhanov. Unstable trigger waves induce various intricate dynamic regimes in a reaction-diffusion system of blood clotting. *Phys. Rev. Lett.*, 91(13), 138301, 2003.

[110] E. S. Lobanova, E. E. Shnol, and F. I. Ataullakhanov. Complex dynamics of the formation of spatially localized standing structures in the vicinity of saddle-node bifurcations of waves in the reaction-diffusion model of blood clotting. *Phys. Rev. E*, 70, 032903, 2004.

[111] E. S. Lobanova and F. I. Ataullakhanov. Running pulses of complex shape in a reaction-diffusion model. *Phys. Rev. Lett.*, 93, 098303, 2004.

[112] L. Schimansky-Geier, C. Zülicke, and E. Schöll. Domain formation due to Ostwald ripening in bistable systems far from equilibrium. *Z. Phys. B*, 84, 433–441, 1991.

[113] K. Krischer and A. Mikhailov. Bifurcation to traveling spots in reaction-diffusion systems. *Phys. Rev. Lett.*, 73(23), 3165–3168, 1994.

[114] A. Alekseev, S. Bose, P. Rodin, and E. Schöll. Stability of current filaments in a bistable semiconductor system with global coupling. *Phys. Rev. E*, 57(3), 2640–2649, 1998.

[115] D. Battogtokh, M. Hildebrand, K. Krischer, and A. S. Mikhailov. Nucleation kinetics and global coupling in reaction-diffusion systems. *Phys. Rep.*, 288(1–6), 435–456, 1997.

[116] M. A. Tsyganov, J. Brindley, A. V. Holden, and V. N. Biktashev. Soliton-like phenomena in one-dimensional cross-diffusion systems: a predator-prey pursuit and evasion example. *Physica D*, 197(1–2), 18–33, 2004.

[117] M. A. Tsyganov and V. N. Biktashev. Half-soliton interaction of population taxis waves in predator-prey systems with pursuit and evasion. *Phys. Rev. E*, 70, 031901, 2004.

[118] V. N. Biktashev and M. A. Tsyganov. Solitary waves in excitable systems with cross-diffusion. *Proc. Royal Soc. London A*, 461(2064), 3711–3730, 2005.

[119] R. A. Fisher. The wave of advance of an advantageous gene. *Ann. Eugenics*, 7, 355–369, 1937.

[120] A. Kolmogorov, I. Petrovsky, and N. Piscounov. Investigation of a diffusion equation connected to the growth of materials, and application to a problem in biology. *Moscow Univ. Bull. Math. A*, 1, 1–25, 1937.

[121] A. C. Newell and J. A. Whitehead. Finite Bandwidth, finite amplitude convection. *J. Fluid Mech.*, 38(2), 279–303, 1969.

[122] L. A. Segel. Distant side-walls cause slow amplitude modulation of cellular convection. *J. Fluid Mech.*, 38(1), 203, 1969.

[123] Y. B. Zeldovich and D. A. Frank-Kamenetsky. A theory of thermal propagation of flame. *Acta Physicochim. URSS*, 9, 341–350, 1938.

[124] B. H. Gilding and R. Kersner. *Travelling Waves in Nonlinear Diffusion Convection Reaction*. Birkhäuser, Basel, 2004.

[125] U. Ebert and W. van Saarloos. Front propagation into unstable states: universal algebraic convergence towards uniformly translating pulled fronts. *Physica D*, 146, 1–99, 2000.

[126] W. van Saarloos. Front propagation into unstable states. *Phys. Rep.*, 386, 29–222, 2003.

[127] M. Bode. *Beschreibung strukturbildender Prozesse in eindimensionalen Reaktions-Diffusions-Systemen durch Reduktion auf Amplitudengleichungen und Elementarstrukturen*. Dissertation, Institut für Angewandte Physik, Westfälische Wilhelms-Universität Münster, 1993.

[128] L. Schimansky-Geier, C. Zülicke, and E. Schöll. Growth of Domains Under Global Constraints. *Physica A*, 188(1-3), 436–442, 1992.

[129] L. Schimansky-Geier, H. Hempel, R. Bartussel, and C. Zulicke. Analysis of domain-solutions in reaction-diffusion systems. *Z. Phys. B*, 96(3), 417–427, 1995.

[130] E. Meron. Pattern formation in excitable media. *Phys. Rep.*, 218(1), 1–66, 1992.

[131] E. Meron and P. Pelce. Model for spiral wave formation in excitable media. *Phys. Rev. Lett.*, 60(18), 1880–1883, 1988.

[132] D. Barkley. Linear stability analysis of rotating spiral waves in excitable media. *Phys. Rev. Lett.*, 68(13), 2090–3, 1992.

[133] A. S. Mikhailov, V. A. Davydov, and V. S. Zykov. Complex dynamics of spiral waves and motion of curves. *Physica D*, 70(1-2), 1–39, 1994.

[134] R. S. Lillie. Transmission of activation in passive metals as a model of the protoplasmic or nervous type of transmission. *Science*, 48(1229), 51, 1918.

[135] R. Suzuki. Electrochemical neuron model. *Adv. Biophys.*, 9, 115–156, 1976.

[136] K. F. Bonhoeffer. Activation of passive iron as a model for the excitation of nerve. *J. Gen. Physiol.*, 32(1), 69–91, 1947.

[137] C. T. Hamik, N. Manz, and O. Steinbock. Anomalous Dispersion and Attractive Pulse Interaction in the 1,4-Cyclohexanedione Belousov-Zhabotinsky Reaction. *J. Phys. Chem. A*, 105(25), 6144–6153, 2001.

[138] C. T. Hamik and O. Steinbock. Excitation waves in reaction-diffusion media with non-monotonic dispersion relations. *New. J. Phys.*, 5(58), 1–12, 2003.

[139] S. L. Lane and D. Luss. Rotating temperature pulse during hydrogen oxidation on an nickel ring. *Phys. Rev. Lett.*, 70(6), 830–832, 1993.

[140] M. D. Graham, S. L. Lane, and D. Luss. Temperature pulse dynamics on a catalytic ring. *J. Phys. Chem.*, 97(29), 7564–7571, 1993.

[141] S. Y. Yamamoto, C. M. Surko, M. B. Maple, and R. K. Pina. Pulse Propagation in the Catalytic Oxidation of Carbon Monoxide on Platinum. *Phys. Rev. Lett.*, 74(20), 4071–4074, 1995.

[142] M. D. Graham, U. Middya, and D. Luss. Pulses and Global Bifurcations in a Nonlocal Reaction-Diffusion System. *Phys. Rev. E*, 48(4), 2917–2923, 1993.

[143] T. Ohta, J. Kiyose, and M. Mimura. Collision of propagating pulses in a reaction-diffusion system. *J. Phys. Soc. Japan*, 66(5), 1551–1558, 1997.

[144] H. Willebrand, T. Hünteler, F.-J. Niedernostheide, R. Dohmen, and H.-G. Purwins. Periodic and Turbulent Behavior of Solitary Structures in Distributed Active Media. *Phys. Rev. A*, 45(12), 8766–8775, 1992.

[145] H. Willebrand, F.-J. Niedernostheide, R. Dohmen, and H.-G. Purwins. Stationary and Dynamic Patterns of Current Density in Gas-Discharge Systems. In L. Rensing, editor, *Oscillations and Morphogenesis*, pages 81–109. M. Dekker, New York, 1993.

[146] E. Ammelt, Yu. Astrov, and H.-G. Purwins. Pattern Formation in Gas Discharge Systems. In H. Engel, F.-J. Niedernostheide, H.-G. Purwins, and E. Schöll, editors, *Self-Organization in Activator-Inhibitor-Systems: Semiconductors, Gas-Discharge, and Chemical Media*, pages 22–27, 1996.

[147] F.-J. Niedernostheide, B. S. Kerner, and H.-G. Purwins. Spontanous Appearance of Rocking Localized Current Filaments in a Nonequilibrium Distributive System. *Phys. Rev. B*, 46, 7559, 1992.

[148] F.-J. Niedernostheide. *Nonlinear Dynamics and Pattern Formation in Semiconductors and Devices*. Springer, Berlin, 1995.

[149] S. Koga and Y. Kuramoto. Localized patterns in reaction-diffusion systems. *Prog. Theor. Phys.*, 63(1), 106–121, 1980.

[150] T. Ohta, A. Ito, and A. Tetsuka. Self-organization in an excitable reaction-diffusion system: synchronization of oscillatory domains in one dimension. *Phys. Rev. A*, 42(6), 3225–32, 1990.

[151] Y. Nishiura and M. Mimura. Layer oscillations in reaction-diffusion systems. *SIAM J. Appl. Math.*, 49(2), 481–514, 1989.

[152] C. P. Schenk. *Numerische und analytische Untersuchung solitärer Strukturen in zwei- und dreikomponentigen Reaktions-Diffusions-Systemen*. Dissertation, Institut für Angewandte Physik, Westfälische Wilhelms-Universität Münster, 1999.

[153] F.-J. Niedernostheide, R. Dohmen, H. Willebrand, B. S. Kerner, and H.-G. Purwins. Transition from Pulsating to Rocking Localized Structures in Nonlinear Dissipative Distributive Media with Global Inhibition. *Physica D*, 69, 425–435, 1993.

[154] L. M. Pismen. Nonlocal Boundary Dynamics of Traveling Spots in a Reaction-Diffusion System. *Phys. Rev. Lett.*, 86(15), 548–551, 2001.

[155] H.-G. Purwins, G. Klempt, and J. Berkemeier. Temporal and Spatial Structures of Nonlinear Dynamical Systems. *Festkörperprobleme*, 27, 27–61, 1987.

[156] T. Ohta. Pulse dynamics in a reaction-diffusion system. *Physica D*, 151(1), 61–72, 2001.

[157] H. U. Bödeker, M. C. Röttger, A. W. Liehr, T. D. Frank, R. Friedrich, and H.-G. Purwins. Noise-covered drift bifurcation of dissipative solitons in a planar gas-discharge system. *Phys. Rev. E*, 67, 056220, 2003.

[158] A. W. Liehr, H. U. Bödeker, M. C. Röttger, T. D. Frank, R. Friedrich, and H.-G. Purwins. Drift bifurcation detection for dissipative solitons. *New. J. Phys.*, 5, 89.1–89.9, 2003.

[159] E. Yanagida. Branching of double pulse solutions from single solutions in nerve axon equations. *J. Diff. Eq.*, 66, 243–262, 1987.

[160] M. Or-Guil, I. G. Kevrekidis, and M. Bär. Stable bound states of pulses in an excitable medium. *Physica D*, 135(1-2), 154–174, 2000.

[161] N. Manz and O. Steinbock. Dynamics of excitation pulses with attractive interaction: Kinematic analysis and chemical wave experiments. *Phys. Rev. E*, 70, 066213, 12004.

[162] B. Sandstede and A. Scheel. Gluing unstable fronts and backs together can produce stable pulses. *Nonlinearity*, 13(5), 1465–1482, 2000.

[163] K.-J. Lee, W. D. McCormick, J. E. Pearson, and H. L. Swinney. Experimental observation of self-replicating spots in a reaction-diffusion system. *Nature*, 369, 215–218, 1994.

[164] A. W. Liehr, A. S. Moskalenko, M. C. Röttger, J. Berkemeier, and H.-G. Purwins. Replication of Dissipative Solitons by Many-Particle Interaction. In E. Krause and W. Jäger, editors, *High Performance Computing in Science and Engineering '02*, pages 48–61. Springer, 2003.

[165] C. B. Muratov. Self-replication and splitting of domain patterns in reaction-diffusion systems with the fast inhibitor. *Phys. Rev. E*, 54(4), 3369–3376, 1996.

[166] Y. Hayase and T. Ohta. Self-replicating pulses and Sierpinski gaskets in excitable media. *Phys. Rev. E*, 62(5), 5998–6003, 2000.

[167] H. Meinhardt. Out-of-phase oscillations and traveliong waves with unusual properties: the use of three-component systems in biology. *Physica D*, 99, 264–277, 2004.

[168] A. W. Liehr, M. Bode, and H.-G. Purwins. The Generation of Dissipative Quasi-Particles near Turing's Bifurcation in Three-Dimensional Reaction-Diffusion-Systems. In E. Krause and W. Jäger, editors, *High Performance Computing in Science and Engineering 2000. Transactions of the High Performance Computing Center, Stuttgart (HLRS) 2000*, pages 425–439. Springer, 2001.

[169] A. W. Liehr, A. S. Moskalenko, Yu. A. Astrov, M. Bode, and H.-G. Purwins. Rotating Bound States of Dissipative Solitons in systems of reaction-diffusion type. *Europ. Phys. J. B*, 37, 199–204, 2004.

[170] L. Yang, A. M. Zhabotinsky, and I. R. Epstein. Jumping solitary waves in an autonomous reaction-diffusion system with subcritical wave instability. *Phys. Chem. Chem. Phys.*, 8, 4647–4651, 2006.

[171] Y. A. Astrov and Y. A. Logvin. Formation of Clusters of Localized States in a Gas Discharge System via a Self-Completion Scenario. *Phys. Rev. Lett.*, 79(16), 2983–2986, 1997.

[172] Y. A. Astrov and H.-G. Purwins. Plasma Spots in a Gas Discharge System: Birth, Scattering and Formation of Molecules. *Phys. Lett. A*, 283, 349–354, 2001.

[173] H. U. Bödeker, A. W. Liehr, T. D. Frank, R. Friedrich, and H.-G. Purwins. Measuring the interaction law of dissipative solitons. *New. J. Phys.*, 6, 62.1–62.18, 2004.

[174] M. Bär, M. Eiswirth, H. H. Rotermund, and G. Ertl. Solitary-wave phenomena in an excitable surface reaction. *Phys. Rev. Lett.*, 69(6), 945–948, 1992.

[175] V. L. Ginzburg and L. D. Landau. On the theory of superconductivity. *Sov. Phys. JETP*, 20, 1064–1082, 1950.

[176] I. S. Aranson and L. Kramer. The complex Ginzburg-Landau equation. *Rev. Mod. Phys.*, 74(1), 99–143, 2002.

[177] A. C. Newell and J. A. Whitehead. Review of the finite bandwidth concept. In H. H. E. Leipholz, editor, *Instability of Continuous Systems*, pages 284–289. Springer-Verlag, Berlin, 1971.

[178] H. R. Brand and R. J. Deissler. Stable localized solutions in nonlinear optics with large dissipation. *Physica A*, 204(1-4), 87–95, 1994.

[179] S. V. Fedotov, A. G. Vladimirov, G. V. Khodova, and N. N. Rosanov. Effect of frequency detuning and finite relaxation rates on laser localized structures. *Phys. Rev. E*, 61(5), 5814–5824, 2000.

[180] V. B. Tarananko, K. Staliunas, and C. O. Weiss. Spatial soliton laser: localized structure in a laser with a saturable absorber in a self-imaging resonator. *Phys. Rev. A*, 56, 1582–1591, 1997.

[181] K. Staliunas and V. J. Sánchez-Morcillo. *Transverse Patterns in Nonlinear Optical Resonators*, volume 183 of *Springer Tracts in Modern Physics*. Springer, Berlin, 2003.

[182] C. Normand and Y. Pomeau. Convective instability: a physicist‘s approach. *Rev. Mod. Phys.*, 49(3), 581–623, 1977.

[183] W. Schöpf and W. Zimmermann. Results on wave patterns in binary fluid convection. *Phys. Rev. A*, 41(2), 1145–1148, 1990.

[184] G.L. Oppo, G. D'Alessandro, and W. J. Firth. Spatiotemporal instabilities of lasers in models reduced via center manifold techniques. *Phys. Rev. A*, 44(7), 4712–4720, 1991.

[185] K. Staliunas. Laser Ginzburg-Landau equation and laser hydrodynamics. *Phys. Rev. A*, 48(2), 1573–1581, 1993.

[186] A. Hasegawa and Y. Kodama, editors. *Solitons in Optical Communications*. Oxford University Press, New York, 1995.

[187] N. N. Rosanov. *Spatial Hysteresis and Optical Patterns*. Springer, Berlin, 2002.

[188] Y. Kuramoto. *Chemical Oscillations, Waves and Turbulence*, volume 19 of *Springer Series in Synergetics*. Springer, Berlin, 1984.

[189] F. Hynne, P. G. Sørensen, and T. Møller. Complete optimization of models of the Belousov-Zhabotinsky reaction at a Hopf bifurcation. *J. Chem. Phys.*, 98(1), 219–230, 1993.

[190] H. R. Brand, P. S. Lomdahl, and A. C. Newell. Benjamin-Deir turbulence in convective binary fluid mixtures. *Physica D*, 23(1-3), 345–361, 1986.

[191] H. R. Brand, P. S. Lomdahl, and A. C. Newell. Evolution of the order parameter in situations with broken rotational symmetry. *Phys. Lett. A*, 118(2), 67–73, 1986.

[192] L. S. Tsimring and I. S. Aranson. Localized and Cellular Patterns in a Vibrated Granular Layer. *Phys. Rev. Lett.*, 79(2), 213–216, 1997.

[193] J. J. Rasmussen and K. Rypdal. Blowup in nonlinear Schrödinger equation I: a general review. *Phys. Scr.*, 33, 481–497, 1986.

[194] T. Kapitula and B. Sandstede. Stability of bright solitary-wave solutions to perturbed nonlinear Schrödinger equations. *Physica D*, 124(1-3), 58–103, 1998.

[195] W. van Saarloos and P. C. Hohenberg. Fronts, pulses, sources and sinks in generalized complex Ginzburg-Landau equations. *Physica D*, 56(4), 303–67, 1992.

[196] P. Marcq, H. Chaté, and R. Conte. Exact solutions of the one-dimensional quintic complex Ginzburg-Landau equation. *Physica D*, 73, 305–317, 1994.

[197] N. N. Akhmediev, A. Ankiewicz, and J. M. Soto-Crespo. Singularities and special solutions of the cubic-quintic Ginzburg-Landau equation. *Phys. Rev. E*, 53(1), 1190–1201, 1997.

[198] J. M. Soto-Crespo, N. Akhmediev, and A. Ankiewicz. Stability of the pulselike solutions of the quintic complex Gilzburg-Landau equation. *J. Opt. Soc. Am. B*, 13(7), 1439–1449, 1996.

[199] E. N. Tsoy. Dynamic models for dissipative localized waves of the complex Ginzburg-Landau equation. *Phys. Rev. E*, 73, 036621, 2006.

[200] W. J. Firth and A. J. Scroggie. Optical bullet holes: robust controllable localized states of a nonlinear cavity. *Phys. Rev. Lett.*, 76, 1623–1626, 1996.

[201] L.-C. Crasovan, B. A. Malomed, and D. Mihalache. Stable vortex solitons in the two-dimensional Ginzburg-Landau equation. *Phys. Rev. E*, 63, 016605, 2000.

[202] A. G. Vladimirov, S. V. Fedorov, N. A. Kaliteevskii, G. V. Khodova, and N. N. Rosanov. Numerical investigation of laser localized structures. *J. Opt. B*, 1, 101–106, 1999.

[203] V. V. Afanasjev, N. Akhmediev, and J. M. Soto-Crespo. Three forms of localized solutions for the quintic complex Ginzburg-Landau equation. *Phys. Rev. E*, 53(2), 1931–1939, 1996.

[204] G. Slekys, K. Staliunas, and C. O. Weiss. Spatial localized structures in resonators with saturable absorber. *Opt. Comm.*, 149(1-3), 113–116, 1998.

[205] B. Schäpers, T. Ackemann, and W. Lange. Robust control of switching of localized structures and its dynamics in a single-mirror feedback scheme. *J. Opt. Soc. Am. B*, 19(4), 707–715, 2002.

[206] M. Pesch, E. Große-Westhoff, T. Ackemann, and W. Lange. Observation of a Discrete Family of Dissipative Solitons in a Nonlinear Optical System. *Phys. Rev. Lett.*, 95, 143906, 2005.

[207] N. N. Rozanov. Localized Optical Structures in the SCheme of a Nonlinear Layer with a Feedback Mirror. *Opt. Spectrosc.*, 88(2), 276–279, 2000.

[208] I. S. Aranson and L. S. Tsimring. Pattern and collective behavior in granular media: Theoretical Concepts. *Rev. Mod. Phys.*, 78, 641–692, 2006.

[209] J. J. Niemela, G. Ahlers, and D. S. Cannell. Localized Traveling-Wave States in Binary-Fluid Convection. *Phys. Rev. Lett.*, 64(12), 1365–1368, 1990.

[210] K. E. Anderson and R. P. Behringer. Traveling wave convection patterns in an annular cell. *Physica D*, 51(1-3), 444–449, 1991.

[211] P. Kolodner. Stable, unstable, and defected confined states of traveling-wave convection. *Phys. Rev. E*, 50(4), 2731–2755, 1994.

[212] O. Descalzi. Static, oscillating modulus, and moving pulses in the one-dimensional quintic complex Ginzburg-Landau equation: An analytic approach. *Phys. Rev. E*, 72, 046210, 2005.

[213] E. N. Tsoy and N. Akhmediev. Bifurcation from stationary to pulsating solitons in the cubic-quintic complex Ginzburg-Landau equation. *Phys. Lett. A*, 343, 417–422, 2005.

[214] J. M. Soto-Crespo, N. Akhmediev, and A. Ankiewicz. Pulsating, creeping, and erupting solitons in dissipative systems. *Phys. Rev. Lett.*, 85(14), 2937–2940, 2000.

[215] V. V. Afanasjev, B. A. Malomed, and P. L. Chu. Stability of Bound States of Pulses in the Ginzburg-Landau Equations. *Phys. Rev. E*, 56(5), 6020–6025, 1997.

[216] B. A. Malomed. Potential of interaction between two- and three-dimensional solitons. *Phys. Rev. E*, 58(6), 7928–7933, 1998.

[217] A. G. Vladimirov, G. V. Khodova, and N. N. Rosanov. Stable bound states of one-dimensional autosolitons in a bistable layer. *Phys. Rev. E*, 63(056607), 1–6, 2001.

[218] N. N. Rosanov, S. V. Fedorov, and A. N. Shatsev. Motion of clusters of weakly coupled two-dimensional cavity solitons. *J. Exp. Theor. Phys.*, 102(4), 547–555, 2006.

[219] C. Denz, M. Schwab, and C. Weilnau. *Transverse-Pattern Formation in Photorefractive Optics*, volume 188 of *Springer Tracts in Modern Physics*. Springer, Berlin, 2003.

[220] H. Sakaguchi and B. A. Malomed. Stable localized pulses and zigzag striptes in a two-dimensional diffractive-diffusive Ginzburg-Landau equation. *Physica D*, 159(1-2), 91–100, 2001.

[221] S. Longhi. Perturbation of parametrically excited solitary waves. *Phys. Rev. E*, 55(1), 1060–1070, 1997.

[222] G. J. de Valcárcel, E. Roldán, and K. Staliunas. Cavity solitons in nondegenerate optical parametric oscillation. *Opt. Comm.*, 181, 207–213, 2000.

[223] L.-C. Crasovan, B. A. Malomed, D. Mihalache, D. Mazilu, and F. Lederer. Stable solitons of quadratic Ginzburg-Landau equations. *Phys. Rev. E*, 62(1), 1322–1327, 2000.

[224] A. V. Buryak, P. Di Trapani, D. V. Skryabin, and S. Trillo. Optical solitons due to quadratic nonlinearities: from basic physics to futuristic applications. *Phys. Rep.*, 370, 63–235, 2002.

[225] H. Riecke. Self-Trapping of Travelling-Wave Pulses in Binary Mixture Convection. *Phys. Rev. Lett.*, 68(3), 301–304, 1992.

[226] H. Riecke and W.-J. Rappel. Coexisting Pulses in a Model for Binary-Mixture Convection. *Phys. Rev. Lett.*, 68(3), 4035–4038, 1995.

[227] R. J. Deissler and H. R. Brand. Interaction of two-dimensional localized solutions near a weakly inverted bifurcation. *Phys. Rev. A*, 44(6), R3411–R3414, 1991.

[228] R. J. Deissler and H. R. Brand. Interaction of Breathing Localized Solutions for Subcritical Bifurcations. *Phys. Rev. Lett.*, 74(24), 4847–4850, 1995.

[229] V. J. Sánchez-Morcillo, I. Pérez-Arjona, F. Silva, G. J. de Valcárcel, and E. Roldán. Vectorial Kerr-cavity solitons. *Opt. Lett.*, 25(13), 957–959, 2000.

[230] R. Kheradmand, L. A. Lugiato, G. Tissoni, M. Brambilla, and H. Tajalli. Rotating and Fugitive Cavity Solitons in semiconductor microresonators. *Opt. Expr.*, 11(26), 3612–3621, 2005.

[231] N. K. Efremidis and D. N. Christodoulides. Discrete Ginzburg-Landau solitons. *Phys. Rev. E*, 67, 026606, 2003.

[232] F. K. Abdullaev, A. A. Abdumahkm, and B. A. Umarov. Autosoliton in Ablowitz-Ladik chain-with linear damping and nonlinear amplification. *Phys. Lett. A*, 305(6), 371–376, 2002.

[233] K.-I. Maruno, A. Ankiewicz, and N. Akhmediev. Dissipative solitons of the discrete complex cubic-quintic Ginzburg-Landau equation. *Phys. Lett. A*, 347, 231–240, 2005.

[234] J. M. Soto-Crespo, A. Ankiewicz, and N. Akhmediev. Motion and stability properties of solitons in discrete dissipative structures. *Phys. Lett. A*, 314(1-2), 126–130, 2003.

[235] V. Hakim, M. Rabaud, H. Thomé, and Y. Couder. Directional growth in viscous fingering. In P. Coullet, editor, *New trends in nonlinear dynamics and pattern-forming phenomena: the geometry of nonequilibrium*, page 327 ff. Plenum Press, New York, 1990.

[236] B. A. Malomed, A. G. Vladimirov, G. V. Khodova, and N. N. Rosanov. Stable autosolitons in dispersive media with saturable gain and absorption. *Phys. Lett. A*, 274(3-4), 111–116, 2000.

[237] M. Tlidi, P. Mandel, and R. Lefever. Localized Structures and Localized Patterns in Optical Bistability. *Phys. Rev. Lett.*, 73(5), 640–643, 1994.

[238] L. Y. Glebsky and L. M. Lerman. On small stationary lolcaized solutions for the generalized 1-D Swift-Hohenberg equation. *Chaos*, 5(2), 1054–1500, 1995.

[239] H. Sakaguchi and H. R. Brandt. Stable localized solutions of arbitrary length for the quintic Swift-Hohenberg equation. *Physica D*, 97(1-3), 274–285, 1996.

[240] K. Staliunas and V. J. Sánchez-Morcillo. Dynamics of phase domains in the Swift-Hohenberg equation. *Phys. Lett. A*, 241, 28–34, 1998.

[241] V. J. Sánchez-Morcillo and K. Staliunas. Stability of localized structures in the Swift-Hohenberg equation. *Phys. Rev. E*, 60, 6153–6156, 1999.

[242] C. J. Budd and R. Kuske. Localized periodic patterns for the non-symmetric generalized Swift-Hohenberg equation. *Physica D*, 208, 73–95, 2005.

[243] J. Burke and E. Knobloch. Localized states in the generalized Swift-Hohenberg equation. *Phys. Rev. E*, 73, 056211, 2006.

[244] C. Crawford and H. Riecke. Oscillon-type structures and their interaction in a Swift-Hohenberg model. *Physica D*, 129, 83–92, 1999.

[245] Y. Tu. Worm structure in the modified Swift-Hohenberg equation for electroconvection. *Phys. Rev. E*, 56(4), R3765–R3768, 1997.

[246] H. Sakaguchi and H. R. Brandt. Standing Wave Localized Squares in Pattern-Forming Nonequilibrium Systems. *J. Phys. II*, 7, 1325–1330, 1997.

[247] V. J. Sánchez-Morcillo, E. Roldán, G. J. de Valcárcel, and K. Staliunas. Generalized complex Swift-Hohenberg equation for optical parametric oscillators. *Phys. Rev. A*, 56(4), 3237–3244, 1997.

[248] S. Trillo and W. Torruellas. *Spatial Solitons*, volume 82 of *Springer Series in Optical Sciences*. Springer, Berlin, 2001.

[249] Y. S. Kivshar and G. P. Agrawal. *Optical Solitons. From Fibers to Photonic Crystals*. Academic press, London, 2003.

[250] K. Staliunas, M. F. H. Tarrojo, G. Slekys, C. O. Weiss, and L. Dambly. Analogy between photorefractive oscillators and class-A lasers. *Phys. Rev. A*, 51(5), 4140–4151, 1995.

[251] J. LEga, J. V. Moloney, and A. C. Newell. Universal description of laser dynamics near threshold. *Physica D*, 83(4), 478–498, 1995.

[252] S. Longhi and A. Geraci. Swift-Hohenberg equation for optical parametric oscillators. *Phys. Rev. A*, 54(5), 4581–4584, 1996.

[253] A. A. Golovin, B. J. Matkowsky, and A. A. Nepomnyashchy. A complex Swift-Hohenberg equation coupled to the Goldstone mode in the nonlinear dynamics of flames. *Physica D*, 179, 183–210, 2003.

[254] J. M. Soto-Crespo and N. Akhmediev. Composite solitons and two-pulse generation in passively mode-locked lasers modeled by the complex quintic Swift-Hohenberg equation. *Phys. Rev. E*, 66, 066610, 2002.

[255] Y. Pomeau. Front motion, metastability and subcritical bifurcations in hydrodynamics. *Physica D*, 23, 3–11, 1986.

[256] V. B. Tarananko, M. Zander, P. Wobben, and C. O. Weiss. Stability of localized structures in degenerate wave mixing. *Appl. Phys. B*, 69, 337–339, 1999.

[257] V. B. Tarananko, K. Staliunas, and C. O. Weiss. Pattern formation and localized structures in degenerate optical parametric mixing. *Phys. Rev. Lett.*, 81, 2236–2239, 1998.

[258] G. J. de Valcárcel, K. Staliunas, E. Roldán, and V. J. Sánchez-Morcillo. Transverse patterns in degenerate optical parametric oscillation and degenerate four-wave mixing. *Phys. Rev. A*, 54(2), 1609–1624, 2000.

[259] C. O. Weiss, M. Vaupel, K. Staliunas, G. Slekys, and W. B. Taranenko. Solitons and vortices in lasers. *Appl. Phys. B*, 68, 151–168, 1999.

[260] V. Petrov, Q. Ouyang, and H. L. Swinney. Resonant pattern formation in a chemical system. *Nature*, 388(6643), 655–657, 1997.

[261] J. von Hardenberg, E. Meron, M. Shachak, and Y. Zarmi. Diversity of Vegetation Patterns and Desertification. *Phys. Rev. Lett.*, 87(19), 198101, 2001.

[262] L. Stollenwerk, S. Amiranashvili, J.-P. Boeuf, and H.-G. Purwins. Measurement and 3D simulation of self-organized filaments in a barrier discharge. *Phys. Rev. Lett.*, 96(25), 255001, 2006.

[263] Y. Kobayashi and M. Sano. Aggregated spots and waving loops in a reaction-advection-diffusion system with a global coupling. *Phys. Rev. E*, 73(1), 015104, 2006.

[264] H. Haken. *Synergetics, An Introduction.* 3rd ed. Springer Ser. Synergetics, Berlin, Heidelberg, New York, 1983.

[265] H. Haken. *Advanced Synergetics. Instability Hierarchies of Self-Organizing Systems and Devices*, volume 20 of *Springer Ser. Syn.* Berlin, 2 edition, 1987.

[266] J. Guckenheimer and P. Holmes. *Nonlinear Oscillations, Dynamical Systems and Bifurcations of Vector Fields.* Springer, New York, 1983.

[267] V. I. Karpman. Soliton evolution in the presence of perturbation. *Phys. Scr.*, 20(3–4), 462–478, 1979.

[268] D. J. Kaup and A. C. Newell. Evolution equations, singular dispersion-relations, and moving eigenvalues. *Adv. Math.*, 31(1), 67–100, 1979.

[269] A. Ankiewicz and N. Akhmediev. Moving fronts for complex Ginzburg-Landau equation with Raman term. *Phys. Rev. E*, 58(5), 6723–6727, 1998.

[270] G. Lythe and F. G. Mertens. Rice's ansatz for overdamped ϕ^4 kinks at finite temperature. *Phys. Rev. E*, 67, 027601, 2003.

[271] M. Meister, F. G. Mertens, and A. Sánchez. Soliton diffusion on the classical, isotropic Heisenberg chain. *Europ. J. Phys. B*, 20, 405–417, 2003.

[272] J. P. Zagarodny, Y. Gaididei, D. D. Sheka, J.-G. Caputo, and F. G. Mertens. Importance of the Internal Shape Mode in Magnetic Vortex Dynamics. *Phys. Rev. Lett.*, 93(16), 167201, 2004.

[273] P. Tchofo Dinda, A. B. Moubissi, and K. Nakkeeran. Collective variable theory for optical solitons in fibers. *Phys. Rev. E*, 64, 016608, 2000.

[274] P. Tchofo Dinda, A. B. Moubissi, and K. Nakkeeran. A collective variable approach for dispersion-managed solitons. *J. Phys. A*, 34, L103–L110, 2001.

[275] S. I. Fewo, J. Atangana, A. Kenfack-Jiotsa, and T. C. Kofane. Dispersion-managed solitons in the cubic complex Ginzburg-Landau equation as perturbations of nonlinear Schrödinger equation. *Opt. Comm.*, 252, 138–149, 2005.

[276] C. Elphick and E. Meron. Localized structures in surface waves. *Phys. Rev. A*, 40(6), 3226–3229, 1989.

[277] C. Elphick, A. Hagberg, B. A. Malomed, and E. Meron. On the Origin of Traveling Pulses in Bistable Systems. *Phys. Lett. A*, 230(1-2), 33–37, 1997.

[278] M. Bode. Front-bifurcations in reaction-diffusion systems with inhomogeneous parameter distributions. *Physica D*, 106(3–4), 270–286, 1997.

[279] C. M. Alfaro, R. D. Benguria, and M. C. Depassier. Finite mode analysis of the generalized Kuramoto-Sivashinsky equation. *Physica D*, 61, 1–5, 1992.

[280] V. S. Gerdjikov, I. M. Uzunov, E. G. Evstatiev, and G. L. Diankov. Nonlinear Schrödinger equation and N-soliton interactions: Generalized Karpman-Solov'ev approach and the complex Toda chain. *Phys. Rev. E*, 55, 6039–6060, 1997.

[281] V. S. Gerdjikov, B. B. Baizakov, M. Salerno, and N. A. Kostov. Adiabatic N-soliton interactions of Bode-Einstein condensates in external potentials. *Phys. Rev. E*, 73, 046606, 2006.

[282] D. Anderson and M. Lisak. Bandwidth limits due to mutual pulse interaction in optical soliton communication systems. *Opt. Lett.*, 11(3), 174–176, 1986.

[283] I. V. Barashenkov and E. V. Zemlyanaya. Stable Complexes of Parametrically Driven, Damped Nonlinear Schrödinger Solitons. *Phys. Rev. Lett.*, 83(13), 2568–2571, 1999.

[284] A. V. Buryak, Y. S. Kivshar, M.-F. Shih, and M. Segev. Induced Coherence and Stable Soliton Spiraling. *Phys. Rev. Lett.*, 82(1), 81–84, 1999.

[285] J. A. Posth, E. W. Laedke, T. Schäfer, and K. H. Spatschek. Quasi-particle approach for interacting optical multiple pulses. *Opt. Comm.*, 246, 529–544, 2005.

[286] B. A. Malomed. Bound Solitons in the Nonlinear Schrödinger-Ginzburg-Landau Equation. *Phys. Rev. A*, 44(10), 6954–6957, 1991.

[287] A. Maimistov, B. Malomed, and A. Desyatnikov. A potential of incoherent appraction between multidimensional solitons. *Phys. Lett. A*, 254, 179–184, 1999.

[288] P. G. Kevredikis, A. Khare, and A. Saxena. Solitary wave interactions in dispersive equations using Manton's approach. *Phys. Rev. E*, 70, 057603, 2004.

[289] C. Elphick, E. Meron, J. Rinzel, and E. A. Spiegel. Impulse patterning and relaxational propagation in excitable media. *J. Theor. Biol.*, 146, 149–268, 1990.

[290] C. Elphick, E. Meron, and E. A. Spiegel. Patterns of propagating pulses. *SIAM J. Appl. Math.*, 50(2), 490–503, 1990.

[291] C. Elphick, G. R. Ierley, O. Regev, and E. A. Spiegel. Interacting localized structures with Galilean invariance. *Phys. Rev. A*, 44(2), 1110–1122, 1991.

[292] S.-I. Ei and T. Ohta. Equation of motion for interacting pulses. *Phys. Rev. E*, 50(6), 4672–4678, 1994.

[293] S. Saprykin, E. A. Demekhin, and Kalliadasis S. Self-Organization of Two-Dimensional Waves in an Active Dispersive-Dissipative Nonlinear Medium. *Phys. Rev. Lett.*, 94, 224101, 2005.

[294] P. C. Bressloff. Weakly interacting pulses in synaptically coupled neural networks. *SIAM J. Appl. Math.*, 66(1), 57–81, 2005.

[295] A. I. Maimistov. Evolution of solitary waves which are approximately solitons of a nonlinear Schrödinger equation. *J. Exp. Theor. Phys.*, 77(5), 727–731, 1993.

[296] V. I. Kruglov, V. M. Volkol, R. A. Vlasov, and V. V. Drits. Anto-waveguide propagation and the collapse of spiral light beams in non-linear media. *J. Phys. A*, 21, 4381–4395, 1988.

[297] V. Skarka and N. B. Aleksić. Stability Criterion for Dissipative Solutions of the One-, Two-, and Three-dimensional Complex Cubic-Quintic Ginzburg-Landau Equations. *Phys. Rev. Lett.*, 96, 013903, 2006.

[298] D. Anderson. Variational approach to nonlinear pulse propagation in optical fibers. *Phys. Rev. A*, 27(6), 3135–3145, 1983.

[299] R. Friedrich. Group Theoretic Methods in the Theory of Pattern Formation. In G. Radons, W. Just, and P. Häussler, editors, *Collective dynamics of nonlinear and disordered systems*, pages 61–84. Springer, Berlin, 2004.

[300] R. D. Richtmyer. *Principles of Advanced Mathematical Physics*, volume I. Springer-Verlag, Berlin, 1985.

[301] V. B. Taranenko, C. O. Weiss, and W. Stolz. Spatial solitons in a pumped semiconductor resonator. *Opt. Lett.*, 26(20), 1574–1576, 2001.

[302] V. B. Taranenko, G. Slekys, and C. O. Weiss. Spatial resonator solitons. *Chaos*, 13(2), 777–790, 2003.

[303] P. Schütz, M. Bode, and H.-G. Purwins. Bifurcations of Front Dynamics in a Reaction-Diffusion System with Spatial Inhomogeneities. *Physica D*, 82(4), 382–397, 1995.

[304] A. Kulka, M. Bode, and H.-G. Purwins. On the Influence of Inhomogeneities in a Reaction Diffusion System. *Phys. Lett. A*, 203, 33–39, 1995.

[305] T. Maggipinto, M. Brambilla, G. K. Harkness, and W. J. Firth. Cavity solitons in semiconductor microresonators: Existence, stability, and dynamical properties. *Phys. Rev. E*, 62(6), 8726–8739, 2000.

[306] A. J. Scroggie, J. Jeffers, G. McCartney, and G.-L. Oppo. Reversible soliton motion. *Phys. Rev. E*, 71, 046602, 2005.

[307] V. B. Taranenko, I. Ganne, R. J. Kuszelewecz, and C. O. Weiss. Patterns and localized structures in semiconductor resonators. *Phys. Rev. A*, 61, 063818, 2000.

[308] S. Barland, J. R. Tredicce, M. Brambilla, L. A. Lugiato, S. Balle, M. Giudici, T. Maggipinto, L. Spinelli, G. Tissoni, T. Knödl, M. Miller, and R. Jäger. Cavity solitons as pixels in semiconductor microcavities. *Nature*, 419(6980), 699–702, 2002.

[309] X. Hachair, S. Barland, L. Furfaro, M. Guidici, S. Balle, J. R. Tredicce, M. Brambilla, T. Maggipinto, I. M. Perrini, G. Tissoni, and L. Luigato. Cavity solitons in broad-area vertical-cavity surface-emitting lasers below threshold. *Phys. Rev. A*, 69, 043817, 2004.

[310] M. Saffman, D. Montgomery, and D. Z. Anderson. Collapse of transverse-mode continuum in a self-imaging photorefractively pumped ring resonator. *Opt. Lett.*, 19, 518–520, 1994.

[311] B. Gütlich, R. Neubecker, M. Kreutzer, and T. Tschudi. Control and manipulation of solitary structures in a nonlinear optical single feedback experiment. *Chaos*, 13(1), 239–246, 2003.

[312] B. Gütlich, H. Zimmermann, C. Denz, R. Neubecker, M. Kreutzer, and T. Tschudi. Forcing and control of localized states in optical single feedback systems. *Appl. Phys. B*, 81, 927–936, 2005.

[313] A. S. Moskalenko. Dynamische gebundene Zustände und Drift-Rotations-Dynamik von dissipativen Solitonen. Master's thesis, Institut für Angewandte Physik, Westfälische Wilhelms-Universität Münster, 2002.

[314] S. V. Gurevich, Sh. Amiranashvili, and H.-G. Purwins. Breathing dissipative solitons in three-component reaction-diffusion system. *Phys. Rev. E*, 74, 066201, 2006.

[315] K. Staliunas, V. B. Taranenko, G. Slekys, R. Viselga, and C. O. Weiss. Moving spatial solitons in active nonlinear-optical resonators. *Phys. Rev. A*, 57(1), 599–604, 1998.

[316] J. P. Gollub and C. W. Meyer. Symmetry-breaking instability on a fluid surface. *Physica D*, 6, 337–346, 1983.

[317] G. H. Gunaratne, M. E., and M. Gorman. Asymmetric cells and rotating rings in cellular flames. *Mod. Phys. Lett. B*, 10(28), 1379–1387, 1996.

[318] M. Rabaud, Y. Couder, and S. Michalland. Wavelength selection and transients in the one-dimensional array of cells of the printer's instability. *Europ. J. Mech. B*, 10(2), 253–260, 1991.

[319] V. Steinberg, G. Ahlers, and D. S. Cannell. Pattern formation and wave-number selection by Rayleigh-Bénard convection in a cylindrical container. *Phys. Scr.*, 32, 534–547, 1985.

[320] L. Stollenwerk and H.-G. Purwins. Drift Bifurcation of Dissipative Solitons in Barrier Gas Discharge. *Europhy. Lett.*, 70(1), 22–28, 2005.

[321] M. C. Cross and P. C. Hohenberg. Pattern formation outside of equilibrium. *Rev. Mod. Phys.*, 65(3), 851–1112, 1993.

[322] K. A. Gorshkov, L. A. Ostrovskiy, and V. V. Papko. Interactions and bound states of solitons as classical particles. *J. Exp. Theor. Phys.*, 44, 306–311, 1976.

[323] Y. Kodama and K. Nozaki. Soliton interaction in optical fibers. *Opt. Lett.*, 12(12), 1038–1040, 1987.

[324] V. I. Karpman and V. V. Solov'ev. A perturbational approach to the two-soliton systems. *Physical D*, 3(3), 487–502, 1981.

[325] H. Willebrand. *Strukturbildung in lateral ausgedehnten Gasentladungssystemen.* Dissertation, Institut für Angewandte Physik, Westfälische Wilhelms-Universität Münster, 1992.

[326] S. Nasuno. Dancing "atoms" and "molecules" of luminous gas-discharge spots. *Chaos*, 13(3), 1010–1013, 2003.

[327] K. H. Schoenbach, M. Moselhy, and W. Shi. Self-organization in cathode boundary layer microdischarges. *Plasma Sources Sci. Techn.*, 13, 177–185, 2004.

[328] I. Brauer. *Experimentelle und numerische Untersuchungen zur Strukturbildung in dielektrischen Barrierenentladungen.* PhD thesis, Westfälische Wilhelms–Universität Münster, 2000.

[329] O. Lioubashevski, H. Arbell, and J. Fineberg. Dissipative Solitary States in Driven Surface Waves. *Phys. Rev. Lett.*, 76(21), 3959–3962, 1996.

[330] O. Lioubashevski, Y. Hamiel, A. Agnon, Z. Reches, and J. Fineberg. Oscillons and propagating solitary waves in a vertically vibrated colloidal suspension. *Phys. Rev. Lett.*, 83(16), 3190–3193, 1999.

[331] R. Schmeling. *Experimentelle und numberische Untersuchungen von Strukturen in einem Reaktions-Diffusions-System anhand eines elektrischen Netzwerkes.* Dissertation, Institut für Angewandte Physik, Westfälische Wilhelms-Universität Münster, 1994.

[332] S. Residori and T. Nagaya A. Petrossian. Optocal localised structures and their dynamics. *Europhy. Lett.*, 63(4), 531–537, 2003.

[333] S. Residori, A. Petrossian, T. Nagaya, C. S. Riera, and M. G. Clerc. Fronts and localized structures in an liquid-crystal-light-valve with optical feedback. *Physica D*, 199(1-2), 149–165, 2004.

[334] M. G. Clerc, A. Petrossian, and S. Residori. Bouncing localized states in a liquid-crystal light-valve experiment. *Phys. Rev. E*, 71, 015205, 2005.

[335] Y. Larionova and C. O. Weiss. Spatial semiconductor resonator solitons with optical pumping. *Opt. Expr.*, 13(26), 10711–10716, 2005.

[336] P. L. Ramazza, E. Benkler, S. Ducci, S. Boccaletti, and F. T. Arecci. Tailoring the profile and interaction of optical localized structures. *Phys. Rev. E*, 65, 066204, 2002.

[337] P. L. Ramazza, S. Boccaletti, U. Bortolozzo, and F. T. Arecci. Control of localized structures in an optical feedback interferometer. *Chaos*, 13(1), 335–341, 2003.

[338] B. Lindner, J. García-Ojalvo, A. Neiman, and L. Schimansky-Geier. Effects of noise in excitable systems. *Phys. Rep.*, 392, 321–424, 2004.

[339] L. Schimansky-Geier and C. Zülicke. Kink propagation induced by multiplicative noise. *Z. Phys. B*, 82, 157–162, 1991.

[340] C. W. Gardiner. *Handbook of stochastic methods*. Springer, Berlin, 2 edition, 1997.

[341] H. Haken. *Synergetics: Introduction and Advanced topics*. Springer, Berlin, 2004.

[342] W. Horsthemke and R. Lefever. *Noise-induced transitions*. Springer, Berlin, 1984.

[343] W. C. Kerr and A. J. Graham. Generalized phase space version of Langevin equations and associated Fokker-Planck equations. *Europ. Phys. J. B*, 15, 305–311, 2000.

[344] L. Bachelier. Theorie de la speculation. *Ann. Scient. Ecole Norm. Super.*, 17, 21–86, 1900.

[345] M. von Smoluchowski. Zur kinetischen Theorie der Brownschen Molekularbewegung und der Suspensionen. *Ann. Phys.*, 21, 756–780, 1906.

[346] A. Einstein. Zur Theorie der Brownschen Bewegung. *Ann. Phys.*, 17, 549, 1905.

[347] S. Kim. Brownian motion in assemblies of coupled harmonic oscillators. *J. Math. Phys.*, 15(5), 578–582, 1974.

[348] J. Dunkel, W. Ebeling, and S. A. Trigger. Active and passive Brownian motion of charged particles in two-dimensional plasma models. *Phys. Rev. E*, 70(2), 046406, 2004.

[349] F. Jülicher and J. Prost. Cooperative Molecular Motors. *Phys. Rev. Lett.*, 75(13), 2618–2621, 1995.

[350] A. Buonocore and L. M. Ricciardi. Exploiting thermal noise for an efficient acto-myosin sliding mechanism. *Math. Biosci.*, 182(1), 139–149, 2003.

[351] N. Komin, U. Erdmann, and L. Schimasky-Geier. Random walk theory applied to Daphnia motion. *Fluct. Noise Lett.*, 4(1), L151–L159, 2004.

[352] D. Helbing. Traffic and related self-driven many-particle systems. *Rev. Mod. Phys.*, 73(4), 1067–1141, 2001.

[353] F. Schweitzer and J. A. Holyst. Modelling collective opinion formation by means of active Brownian particles. *Europ. Phys. J. B*, 15(4), 723–732, 2000.

[354] H. Risken. *The Fokker-Planck-Equation. Methods of Solution and Applications.* Springer, Berlin, 2 edition, 1996.

[355] A. S. Mikhailov and D. Meinköhn. *Self-motion in physico-chemical systems far from thermal equilibrium*, volume 484 of *Lecture Notes in Physics*, pages 334–345. Springer, 1997.

[356] U. Erdmann, W. Ebeling, L. Schimansky-Geier, and F. Schweitzer. Brownian particles far from equilibrium. *Europ. Phys. J. B*, 15, 105–113, 2000.

[357] W. Ebeling and I. M. Sokolov. *Statistical Thermodynamics and Stochastic Theory of Nonequilibrium Systems.* World Scientific, Singapore, 2004.

[358] U. Erdmann, W. Ebeling, and A. S. Mikhailov. Noise-induced transition from translational to rotational motion of swarms. *Phys. Rev. E*, 71, 051904, 2005.

[359] F. Verhulst. *Nonlinear differential equations and dynamical systems.* Springer, Berlin, 2 edition, 1996.

[360] H. U. Bödeker, T. D. Frank, R. Friedrich, and H.-G. Purwins. *Stochastic dynamics of dissipative solitons in gas-discharge systems*, volume 89 of *Special Review Book for Research Signpost.* Transworld Research Network, 2006.

[361] M. C. Röttger. Numerische Untersuchungen zur reduzierten Dynamik dissipativer Solitonen in einem dreikomponentigen Reaktions-Diffusions-System. Master's thesis, Institut für Angewandte Physik, Westfälische Wilhelms-Universität Münster, 2003.

[362] A. L. Zanin, E. L. Gurevich, A. S. Moskalenko, H. U. Boedeker, and H.-G. Purwins. Rotating hexagonal pattern in a dielectric barrier discharge system. *Phys. Rev. E*, 70(3), 036202, 2004.

[363] J. H. Chu and I. Lin. Direct Observation of Coulomb Crystals and Liquids in Strongly Coupled RF Dusty Plasmas. *Phys. Rev. Lett.*, 72(25), 4009–4012, 1994.

[364] F. Schweitzer. *Brownian Agents and Active Particles. Collective Dynamics in the Natural and Social Sciences*, volume 16 of *Springer Series in Synergetics.* Springer, Berlin, 2003.

[365] F. Schweitzer, W. Ebeling, and B. Tilch. Statistical mechanics of canonical-dissipative systems and applicaltions to swarm dynamics. *Phys. Rev. E*, 64, 021110, 2001.

[366] M. L Deng and W. Q. Zhu. Stationary motion of active Brownian particles. *Phys. Rev. E*, 69, 046105, 2004.

[367] A. S. Mikhailov and D. H. Zanette. Noise-induced breakdown of coherent collective motion in swarms. *Phys. Rev. E*, 60(4), 4571–4575, 1999.

[368] F. Schweitzer and L. Schimansky-Geier. Clustering of active walkers in a two component system. *Physica A*, 206(4-6), 359–379, 1994.

[369] R. D. Kayser, L. K. Aberle, R. D. Pochy, and L. Lam. Active walker models - tracks and landscapes. *Physica A*, 191(1-4), 17–24, 1992.

[370] R. D. Pochy, R. D. Kayser, L. K. Aberle, and L. Lam. Boltzmann active walkers and rough surfaces. *Physica D*, 66(1-2), 166–171, 1993.

[371] U. Erdmann, W. Ebeling, and V. S. Anishchenko. Excitation of rotational modes in two-dimensional systems of driven Brownian particles. *Phys. Rev. E*, 65(6), 061106, 2002.

[372] U. Erdmann, W. Ebeling, L. Schimansky-Geier, and F. Schweitzer. Collective motion of Brownian particles with hydrodynamic interactions. *Fluct. Noise Lett.*, 3(2), L145–L154, 2003.

[373] R. Mach and F. Schweitzer. Multi-agent model of biological swarming. *Advances in artificial life, Proceedings lecture notes in artificial intelligence*, 2801, 810–820, 2003.

[374] P. Ehrenfest. Phasenumwandlungen im üblichen und erweiterten Sinn, klassifiziert nach den entsprechenden Singularitäten des thermodynamischen Potentials. *Proc. Kon. Akad. Amsterdam*, 36(75b), 153–157, 1934.

[375] M. D'Agostino, F. Gulminelli, P. Chomaz, M. Bruno, F. Cannata, R. Bougault, F. Gramegna, I. Iori, N. Le Neindre, G.V. Margagliotti, A. Moroni, and G. Vannini. Negative heat capacity in the critical region of nuclear fragmentation: an experimental evidence of the liquid-gas phase transition. *Physics Letters B*, 473, 219–225, 2000.

[376] M. Schmidt, R. Kusche, T. Hippler, J. Donges, W. Kronmüller, B. von Issendorff, and H. Haberland. Negative Heat Capacity for a Cluster of 147 Sodium Atoms. *Phys. Rev. Lett.*, 86(7), 1191–1194, 2001.

[377] M. Plazanet, C. Floare, M. R. Johnson, R. Schweins, and H. P. Trommsdorff. Freezing on heating of liquid solutions. *J. Chem. Phys.*, 121(11), 5031–5034, 2004.

[378] J. W. Tester and M. Modell. *Thermodynamics and Its Applications*. Prentice Hall International Series in the Physical and Chemical Engineering Sciences. Prentice Hall PTR, New Jersey, 3 edition, 1997.

[379] M. A. Pokrant, A. A. Broyles, and T. Dunn. Pair-correlation functions for partially ionized hydrogen. *Phys. Rev. A*, 10(1), 379–392, 1974.

[380] D. E. O'Reilly. Oxygen-oxygen pair correlation function for computer-simulated liquid water. *J. Chem. Phys.*, 63(12), 5432–5433, 1975.

[381] D. G. Grier and C. A. Murray. The microscopic dynamics of freezing in supercooled colloidal fluids. *J. Chem. Phys.*, 100(12), 9088–9095, 1994.

[382] R. A. Quinn, C. Cui, J. Goree, J. B. Pieper, H. Thomas, and G. E. Morfill. Structural analysis of a Coulomb lattice in a disty plasma. *Phys. Rev. E*, 53(3), R2049–R2052, 1996.

[383] I. Müller, E. Ammelt, and H.-G. Purwins. Interaction of Filaments in a A.C.-Driven Planar Gas Discharge System. In *Int. Conf. on Phenoma in Ionized Gases ICPIG XXIII*, volume II-182 - II-183, Toulouse, France, 17.7.-22.7.1997, 1997.

[384] U. Bortolozzo and S. Residori. Storage of Localized Structure Matrices in Nematic Liquid Crystals. *Phys. Rev. Lett.*, 96, 037801, 2006.

[385] J. D. Murray. *Mathematical Biology*. Springer, Berlin, 1993.

[386] H. Meinhardt and M. Klingler. A Model for Pattern Formation on the Shells of Molluscs. *J. Theor. Biol.*, 126, 63–89, 1987.

[387] B. N. Vasiev, P. Hogeweg, and A. V. Panfilov. Simulation of Dictyostelium discoideum aggregation via reaction-diffusion model. *Phys. Rev. Lett.*, 73(23), 3173–3176, 1994.

[388] B. Vasiev, F. Siegert, and C. J. Weijer. A Hydrodynamic model for Dictyostelium discoideum Mound Formation. *J. Theor. Biol.*, 184(4), 441–50, 1997.

[389] H. Meinhardt and A. Gierer. Pattern formation by local self-activation and lateral inhibition. *BioEssays*, 22, 752–760, 2000.

[390] R. H. Kessin. *Dictyostelium: Evolution, Cell Biology, and the Development of Multicellularity*. Cambridge University Press, Philadelphia, 2001.

[391] R. A. Arkowitz. Responding to attraction: chemotaxis and chemotropism in Dictyostelium and yeast. *Trends Cell Biol.*, 9(1), 20–27, 1999.

[392] R. L Chisholm and R. A. Firtel. Insights into morphogenesis from a simple developmental system. *Nature Rev. Molec. Cell Biol.*, 5(7), 531–541, 2004.

[393] R. A. Firtel and R. Meili. Dictyostelium: a model for regulated cell movement during morphogenesis. *Curr. Op. Gen. Dev.*, 10(4), 421–427, 2000.

[394] A. R. Kimmel and C. A. Parent. The signal to move: D. discoideum go orienteering. *Science*, 300(5625), 1525–1527, 2003.

[395] M. Meima and P. Schaap. Dictyostelium development - Socializing through cAMP. *Sem. Cell Dev. Biol.*, 10(6), 567–576, 1999.

[396] H. P. Williams and A. J. Harwood. Cell polarity and Dictyostelium development. *Curr. Op. Microbiol.*, 6(6), 621–627, 2003.

[397] P. J. M. van Haastert and P. N. Devreotes. Chemotaxis: signalling the way forward. *Nature Rev. Mol. Cell Biol.*, 5, 626–634, 2004.

[398] C. A. Parent and P. N. Devreotes. A cell's sense of direction. *Science*, 284(5415), 765–770, 1999.

[399] S. Boyden. The chemotactic effect of mixtures of antibody and antigen on polymorphonuclear leukocytes. *J. Exp. Med.*, 115, 453–459, 1962.

[400] J. E. Cutler and J. J. Munoz. A simple in vitro method for studies on chemotaxis. *Proc. Soc. Exp. Biol. Med.*, 147(2), 471–474, 1974.

[401] P. R. Fisher, R. Merkl, and G. Gerisch. Quantitative analysis of cell motility and chemotaxis in Dictyostelium discoideum by using an image processing system and a novel chemotaxis chamber providing stationary chemical gradients. *J. Cell Biol.*, 108, 973–984, 1989.

[402] R. D. Nelson, P. G. Quie, and R. L. Simmons. Chemotaxis under agarose: a new and simple method for measuring chemotaxis and spontaneous migration of human polymorphonuclear leukocytes and monocytes. *J. Immunol.*, 115(6), 1650–1656, 1975.

[403] D. Zicha, G. A. Dunn, and A. F. Brown. A new direct viewing chemotaxis chamber. *J. Cell Sci.*, 99(4), 769–775, 1991.

[404] S. H. Zigmond. Mechanisms of sensing chemical gradients by polymorphonuclear leukocytes. *Nature*, 249(456), 450–452, 1974.

[405] S. H. Zigmond. Ability of polymorphonuclear leukocytes to orient in gradients of chemotactic factors. *J. Cell Biol.*, 75(2), 606–616, 1977.

[406] D. T. Chiu, N. L. Jeon, S. Huang, R. S. Kane, C. J. Wargo, I. S. Choi, D. E. Ingber, and G. M. Whitesides. Patterned deposition of cells and proteins onto surfaces by using three-dimensional microfluidic systems. *Proc. Nat. Acad. Sci. USA*, 97(6), 2408–2413, 2000.

[407] N. L. Jeon, S. K. W. Dertinger, D. T. Chiu, I. S. Choi, A. D. Stroock, and G. M. Whitesides. Generation of solution and surface gradients using microfluidic systems. *Langmuir*, 16(22), 8311–8316, 2000.

[408] N. L. Jeon, H. Baskaran, S. K. W. Dertinger, G. M. Whitesides, L. van de Watern, and M. Toner. Neutrophil chemotaxis in linear and complex gradients of interleukin-8 formed in a microfabricated device. *Nature Biotech.*, 20(82), 826–830, 2002.

[409] F. Lin, W. Saadi, S. W. Rhee, S. J. Wang, S. Mittal, and N. L. Jeon. Generation of dynamic temporal and spatial concentration gradients using microfluidic devices. *Lab on a Chip*, 4(3), 164–167, 2004.

[410] R. Thar and M. Kuhl. Bacteria are not too small for spatial sensing of chemical gradients: an experimental evidence. *Proc. Nat. Acad. Sci. USA*, 100(10), 5748–5753, 2003.

[411] S. J. Wang, W. Saadi, F. Lin, C.M.-C. Nguyen, and N. L. Jeon. Differential effects of EGF gradient profiles on MDA-MB-231 breast cancer cell chemotaxis. *Exp. Cell Research*, 300(1), 180–189, 2004.

[412] D. S. Rhoads, S. M. Nadkarni, L. Song, C. Voeltz, E. Bodenschatz, and J. L. Guan. Using microfluidic channel networks to generate gradients for studying cell migration. *Meth. Mol. Biol.*, 294, 347–357, 2005.

[413] W. J. Bowen and H. L. Martin. The diffusion of adenosine triphosphate through aqueous solutions. *Arch. Biochem. Biophys.*, 107, 30–36, 1964.

[414] D. J. Wessels, H. Zhang, J. Reynolds, K. Daniels, P. Heid, S. J. Lu, A. Kuspa, G. Shaulsky, W. F. Loomis, and D. R. Soll. The internal phosphodiesterase RegA is essential for the suppression of lateral pseudopods during Dictyostelium chemotaxis. *Molec. Biol. Cell*, 11(8), 2803–2820, 2000.

[415] D. J. Wessels, R. Bricks, S. Kuhl, V. Stepanovic, K. J. Daniels, G. Weeks, C. J. Lim, G. Spiegelman, D. Fuller, N. Iranfar, W. F. Loomis, and D. R. Soll. RasC plays a role in transduction of temporal gradient information in the cyclic-AMP wave of Dictyostelium discoideum. *Eukar. cell*, 3(3), 6466–662, 2004.

[416] V. Stepanovic, D. Wessels, K. Daniels, W. F. Loomis, and D. R. Soll. Intracellular role of adenylyl cyclase in regulation of lateral pseudopod formation during Dictyostelium chemotaxis. *Eukar. Cell*, 4(4), 775–786, 2005.

[417] R. F. Probstein. *Physico-Chemical Hydrodynamics*. Wiley-Interscience, New York, 1994.

[418] P. M. W. Janssens and P. J. M. van Haastert. Molecular basis of transmembrane signal transduction in Dictyostelium discoideum. *Microbiol. Rev.*, 51(4), 396–418, 1987.

[419] D. Dormann, J. Y. Kim, P. N. Devreotes, and C. J. Weijer. cAMP receptor affinity controls wave dynamics, geometry and morphogenesis in Dictyostelium. *J. Cell Sci.*, 114(13), 2513–2523, 2001.

[420] R. L. Johnson, R. A. Vaughan, M. J. Caterina, P. J. M. Van Haastert, and P. N. Devreotes. Overexpression of the cAMP Receptor 1 in Growing Dictyostelium Cells. *Biochem.*, 30(28), 6982–6986, 1991.

[421] M. Ueda, Y. Sako, T. Tanaka, P. Devreotes, and T. Yanagida. Single-molecule analysis of chemotactic signalling in Dictyostelium. *Science*, 294(5543), 864–867, 2001.

[422] M. Postma and P. J. M. van Haastert. A Diffusion-Translocation model for Gradient Sensing by Chemotactic Cells. *Biophys. J.*, 81(3), 1314–1323, 2001.

[423] D. Ishii, K. L. Ishikawa, T. Fujita, and M. Nakazawa. Stochastic modelling for gradient sensing by chemotactic cells. *Sci. Technol. Adv. Mat.*, 5, 715–718, 2004.

[424] J. M. Mato, A. Losada, V. Nanjundiah, and T. M. Konijn. Signal input for a chemotactic response in the cellular slime mold Dictyostelium discoideum. *Proc. Nat. Acad. Sci. USA*, 72(12), 4991–4993, 1975.

[425] B. Varnum and D. R. Soll. Effects of cAMP on single cell motility in Dictyostelium. *J. Cell Biol.*, 99(3), 1151–1155, 1984.

[426] M. G. Vicker, W. Schill, and K. Drescher. Chemoattraction and chemotaxis in Dictyostelium discoideum: myxameba cannot read spatial gradients of cyclic adenosine-monophosphate. *J. Cell Biol.*, 98, 2204–2214, 1984.

[427] K. V. Mardia and P. E. Jupp. *Directional Statistics*. Wiley, Chichester, New York, 2000.

[428] H. C. Berg. *E. coli in motion*. Springer, New York, 2003.

[429] R. Fürth. Die Brownsche Bewegung bei Berücksichtigung einer Persistenz der Bewegungsrichtung. Mit Anwendungen auf die Bewegung lebender Infusorien. *Z. Phys. A*, 2(3), 244–256, 1920.

[430] M. H. Gail and C. W. Boone. The locomotion of mouse fibroblasts in tissue culture. *Biophys. J.*, 10(10), 980–992, 1970.

[431] G. A. Dunn and A. F. Brown. A unified approach to analysing cell motility. *J. Cell Sci. Suppl.*, 8, 81–102, 1987.

[432] R. S. Hartman, K. Lau, W. Chou, and T. D. Coates. The fundamental motor of the human neutrophil is not random: evidence for local non-Markov movement in neutrophils. *Biophys. J.*, 76(6), 2535–2545, 1994.

[433] E. L. Ionides, K. S. Fang, R. R. Isseroff, and G. F. Oster. Stochastic models for cell motion and taxis. *J. Math. Biol.*, 48, 23–37, 2004.

[434] D. Selmeczi, S. Mosler, P. H. Hagedorn, N. B. Larsen, and H. Flyvbjerg. Cell Motility as Persistent Random Motion: Theories from Experiments. *Biophys. J.*, 89(2), 912–931, 2005.

[435] A. Czirók, K. Schlett, E. Madarász, and T. Vicsek. Exponential Distribution of Locomotion Activity in Cell Cultures. *Phys. Rev. Lett.*, 81(14), 3038–3041, 1998.

[436] A. Upadhyaya, J. P. Rieu, J. A. Glazier, and Y. Sawada. Anomalous diffusion and non-Gaussian velocity distribution of Hydra cells in cellular aggragates. *Physica A*, 293, 549–558, 2001.

[437] S. Thurner, N. Wick, R. Hanel, R. Sedivy, and L. Huber. Anomalous diffusion on dynamical networks: a model for interacting epithelial cell migration. *Physica A*, 320, 475–484, 2003.

[438] M. Lewandowsky, B. S. White, and F. L. Schuster. Random Movement of Soil Amebas. *Acta Protozool.*, 36, 237–248, 1997.

[439] C. Tsallis. Possible generalization of Boltzmann-Gibbs statistics. *J. Stat. Phys.*, 52(1-2), 479–487, 1988.

[440] C. Tsallis, S. V. F. Levy, A. M. C. Souza, and R. Maynard. Statistical-mechanical foundation of the ubiquity of Lévy distributions in nature. *Phys. Rev. Lett.*, 75(20), 3589–3593, 1995.

[441] S. Abe and Y. Okamoto. *Nonextensive statistical mechanics and its applications*. Springer, Berlin, 2001.

[442] J.-P. Bouchaud and A. Georges. Preswitching electrical properties, 'forming', and switching in amorphous chalcogenide alloy threshold and memory devices. *Phys. Rep.*, 195(4-5), 127–293, 1990.

[443] M. F. Shlesinger, G. M. Zaslavsky, and J. Klafter. Strange Kinetics. *Nature*, 363(6424), 31–37, 1993.

[444] G. M. Viswanathan, S. Buldyrev, S. Havlin, G. M. E. da Luz, E. P. Raposo, and H. E. Stanley. Optimizing the success of random searches. *Nature*, 401, 911–914, 1999.

[445] G. M. Viswanathan, V. Afanasyev, S. V. Buldyrev, E. J. Murphy, P. A. Prince, and H. E. Stanley. Lévy flight search patterns of wandering albatrosses. *Nature*, 381, 413–415, 1996.

[446] C. Beck and E. G. D. Cohen. Superstatistics. *Physica A*, 322, 267–275, 2003.

[447] A. D. Shenderov and M. P. Sheetz. Inversely correlated cycles in speed and turning in an Ameba: An oscillatory model of cell locomotion. *Biophys. J.*, 72(5), 2382–2389, 1997.

I am deeply indebted to Prof. Dr. H.-G. Purwins for allowing me to carry out this work and providing me with many opportunities for stimulating discussions that greatly improved my understanding of basic physical problems.

Dr. J. Berkemeier provided practical help and support in many situations.

I am also very grateful to the members of my workgroup "Pattern formation in Nonlinear Systems" for the permanent exchange of knowledge, the mutual help and the pleasant atmosphere. In particular I would like to acknowledge the help by Dr. Sh. Amiranashvili, Dr. S. Gurevich and Dr. A. W. Liehr on many theoretical and numerical problems.

Dr. T. D. Frank and Prof. Dr. R. Friedrich provided advice and experience in many problems related to stochastic problems and the reduced particle description.

Many thanks go to Prof. Dr. E. Bodenschatz for providing me with the possibility to work in his group at Cornell University and to carry out a fruitful collaboration on the dynamics of cells together with Dr. C. Beta and various other colleagues.

Finally, I would like to acknowledge the support of my parents, relatives and friends who have helped me in various ways. Very special thanks go to S. Halfmann for giving me strength and confidence at all times.

Münster, 04.03.2007